# Visibility and charge density imaging of 2-dimensional semiconductors and devices studied using optical microscopy techniques IRM and BALM

Nathan Ullberg

## To cite this version:

Nathan Ullberg. Visibility and charge density imaging of 2-dimensional semiconductors and devices studied using optical microscopy techniques IRM and BALM. Materials Science [cond-mat.mtrl-sci]. Université Paris-Saclay, 2023. English. NNT : 2023UPAST219 . tel-04812769

HAL Id: tel-04812769
https://theses.hal.science/tel-04812769v1

Submitted on 1 Dec 2024

# Visibility and charge density imaging of 2-dimensional semiconductors and devices studied using optical microscopy techniques IRM and BALM

## *Étude de la visibilité de matériaux 2D semiconducteurs et de leur densité de charge dans des dispositifs électroniques par les techniques de microscopie optique IRM et BALM*

**Thèse de doctorat de l'université Paris-Saclay**

École doctorale n° 575 : *Electrical, Optical, Bio: Physics and Engineering*
Spécialité du doctorat : Électronique, Photonique et Micro-Nanotechnologies
Graduate School : Sciences de l'ingénierie et des systèmes
Référent : Faculté des sciences d'Orsay

Thèse préparée dans l'unité de recherche **NIMBE** (Université Paris-Saclay, CEA, CNRS), sous la direction de **Vincent DERYCKE**, directeur de recherche

**Thèse soutenue à Paris-Saclay, le 20 décembre 2023, par**

**Nathan ULLBERG**

## Composition du jury

Membres du jury avec voix délibérative

| | |
|---|---|
| **Emmanuelle DELEPORTE**<br>Professeure, ENS Paris-Saclay, LUMIN | Présidente |
| **Etienne GAUFRÈS**<br>Chargé de recherche (HDR), Université de Bordeaux, LP2N | Rapporteur & Examinateur |
| **Stéphane LENFANT**<br>Directeur de recherche, Université de Lille, IEMN | Rapporteur & Examinateur |
| **Stéphane BERCIAUD**<br>Professeur, Université de Strasbourg, IPCMS | Examinateur |

THÈSE DE DOCTORAT

NNT : 2023UPAST219

**ÉCOLE DOCTORALE**
Physique et ingénierie :
Electrons, Photons,
Sciences du vivant (EOBE)

**Title:** Visibility and charge density imaging of 2-dimensional semiconductors and devices studied using optical microscopy techniques IRM and BALM

**Keywords:** 2D materials, TMD, MoS2, interference reflection microscopy, BALM, field-effect transistor

**Abstract:** Optical microscopy has played an instrumental role in 2-dimensional (2D) materials research. In particular, the phenomenon of thin-film interference of light has been leveraged to improve contrast and vertical resolution of 2D materials down to the sub-nanometer scale, often via Fabry-Pérot (FP) thin-film resonators. In this thesis, interference reflection microscopy (IRM) and backside absorbing layer microscopy (BALM), both of which harbor FP effects, are developed and utilized to study visibility and topographic inhomogeneities of the 2D semiconductor $MoS_2$. Experimental contrast data are compared against Fresnel-based simulations of contrast. For IRM, an optimal configuration was found by tuning of incident wavelength and top medium refractive index, yielding $\approx 80\%$ contrast. For BALM, the optical properties were measured for both the anti-reflective absorbing layer of nanometric Cr/Au, and an additional insulating $AlO_x$ layer, where for the first time the contrast spectrum for this system was acquired and simulated, yielding a maximum experimental contrast of $\approx 79\%$ for 2D $MoS_2$. Simulations of the optical stack across a variable range of aperture stop diameters and FP layer thicknesses predict further improvement of BALM conditions for high-contrast $MoS_2$ visibility. Additional aspects including z-focus, optical noise, image post-processing, and others were also considered.

Building on the visibility aspects, a charge density imaging capability for 2D $MoS_2$ and other transition metal dichalcogenide crystals was developed by leveraging the charge-dependent complex refractive index near the wavelengths of the excitons. Capacitors and field-effect transistors (FET) of $MoS_2$ were realized, with multiple *in operando* experiments performed in widefield at throughputs up to 4 fps. In IRM mode, a liquid electrolyte gate was used, where charging delays and inhomogeneities due to intra- and inter-flakes resistances in polycrystalline $MoS_2$ are presented. For Schottky barrier $MoS_2$ FETs, the drain versus gate voltage competition for control of the local charge density in the channel was studied for the first time by optical microscopy. Solid-state $MoS_2$ capacitor devices integrated in a BALM optical stack are also presented for the first time, both by experiments and simulations. A preliminary solid-state FET device was realized, exemplifying the powerful idea of combining optical charge imaging with electrical characterization in tandem. This work on visibility and charge imaging aspects aims to widen the role and impact of optical microscopy techniques in the space of 2D materials research.

universite PARIS-SACLAY

ÉCOLE DOCTORALE
Physique et ingénierie :
Electrons, Photons,
Sciences du vivant (EOBE)

**Titre:** Étude de la visibilité de matériaux 2D semiconduteurs et de leur densité de charge dans des dispositifs électroniques par les techniques de microscopie optique IRM et BALM

**Mots clés:** matériaux 2D, TMD, MoS2, IRM, BALM, transistor à effet de champ

**Résumé:** La microscopie optique a joué un rôle déterminant dans la recherche sur les matériaux bidimensionnels (2D). En particulier, les phénomènes d'interférences dans des couches minces ont été exploités pour améliorer le contraste et la résolution verticale lors de l'observation des matériaux 2D et ce jusqu'à l'échelle sub-nanométrique, souvent par l'intermédiaire de résonateurs Fabry-Pérot (FP). Dans cette thèse, la microscopie IRM (interference reflection microscopy) et la microscopie BALM (backside absorbing layer microscopy), qui abritent tous deux des effets FP, sont développées et utilisées pour étudier la visibilité et les inhomogénéités topographiques du $MoS_2$ bidimensionnel. Les données expérimentales de contraste sont comparées à des simulations. Pour l'IRM, une configuration optimale est proposée en ajustant la longueur d'onde incidente et l'indice de réfraction du milieu supérieur, ce qui permet d'obtenir un contraste de $\approx$ 80%. Pour la technique BALM, les propriétés optiques sont mesurées à la fois pour la couche absorbante antireflet de Cr/Au nanométrique et pour une couche isolante supplémentaire d'$AlO_x$. Pour la première fois, le spectre de contraste de ce système a été mesuré et simulé, ce qui a permis d'obtenir un contraste expérimental maximal de $\approx$ 79% pour le $MoS_2$ 2D. Des simulations supplémentaires de l'empilement optique sur une gamme variable d'ouvertures du diaphragme et d'épaisseurs des couches FP prévoient une optimisation possible des conditions BALM pour un contraste encore augmenté. D'autres paramètres ont également été pris en compte, notamment la focalisation en z, le bruit dû aux chemins optiques parasites, les traitements d'image, etc.

En s'appuyant sur ces études de contraste, une technique permettant d'imager la densité de charge dans le $MoS_2$ 2D et d'autres cristaux de dichalcogénures de métaux de transition a été développée. Celle-ci exploite la dépendance de l'indice de réfraction complexe en fonction de la charge aux longueurs d'onde proches de celles des excitons. Des condensateurs et des transistors à effet de champ (FET) en $MoS_2$ ont été fabriqués et de multiples expériences in operando ont été réalisées. En mode IRM, une grille électrolytique a été utilisée. Cela a permis de visualiser les délais et les inhomogénéités de chargement dus aux résistances intra- et inter-feuillets du $MoS_2$ polycristallin. Pour les transistors à effet de champ en $MoS_2$ (de type Schottky) la compétition entre les tensions de drain et de grille pour le contrôle de la densité de charge locale dans le canal a été étudiée pour la première fois par microscopie optique. Des condensateurs en $MoS_2$ à l'état solide intégrés avec l'empilement antireflet en conditions BALM sont également présentés pour la première fois, expérimentalement et au travers de simulations. Un dispositif transistor à l'état solide préliminaire a enfin été réalisé, illustrant les mérites de combiner à l'avenir l'imagerie de charge et les mesures électriques. Ce travail sur les aspects de contraste amélioré et d'imagerie de charge vise à élargir le rôle et l'impact des techniques de microscopie optique dans le domaine des matériaux 2D.

ORCID 0000-0002-7264-7992

# Contents

# Acknowledgments

In this journey, I have had the great pleasure of working with and learning from many individuals. First, I want to thank my PhD supervisor, Vincent Derycke. He has been supportive in multiple regards and taught me many things on how to be a good researcher and scientist. His insights, experience, guidance and presence have been invaluable to my thesis experience. I thank the jury, who agreed to evaluate the work; this includes the two *Rapporteurs* Etienne Gaufrès and Stéphane Lenfant, and the two *Examinateurs* Stéphane Berciaud and Emmanuelle Deleporte the latter of whom served as president of the jury. The discussions during the defense were very fruitful. I thank my mid-thesis committee Julien Chaste and Pierre Legagneux who provided valuable input.

I thank my doctoral school EOBE (No. 575) of Université Paris-Saclay who awarded me a grant from the French Ministry of Higher Education and Research (MESR) which fully sponsored my PhD. This grant has been of great value to me. I thank the head of the EOBE Jean-Christophe Ginefri who is deeply committed to helping PhD students. I thank my *référent* Frédéric Mazaleyrat who discussed with me at length each year and helped me understand my PhD requirements.

I am thankful for the grants 2D-ON-DEMAND (ANR-20-CE09-0026) and MATRA-2D (ANR-20-CE24-0017) from the French *Agence Nationale de la Recherche* (ANR), which helped cover some of the costs of this research. I am thankful for the *CEA Programme Exploratoire Bottom-up : HYPoTHes* project grant. This project, coordinated by Benjamin Grévin, funded my Master Thesis at LICSEN prior to the PhD via a grant. I thank the GDR-HOWDI for two conference grants.

I thank Arianna Filoramo for help with Raman and PL characterization, optics aspects, and for fruitful discussions and input. I thank Stéphane Campidelli for help with chemistry aspects and for fruitful discussions and input. I thank Aldwin Pinto for his technical help on sample preparation and fabrication. I thank Quentin Cogoni and Fabien Gautier for their internship work. I thank Bartłomiej Tywoniuk for our discussions.

In the PhD I had the great pleasure of collaborating with Michele Magnozzi and Ermes Peci from the OptMatLab group of the *Università di Genova* physics department. Their diligent work on ellipsometry characterization and analysis, along with various other aspects added valuable insights into the research, for which I am very grateful and therefore I thank them.

I thank our collaborators at the Centre for Nanoscience and Nanotechnology (C2N), in particular Aymen Mahmoudi, Abdelkarim Ouerghi, Fabrice Oehler, Julien Chaste; with whom we worked with on the study $WSe_2$. I thank Aloïs Arrighi, Benjamin Grévin and Vincent for our collaboration on electrostatic-free topographic measurements of $MoS_2$ on $SiO_2$. I thank Benjamin and Dmitry Aldakov for our collaboration on studying $CbPbBr_3$ nanoparticle perovskites on $MoS_2$ via IRM/BALM.

I thank Bruno Jousselme, Renaud Cornut, Frédéric Oswald, Jean-Christophe Gabriel, Ludovic Tortech, Fanny Hauquier, Guy Deniau, Pascal Viel, Mélanie François, Jocelyne Leroy for their help and for fruitful discussions.

I thank Jean-Roch Huntzinger for our in-depth discussions at the Montpellier SSLDS 2022 PhD summer school.

I thank Mark Levenstein for his advice and for fruitful discussions.

I thank Daniel Medina-Lopez, Cynthia Banga-Kpako, Yuemin Deng, Lina Cherni, Ndrina Limani, Robin Dürr, Raphaël Lamare, Manel Hanana, Lucille Weiss, Roxanne Simoës, Fabien Olivier, Sarah Chevrier, Alexandre Pistol, Alice Boudet, Kévin Chighine, Mahmoud Attia, Roman Chyzh, Konstantin Romanenko, for our discussions.

I thank the former director of NIMBE Serge Palacin for his help. I thank the new director of NIMBE Martine Mayne for her help. I thank Philippe Surugue, Bruno Clotrinari, Thierry Bernard, Nabila Debou, Pierre-François Orfila, Sébastien Delprat, for technical help. I thank the staff of the NIMBE administration Céline Delobel, Stéphanie Testamalle, Bruno Lectard and Emmanuel Convers. I thank the secretaries of EOBE Emilia Davodeau and Julie Delegrange.

I thank all the members of LICSEN and all the members of NIMBE. I enjoyed the many interactions and fruitful discussions.

There are multiple people from the former research groups that I worked in who played an important role on my path towards this PhD project. I am very grateful to these individuals. From Boston University 2D materials group, I thank my former PI Anna K. Swan for her guidance, help, and support. From this group I also thank Bennett Goldberg, Jason Woodrow

Christopher, Xuanye (Fish) Wang, Mounika Vutukuru, Pablo Ferreyra, David Barton, Zhuofa (Marco) Chen, Ryan Cornelius. From my time at the LIRMM laboratory in Montpellier I thank Aida Todri-Sanial, Abhishek Singh Dahiya, Dilek Cakiroglu.

From the Boston University physics department I thank Robert Carey, Ed Kearns, Shyamsunder Erramilli, Claudio Chamon, So-Young Pi, Steve Ahlen.

From Uppsala University I am thankful for scientific discussions on the topic of 2D materials with Carla Puglia, Tomas Edvinsson, Martin Pavelka, Philipp Wolf, Lennart Spode.

I am thankful for scientific discussions that originated in the Paris region; I thank Delphine Cabaret, Olivier Pluchery, Divyansh Anil Khurana, NianJheng Wu, Surabhi K. Sreenivas, Kawther Hadef.

I thank my high-school physics teacher Lt. Col. William (Bill) Luttrell Chamblee. May you rest in peace.

On a personal level, I thank all of my awesome friends.

I thank my parents Eskil and Anne, and my sister Esther, who have supported me and my academic endeavors for many years. Their support has been invaluable.

I thank my extended family.

I thank Jahnavi, who has been with me during my entire PhD journey. She has been a great supporter and wonderful to have by my side!

Finally, I thank *you*, the reader. I hope you will find this thesis interesting and useful.

# Acronyms

| | |
|---|---|
| 2D | 2-dimensional |
| AFM | atomic force microscopy |
| AR layer | anti-reflective layer |
| ARA layer | anti-reflective absorbing layer |
| BALM | backside absorbing layer microscopy |
| BFP | back focal plane |
| $C_{\text{pc}}$ | percent change contrast |
| CAFM | conductive atomic force microscopy |
| CDP | charge density profile |
| CPD | contact potential difference |
| CVD | chemical vapor deposition |
| DEME-TFSI | diethylmethyl(2- methoxyethyl)ammonium bis(trifluoromethylsulfonyl)imide |
| DOS | density of states |
| EOM | electro-optic modulator |
| FET | field-effect transistor |
| FP | Fabry-Pérot |
| GB | grain boundary |
| IL | ionic liquid |
| IRM | interference reflection microscopy |
| KK | Kramers-Krönig |
| KPFM | kelvin probe force microscopy |
| MIM | microwave impedance microscopy |
| MSE | mean squared error |
| NA / INA / CNA | numerical aperture / incident NA / collection NA |
| NP | nanoparticle |
| OD | optical density |
| OM | optical microscopy |
| OPL | optical path length |
| PL | photoluminescence |
| RI | refractive index |
| RICM | reflection interference contrast microscopy |
| ROI | region of interest |
| SE | spectroscopic ellipsometry |
| SEM | scanning electron microscopy |
| SPR | surface plasmon resonance |
| SPRi / SPRM | surface plasmon resonance imaging (or microscopy) |
| TMD | transition metal dichalcogenide |
| TMM | transfer matrix method |
| TSOM | through-focus scanning optical microscopy |
| VASE | variable angle spectroscopic ellipsometry |
| WF | work function |
| XRM | eXcitonic Reflection Microscopy |

# Introduction

Research on 2-dimensional (2D) nanomaterials has emerged as important for fundamental science and for applications in various technologies. Within this class of materials are crystalline semiconducting 2D transition metal dichalcogenides (TMD), a chorus which includes the likes of $MoS_2$, $WS_2$, $SnS_2$, $MoSe_2$, $WSe_2$, $PtSe_2$ to name a few.

A lot of research activity has taken place in this space since the mid-2000s when a 2D TMD was first isolated from its bulk form [1]. Since then, a wide range of properties and prototype devices based on these materials have been explored.

Interestingly, the 2D form of the TMD crystal behaves dramatically different from its 3D counterpart, due to the dimensional confinement along one axis that is imposed which results in a change in various properties. These novel properties can be harnessed in some cases to improve the state of the art of current "3D technologies", such as in the sectors of electronics [2, 3], optics [4, 5, 6], photonics [4, 7, 8], optoelectronics [9, 10] and energy [11, 12].

To achieve novel devices that harness the power of these 2D TMDs require processing steps which are equally important to the synthesis of the 2D TMD itself. Some examples include chemical functionalization, thermal treatment, doping and microfabrication. These processes affect the properties of the 2D material itself or the system in question of which different parts may be coupled.

Furthermore, 2D TMDs are rarely monocrystalline and often are subject to non-homogenous mechanisms either by imperfections or by design. It is therefore highly relevant to perform spatially-resolved characterization of various kinds, including under *in situ* conditions during interactions of various kinds. Among different characterization tools are those based on optical microscopy (OM) techniques.

Furthermore, various devices of 2D TMDs rely on modulation of the charge density, and therefore it is of intrest to perform local measurement of charge variations during *in situ* operation of those devices (also called *in operando*). These include the likes of field-effect transistors (FET) for electronics, modulators for photonics, or redox electrodes in electrochemistry.

Optical interference reflection microscopy (IRM), and backside absorbing layer microscopy

(BALM) have emerged as powerful techniques to study 2D materials both for high-contrast topographical analysis as well as for *in situ* studies of various kinds [13]. Yet, their use remains largely unexplored, especially for 2D semiconductors and devices. For the latter, thanks to a strong correlation between charge and optical properites for the specific case of 2D TMDs, a modality is possible for charge density imaging which also remains unexplored.

**In this context, the objective of this thesis is two-fold: (1) contributing developments of IRM and BALM to study 2D $MoS_2$ topography via both experiment and simulation, and (2) introducing a new charge density imaging mode for $MoS_2$ capacitor and FET devices via both liquid gate and dry solid-state configurations for IRM and BALM respectively.**

The thesis consists of three chapters, and is organized as follows:

In Chapter 1, various properties of 2D TMD crystals including $MoS_2$ are introduced, with a focus on aspects that are relevant in the thesis work. Some literature is also covered, although literature background more specific to the actual thesis work is included in the beginnings of the other two chapters. After the portion on properties and background, various standard characterizations and data of our in-house CVD-grown $MoS_2$ are presented.

Chapter 2 is concerned with the visibility aspects of $MoS_2$ (and a few other 2D materials) in the context of IRM and BALM. The techniques themselves are covered in detail along with the optics theory that serves as basis for the code used to simulated optical response. Together with experimental results, the chapter presents a physical understanding of the factors that influence optical contrast and topographic visibility, as well as ways to improve them, and finally how they were utilized for high-contrast imaging of mostly 2D $MoS_2$. Agnostic to 2D materials, novel experimental and simulated results for BALM are also presented.

Chapter 3, which builds on the previous chapter, is concerned with the use of IRM and BALM for charge density imaging of 2D $MoS_2$ capacitors and devices. After introducing the state of the art for *in operando* studies of such devices, the physical mechanism for how reflectivity can be correlated to charge density is covered. In the results, first the IRM charge density imaging mode is covered where an electrolytic liquid gate was used. Then preliminary results making use of a BALM optical stack are covered, which consists of a solid-state transistor configuration in the dry state. More broadly, I refer to these kinds of imaging as eXcitonic reflection microscopy

(XRM) due to the fundamental role that excitons play in allowing for this mode.

In the final chapter, conclusions and perspectives are covered. The broader picture is addressed, along with discussions on the next steps that could be envisaged for this topic.

# Chapter 1

# Properties of 2D TMDs: background & characterization

## 1.1 . Background

### 1.1.1 . Introduction

2-dimensional (2D) nanomaterials were studied theoretically in the 20th century, but they did not receive widespread attention until 2004. That year, A. Geim, K. S. Novoselov and co-authors unambiguously isolated and measured various properties of graphene [14]—a single (mono) layer of bulk 3D graphite. A key finding was that graphene had significantly different properties compared to its bulk graphite counterpart.

3D graphite is a type of van der Waals (vdW) material, because it consists of stacked monolayers where each layer is weakly bonded to adjacent layers by vdW forces. This makes it practically possible to cleave a single layer from the bulk, for example using adhesive tape—a process known as mechanical exfoliation. This was the method used by the authors to obtain graphene.

The same group also was the first to isolate a 2D layer of a transition metal dichalcogenide (TMD) crystal in 2005 [1], also by exfoliation. TMD crystals consist chemically of one transition metal (M) for every two chalcogen (X) atoms, in the form $MX_2$, where M is typically Mo, W, Pt and X is S, Se, Te, as shown in Figure 1.1(a). Their 3D form was already studied in the 20th century by various techniques, for example by reflection spectroscopy in 1979 [17]. In fact, TMDs like $MoS_2$ have been used as industrial lubricants for many decades.

Like with graphene, the 2D form of a TMD crystal has very different properties from its 3D counterpart. For example, whilst the 3D form is a semiconductor with an indirect bandgap of 1.2 eV, the 2D form has a direct bandgap of $\approx 1.9$ eV. This was shown by T. F. Heinz group in

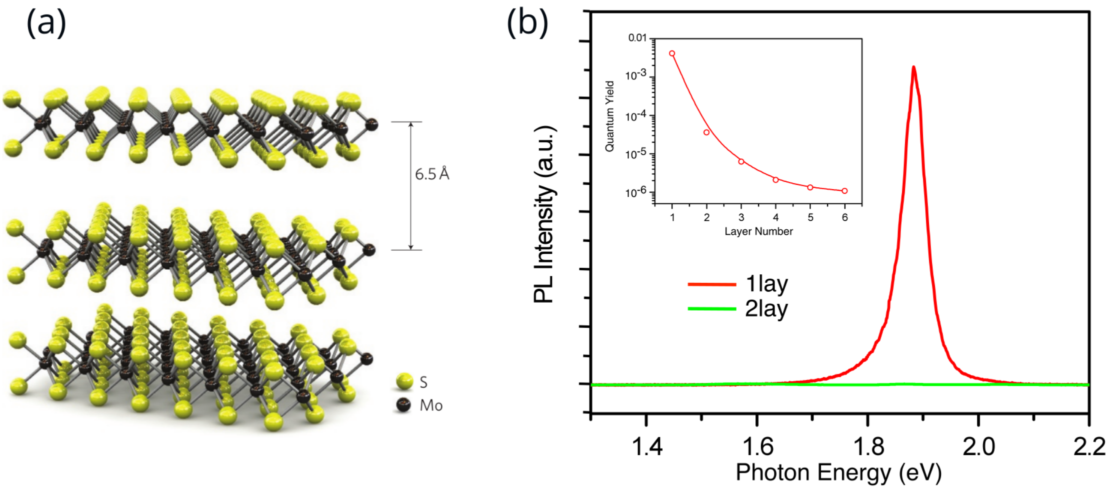

Figure 1.1: (a) Diagram of $MoS_2$ crystal structure, from [15]. (b) Photoluminescence intensity of $MoS_2$ for monolayer, bilayer, trilayer, 4, 5, 6 layer, reproduced from [16].

2010 [16]. Photoluminescence (PL) spectra for different layer numbers of $MoS_2$ were acquired in this article and have been reproduced in Figure 1.1(b). The spectra show that the quantum yield of PL changes by several orders of magnitude as layer number is reduced, and by 2 orders of magnitude from bilayer to monolayer.

The semiconducting nature of 2D TMDs, in contrast to graphene which is a semi-metal, is in part what has led to their widespread attention from researchers in the past $\sim$ 15 years. While metals typically have a Fermi level $E_F$ inside a band of relatively abundant density of states (DOS) of electrons, graphene is different. Its $E_F$ lies at the intersection of two cones of DOS (upper for electrons and lower for holes), where at $T = 0$ K and no defects the DOS is zero. It is thus a semiconductor with zero-bandgap, also called a semi-metal. Although the unique band structure of graphene has fascinated physicists and has certain advantages in some types of applications, it is problematic for applications that require a non-zero bandgap; hence the interest in 2D TMDs.

Various applications of 2D TMDs have been prototyped, including in the fields of electronics, photonics, optics, electrochemistry, and others. This thesis is particularly relevant for the fields enumerated. For electronics, field-effect transistor (FET) devices of 2D TMDs are great candidates for next-generation chips, with potentially better efficiency, performance, and scaling than the current state of the art [2]. The interest for electronics is particlarly evidenced by the involvement of TSMC [18] and Samsung Electronics [19] in recent years.

There is also a relevance in optoelectronics devices such as light-emitting diodes (LED) [9] and photovoltaic (PV) cells [20]. An advantage is also that 2D TMDs are compatible with flexible substrates, which also has been extensively demonstrated [21, 22], including at LICSEN [23]. 2D TMDs have tunable optical (and sometimes infra-red) properties, which could be leveraged in photonic devices like electro-optic modulators (EOM) [24, 25]. This property can also be leveraged for meta-surfaces like tunable metalenses [6] and for beam steering [26].

### 1.1.2 . Crystal structures of mono-,few-,multi- layers

I shall here discuss briefly the crystal structure of a monolayer, as well as few-layered TMDs. Although monolayers are the zenith of 2D materials, equally important are few-homolayer stacks such as bilayers and trilayers. Homolayers consist of stacking the same 2D material, while heterolayers consist of stacking of different 2D materials, which also is an active area of research.

In the thesis, some experiments and simulations concerned homobilayers. Among other results one of them involved the use of IRM to differentiate the stacking order of $WSe_2$ layers (grown by C2N) [27], discussed at the end of Chapter 2.

| Polytype | X-M-X order | Space group | Polytype symbol | Polytype description |
|---|---|---|---|---|
| 2H (AB) | AbA BaB | $P6_3/mmc$ | H | hexagonal |
| 3R (AA) | AbA BcB CaC | $R3m$ | R | trigonal (w. rhombohedral Bravais lattice) |
| 1T | AbC | $P\bar{3}m1$ | T | trigonal (w. hexagonal Bravais lattice) |

Table 1.1: Crystal parameters for the 3 most commonly discussed TMD stacking orders, which include 2H, 3R, 1T. (Polytype descriptions based on [28].)

TMDs are vdW crystals like graphite, also making them easy to exfoliate. For a given stack, a wide variety of stacking orders are possible. First let us note however that, in fact within the monolayer itself the stacking of the chalcogenide–metal–chalcogenide (X-M-X) can also take on different forms, which actually can determine whether the monolayer is semiconducting or metallic. This thesis is only concerned with the monolayer "2H" semiconducting phase, but the "1T" metallic phase can also be attained. Now, regarding the stacking order of multiple layers, the main types are described as either 2H (AB) or 3R (AA).

The described X-M-X order and bilayer stacking orders are summarized in Table 1.1. Diagrams of the stacking orders have been reproduced from [29] in Figure 1.2(a). In 1.2(b), an optical

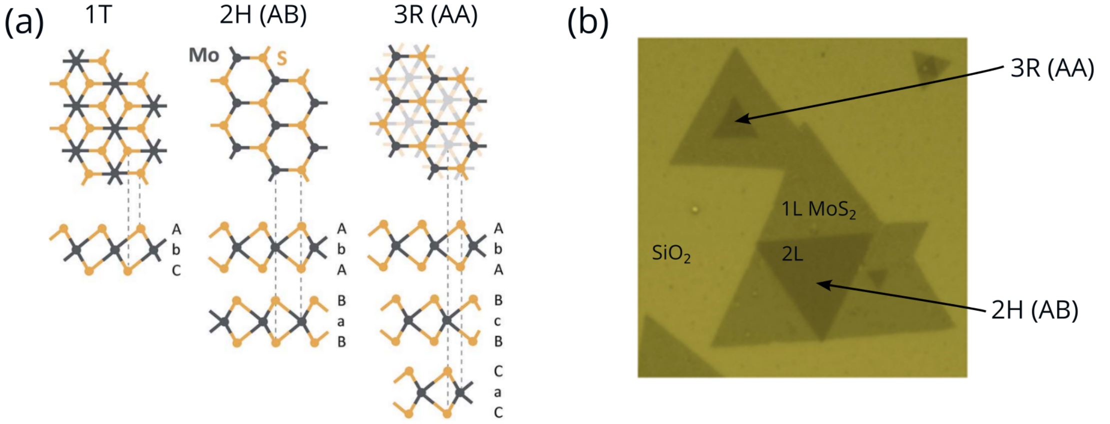

Figure 1.2: (a) Diagrams from [29], showing both the monolayer X-M-X orders of AbC (1T) and AbA (2H), and two possible bilayer stacking orders of 2H (AB) and 3R (AA). The latter 3R depicts three layers in the drawing to clarify the stacking trend, while only two are needed for the 2H (AB) case. (b) From [30], an optical micrograph of CVD-grown $MoS_2$, showing triangle-shaped monolayers which often take on this shape with side-lengths of the order of tens of $\mu$m. The bilayers grow opposite or aligned based on the stacking order as labeled.

micrograph of $MoS_2$ on a $SiO_2$/Si substrate grown by chemical vapor deposition (CVD) is reproduced from [30]. The base triangles are of monolayer thickness, while the bilayer also forms a triangle. In fact, CVD-grown TMDs often form triangles or other regular polygons like hexagons in general. Regarding the bilayer, the general trend is that bilayers of 2H stacking order grow in a 180° fashion to the monolayer, while 3R bilayers are aligned with the monolayer, indicated in (b).

Various additional stacking orders exist. These include for example the 1T′ phase which is discussed further in [31] and [32]. Additionally there are the phases , A′B, AA′ and AB′, which are investigated more in-depth in [30].

### 1.1.3 . Fundamental properties: electronic, optical, phononic

The properties of 2D TMDs have been extensively covered in many review articles, some cited here [33, 34, 35]. Here I present some fundamental properties which will be more specifically relevant in this thesis. As stated earlier, 2D $MoS_2$ of the kind concerned here is of semiconducting nature. Furthermore, the band structure changes drastically from 3D to 2D such that the bulk 3D has an indirect bandgap while the 2D form has a direct bandgap. This was calculated by DFT and plotted in [36] among other places, and reproduced in Figure 1.3.

C

Figure 1.3: From [36], electronic band structure of bulk (3D) $MoS_2$ (left) and of monolayer (2D) $MoS_2$ (right), from DFT calculations. The latter case has a direct band-gap of $E_g = 1.9$ eV.

From the plot we see that the monolayer direct bandgap is 1.9 eV, while for bulk the indirect bandgap was 1.2 eV. Now, this particular calculation actually does not predict a very important feature of 2D $MoS_2$ electronic band structure which is the spin–orbit splitting that splits the valence band at the K-point into two, separated by $E_{so}$. This is shown diagramatically in Figure 1.4(a).

Before describing this further, it is important to introduce the concept of an exciton and trion. In semiconductors, an electron that is excited and residing in the conduction band leaves a hole of corresponding positive charge in the valence band. This electron–hole pair is bound by the Coulomb force, and is called an exciton. The effect is particularly evident when it comes to light absorption and emission mechanisms of a semiconductor. In fact, due to the binding energy of the electron–hole pair, it is possible to excite an electron–hole pair at an energy lower than the "electronic band-gap", which leads to the concept of an "optical bandgap", where $E_g^{\text{elec}} = E_g^{\text{opt}} + E_{b,X}$ where $E_{b,X}$ is the binding energy of the exciton.

The binding energy can be expressed in terms of the hydrogenic model, because the same Coulomb attraction formula as for the proton and electron, holds for the exciton. The formulation differs in that one considers the effective masses of the electron and hole.

The excitons in 2D $MoS_2$ are labeled "A" and "B" based on the two excitons as seen in the simplified band-structure drawing in Figure 1.4(a). In (b) the imaginary relative permittivity was measured by [37] which is related to the resulting absorption coefficient $\alpha(\omega)$. Clearly the A, B, and additional C peak can be seen in the $\varepsilon''$ spectrum. Finally in (c) reproduced from [38], the effects of 3D vs. 2D density of states is illustrated semi-quantitatively, with their effect on resultant absorption. This same paper highlights other excitonic effects in 2D, including the fact that 2D semiconductors have significantly higher exciton binding energies than in 3D semiconductors. This is an important aspect which is highlighted later.

Now, it is also possible for excitons to get charged, in which either another electron or another hole becomes a negative trion ($X^-$) or positive trion ($X^+$). This too has a significant effects on optical properties, and in fact allows the exciton/trion ratio to be tuned via a gate voltage.

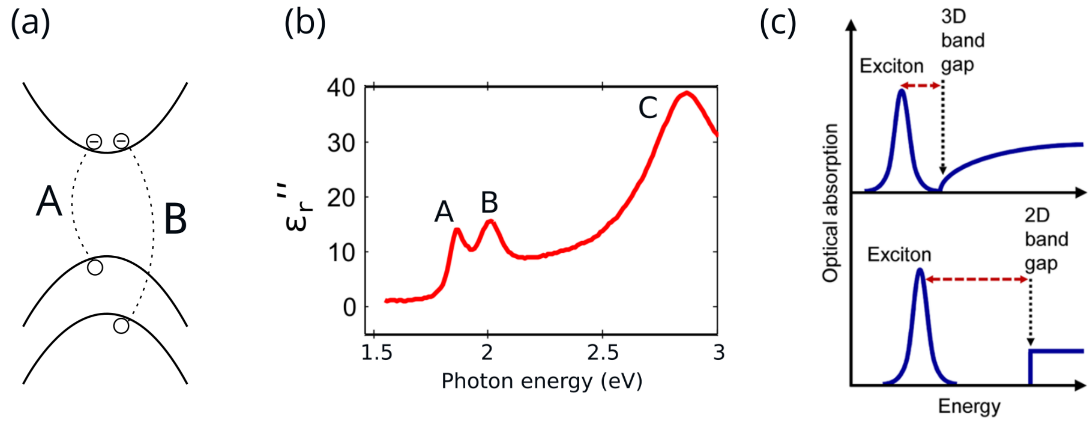

Figure 1.4: (a) Simplified band diagram of monolayer $MoS_2$ with two split-off valence bands and a conduction band. Resultant electron–hole (exciton) transitions shown, which are called "A" and "B" accordingly. (b) From [37] (T. Heinz group), the measured imaginary part of the complex dialectric function of 2D $MoS_2$, corresponding to absorption coefficient. The A, B, C excitons can be seen. (c) From [38], drawing of difference in absorption in a 3D versus 2D semiconductor, due to the differing mathematics of the density of states (DOS)

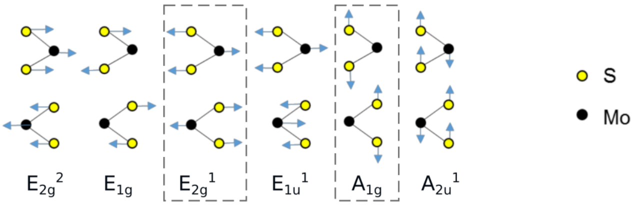

Figure 1.5: From [39], main Raman and IR modes in 2D $MoS_2$, where the Raman-active modes have been boxed.

As discussed later in Chapter 3 this serves as the basis for the charge density imaging.

Finally these 2D TMD semiconductors also have phonon disperions, which determie various properties. Various infra-red (IR) and Raman active modes are reproduced from [39] in Figure 1.5, with the main Raman-active cases enclosed by dashed rectangles. These modes can be measured via optical Raman spectroscopy, which is a very common way to characterize 2D TMDs. Raman spectra that were acquired are shown later in Figure 1.15.

### 1.1.4 . Synthesis of 2D TMDs

The 2D $MoS_2$ used in the thesis is grown in-house by chemical vapor deposition (CVD), and thus it is relevant to cover some aspects of synthesis of 2D TMDs. As mentioned earlier, mechanical exfoliation was initially the primary means of attaining a 2D form of graphite and TMDs. The advantage with exfoliation is that the crystals attained typically have very good purity, decent surface area (hundreds of square microns), and the process is reasonably straightforward. However as the process is very manual and cannot really be integrated in an assembly line it is not feasible for large-scale production and integration with device fabrication processes. Therefore a lot of work has been done on various bottom-up synthesis approaches. Among various approaches, CVD has been developed extensively, along with other approaches like molecular beam epitaxy (MBE), atomic layer deposition (ALD), liquid phase exfoliation (LPE) and metal–organic CVD (MOCVD).

CVD growth is realized by flowing the chemical precursors of a desired material in gas-phase in a tube furnace. The system is arranged such that a chemical reaction results in the growth of the desired material with its desired crystal arrangement, on a target substrate. Early work on CVD synthesis of 2D $MoS_2$ appeared in 2013 [40, 41].

### 1.1.5 . Inhomogeneities part 1: µm-scale

The resulting CVD-grown 2D $MoS_2$ take on a multitude of different morphologies and adlayers. In a "perfect world" one could have a defect-free pure monolayer single crystal but that is rarely the case. Even the most prime CVD-grown 2D $MoS_2$ materials result in a poly-crystalline structure [9], at least as of today, to the author's knowledge. Also, in most cases, instead of attaining a single film, resulting growths consist of isolated or inter-connected polygon morphologies like triangles and hexagons.

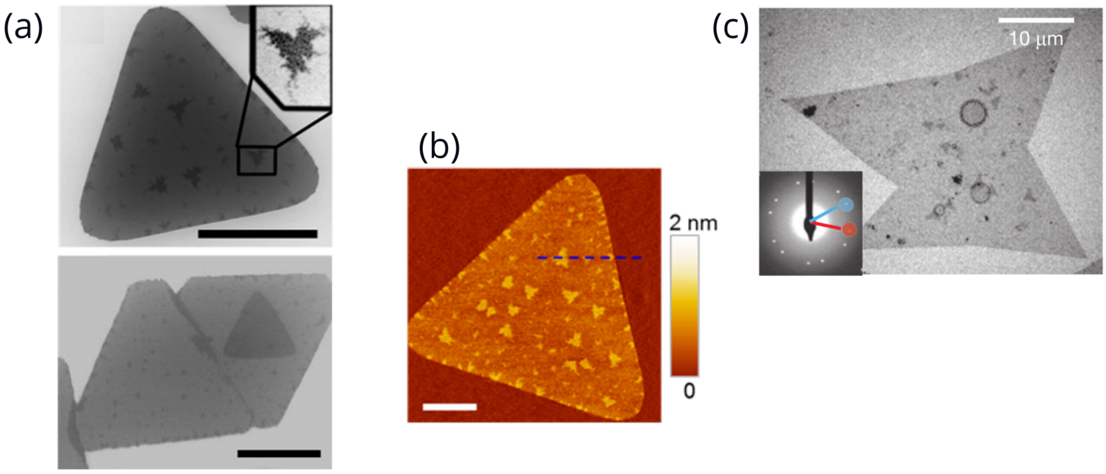

Figure 1.6: (a) SEM images from [42] of CVD-grown $MoS_2$ monolayers, which are covered by dendrite adlayers. Both scale bars are 20 µm. (b) AFM image also from [42] revealing nanometric height profiles of the adlayers. (c) TEM image from [40] of CVD $MoS_2$, showing a variety of adlayers on the monolayer.

Furthermore, it can be difficult to prevent a bi- or multi-layer from forming on the monolayer.

Sometimes, this is desired as was discussed earlier. However, adlayers of differing crystal forms (sometimes amorphous) also are common-place, for example in the form of dendrites (tree-like crystals) [42], or other structures and particulates. Dendrites are shown in Figure 1.6(a), an SEM micrograph reproduced from [42]. Other micron-sized adlayers can be seen by the AFM image in 1.6(b) reproduced from [42], and also from the TEM micrograph in (c) reproduced from [40]. Note that these adlayers are on the µm or 100's nm scale, and can thus be termed "mesoscale" imperfections, which are different than atomistic imperfections like point defects, which are discussed in the next section.

Mesoscale adlayers are not all bad—there are some cases where such adlayers are actually desired. They can for example increase redox activity of a TMD-based electrochemical device [43, 44, 45, 46]. Furthermore, increasing and tuning of the edge sites can improve redox activity as well [11]. Another case where grain boundaries (GB) and other adlayers can improve performance are FET-based sensors where such defects can improve sensitivity to certain analytes. This has been demonstrated for 2D $MoS_2$ FETs by [47, 48] and for graphene FETs by [49, 50, 51]. Furthermore, GB-based SPR sensors with $WS_2$ has been demonstrated [52].

Nevertheless, often such adlayers and GBs are parasitic. For FET devices outside the context of sensing, such as digital logic devices or other analog electronics, it is not desired as it can degrade the charge carrier mobility. Since adlayers of various forms play an important role though, it is important to characterize them and understand their role for a given TMD system.

Adlayers aside, considering the single monolayer itself, various additional mesoscale inhomogeneities can be present. Sometimes they are "clear-cut", for instance in M. Magnozzi et al. 2021 [53] a $WS_2$ monolayer was shown to exhibit three different bisectors of differing optical properties. Some of this data is reproduced in Figure 1.7(a), which consist of an optical micrograph, ellipsometric $\Delta$-parameter map, and PL intensity map in that order.

Raman and PL mapping have arguably been the primary optical techniques to study mesoscale inhomogeneities of monolayer 2D materials, due to factors such as charge and strain [56, 57, 58, 59, 60]. Charge can vary due to defect density but also due to trapped charges in substrate and in adsorbates. For strain, it has its origins mainly during the CVD process due to differences in thermal expansion of TMD and substrate. Furthermore, strain is not released in the same way at the edges or grain boundaries, resulting in strain variations.

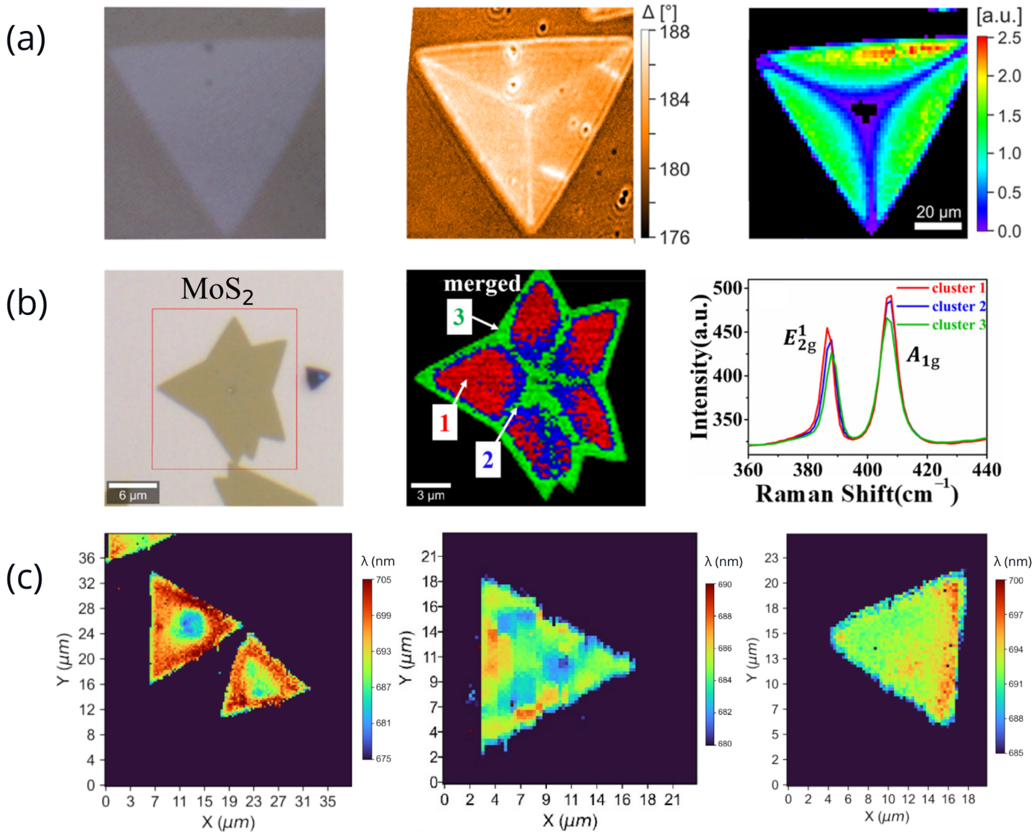

Figure 1.7: (a) From [53], going left to right, an optical micrograph of CVD $WS_2$, a imaging ellipsometry $\Delta$ map, and PL intensity map. Data reveals a rather geometric inhomogeneity of optical properties and PL emission trend. (b) From [54], going left to right, an optical micrograph of CVD $MoS_2$, a Raman map, and representative Raman spectra from the three indicated regions. Inhomogeneity in Raman response is also somewhat geometric trends divided between edge, center, and sector. (c) From [55], PL intensity images of three CVD $MoS_2$ flakes. In this case, the inhomogeneity of PL intensity is more aleatoric.

Among many papers, Xin et al. 2022 [54] revealed inhomogeneities by Raman mapping, some data of which is reproduced in Figure 1.7(b), which shows an optical micrograph, Raman map, and representative spectra from each of the three types of behavior. In this case, there is also a systematic trend with sectors and edge effects. Often though, the variations are more random, as for example illustrated by various PL maps taken by Senkić et al. 2022 [55], some data of which is reproduced in Figure 1.7(c). Finally, scanning probe techniques like KPFM can reveal such variations in charge and other effects, and the literature of which is partially covered in Chapter 3.

### 1.1.6 . Inhomogeneities part 2: atomistic

Having introduced mesoscale inhomogeneities, equally important are the atomistic defects and inhomogeneities. A very common atomistic defect in CVD-grown $MoS_2$ is the presence of sulfur vacancies, a type of point defect, which results in a stoichiometry of the form $MoS_{2-x}$. In fact, the resulting "macroscopic" morphology of flake on the μm-scale is affected by the amount of sulfur available proportionally to the Mo during the growth, as reproduced from Senkić et al. [55] in Figure 1.8(a) (optical micrographs). When there is sufficient sulfur ("sulfur-rich" conditions) the $MoS_2$ takes on a nice equilateral triangle shape, whilst "sulfur-deficient" conditions result in compressed side-lengths.

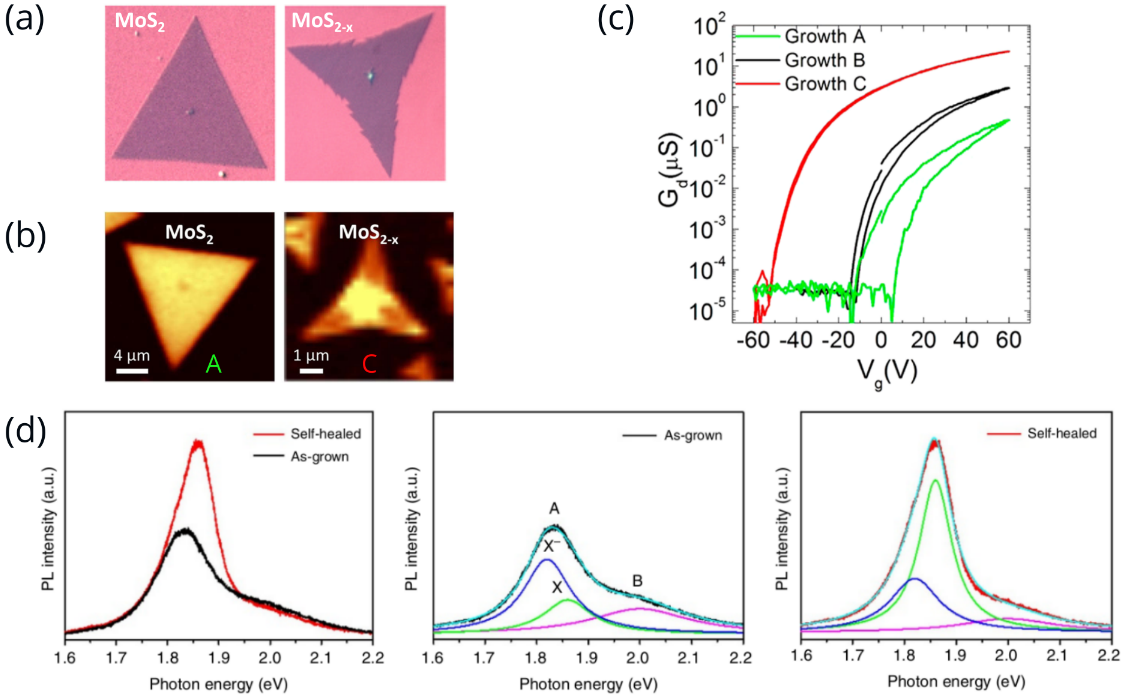

Figure 1.8: (a) From [55], two optical micrographs of CVD $MoS_2$ of differing stoichiometry. Left image is stoichiometric while right image is sulfur deficient. (b) From [61], PL maps of stoichiometric ("growth A") and sulfur deficient ("growth B") CVD $MoS_2$, and corresponding electrical transfer characteristic in (c). (d) From [62], PL spectra of as-grown and self-healed CVD $MoS_2$, where for this group's process the as-grown $MoS_2$ contained various sulfur defects resulting in a prominent trion peak with less prominent neutral exciton peak. After a healing procedure the neutral exciton becomes the prominent peak.

The stoichiometry affects the resulting material properties, including photoluminescence, as reproduced in Figure 1.8(b) from [61] where PL maps were acquired for the different stoichiometries. In fact, while the stoichiometric case (left) has a relatively even PL (labeled "growth A" by the authors), the non-stoichiometric case ("growth C") has mesoscale variations in the PL. The authors also took electrical transfer characteristics of the different growths via FET devices of the flakes, which reveal significantly different transfer characteristics as reproduced in Figure 1.8(c). It is clear in this example that S vacancies result in a strong $n$-type doping.

PL spectra and the fitted exciton/trion energies and linewidths also reveal the effect of atomistic defects. This is reproduced in Figure 1.8(d) from [62]. In their case, the as-grown spectrum reveals a prominent trion peak because of defects. Then, after a healing process that they used, using an acid called PSS, the spectrum changes to a more prominent neutral exciton ($X^0$) peak and less prominent trion ($X^-$) peak, which is more typical of more "intrinsic" 2D $MoS_2$ in ambient conditions.

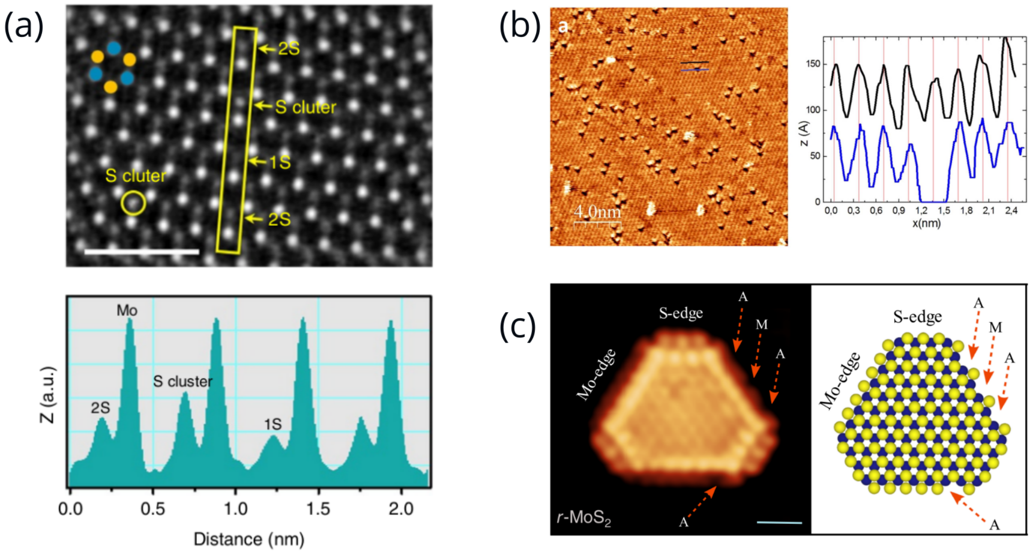

Figure 1.9: (a) From [62], a STEM HAADF image (above) and z-profile (below) of as-grown CVD $MoS_2$, revealing 3 types of atomistic sulfur defects. (b) From [63], an STM image of monolayer $MoS_2$ (left) and line profile (right), revealing atomistic sulfur vacancies. (c) From [46], STM image (left) and diagram (right) revealing atomistic edge behavior differing from the non-edge regions.

Resolution on the atomistic scale can be revealed by (scanning) transmission electron microscopy (TEM), and by related modes like STEM high-angle annular dark field (HAADF). The same group [62] acquired HAADF data of the $MoS_2$ before and after healing. The before case is reproduced in Figure 1.9(a) where various types of sulfur defects are revealed, labeled as S cluster, 1S, 2S. The bottom panel is a line profile of the image (z-contrast). The "after healing" reveals an absence of these defects in the HAADF data.

Scanning tunneling microscopy (STM) also has sufficient resolution and tunneling current contrast to image atomistic defects. This was done for example by Vancsó et al. 2016 [63] as reproduced in Figure 1.9(b), where sulfur vacancies can be seen. Another article from 2020, Salazar et al. [46], examines edge sites in detail with varying types of edge defects. Some of this data is reproduced in 1.9(c) In fact, STM data of $MoS_2$ edge sites can be found as early as 2007 [45].

Reflectance spectra also show changes depending on density of defects, as for example discussed in [64]. This makes sense as reflectance spectra are partly dependent on the absorption coefficient $\alpha$ which in turn is related to emission (PL) [53].

To recap, one must be wary of the various effects of atomistic defects in CVD-grown 2D $MoS_2$ as they can significantly influence the material properties. This is relevant both in Chapters 2 and 3 because of the fact that optical properties ($n(\lambda)$,$\kappa(\lambda)$) and their gate-tunable response are affected by defects.

## 1.1.7 . Effect of environment on TMD properties

Not to be neglected is also the effect of the atmosphere and environment that the 2D material is subject to. The presence of oxygen and water molecules in ambient environment influences both electrical and optical properties, sometimes in a significant manner.

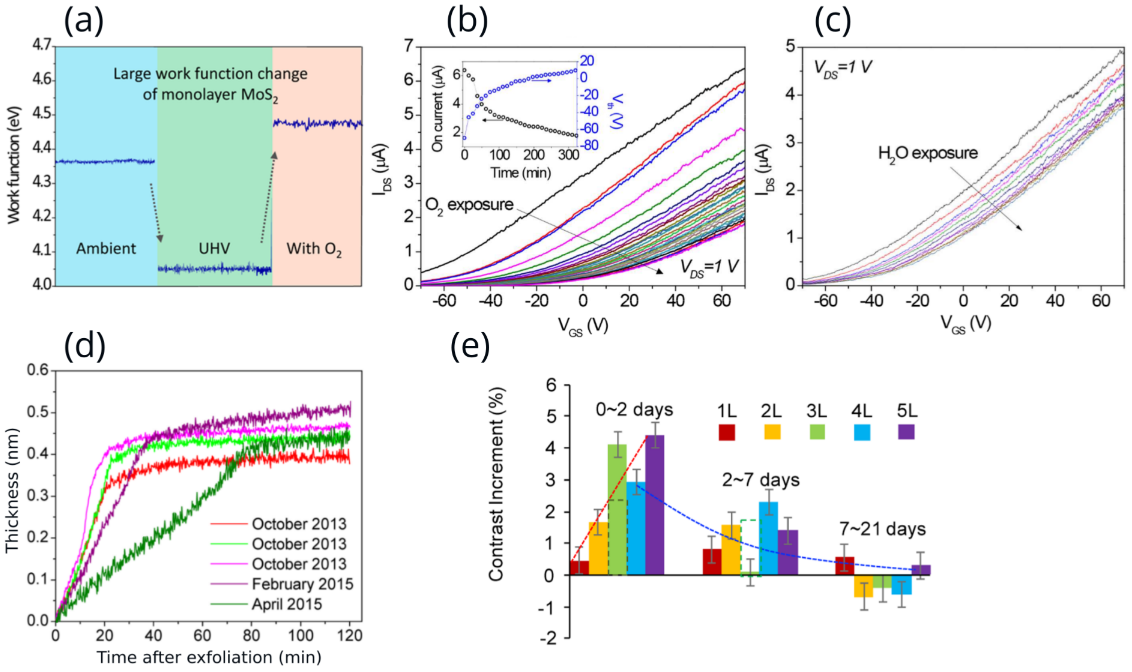

Figure 1.10: (a) From [65], measured work function of 2D $MoS_2$ in ambient, UHV, and $O_2$ conditions. (b) and (c) also from [65] showing how $O_2$ and $H_2O$ exposure both shift the threshold voltage in the $MoS_2$ FET. (d) From [66] showing the thickness of ambient hydrocarbons increasing on a $MoS_2$ monolayer after exfoliation, measured by ellipsometry. (e) From [67], contrast increment changing over the course of days on graphene of different layers, due to hydrocarbons from ambient being deposited.

Many papers have explored the effect of ambient vs. vacuum vs. pure oxygen conditions among others. One such study is Lee et al. 2016 [65], some results of which are reproduced in Figure 1.10(a,b,c). The work function of a TMD can be altered by several hundred meV, by changing ambient, UHV, $O_2$ conditions. In (b), the threshold voltage ($V_{TH}$) of a 2D TMD FET is seen to change upon exposure to oxygen, while the same is also true for exposure to $H_2O$ as shown in (c). Ahn et al. 2017 [68] also provide many insights into ambient effects.

The effect of atmosphere on PL has also been widely investigated, such as by Klement et al. 2018 [69]. In this study, PL spectra were taken in $O_2$ and $N_2$ atmospheres, at the gate voltages $-100, 0, +100$ V. The result of the paper indicates a significant change in the relative intensities of the neutral exciton peak ($X^0$) and trion peak ($X^-$).

Ambient hydrocarbons from the air also can get deposited on 2D materials. Kozbial et al. 2015 [66] showed how the thickness and wettability of freshly exfoliated $MoS_2$ changes as a function of time. One result is reproduced in Figure 1.10(d), where the thickness evolution of ambient hydrocarbons over time was measured using ellipsometry. The nature and amount of hydrocarbon deposition varies depending on various factors. F. Huang group showed in 2018 [67] how the deposition of ambient amorphous carbon films could be detected on graphene mono and multilayers (1L–5L) by optical contrast. Some data is reproduced in Figure 1.10(e) where the contrast increment is changing over the course of days. Apart from [67], the visibility of deposited hydrocarbons by optical microscopy techniques has also been studied by other groups such as in [70] by polarization microscopy.

To recapitulate, it is thus evident that various ambient effects including the gaseous atmosphere and presence of hydrocarbons can alter resulting properties of 2D materials and thus this point should be kept in mind.

# 1.2 . In-house synthesis & characterization

## 1.2.1 . Synthesis

The CVD system we use in-house is fairly standard and is shown in Figure 1.11. We use $SiO_2$/Si as the growth substrate, onto which a seed promoter is spun prior to growth. The promoter we use is perylene-3,4,9,10-tetracarboxylic acid tetrapotassium salt (PTAS). Sulfur powder and $MoO_3$ are used as sources and are sublimated by the furnace which is ramped slowly to 750°C and held for 10 minutes, after which it is cooled.

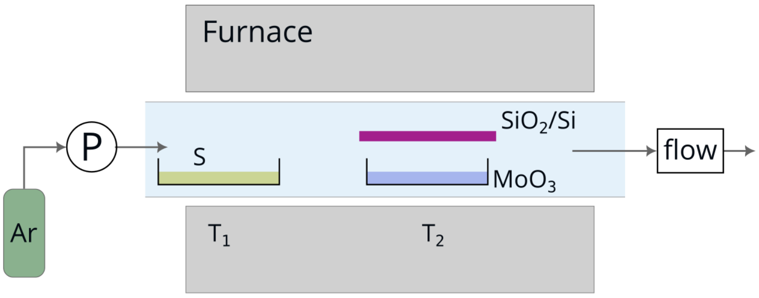

Figure 1.11: Chemical vapor deposition (CVD) setup used at LICSEN to grow 2D $MoS_2$ and other 2D TMDs. A chemical reaction between the sublimated sulfur and $MoO_3$ result in 2D $MoS_2$ on the substrate. Many tunable parameters as shown in the furnance impact the result making it very challenging to consistently grow 2D $MoS_2$. Some include carrier gas, pressure, flow rate, temperatures $T_1$ and $T_2$, sulfur and $MoO_3$ quantities, and many more.

There are a variety of parameters that impact the growth result, many of which cannot be controlled to perfection. This explains why in general a wide variety of morphologies of $MoS_2$ is attained. Some of the parameters include the two temperatures indicated $(T_1, T_2)$, the sulfur quantity, the $MoO_3$ quantity, gas pressure and flow rate, humidity, nature of prepared PTAS and the way it is spun, and many more. In general, CVD processes are difficult to control, due to the nature of the chemical reactions, compared to ALD for example. Yet it provides a practical venue to obtain these materials. Various representative growths were characterized by different methods elaborated below, which enable us to confirm that indeed the 2D $MoS_2$ we grow exhibits the material fingerprints that do match that of state of the art $MoS_2$.

## 1.2.2 . AFM, OM, SEM

In Figure 1.12, atomic force microscopy (AFM) images were attained, of a representative high-quality CVD 2D $MoS_2$ sample. In 1.12(a), three monolayer triangles are present, one of which has a 3R bilayer. Their lateral size is around 5–10 µm which is typical. In 1.12(b) an averaged line profile was taken, and it is seen that between substrate and monolayer there is about 0.91 nm, whilst a smaller 0.47 nm gap from mono to bi-layer. This is in the ballpark of an expected 0.65 nm monolayer thickness. The discrepancy can be due to a few things, such as molecules trapped under the monolayer, or adsorbates on top of it. Yet it is sufficient to confirm a monolayer.

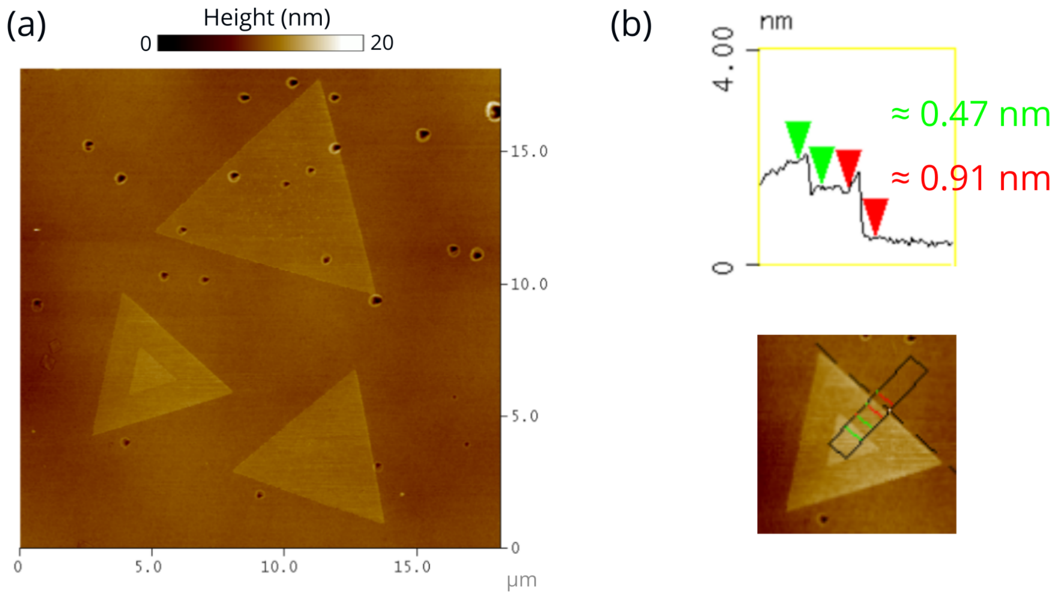

Figure 1.12: (a) AFM image acquired at LICSEN of monolayer (and bilayer) $MoS_2$ grown by CVD. This sample is rather smooth and defect-free, with one flake containing a 3R stacked bilayer. (b) Averaged line profile of the mono/bi-layer flake, giving an approximate value of height as shown. This is relatively consistent with the textbook value of 0.65 nm. Different factors can influence the measured height such as the presence of adsorbates above or below the mono/bi-layer.

The CVD $MoS_2$ topography can also be visualized with high vertical resolution using optical microscopy techniques—which is of course a main objective of the thesis work. Without going into detail since it will be discussed extensively later, a BALM micrograph of CVD $MoS_2$ that I obtained is shown in Figure 1.13(a).

This is an 8-bit (0–255) grayscale image and it is often helpful to adjust the limits, as is done in AFM, for improved visibility. (In this case they are 27–92). The flakes are clearly visible, with the ones on the left resembling those of the AFM image, with 3R bilayers. In 1.13(b)

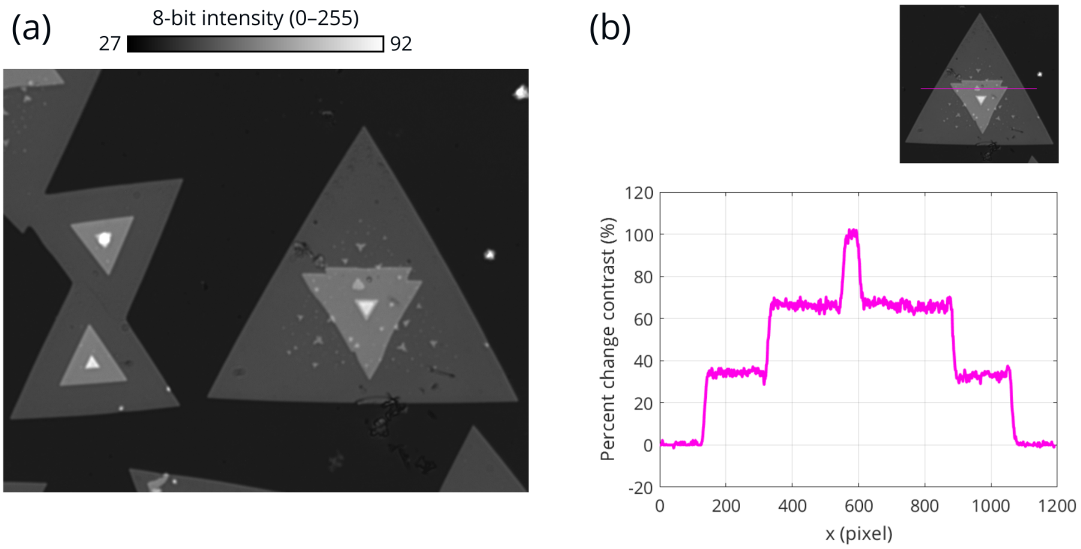

Figure 1.13: (a) Backside absorbing layer microscopy (BALM) 8-bit (0–255) grayscale image of transferred CVD $MoS_2$. The visibility and contrast is significant, showing clearly the mono and multi layers as well as various other adlayers and defects. (b) Single-pixel line profile across substrate, mono, bi, tri layered $MoS_2$. The percent change contrast is significant, at around 40% per layer.

the flake on the right was taken with a single line profile (not averaged) across just 1 pixel. The signal-to-noise is astonishing, and thus the height profile is clearly seen. The substrate was used as an intensity reference and the $MoS_2$ is thus a percent change of the substrate intensity.

Scanning electron microscopy (SEM) images were also taken, shown in Figure 1.14(a) and (b) at different magnifications. SEM allows visualizing to some extent the various adlayers and topographic, with fairly good contrast.

### 1.2.3 . Raman & photoluminescence

Raman spectroscopy is a very useful technique to fingerprint 2D materials and to study their intrinisic material properties, including material parameters like chemical composition, material quality, charge density, strain, and others. Indeed, Raman provides a means for us to check the quality of our in-house CVD grown 2D $MoS_2$. It is expected that there should be two main Raman-active modes, the $A_{1g}$ (out-of-plane) and $E_{2g}$ (in-plane) modes, as was earlier reproduced schematically from [39] in Figure 1.5.

In order to check the Raman, we chose a representative sample and took spectra after growth, as well as taking spectra after a typical transfer. The reason for this is that, since all experiments

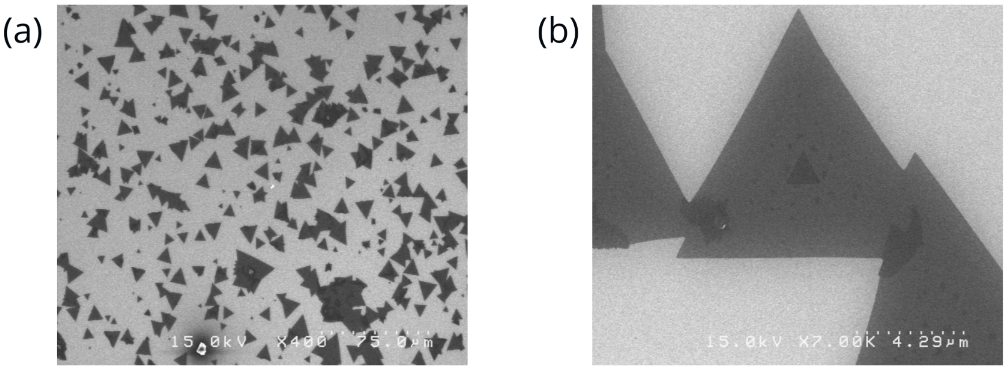

Figure 1.14: Scanning electron microscopy (SEM) images of in-house grown CVD $MoS_2$, at the magnifications (a) 400x with 75 μm scale-bar and (b) 7000x with 4.29 μm scale-bar. The former image shows that many of the single or multi domains are isolated from one another, which is useful when fabricating devices as discussed later. The latter image also reveals various topographical details.

in this work are of samples that were transferred once to the coverslip substrates for IRM and BALM, it is important to check that the Raman is not significantly altered following a transfer. A micrograph of the sample is shown in Figure 1.15(b), with spectra before and after transfer in 1.15(c).

| # layers | Mode | $\omega$ (cm$^{-1}$) before | $\omega$ (cm$^{-1}$) after | $\Gamma$ (cm$^{-1}$) before | $\Gamma$ (cm$^{-1}$) after |
|---|---|---|---|---|---|
| 1L | $E_{2g}^1$ | 387.08 | 388.10 | 2.41 | 2.39 |
| 1L | $A_{1g}$ | 406.13 | 406.04 | 4.84 | 4.66 |
| 2L | $E_{2g}^1$ | 386.12 | 386.18 | 3.05 | 3.66 |
| 2L | $A_{1g}$ | 408.46 | 409.09 | 4.73 | 4.18 |
| multi | $E_{2g}^1$ | 385.28 | 386.09 | 2.14 | 2.54 |
| multi | $A_{1g}$ | 410.78 | 409.72 | 2.81 | 4.88 |

Table 1.2: Raman peak parameters of mono- (1L) bi- (2L) and multi- layered $MoS_2$.

Based on fits of the peaks, the energies ($\omega$) and FWHM linewidths ($\Gamma$) were found and reproduced in Table 1.2. For the monolayer, $E_{2g}$ the mode energies were 387.08 and 388.10 cm$^{-1}$ before and after transfer respectively, while the $A_{1g}$ mode energies were 406.13 and 406.04 cm$^{-1}$ before and after. Thus, $E_{2g}$ mode shifted by about +1 cm$^{-1}$, which is a typical result of CVD-induced strain being partially released upon transfer [71]. For the linewidths, the $E_{2g}$ case was $2.41 \rightarrow 2.39$ cm$^{-1}$ before and after, while for $A_{1g}$ it was $4.84 \rightarrow 4.66$ cm$^{-1}$. These values, as well as the bi and multi layer values, are consistent with those reported in the literature, some of which are cited here [39, 71].

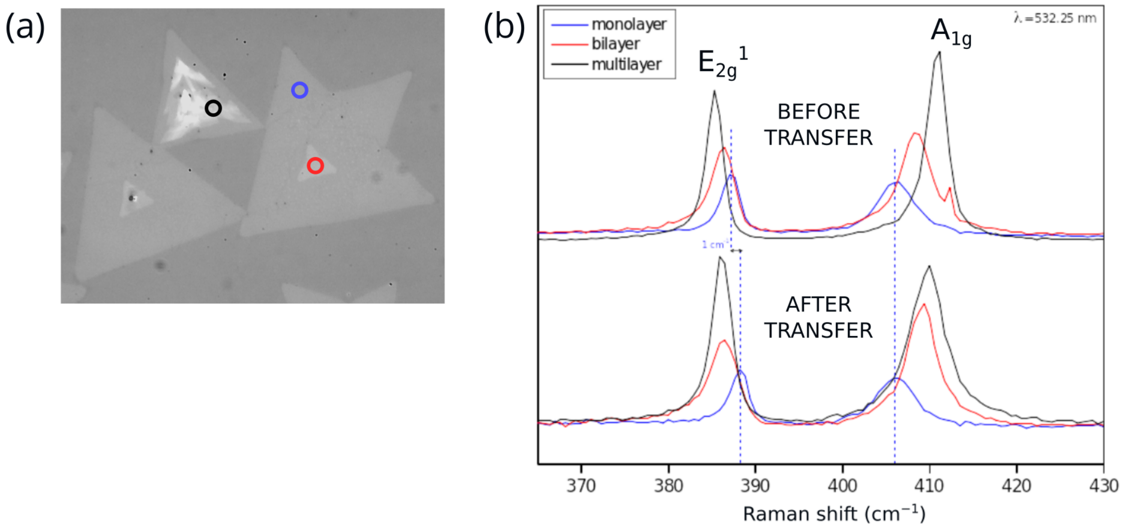

Figure 1.15: (a) Optical micrograph of CVD $MoS_2$ after growth, consisting of monolayer, 3R bilayer, and multilayer flake. (b) Raman spectra of the indicated circles in (a), before and after a transfer from $SiO_2$/Si to $SiO_2$/Si. As elaborated in the main text, the results are consistent with the literature on 1L, 2L, multilayer. Also, the data reveals that the transfer process does not have any significant effect on the $MoS_2$. ($\lambda_0 = 532$ nm was used as the Raman excitation wavelength.)

Photoluminescence (PL) also reveals a plethora of information, in particular the energies, linewidths and relative intensities of the neutral and charged excitons. A representative sample was sent to *OptMatLab* at University of Genova, where E. Peci and M. Magnozzi acquired a PL map of a representative flake. These results are reproduced in Figure 1.16, with (a) showing a representative spectra and (b) the intensity map.

In (a), Lorentzians were fit to the emission peaks revealing the balance of the neutral ($X^0$) and charged ($X^-$) excitons. We see that the $X^0$ is dominating the emission, which is a good sign as a dominant $X^-$ would be a sign of significant doping, such as by excessive trapped charges in the substrate or non-stoichiometric $MoS_2$ that would lead to effective doping. In 1.16(b), it is seen that the PL intensity local variations are relatively homogeneous in this particular case, with some variation throughout the flake.

## 1.2.4 . Ellipsometry & transmittance spectrocopies

Finally, as is discussed more at length in later sections, UV-Vis transmittance spectra, and spectroscopic ellipsometry were used to characterize in-house CVD $MoS_2$ samples. The former were carried out at LICSEN and the latter by *OptMatLab* at University of Genova, specifically E. Peci and M. Magnozzi.

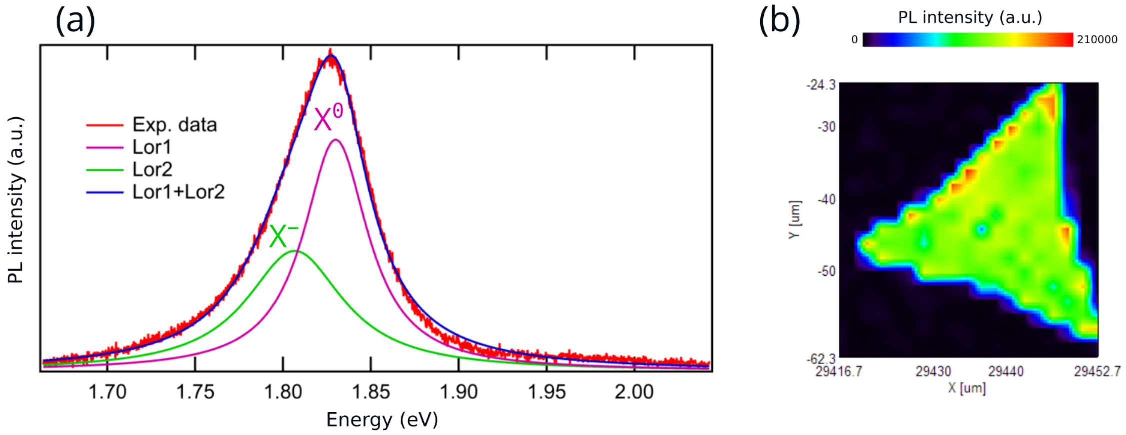

Figure 1.16: (a) PL spectrum and (b) PL map of LICSEN-grown 1 L $MoS_2$, acquired by *OptMatLab* at University of Genova. The spectrum was fit with two Lorentzians as indicated, one for neutral exciton ($X^0$) and one for negatively charged exciton ($X^-$) trion. It is a good sign that $X^0$ is dominant as the reverse case usually mean excissive $n$-doping via sulfur defects. The map shows a relatively uniform response in the PL intensity.

In Figure 1.17(a), a transmittance spectrum is shown for 2D $MoS_2$ that was grown on $SiO_2$/Si and then transferred to double-polished sapphire, the latter of which is highly transparent including at a wide range of wavelengths including 300 nm, although it starts to absorb towards 200 nm. The inset is the actual substrate, with a relatively dense but not multi-layer film of the yellow-ish $MoS_2$. The transmittance of the sapphire substrate was subtracted, which reveals approximately the peaks corresponding to the A, B, C excitons. The spectrum is an indication that the expected exciton peaks are present and is a good sign that our $MoS_2$ is of good quality.

*OptMatLab* measured the same growth sample on a single-polished sapphire substrate via variable angle spectroscopic ellipsometry (VASE) which is explained later in the text. From the raw $(\Psi, \Delta)$ data, the complex refractive index $\tilde{n} = n + i\kappa$ was attained via a dispersion model. The data was also compared with the obtained result for a commercial CVD $MoS_2$ sample from 2D SEMICONDUCTORS Inc. The results are shown in Figure 1.17(b), which are very similar, and a great indication of the high quality of $MoS_2$ we are able to grow in the lab.

To briefly conclude on this introductory chapter, the main properties of 2D TMD crystals—especially $MoS_2$—were discussed, with a focus on aspects relevant to this thesis. Then, the 2D $MoS_2$ we grow in-house was presented and characterized with different techniques. An emphasis was put on inhomogeneities which play a key role in devices and are of interest in Chapters 2 and 3. Next, in Chapter 2, the IRM and BALM visibility aspects of the thesis is

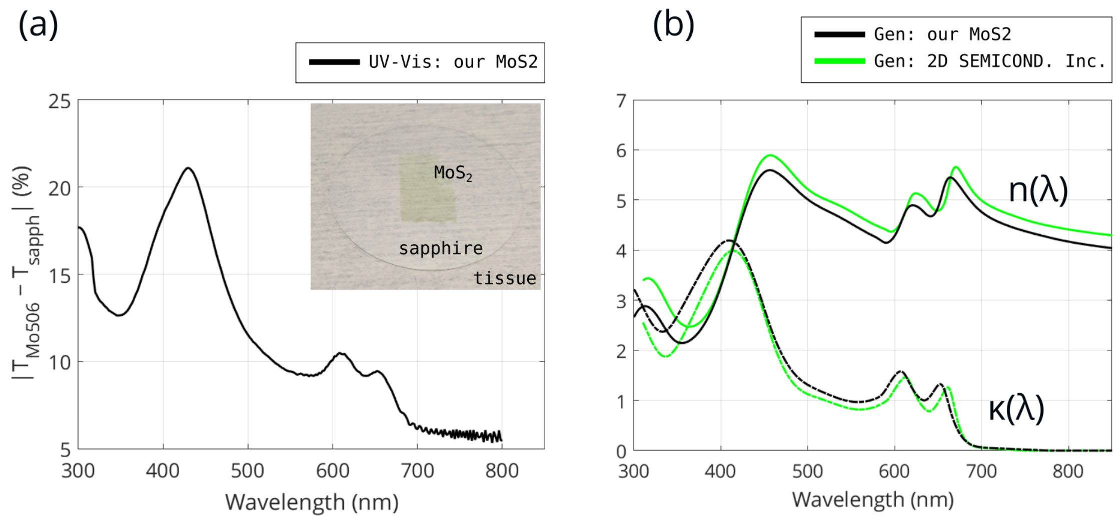

Figure 1.17: (a) UV-Vis transmittance spectrum of CVD $MoS_2$ transferred to double-polished sapphire. (b) Ellipsometry of both LICSEN-grown $MoS_2$ and commercial $MoS_2$ from 2D SEMICONDUCTOR INC.

covered, mostly for the case of $MoS_2$ but also some other 2D materials.

# Chapter 2

# Improving $MoS_2$ optical contrast for IRM and BALM

This chapter will begin with a section (2.1) containing an overview of various contrast-enhancing optical microscopy techniques that have been used in the literature to better visualize 2D materials (as well as other materials). Interference reflection microscopy (IRM) and backside absorbing layer microscopy (BALM) will also be introduced in this context.

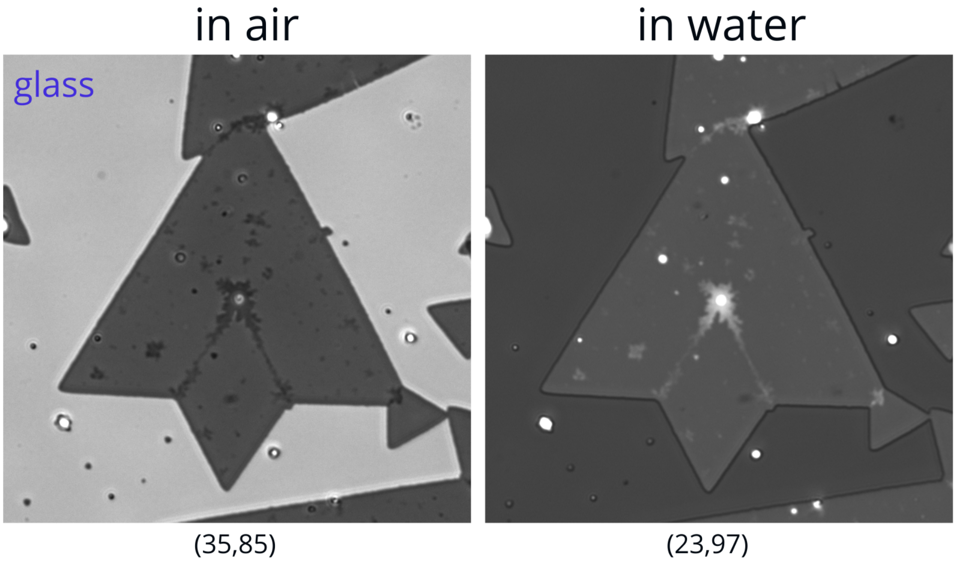

Figure 2.1: (Please see electronic PDF for better rendering.) IRM micrograph obtained during this thesis at $\lambda_0$ = 450 nm of a monolayer $MoS_2$ flake in air (left) with grayscale range adjusted to (35,85), and in water (right) with grayscale of (23,97). The visibility and contrast of the monolayer as well as the adlayers and grain boundaries are of high quality, and the effect of changing the refractive index fo the top medium (air to water) is evident.

As we shall see, IRM is capable of imaging 2D $MoS_2$ with very good contrast, revealing various topographic details of a given sample. A preview result from this thesis work is shown in Figure 2.1, which was taken using a 450 nm bandpass filter of 10 nm bandwidth (the effect of wavelength is important as explained later). On the left is an IRM image of CVD $MoS_2$

in air where the 8-bit grayscale was adjusted to (35,85) for improved visibility. On the right, the image is taken after adding water at the top of the substrate, with grayscale adjusted to (23,97). As is seen here and discussed later, the water changes the interference conditions and thus the resulting contrast landscape, which can be a useful asset.

For BALM, a different data preview with $MoS_2$ was shown earlier in Chapter 1 in Figure 1.13. BALM is essentially IRM but with an added nanometric anti-reflection absorbing (ARA) layer of gold, with chromium as the adhesive, which changes significantly the interference conditions and can be leveraged for improved contrast. Due to the enormous and largely unexplored potential of IRM and BALM to visualize various topographic details of CVD TMD monolayers and few-layered samples, a significant part of thesis was dedicated to this endeavor, via both experimental and simulation approaches.

After section 2.1, a more in-depth section (2.2) follows on IRM related background and theory. This includes relevant theory and background on optical microscopy, such as the Köhler illumination scheme and role of aperture and field diaphragms. Various optical contrast definitions are covered as well, since a multitude of definitions exist and must be understood. (I mainly will use the percent change contrast definition.)

The last subsection of 2.2 is mostly focused on thin-film optics theory and other phenomena of light-matter interactions. These lie at the heart of IRM and BALM. Much of the formulae of this section I implemented in code, where sometimes I built on freely available code cited in the text. This allowed for various experimental systems of the thesis to be simulated and compared with data.

After this, both data and simulation results using IRM are presented in the subsections of 2.3 with a focus on monolayered $MoS_2$. In 2.4, results on TMD homobilayers are presented. Then, in section 2.5, I shift gears to BALM, covering background and theory aspects of it. This is followed by multiple results sections (2.6, 2.7, 2.8) that also include both data and simulations. In addition to BALM results, transmittance spectroscopy is covered, which we used to better understand the optics of the thin-films involved. These results also consists both of data and simulation.

The various background, theory, and results of this chapter are foundational to Chapter 3, where the *in operando* charge density imaging of 2D $MoS_2$ capacitors and field-effect transistors were performed both in IRM and BALM configurations.

## 2.1 . Optical contrast of 2D materials

An important question when considering 2D materials, is whether they can be seen with the naked eye or not. Furthermore, whether they are visible with a standard optical microscope. The short answer is that it depends on the 2D material in question and also on the configuration of the optical system. It may seem impossible that a 2D crystal of ≈ half of a nanometer could be seen at all, but nanometric vertical resolution is actually not that unusual in optical microscopy. Yet, it can be elusive and may require some modification of the optics.

For instance for graphene, a relatively transparent and thin 2D material ($d \approx 0.335$ nm and $\tilde{n}_{\text{opt}} \approx 2.6+1.3i$ [67]), it is sometimes said that it cannot be seen with a microscope if it is on a transparent substrate, and that a Fabry-Pérot (FP) substrate like $SiO_2$/Si is required. However, this is not really true if a simple band-pass filter of 550/10 nm is used, as shown by Gaskell et al. in 2009 [72]. In Figure 2.2(a) some of this data has been reproduced, where the monolayer can be seen with a percent change contrast of $C_{\text{pc}} = +7\%$ (and Weber contrast of the same, at $C_{\text{Weber}} = +7\%$). Furthermore, in an IRM configuration discussed later (also consisting of a transparent substrate but illuminated from the back with an oil immersion objective), $C_{\text{pc}} \approx -28\%$ ($C_{\text{Weber}} = +39\%$) can be attained as shown by Ke Xu's group in 2016 with a 532/10 nm bandpass filter [73]. Thus IRM provides a superior Weber contrast. (See section xxx for a detailed discussion of contrast definitions and why they are important.)

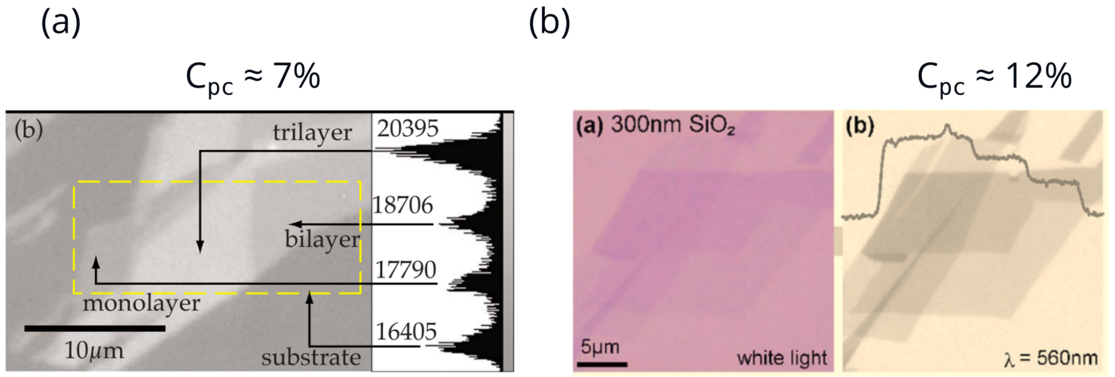

Figure 2.2: (a) From Gaskell et al. 2009 [72], graphene of 1,2,3 layers observed with good contrast (7% for 1L) on a transparent substrate thanks to the use of a 550/10 nm bandpass filter. (b) From Blake et al. 2007 [74], graphene on 300 nm $SiO_2$/Si in white light and at 560 nm. The latter case results in 12% contrast for the monolayer, thanks to the Fabry-Pérot interference enhancement from the $SiO_2$ thin film.

Yet, Fabry-Pérot substrates still can be very beneficial when white light illumination is required or when higher contrast is desired. Thus early work focused on finding an optimal $SiO_2$ thickness on Si which by thin-film interference results in a Fabry-Pérot resonance, enhancing graphene contrast, as shown in *Making graphene visible* in 2007 [74] for example. Some of the results are reproduced in Figure 2.2(b), where a 300 nm $SiO_2$ layer is used, with a 560 nm filter.

Many other contrast-enhancing configurations have been explored. For example, the use of a confocal laser scanning microscope (CLSM), which has a very narrow depth-of-field (DOF), also improves visibility and contrast of graphene, as shown in [75] and reproduced in Figure 2.3(a). A widefield configuration is plagued by a deeper axial DOF and thus light from adjacent focal planes of the sample are convoluted together with the field image of the sample. In a CLSM, a tiny pinhole is placed in the collection optics at a (confocal) field plane, which filters out the out-of-focus planes. This requires each point to be scanned but in fact modern CLSM systems can do a full scan in $\approx 1$ second, and furthermore a spinning disk confocal microscope can even attain $< 1$ ms acquisition time.

Another contrast-enhancing mechanism is to illuminate at angles where the contrast is the highest, which typically is at or near the Brewster angle. This technique is called Brewster Angle Microscopy (BAM). Romagnoli et al. [76] reported $C_{\text{pc}} = 2600\%$ contrast for graphene which is reproduced in Figure 2.3(b).

Another way is by Ellipsometric Contrast Microscopy (ECM) [79]. This method consists of acquiring maps of one or both of the ellipsometric parameters $\Psi$ and $\Delta$, at a wavelength and angle of incidence that maximizes contrast. A recent example is a 2023 paper [77], where monolayers and bilayers of graphene can be distinguished with high contrast, as reproduced in Figure 2.3(c). Furthermore they show that bilayers of different twist angles can be distinguished with high contrast as well with this technique. D. Ausserrée, the inventor of BALM, discussed later, also developed ECM using surface enhancing layers, which he and co-authors termed surface enhanced ellipsometric contrast (SEEC) [80, 81].

Yet another example is the use of phase-contrast microscopy (PCM) to improve contrast of 2D materials. In this technique, which is widely used in biology, phase change of light is converted to intensity, often revealing samples with improved contrast. A recent example is a 2023 paper [78], where hBN (which is even more elusive than graphene in the optical regime) is imaged with relatively good contrast, reproduced in Figure 2.3(d). The group furthermore showed how PCM reveals with good contrast and visibility heterostructures of graphene and hBN, whereby

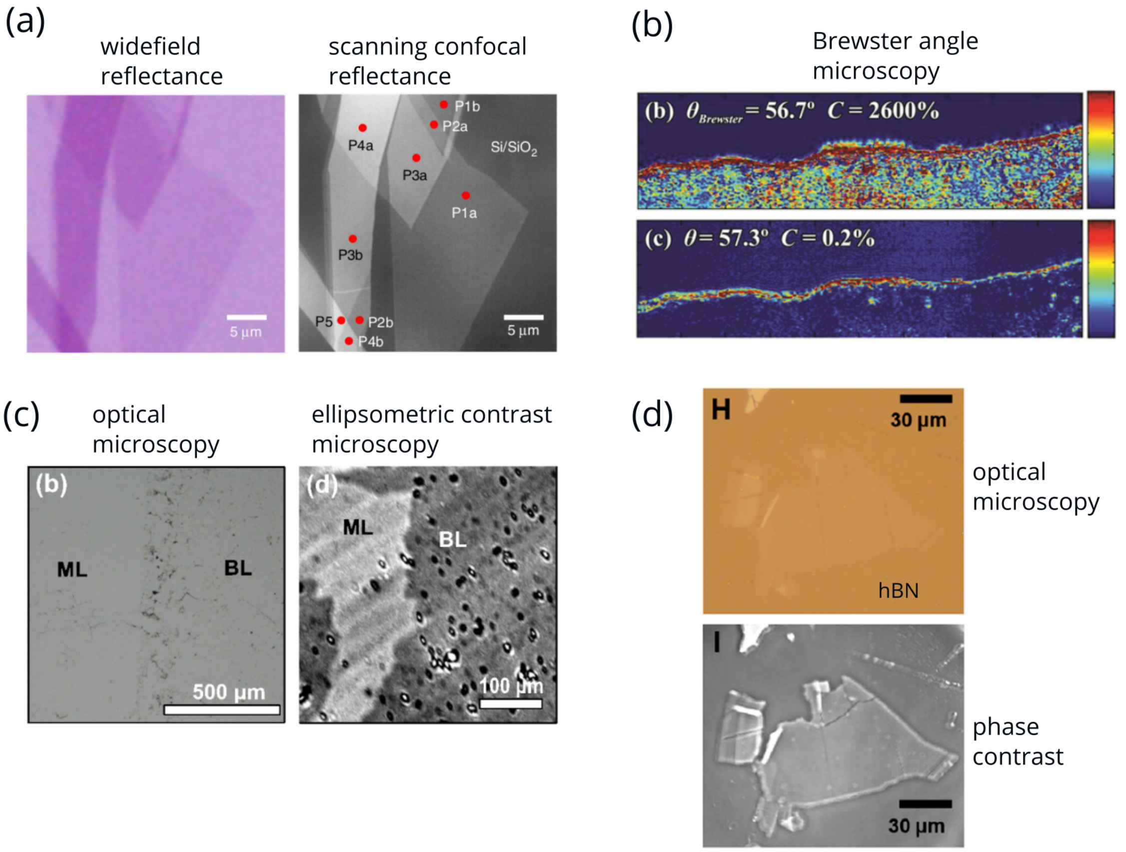

Figure 2.3: (a) From [75], side-by-side comparison of graphene micrographs obtained in both widefield reflectance and laser scanning confocal reflectance, the latter of which is improved thanks to the narrow depth of field. (b) From [76], graphene micrograph obtained at differing angles, the first of which is at $\theta_{\text{Brewster}}$ resulting in improved contrast. (c) From [77], side-by-side comparison of normal micrograph versus ellipsometric contrast of a 1L/2L graphene, the latter of which shows improved contrast. (d) From [78], a hBN flake whose visibility is improved by use of phase contrast compared with normal epi-illumination.

the graphene inside hBN can be seen.

As previously mentioned, interference reflection microscopy (IRM), which is a main focus of the thesis, also provides significant contrast improvement, with attained Weber contrast of $\approx 38\%$ for graphene as shown by Ke Xu group in 2016 [73]. Some data is reproduced in Figure 2.4(a). The same group performed additional studies of *in situ* oxidation and reduction [83, 84], with good vertical resolution of the electrochemical processes.

The group of J. R. Samaniuk also used IRM to study mono- and multi-layered $MoS_2$ in 2020 [82], reproduced in Figure 2.4(b). Their setup includes a 532/10 nm bandpass with a water immersion objective. They report $C_{\text{Weber}} \approx 19\%$ for monolayer $MoS_2$. They performed further studies in 2021 [85] and for graphene in 2021 also [86].

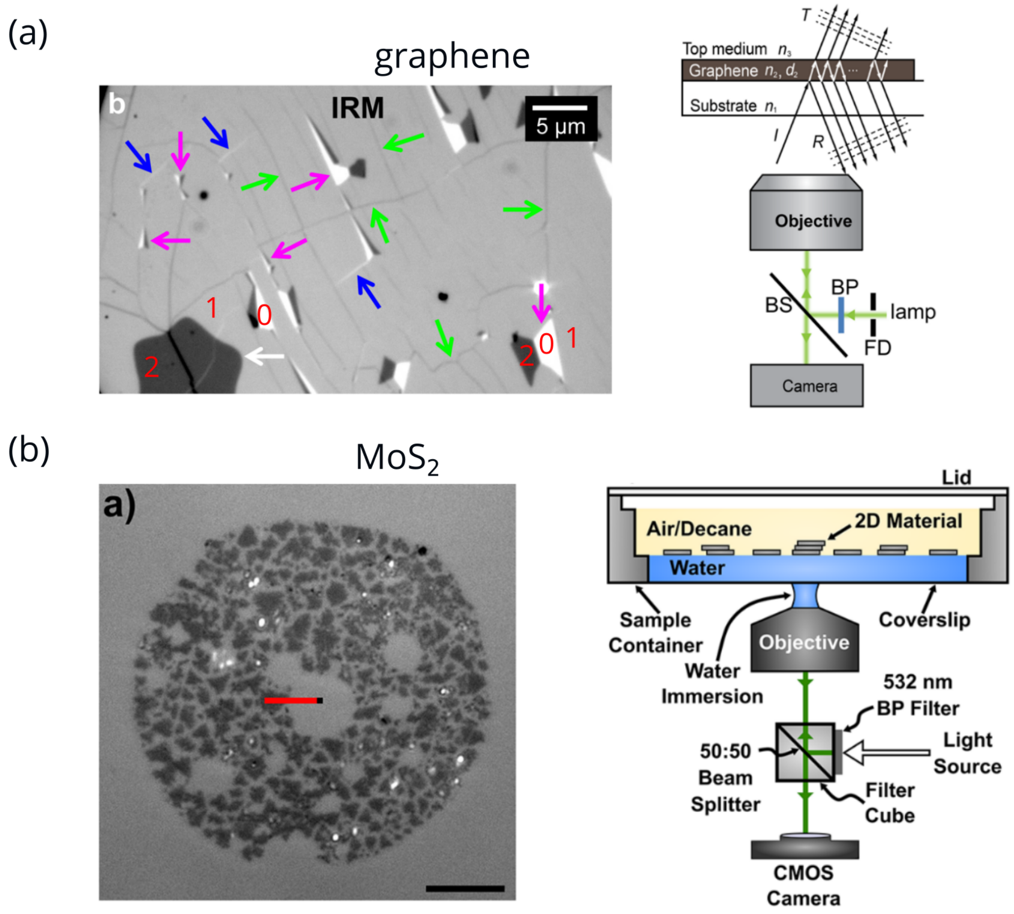

Figure 2.4: (a) From [73], interference reflection microscopy (IRM) image of CVD graphene, with high (negative) contrast between substrate (0), monolayer (1) and bilayer (2). Schematic of IRM microscope on the right. (b) From [82], IRM image of 2D $MoS_2$ at a water/glass interface, with the IRM microscope on the right.

In 2014, D. Ausserée and co-authors introduced an IRM based technique called backside absorbing layer microscopy (BALM) [88]. It consists of an IRM configuration but with a thin nanometric gold film on the coverslip substrate, which acts as a FP resonator and in some cases can significantly improve contrast of 2D and other materials, with the added ability to use the film as an electrode for various *in situ* experiments. Some results from a 2017 paper [87] are reproduced in Figure 2.5, with a diagram of the setup in (d).

Since BALM is a main focus of the thesis it is described in more detail later. However to get an idea of the technique, the case of graphene oxide from the same reference [87] is reproduced in (a). Graphene oxide (GO) is in fact more transparent and elusive than graphene. A Weber contrast of 20% was attained ($C_{\text{pc}} \approx -17\%$) from this micrograph. Furthermore, the authors showed how reduced graphene oxide (r-GO) and GO can be distinguished from each other also

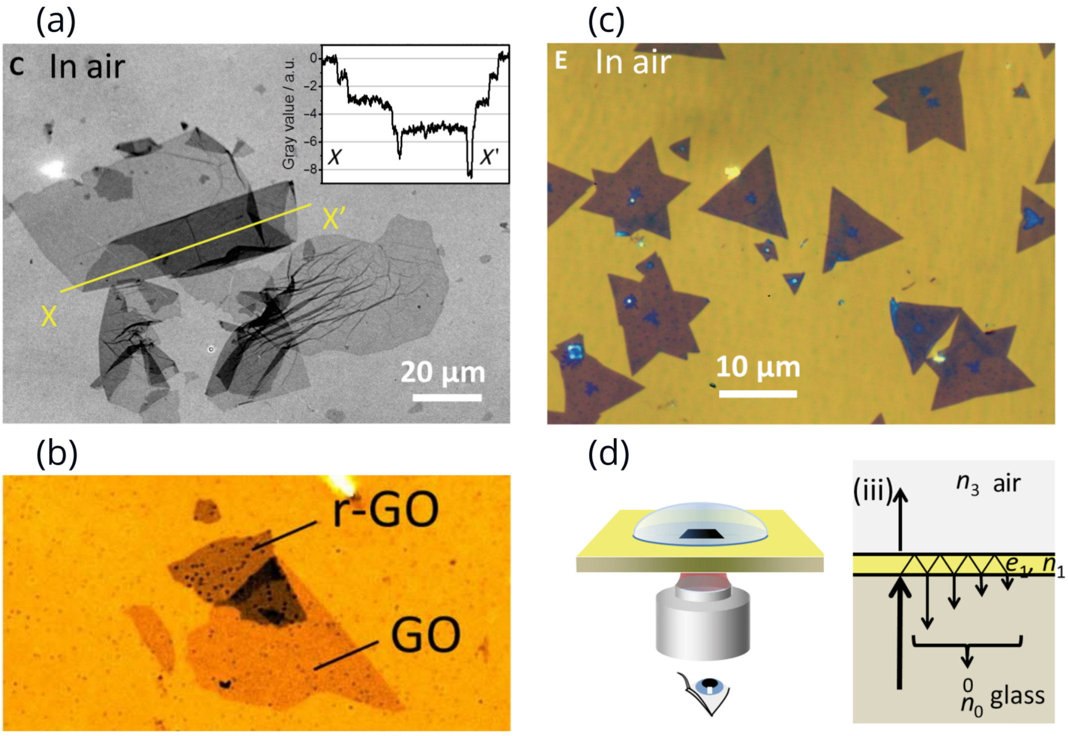

Figure 2.5: From [87], a 2017 paper on backside absorbing layer microscopy (BALM), showing (a) graphene oxide with high contrast, (b) graphene oxide and reduced graphene oxide difference with high contrast, and (c) first 2D $MoS_2$ BALM image ever published, and (d) diagram of BALM configuration which is an IRM microscope but with the added thin gold anti-reflective absorbing (ARA) layer.

with high contrast as reproduced in (b). Finally this paper also introduced the first BALM micrograph ever of 2D $MoS_2$ (grown at LICSEN).

Having brought up BALM, it is relvant to mention surface plasmon resonance imaging (SPRi), also called SPR microscopy (SPRM), as it in fact has some aspects in common with the BALM configuration. SPRi is addressed in more detail in a later section, but in short it is also microscopy based utilizing a Cr/Au coated coverslip, but illuminated at a specific angle (and with $p$-polarization only), where there is a surface plasmon resonance effect. The setup is shown in Figure 2.6(a) reproduced from [89] with (b) also from the same reference, showing nanometric viruses that were imaged, albeit with a parabolic artifact as elaborated on later in the text.

The list of contrast-enhancing techniques in optics is long. Here, the ones bearing most resemblance or relvance to IRM and BALM have been covered. All in all it is evident that contrast-enhancing OM techniques are a hot area of research with 2D materials, and are often coupled with other experiments.

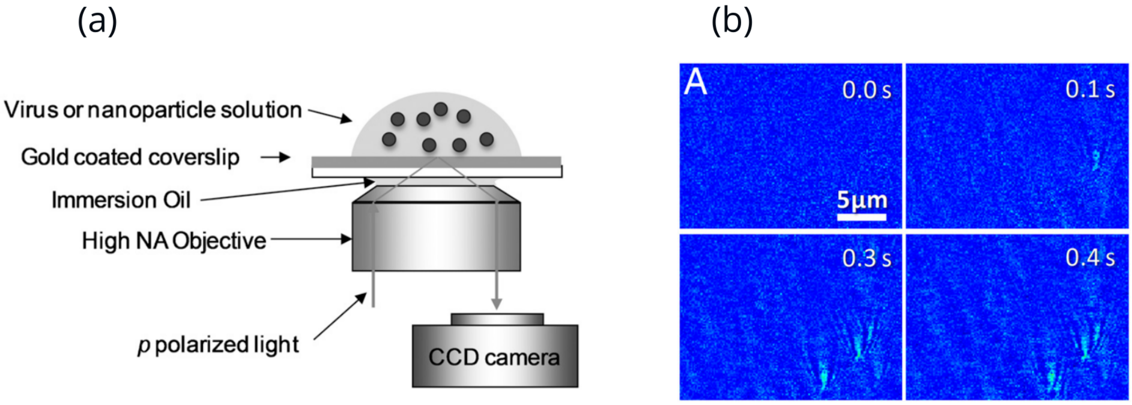

Figure 2.6: From [89], showing (a) setup of a surface plasmon resonance imaging (SPRi) system, and (b) micrographs of nanometric viruses as a function of time.

Now, finally it is relvant to make a distinction between contrast-enhancing techniques which are concerned with specular reflection, versus diffusive reflection. When a surface or stack consists of one or many planar low-rugosity layer(s), then the light reflects specularly, i.e. the law of reflection is satisfied, which states that the angle of incidence equals the angle of reflection ($\theta_{\text{inc}} = \theta_{\text{refl}}$) [90, pp. 98–100]. However, for a highly rugose surface, or for any isolated particle/microstructure/nanostructure(s), incident rays are diffused in many different directions [90, pp. 98–100]. Often, this necessitates the use of Mie scattering theory to understand the resultant scattered field [91]. Such a situation would be relevant in this context, if for example the goal is to better visualize small particulates or structures on top of a TMD monolayer like sub-micron adlayers of $\text{MoS}_x$ dendrites.

For this purpose, one technique is the so-called interferometric scattering microscopy (iSCAT) [94, 92]. This OM technique relies on the diffusive scattered field of nano-sized objects and their interference with a reference field, along with some other aspects, to image them. It also usually requires a laser. An example of data and the configuration are reproduced from [92] in Figure 2.7(a).

A related technique which does not require a laser and that relies on a FP stack to enhance contrast is the Interferometric Reflectance Imaging Sensor (iRiS), developed mainly by S. M. Ünlü group and collaborators [93, 95, 96, 97]. The configuration and some data are reproduced in Figure 2.7(b) from [93].

Finally there is also a whole literature on through-focus scanning optical microscopy (TSOM)

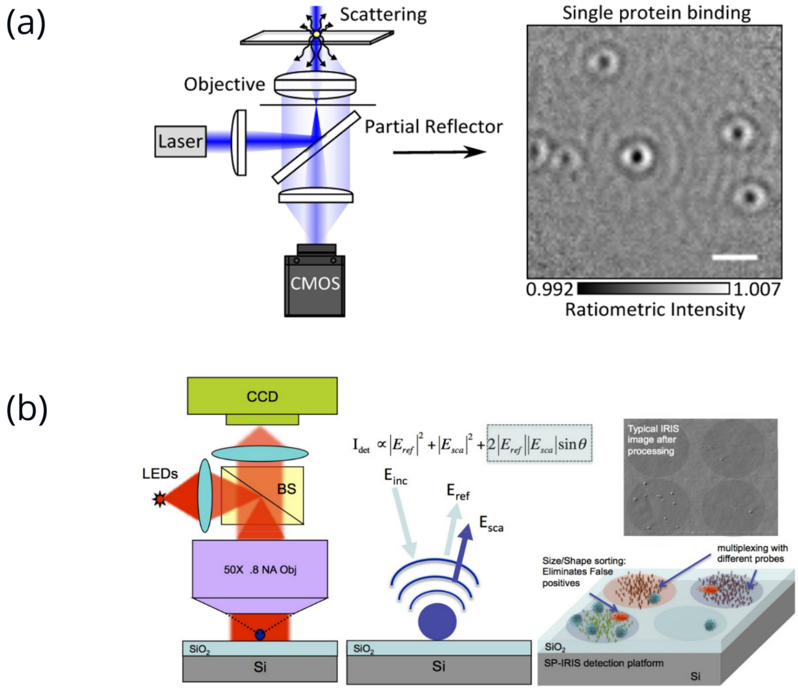

Figure 2.7: (a) From [92], showing the interferometric scattering microscopy (iSCAT) setup, and a image of proteins on the right. (b) From [93], Interferometric Reflectance Imaging Sensor (iRiS), consisting of $SiO_2$ as a FP resonator to improve contrast of nanoparticle.

[98, 99, 100], where the $z$-focus is scanned (then plotted versus a fixed horizontal line-section), hence "through the focus" for a given nano-sized object, enabling a variety of contrast improvement and deconvolution of other properties.

Although the thesis is mainly concerned with specular contrast, diffuse reflections are relevance in some cases.

# 2.2 . IRM background & theory

## 2.2.1 . IRM and RICM

What exactly is interference reflection microscopy (IRM)? It is a reflection microscope that meets certain criteria. These include: the use of an inverted oil immersion objective, a transparent coverslip as the substrate, a bandpass filter to increase the temporal coherence, and finally the presence of thin-film interference either in the sample itself or in the space between sample and substrate [101].

The IRM modality was introduced in 1964 by A. S. G. Curtis, who coined the term [102]. He used it to study adhesion mechanisms of cells on the glass coverslip. The interferences in this case take place in the thin air gap between the glass coverslip and cell, as opposed to interferences within the cell itself being the primary mechanism. This is different from the case of 2D materials, where there is no air gap and thus the interferences take place in the 2D material itself (and in any other thin-film layers that may be present).

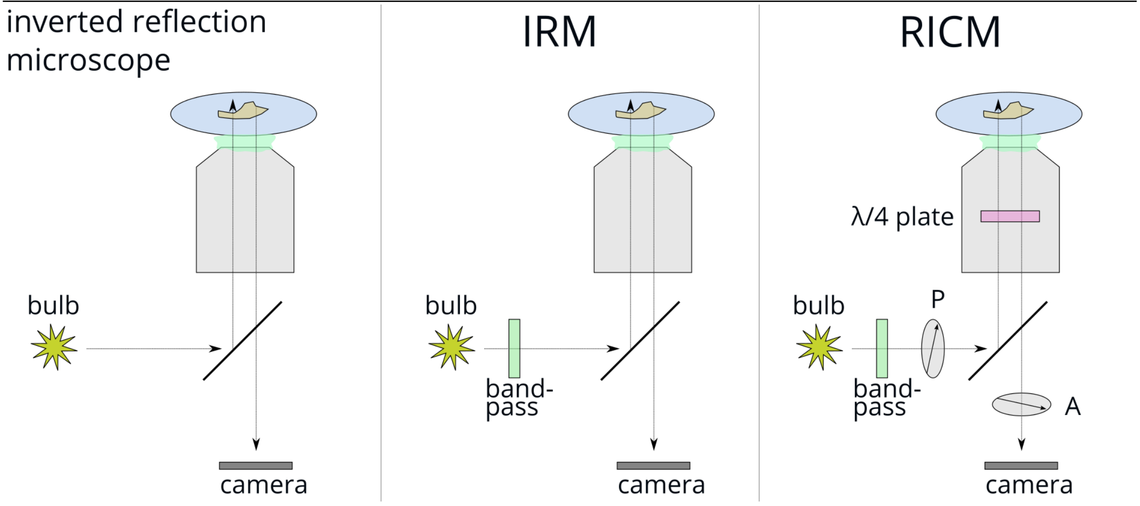

Figure 2.8: Diagrams illustrating differences between an inverted reflection microscope (left), an interference reflection microscope (IRM) in the center, and a reflection interference contrast microscope (RICM) on the right.

The technique became popular for a while in biology communities. Then, in 1973, an improvement to IRM was introduced by J. S. Ploem, at the *Second Conference on Mononuclear Phagocytes* in Leiden, Netherlands, with further details documented by Ploem in the associated conference proceeding [103]. The improvement, which Ploem termed reflection-contrast microscopy (RCM), consists of adding crossed polarizers at the input and output of the epi-illumination cube, together with use of a so-called "anti-flex" objective which contains a quarter-wave plate, discussed further below.

Today, the term reflection contrast interference microscopy (RICM) is more commonly used than RCM, although they are the same. Figure 2.8 summarizes the differences between a normal epi-illumination inverted reflection microscope, an IRM and an RICM configuration.

The theory of IRM was further developed in publications by C. S. Izzard and L. R. Lochner in 1976 [104], and D. Gingell and I. Todd [105] in 1979. These papers explore in some detail the infuence of illuminating numerical aperture (INA) on contrast, among other aspects. In 1981 K. Beck and J. Bereiter-Hahn [106] investigated further optics considerations for RICM. In fact, it is this publication that seems to be the first to introduce the term "RICM" over "RCM". In 1985, H. Verschueren [107] further developed IRM and RICM, as well as explaining the difference between the two very clearly. He also clarified that in the literature, authors often use "IRM" for a RICM configuration, and he in fact proceeds to do so himself as well. I will distinguish between the two to avoid confusion however.

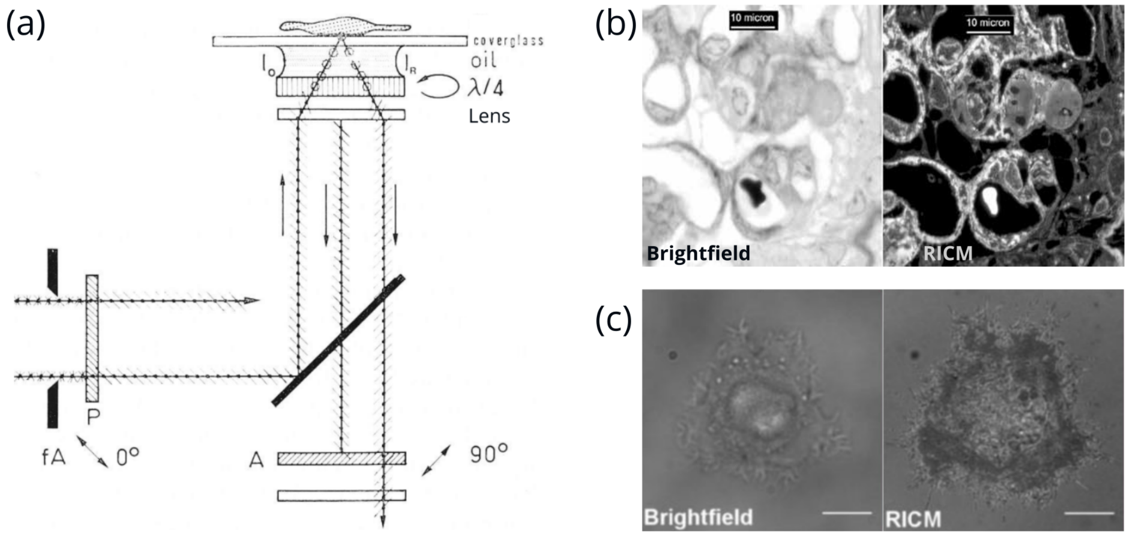

Figure 2.9: (a) From Bereiter-Hahn 1981 [106], diagram illustrating principle of RICM. (b) Ploem and Prins 2017 [108], comparing brightfield with RICM. (c) From Klein et al. 2013 [109], comparing brightfield and RICM.

Now, the mechanism of RICM is illustrated in Figure 2.9(a), reproduced from [106]. As mentioned above, a polarizer is placed before the beam-splitter cube, and an analyzer at the output, 90° rotated (so "crossed"). With a normal objective, this would simply make everything dark. However, instead the so-called "anti-flex" objective is used. This objective contains a $\lambda/4$ plate which turns the linearly polarized light to circularly polarized light. The effect that these added elements have, is that the light which has not undergone interference gets blocked by the analyzer, whilst the light that has undergone interference is let through. Example data is reproduced in 2.9(b) from Ploem et al. 2017 [108], where trans-illumination bright field is compared with RICM for the same sample. It is seen that the substrate is dark in the RICM case. A second example from Klein et al. 2013 is also reproduced, in 2.9(c).

To the author's knowledge, RICM has never before been tested with any 2D material. Only IRM has been used (as was discussed in 2.1), for the case of graphene [73, 83, 84, 86] and 2D $MoS_2$ [82, 85]. As the contrast-improvement and utility of IRM for graphene and $MoS_2$ was significant, it would be of high interest to see whether further improvement is gained by use of the RICM configuration.

Finally, there are two papers that stand out from this century in terms of covering the theory of RICM/IRM. The first is from 2009 in *ChemPhysChem* by L. Limozin and K. Sengupta [110], and the latter from 2010 in *Langmuir* by O. Theodoly, Z.H. Huang and M.-P. Valignat [111]. Both of these actually originate from Marseille which has a strong research activity with RICM.

## 2.2.2 . Optical microscopy theory

### General points

Prior to any discussion on the optical stack that is at the "input" of an IRM or BALM instrument, the entirety of the optical system must be addressed, i.e. the microscope.

An IRM/BALM microscope makes use of the so-called Köhler illumination scheme, which is used by most microscopes. August Köhler introduced this scheme in 1893 [113]. Prior to this, critical illumination (also called Nelsonian illumination) was typically used, in which a light source (which lies at what is called an aperture plane) is simply focused onto the plane of the sample (lying in a so-called field plane). In this scheme, the aperture and field planes actually lie in the same plane, thus they are said to be confocal. This also means that an image of the light source will be seen at the field plane together with an image of the sample. As light sources often are of non-uniform character (such as the filament of an incandescent bulb), it is not quite optimal as the object of interest is the sample, and one does not wish to see an image of the filament. This is the main problem that Köhler was addressing in 1893.

In the Köhler illumination scheme, the aperture and field planes are not confocal, but rather they are out of focus from each other in the most optimal way possible, which means effectively

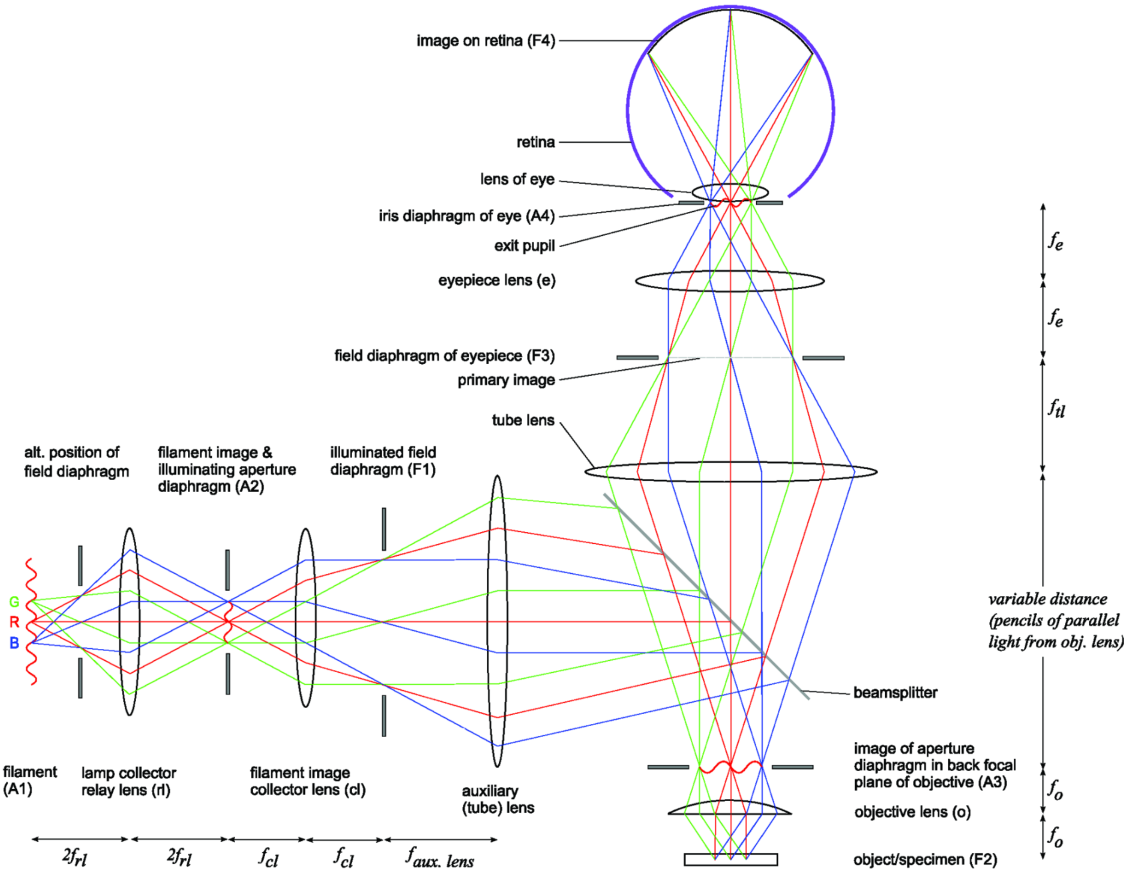

Figure 2.10: From Hammond 2006 [112], a ray-trace of a Köhler epi-illumination scheme, where aperture and field planes are relayed with adjustable diaphragms at various positions along the path. The filament aperture plane is focused to the back focal plane (BFP) of the objective as shown.

placing the light source at the back focal plane (BFP) of the objective lens, making the rays that emerge onto the sample (front focal plane) to be perfectly collimated i.e. parallel. In practice there are many more relay lenses involved but this is the basic idea.

Furthermore, an adjustable diaphragm (also called an iris) is placed at both the aperture plane and field plane. This allows the possibility to effectively adjust the diameter of the light source and the diameter of the illuminated field. Alternatively to diaphragms are so-called "stops", which consist of a wheel of many holes of different diameters that are placed in the light path. These are "stopped into place" by discrete toggles of the wheel. Thus the diaphragms or stops that are placed at the aperture and field planes are known as "aperture/field diaphragm". (In practice "diaphragm", "iris", "stop" are often used interchangeably which is fine, even though strictly speaking they are slightly different.)

The aperture and field stops have multiple very important functions in a Köhler microscope.

To better visualize their function, see Figure 2.10 which is a diagram reproduced from R. Hammond 2006 [112]. The scheme can be divided into two parts, the first of which is the illumination optics, consisting of all the optical elements leading to the actual sample. The second is the collection optics, which includes all the elements that the rays travel through after being reflected by the sample.

For the illumination optics, we first see the light source was placed at 2 times the focal distance of a relay lens on the left side. This has the effect of producing an image of the light source at $2f_{\mathrm{rl}}$ on the right side. This is thus one possible location for the aperture stop. The next lens is called the collector and is placed at just 1 times the focal distance of $f_{\mathrm{cl}}$. The field stop can be placed at $f_{\mathrm{cl}}$ to the right. The rays are then directed by an auxiliarly lens so that the filament image is projected on the BFP of the objective as mentioned earlier, so that rays emerge parallel to the sample (field) plane.

Now, on the collection side, we see that the sample image is eventually focused onto a retina or detector. Along the way though, there are in fact additional planes where aperture and field stops can be placed. Thus, stricly speaking one should differentiate between illuminating vs. collection field/aperture stop. If not specified, then, an illuminating stop is assumed. However sometimes stops are placed in the collection optics for various purposes, a point which has some relevance later in the discussion.

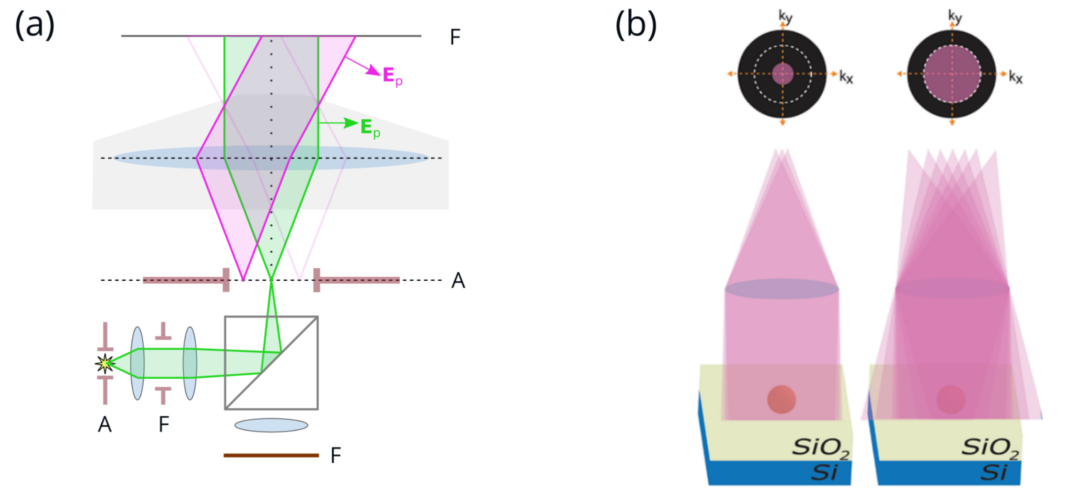

Figure 2.11: (a) Simplified Köhler illumination configuration (not to scale), indicating the aperture (A) and field (F) planes, and nature of incident angles. (b) From Yurdakul et al. 2020 (Ünlü group) [97], illustrating the incident beams for differing radii of back focal plane (Fourier plane) illumination.

Before proceeding further, it is worth noting that a simpler configuration is possible to construct, which is shown in Figure 2.11(a). This configuration has fewer lenses and in some ways is simpler to understand. (It is also inverted, as is the case for a IRM/BALM microscope.) Based on Figures 2.10 and 2.11(a), a few observations can be made. The first is that the aperture stop controls the amount of light received by the sample. Furthermore, it also is controlling the range of angles of incident rays that the sample receives. To understand this, the numerical aperture (NA) needs to be introduced, which is defined as NA $\equiv n \sin \theta_{\text{max}}$, where $n$ is the refractive index of the medium between lens and sample (often air where $n = 1$ but not for oil immersion objectives used in IRM/BALM). $\theta_{\text{max}}$ is the maximum angle that the lens can collect of a ray emmanating from a the point $(x, y, z) = (0, 0, f)$. The NA is a measure of the effective aperture stop that is imposed by the lens due to geometry, hence the terminology of it being a "numerical" aperture and not a physical one. A related quantity is the so-called "f-number" (or "f-stop") $N_f$, which (setting $n = 1$) is related to NA by $N_f = 1/(2\text{NA})$. The f-number in turn is related to the focal distance $f$ of the lens, and the diameter $(D)$ of the entrance pupil of the lens by the relations $N_f = f/D$ and NA $= D/(2f)$.

Now, recall it is the maximum angle ($\theta_{\text{max}}$) that a lens can collect that defines the nominal NA. However, if a physical aperture is placed in the collection optics, then the effective collection NA is reduced. This is done all the time in photography where the f-number of a camera is often altered. Thus to be clear, the collection NA, or CNA should be used to distinguish from the aperture stop in the illumination optics, called the illuminating NA or INA. Thus, if one intends to illuminate the sample with the same nominal NA as the one of the objective, then one must make sure to open the illuminating aperture iris enough so that the light source covers the full rear pupil of the objective. In practice, one can look at the aperture plane of the system by simply removing the eyepiece, or by flipping in a so-called Bertrand lens. Then one will see the objective BFP, the light source, and aperture diaphragm.

It should be clear now that the INA and CNA are not necessarily the same. For example, by stopping down the illuminating aperture to a very small diameter, then INA $\approx 0$, but CNA can be the "nominal" NA of the objective. The case of INA$= 0$ corresponds to the red rays in Figure 2.10, while for Figure 2.11(a) it is the green rays. The latter figure also exaggerates for illustration purposes how the points off-axis result in rays at incident angles. This is also illustrated in 2.11(b) reproduced from [97], where the BFP aperture plane is labeled with coordinate system $(k_x, k_y)$, corresponding to a vector $\boldsymbol{k} = (k_x, k_y)$. The reason for this, is that the BFP is actually a Fourier transform of the field plane $(x, y)$. It is for this reason that

Köhler illumination scheme is actually equivalent to what is known as a $4f$-imaging scheme in the field of Fourier optics [114].

## Nonuniform field

Having introduced general aspects of Köhler illumination and related points, it is a good moment to discuss the illuminated field uniformity. In practice, it is not always the case that the optical elements are aligned perfectly such that the aperture iris is exactly at the aperture plane or the field iris exactly in the field plane. This is true even for high-end commercial microscopes, as was detailed by E. Agocs and R. Attota [115]. This is in part due to chromatic aberration of the lenses, i.e. the fact that most glasses used in lenses have a dispersive RI which is especially apparent when approaching blue wavelengths.

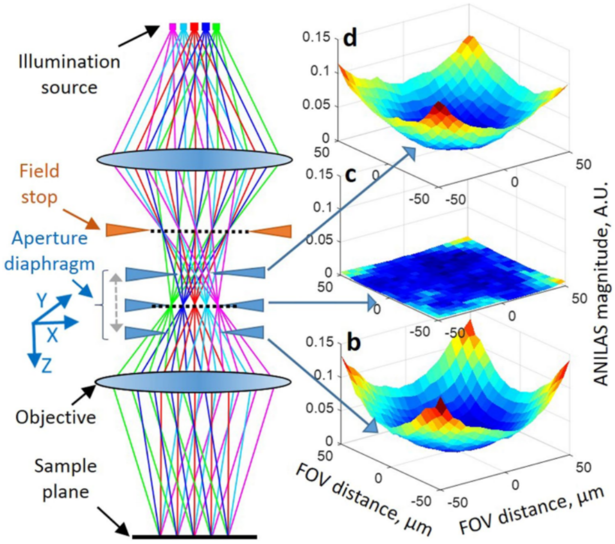

Figure 2.12: From E. Agocs and R. Attota 2018 [115], influence of aperture diaphragm alignment on resulting illuminated field uniformity.

E. Agocs and R. Attota showed how axial positioning of the aperture diaphragm (AD) influence the resultant illuminated field [115], some results of which are reproduced in Figure 2.12. In the figure it is apparent that if the AD is not positioned correctly, there is a resultant parabolic-like shape of the illuminated field. In fact, for optimal result, one would need to realign the aperture diaphragm whenever the wavelength of illumination is changed,. This is in addition to the fact that the $z$-focus changes with wavelength as well also due to chromatic aberration, as I got to experience a lot first-hand.

There is an alternative way to circumvent the problem of non-uniform field though, which is to perform a background subtraction [116]. This entails taking both a picture of the bare substrate, in addition to the picture of the sample. Then, one can subtract the background by

$$I'_{\text{sample}}(x,y) = I_{\text{sample}}(x,y) - I_{\text{bg}}(x,y)$$

This can be a powerful image processing step, and is explored to some extent in the thesis as discussed later (see Figure 2.24). However, it is not always possible to attain a background image for several practical reasons. For instance, there needs to be a portion of the substrate which does not have any "sample" but that is bare. Furthermore, it is difficult to reproduce the exact same conditions, which include $z$-focus, diameters of aperture and field diaphragms, power fed to the bulb, camera settings and others.

It is even more difficult when taking micrographs at multiple wavelengths. Since for each bandpass filter the $z$-focus must be adjusted, along with exposure time (since not all wavelengths are illuminated equally). Thus, after each sample micrograph, the background micrograph on a bare region needs to be taken again each time. This also results in $(x,y)$ drift for each sample micrograph.

## Illumination source

Another aspect of high relevance is the nature of the illumination source. A wide variety of sources are available, including the sun, incandescent bulb, LED, laser, Hg-arc lamp, Xenon lamp and others. There are also optical elements that can play a role in the nature of the source. These include diffusers, fibers, integrated spheres, among others. The choice of source and related elements can have a significant effect on resultant optical phenomena and thus a few paragraphs are dedicated to these aspects here.

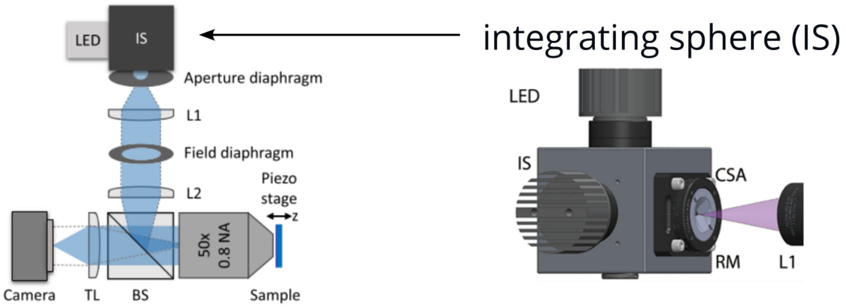

Figure 2.13: Integrating sphere for even illumination in Köhler illumination model, reproduced from [117] and [97] respectively.

Historically, the sun was used as the illumination source for microscopes. Then, for a long time incandescent bulbs were used. Nearly all the data presented in the thesis utilize incandescent bulbs. More specifically, an OSRAM 64657, G6.35 standard, rated at maxima of 250 W and 24 V. In general, a power source in current-limiting mode was operated at 9 A (master) with resultant $\sim$ 23 V (slave), resulting in 207 W of power, under the max 250 W rating.

The main drawback of incandescent bulbs are the non-uniform shape of the filament. The ideal case is for the light source to be spatially uniform. One way to solve this is by using a grit ground glass diffuser that is placed in the path. Another means is by use of an integrating sphere (IS), as shown in Figure 2.13(a) with left and right diagrams reproduced from [117] and [97] respectively.

The IS has reflective sphere inside so that light bounces around, resulting an a even circular light source at the output, where the aperture diaphragm can be placed. The output also is highly spatially incoherent, which also improves the Köhler illumination.

Another alternative is to use a liquid light guide, which guides the light from an external source to the illumination plane. As the light bounces around in a liquid fiber it results in a smooth even illumination plane output, when compared with a traditional optical fiber with many bundeled cores [118, 119].

Even illumination of the BFP ensures the best image quality and resolution. The derivation of the lateral diffraction-limited resolution is based on a perflectly even fully-filled BFP of the microscope objective. Although incandescent filaments, as used in the thesis, do a decent job it would be of interest to explore a more uniform BFP illumination in the future of IRM/BALM of 2D materials.

## Imaging of nanostructures

Regarding the aspects of non-specular diffuse reflections introduced in 2.1, a few additional points of background are presented as it will have some relevance for the Results section. Taking a step back, before diving into more specific techniques like the aforementioned TSOM, it is worth considering whether a typical Köhler illumination microscope is capable of resolving nano-sized objects like nanoparticles of say 100 nm diameter or say even down to 10 nm.

This is in fact possible, but it requires two adjustments, the first being appropriate tuning of INA and CNA, and second being the use of a defocusing scheme. Note that a misconception

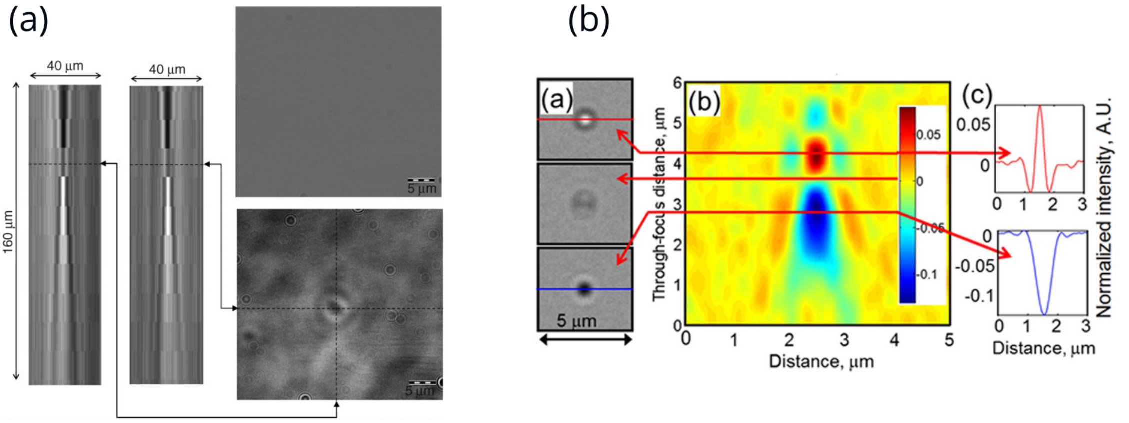

Figure 2.14: (a) Patterson et al. 2008 [120] imaged 10 nm sized Au nanoparticles. Top right is fully opened AD, bottom right is fully closed AD such that INA<CNA. (b) From [98] (Ravikiran group), a through-focus scanning optical microscopy (TSOM) result for a 121 nm Si nanodot of 71 nm height. Illustrate how a nanometric object changes contrast by adjusting the focus.

is that objects less than the diffraction limit of a microscope (often $\sim$ 500 nm) cannot be detected, but this is not true. Lateral resolution is addressed in section 2.2.2, and it relates to the ability to resolve the distance between two objects.

Among other work, a nice example is from 2008, where Patterson et al. [120] imaged 10 nm sized Au nanoparticles via a conventional OM, but it required minimizing the aperture diaphragm (AD) to reduce INA, while CNA was kept the same as the nominal objective NA. This data is reproduced in Figure 2.14(a), where the top right image with a fully open AD is such that INA=CNA and the NP is not visible, while a minimized AD where INA<CNA renders the NP visible in the bottom right image. Furthermore, a $z$-scan was performed as indicated by the left side of the micrographs which further improves visibility.

In fact, such a "through-focus" scan is the basis for the so-called through-focus scanning optical microscopy (TSOM), a technique introduced in 2006 by R. Attota, R. M. Silver and J. Potzich [121]. R. Attota and collaborators have actively published developments on TSOM, including for example in 2014 [98], some data of which is reproduced in Figure 2.14(b). There, a 121 nm Si nanodot was fabricated, with 71 nm height. It is seen that the TSOM scan reveals with good clarity the resulting intensity by which the nano-object can be visualized. Through TSOM scans, various additional information can in fact be gained and deconvoluted on the nature of the nano-object, as shown in [99]. Finally further insights on the mathematics of INA and CNA on the response are published in [100] among others.

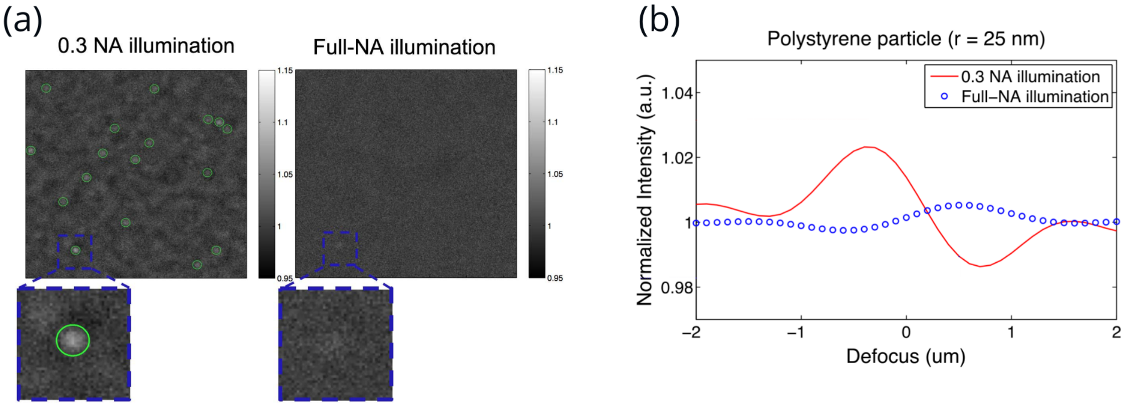

Figure 2.15: (a) Avci et al. 2017 (Ünlü group) [122] imaged 50 nm diameter polystyrene NP, where a lower INA of 0.3 improves visibility compared with full NA 0.8, and (b) the corresponding TSOM profile.

Ünlü group, mentioned earlier, also published many papers on the influence on INA/CNA in the context of the interference reflectance imaging sensor (IRIS) and the associated SP-IRIS which is focused on single-particle (SP) imaging. Data from Avci et al. 2017 (Ünlü group) [122] is reproduced in Figure 2.15. In (a) and (b), a 25 nm polystyrene particle is imaged, where it is shown that reduction of the INA from nominal NA $= 0.8$ down to 0.3 via the aperture diaphragm results in improved visibility. (b) is also a through-focus profile where it is also seen how the NP contrast is improved in the 0.3 case. Additional related papers from Ünlü group are cited here for convenience [95, 93, 96, 97, 117].

Finally it is also useful to note the work of B. Lounis group where absorption and scattering microscopy of single particles were considered [91], including a 5 nm Au nanoparticle [123]. In an IRM configuration, Kanoufi group also simulated and measured the scattered field of Pt nanoparticles particles in Lemineur et al. 2021 [124].

## Resolution

Abbe was the first to propose a formula for diffraction limited resolution [125, p. 278] of the form

$$d_{\text{Abbe}} = \frac{\lambda}{\text{INA} + \text{CNA}}.$$

This $d$ would be the minimum distance two objects would need to be to properly resolve them. Note that if INA $=$ CNA then the formula is $\lambda/(2\text{NA})$.

Rayleigh proposed a version with the factor 1.22. This factor comes from considering the first dark ring surrounding the Airy disc diffraction pattern generated by a point source. Thus this version is [126]

$$d_{\text{Rayleigh}} = 1.22\frac{\lambda}{\text{INA} + \text{CNA}}.$$

For the oil immersion objective used in the thesis, for the wavelengths 450, 550, 650 nm this theoretically gives 196, 239, 283 nm resolving power.

Now, strictly speaking, the Rayleigh version only applies when the two point-sources are fully incoherent with respect to each other. As C. Sheppard points out though [127], although it is the case in fluorescence microscopy for instance where two emitting fluorophores are incoherent with respect to each other, it is not the case for typical reflected or transmitted light illumination. For the case of "normal" operation where INA=CNA, the situation is partially coherent, also called "matched illumination". Furthermore the case INA≪CNA corresponds to rather coherent case.

The $d_{\text{Rayleigh}}$ still probably provides a reasonable approximation, but further work would be needed to more carefully address the lateral resolution limits in IRM/BALM experiments. C. Sheppard provides insights in this regards here [128].

### 2.2.3 . Optical contrast theory

Optical contrast is a measure of how the optical response of an object of interest compares with its background or other reference. Various definitions of contrast exist, and a wide range of definitions are used in the context of 2D materials, which can be confusing. Some relevant definitions are summarized in Table 2.1.

Perhaps the most common definition used is the percent change of intensity $C_{\text{pc}}$ between object and reference, which can be written

$$C_{\text{pc}} \equiv \frac{I_{\text{obj}} - I_{\text{ref}}}{I_{\text{ref}}} = \frac{I_{\text{obj}}}{I_{\text{ref}}} - 1$$

I primarily use this definition throughout the text. A similar but very different definition is the Weber contrast, defined as

$$C_{\text{Weber}} \equiv \frac{I_{\text{max}} - I_{\text{min}}}{I_{\text{min}}} = \frac{I_{\text{max}}}{I_{\text{min}}} - 1$$

Sometimes these definitions are used interchangeably but actually the Weber definition by design

| Name | Formula | Range | Comments |
|---|---|---|---|
| **Percent change** | $C_{\text{pc}} \equiv \frac{I_{\text{obj}} - I_{\text{ref}}}{I_{\text{ref}}}$ | $[-1, +\infty)$ | Also can be written as $I_{\text{obj}}/I_{\text{ref}} - 1$. (Assume $\times 100$ when in %.) |
| **Percent change incl. noise** | $C'_{\text{pc}} \equiv \frac{C_{\text{pc}}}{1 + I_{\text{noise}}/I_{\text{ref}}}$ | $[-1, +\infty)$ | Takes into account noise of stray rays in optical system. Derivation in main text. |
| **alt. Percent change** | $C_{\text{pc,alt}} \equiv \frac{I_{\text{ref}} - I_{\text{obj}}}{I_{\text{obj}}}$ | $(-\infty, 1]$ | Used by F. Huang [129] |
| **Weber contrast** | $C_{\text{W}} \equiv \frac{I_{\text{max}} - I_{\text{min}}}{I_{\text{min}}}$ | $[0, +\infty)$ | Used in psychophysics. |
| **alt. Weber contrast** | $C_{\text{W,alt}} \equiv \begin{cases} \frac{I_{\text{obj}} - I_{\text{ref}}}{I_{\text{ref}}}, & I_{\text{obj}} > I_{\text{ref}} \\ \frac{I_{\text{obj}} - I_{\text{ref}}}{I_{\text{obj}}}, & I_{\text{obj}} < I_{\text{ref}} \end{cases}$ | $(-\infty, +\infty)$ | Alternative definition of Weber contrast. Does not discriminate against negative contrasts. |
| **Michelson contrast** | $C_{\text{M}} \equiv \frac{I_{\text{obj}} - I_{\text{ref}}}{I_{\text{obj}} + I_{\text{ref}}}$ | $[-1, 1]$ | Positive and negative contrasts are symmetric. |

Table 2.1: Summary and information on various definitions of optical contrast.

cannot be negative. There is also the Michelson contrast defined as

$$C_{\text{Michelson}} \equiv \frac{I_{\text{obj}} - I_{\text{ref}}}{I_{\text{obj}} + I_{\text{ref}}}$$

Usually in the literature, the "object" is taken to be the 2D material, while the "reference" is the substrate (but not always). The Michelson contrast by definition can only be $\in [-1, +1]$ (or $[-100\%, +100\%]$ if $\times 100$ is multiplied). Also, if the sample is brighter than the substrate then $C_{\text{M}} > 1$ whilst if it is darker then $C_{\text{M}} < 1$.

This definition has some advantages, such as that it seems intuitive that equal size is given to positive and negative contrasts, and also that the parameter space is finite and symmetric. However there are some disadvantages and arguably it can give misleading results. The percent change definition is not symmetric however, and is highly discriminating against negative contrasts, because whilst its lower bound is $-1$ (or $-100\%$), its upper bound can be $10,000$'s of percent or even more. To illustrate this, consider Figure 2.16a where $I_{\text{ref}}$ is set to $1$, and

$I_{\text{sample}}$ is varied from 0.001 to 10.

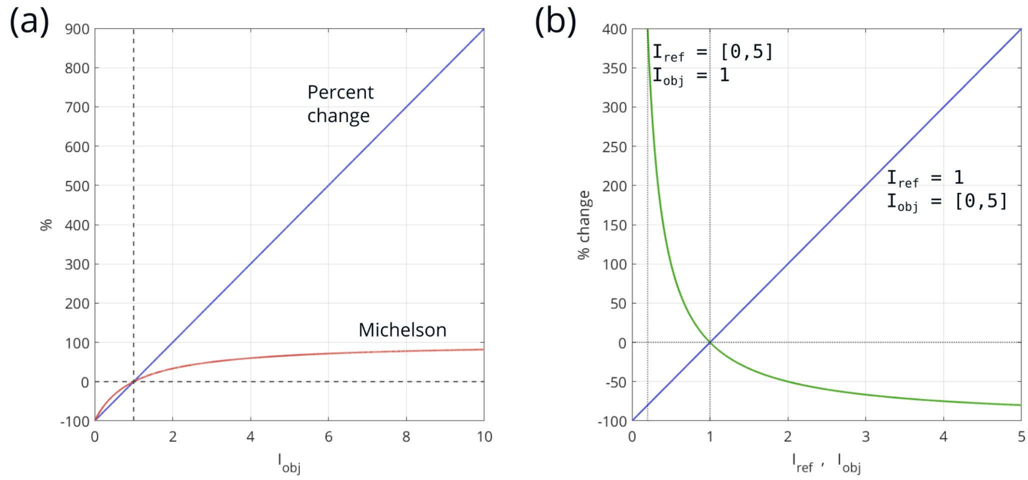

Figure 2.16: (a) Comparison of percent change contrast ($C_{\text{pc}}$) versus Michelson contrast ($C_{\text{M}}$) behavior for $I_{\text{ref}} = 1$ and varied $I_{\text{obj}}$. (b) Result illustrating how choice of reference versus object and swapping them can result in very different contrast values since $> 0$ contrast is unbounded while $< 0$ contrast is bound by $-100\%$.

As can be seen, whilst the percent change contrast has a linear response, the Michelson contrast starts to converge once the sample has about $2\times$ to $3\times$ the intensity of the reference.

Now let us consider the following practical example. Say you have a reflection microscope with an 8-bit camera which has intensity grayscale values from 0–255. The exposure time is adjusted so that the substrate is 7 grayscale. There are two samples on the substrate, where $I_{\text{obj1}} = 200$ and $I_{\text{obj2}} = 250$.

The resulting contrasts for this example are shown in the first two rows of Table 2.2. We see that the percent change contrast changes significantly, but the Michelson contrast appears to be almost unchanged. Furthermore the case is considered where the reference and object are swapped. The result is that the Michelson contrast just changes sign while the Weber contrast appears to discriminate against samples which are darker than the substrate.

Another useful consideration is illustrated in Figure 2.16(b), where $C_{\text{pc}}$ is plotted for $I_{\text{ref}} = 1$, $I_{\text{obj}} = [0, 5]$ and with the swapped case. The result illustrates that when $I_{\text{obj}}$ and $I_{\text{ref}}$ differ by more than 50% (i.e. $-25\%$), things start to get very asymmetric (at "$x$"=0.75). For instance we see that $-75\%$ actually has a lot of power as it corresponds to $+400\%$ of the swapped case.

Now let us consider the Weber definition. The Weber contrast was proposed by Ernst Weber

| Sample | $I_{\text{ref}}$ | $I_{\text{obj}}$ | $C_{\text{pc}}$ (%) | $C_{\text{Michelson}}$ (%) |
|---|---|---|---|---|
| #1 | 7 | 200 | +2757.14 | +93.24 |
| #2 | 7 | 250 | +3471.42 | +94.55 |
| #1 | 200 | 7 | −96.5 | −93.24 |
| #2 | 250 | 7 | −97.2 | −94.55 |

Table 2.2: Example illustrating that $C_{\text{pc}}$ and Michelson contrasts can behave very differently. Also revealed is the non-discriminatory nature of Michelson contrast to positive and negative contrast.

in the late 19th century. Weber was attempting to quantify how humans respond to various physical stimuli. He proposed what is now called **Weber's law**, which states that the just-noticeable difference (JND) that humans can perceive is related to the incremental percent change of the stimuli, and not the relative change [130]. A simple example (which applies also to the eye), is with weights. We can easily perceive 100 g vs. 200 g, but it is very difficult to sense the difference between 10 kg and 10.1 kg. In each case, the relative change $\Delta$weight $=$ 100 g, but in the first case the Weber contrast is 100% while in the second case it is only 1%. It is similar for the eye when it comes to luminous intensity (cd/m$^2$). If a room is very dark, we notice very small changes in light intensity.

Weber's law is commonly used in psychophysics, the field of research concerned with quantifying human response to physical stimuli [130]. The definition ensures that $C \geq 0$ is always met. However the limitation with this law is that the contrast is not signed, which is a feature that can be useful. One possible way out is to use the $C_{\text{W,alt}}$ definition in Table 2.1. Some authors also use a definition of the form $C \equiv C_{\text{pc}} \times [-1]$, which is what F. Huang group does. This group studied ways to improve contrast of various 2D materials including graphene and MoS$_2$ among others [129, 131, 67, 132].

Another consideration in optical contrast is the role of noise. For instance, in a reflection microscope, there are often stray rays which is a form of noise. The effect can be quantified via $I'_{\text{obj}} \equiv I_{\text{obj}} + I_{\text{noise}}$ and $I'_{\text{ref}} \equiv I_{\text{ref}} + I_{\text{noise}}$, which results in

$$C'_{\text{pc}} = \frac{I_{\text{obj}} + I_{\text{noise}} - (I_{\text{ref}} + I_{\text{noise}})}{I_{\text{ref}} + I_{\text{noise}}} = \frac{I_{\text{obj}} - I_{\text{ref}}}{I_{\text{ref}} + I_{\text{noise}}}$$

and

$$C'_{\text{M}} = \frac{I_{\text{obj}} - I_{\text{ref}}}{I_{\text{obj}} + I_{\text{ref}} + 2I_{\text{noise}}}$$

This means that noise lowers contrast, which makes sense. This partly can explain why in practice, as shown later with data, the theoretical 10,000's of percent are not typically manifest.

The above expression can be further written as

$$C'_{\text{pc}} = \frac{I_{\text{obj}} - I_{\text{ref}}}{\left(1 + \frac{I_{\text{noise}}}{I_{\text{ref}}}\right) I_{\text{ref}}} = \frac{\left(I_{\text{obj}} - I_{\text{ref}}\right) \frac{1}{I_{\text{ref}}}}{\left(1 + \frac{I_{\text{noise}}}{I_{\text{ref}}}\right) I_{\text{ref}} \frac{1}{I_{\text{ref}}}}$$

$$\Rightarrow \quad \boxed{C'_{\text{pc}} = \frac{C_{\text{pc}}}{1 + I_{\text{noise}}/I_{\text{ref}}}}$$

Now, one might ask at this point, what contrast definition should be used? Is there one that is superior? Well, it depends. In some sense, contrast is actually meant to be a quantity that is meaningful in the context of the human eye response to light stimuli. With this in mind, the Weber contrast seems to be appropriate. In fact though, strictly speaking there are improved mathematical formulations that exist today that better describe the eye response to light. It turns out that Weber's law only holds in certain ranges of luminance levels [130], and that the so-called Steven's power law is actually the best formulation to date which is valid over a wide range of luminance levels. It is expressed as

$$S = kI^n, \qquad n = 0.33$$

where $S$ is perceived brightness, $k$ is a constant and $I$ is intensity. One could thus argue that in principle Steven's power law should be used.

So far, there has been no deep discussion in the literature on the various definitions of optical contrast in the context of 2D materials, to the author's knowledge. Yet, it is a matter of great importance. In psychophysics however, many papers and resources have been published on the topic, some cited here [130, 133, 134, 135, 136].

In the thesis I will mainly use $C_{\text{pc}}$, which is fine as long as there is an understanding of the asymmetry in positive and negative contrast. It is useful that the definition is simple and signed, and furthermore the ability to account for noise as $C'_{\text{pc}}$ ($C_{\text{pc}}^{\text{noise}}$) is also straight-forward, and I use it in some comparisons with data. I sometimes will make use of the Weber definition and Michelson definitions.

## 2.2.4 . Thin-film optics theory

Having addressed the theoretical considerations of optical microscopy systems, let us now turn the attention to the stack. Let us consider the light ray which is propagating inside the immersion oil, towards the sample. The light can be treated as a classical plane electromagnetic wave of oscillating electric and magnetic fields. The electric field plane wave can be expressed as [137]

$$\boldsymbol{E}(\boldsymbol{r},t) = \text{Re}\left[\boldsymbol{E}_0\, e^{i(\boldsymbol{k}\cdot\boldsymbol{r}-\omega t)}\right] \tag{2.1}$$

where the magnitude of the field $|\boldsymbol{E}(\boldsymbol{r},t)|$ is in SI units of V/m. The field is actually a trigonometric function (sine), but to simplify the mathematics it is often written as a complex exponential—however one need take care to take the real part of the expression to get the true field. Furthermore note that the field is often written without "Re" but it is implied to take the real part when appropriate. [138, p. 17]

$\boldsymbol{k}$ is the wavevector and takes the form $|\boldsymbol{k}| = k = \frac{2\pi}{(\lambda/\tilde{n})}$ where $\tilde{n}$ is the complex refractive index of the medium. The angular frequency $\omega = 2\pi/T$ of the light is related to the wavevector by the linear disperion relationship of light, $\omega(k) = \frac{c}{\tilde{n}}k$. This means that $\omega = \frac{2\pi c}{\lambda}$. This is an important result because it shows that the angular frequency of light (and thus its energy $E = \hbar\omega$) does not change depending on the medium $\tilde{n}$ that it propagates in. Rather it is the wavevector (and thus momentum $\boldsymbol{p} = \hbar\boldsymbol{k}$) that changes depending on the medium. [137]

Notice that when the electric field was defined in Equation 2.1, a stance was taken on the phase definition. The phase convention that I chose is the one used most commonly in physics, but opposite to the one used in electrical engineering. (In the field of optics, both conventions are common.) The two phase conventions are summarized in Table 2.3. The choice of phase convention has a huge consequence as a large number of formulas derived later are affected.

| Community | Electric field definition | Refractive index | Examples |
|---|---|---|---|
| Physics, optics | $\boldsymbol{E}(\boldsymbol{r},t) = \boldsymbol{E}_0\, e^{i(\boldsymbol{k}\cdot\boldsymbol{r}-\omega t)}$ | $\tilde{n} = n + i\kappa$ | Fox [137], Stenzel [139] |
| Electrical engineering, optics | $\boldsymbol{E}(\boldsymbol{r},t) = \boldsymbol{E}_0\, e^{j(\omega t-\boldsymbol{k}\cdot\boldsymbol{r})}$ | $\tilde{n} = n - j\kappa$ | Fujiwara [138],<br>Orfanidis [140],<br>Ausserré [88] |

Table 2.3: Phase conventions in electromagnetism by community, with some example sources.

## Optical properties of media

The electric and magnetic properties of a medium can be described by the complex relative electric permittivity $\tilde{\varepsilon}_r(\omega)$ and by the complex relative magnetic permeability $\tilde{\mu}_r(\omega)$. These quantities have a microscopic physical origin and can be described by various mathematical models, sometimes with great accuracy. Discussion of the microscopic origins can fill entire textbooks. Main factors include the bound electron shells, giving rise to the dielectric properties, whilst free electrons give rise to metallic properties.

The responses are highly dependent on frequency. For instance, metals only behave "metallically" from static frequency ($\omega = 0$) up to around the plasma frequency ($\omega = \omega_p$), beyond which they behave as dielectrics. For many materials, it is the case that $\tilde{\mu}_r(\omega) \approx 1$. This will be assumed throughout the text as this thesis is not concerned with magnetic properties and they will not be relevant.

For $\tilde{\mu}_r = 1$, the complex refractive index (RI) is

$$\tilde{n}(\lambda) = \sqrt{\tilde{\varepsilon}_r(\lambda)}$$

Whilst it is the permittivity (also called dielectric function) which is closer to the intrinsic material properties in terms of the mathematics of the microscopic origins, most real measurements and interactions of fields feel the response of the RI. The complex RI can be broken down into its real and imaginary parts as

$$\tilde{n}(\lambda) = n(\lambda) + i\kappa(\lambda)$$

where $\kappa(\lambda)$ is called the extinction coefficient and $n(\lambda)$ is the real refractive index (sometimes simply called "refractive index").

If a certain range of wavelengths has $\kappa(\lambda) \approx 0$ it means that in that range there is no loss or absorption taking place (transfer of energy into the material itself such as photon creating phonon, or transfer of energy to an electron going to an excited state). It should be noted though that loss does not always imply an absorption process. Scattering can occur as well, which would attenuate the light. Such processes can often be described by Mie theory.

It is for that reason that Beer's law (see [137, pp. 3–5]) is written with the so-called **attenuation**

**coefficient** instead of absorption coefficient.

$$I(d) = I_0 e^{-\mu d}, \qquad \mu = \mu_{\text{abs}} + \mu_{\text{sca}}$$

If $\mu_{\text{sca}} \approx 0$ however then $\mu = \mu_{\text{abs}} = \alpha$ where $\alpha$ is the **absorption coefficient**. This coefficient is related to the extinction coefficient by the following relation:

$$\alpha = \frac{2\omega}{c}\kappa = \frac{4\pi}{\lambda}\kappa$$

## Reflectance, Transmittance, Absorptance, Scattering

Let us now consider what happens when an EM wave encounters an interface between medium $\tilde{n}_1$ to $\tilde{n}_2$. How much of the wave is reflected, or transmitted, or absorbed?

Fresnel was the first to compute this using Maxwell's equations, solved by imposing that the fields (and their derivatives) be continuous across the interface. The associated reflection and transmission coefficients should be a ratio of the fields as follows:

$$r_{12} \equiv \frac{E_R}{E_I}, \qquad t_{12} \equiv \frac{E_T}{E_I}$$

where $E_{\text{I}}$ is the incident field, and $E_{\text{R}}$, $E_{\text{T}}$ are the reflected and transmitted fields. Both $r$ and $t$ are complex, and each can be written as

$$r = |r|e^{i\phi_r}, \qquad t = |t|e^{i\phi_t}$$

where $\phi$ is the phase of the light. One important result which I will return to later, is that if both media are non-absorbing (i.e. $\kappa \approx 0$), then the phase upon reflection is always

$$\phi_r = \begin{cases} 180^\circ, & n_1 < n_2 \\ 0^\circ, & n_1 > n_2 \end{cases} \tag{2.2}$$

For example, for a suspended soap film, the light at air/soap interface experiences $\phi_r = 180^\circ$, but soap/air experiences $\phi_r = 0^\circ$. Anyway, coming back to $r_{12}$, Fresnel found that in terms of $\tilde{n}_1$ and $\tilde{n}_2$, the reflection coefficient at normal incidence is

$$r_{12} = \frac{\tilde{n}_1 - \tilde{n}_2}{\tilde{n}_1 + \tilde{n}_2},$$

To compute the reflectance $R = I_R/I_I$ from this, which is the percent of the incident intensity that is reflected, one can do

$$R = |r_{12}|^2 = r_{12}r_{12}^*$$

where $r_{12}^*$ is the complex conjugate of $r_{12}$. This applies similarly for calculating $T$.

For non-normal incidence, it is necessary to separate the fields into two components based on the so-called plane of incidence of the ray. If the field is parallel to the plane of incidence, it is $s$-polarized ("*senkrecht*" is German for perpendicular), while if the field is parallel to the plane of incidence it is $p$-polarized (so "p" for "parallel") [90, p. 113]. There exist alternative names, which are transverse electric (TE) for the $s$-polarized case, and transverse magnetic (TM) for the $p$-polarized case.

I reproduce below result for the reflection coefficient for the $s$ and $p$ cases [90, p. 113]

$$r_s = \frac{\tilde{n}_1 \cos\theta_1 - \tilde{n}_2 \cos\theta_2}{\tilde{n}_1 \cos\theta_1 + \tilde{n}_2 \cos\theta_2}, \qquad r_p = -\frac{\tilde{n}_1 \cos\theta_2 - \tilde{n}_2 \cos\theta_1}{\tilde{n}_1 \cos\theta_2 + \tilde{n}_2 \cos\theta_1}$$

The transmitted/refracted case also has associated $t_s$ and $t_p$ coefficients. In general, the incident light is a linear superposition of $s$ and $p$ polarized waves. Regarding the reflected light, it means taht the following criteria must be met [67]:

$$R(\theta) = \alpha|r_s(\theta)|^2 + (1-\alpha)|r_p(\theta)|^2$$

where $\alpha \in [0, 1]$. As is discussed later when considering incident angles in IRM and BALM, $\alpha = 0.5$ is the randomly polarized case, which was used throughout the thesis work.

Now, apart from reflectance ($R$) and transmittance ($T$), there is also absorptance ($A$) and scattering ($S$), the two mechanisms of optical loss that can take place, where $L \equiv A + S$ [139, p. 99]. Thus in total, the following condition must be met:

$$1 = R + T + A + S$$

Elastic scattering does not result in a loss of the number of photons, but instead disperse the photons. Thus in the context of the thesis, $S$ is associated with diffuse reflections discussed earlier, loosely speaking. (Specular reflections still involve "diffuse" Rayleigh scatterers but coherent superpositions result in specular behavior [90]).

Regarding **absorptance** $A$ (not to be confused with "absorbance"), various absorption properties can give rise to a non-zero value. This includes the likes of a photon's energy being converted to promoting an electron to a higher electronic (or vibronic or rovibronic) state. Other processes include Coulomb scattering for example. $A$ is intimately linked with the $\kappa(\omega)$ and $\alpha(\omega)$ coefficients, and can also be expressed as $(I_A/I_{\text{inc}})$.

Finally, a few points shall be addressed regarding the difference between absorp**t**ance (discussed above), absorbance, and optical density (OD). Absorption coefficient $\alpha$ is defined as the fraction of the power absorbed in a unit length of the medium. If light is propagating along $z$, and the intensity (optical power per unit area) at $z$ is $I(z)$, then the decrease of intensity in an incremental slice d$z$ is [137, p. 3] $\mathrm{d}I = -\alpha\,\mathrm{d}z \times I(z)$ which can be integrated and gives Beer's law $I(z) = I_0\,e^{-\alpha z}$ which was mentioned earlier. Note $\alpha$ has units inverse length and is typically expressed in cm$^{-1}$. Then there is optical density (OD) which is defined as [137, p. 4]

$$\text{OD} = -\log_{10}\left(\frac{I(d)}{I_0}\right)$$

where $d$ is the length of the abosrbing medium. It is thus related to $\alpha$ by [137, p. 4]

$$\text{OD} = \left(\frac{1}{\ln(10)}\right)\alpha\, d = 0.434\,\alpha\, d$$

Now, finally, comes the concept of "absorbance". According to Stenzel [139, p. 102], this term, as defined by producers of UV-Vis transmittance spectroscopy instruments is a bit misleading. In that context, raw $T(\lambda)$ data is converted to "absorbance" by [139, p. 102]

$$\mathit{absorbance} = -\log_{10}\left(\frac{T}{T_{\text{ref}}}\right)$$

In solution chemistry, the idea is to first take a $T_{\text{ref}}$ spectrum of a reference which usually is a glass cuvette with just the solvent. Then, $T$ is measured with the molecules of interest in that solvent. However, this approach has several problems, as Stenzel points out [139, pp. 102–103], especially if this approach is used for thin film samples. The situation is improved if the $T_{\text{ref}}$ slot is left blank so that $T_{\text{ref}} = 1$. This leads to

$$\mathit{absorbance}[T_{\text{ref}} = 1] = -\log_{10}(T) = -\log_{10}(1 - A - S - R)$$

Here we see that the definition is problematic as scattering processes would show up as absorbance, and so would any non-zero reflection. Thus, in order for absorbance to be linked to OD and $\alpha$, it would need to be the case that $0 = A = S = R$. Among other papers, Pekker et al. [141] is a useful example where care was taken to properly compute OD, where sometimes $R \neq 0$.

The above points have some relevance later because UV-Vis $T$ spectra were acquired and simulated for layers of the BALM optical stack (2.7.4), as well as for our in-house grown CVD $MoS_2$ (3.5).

## Models for optical properties

Various mathematical models and theories exist to describe the microscopic/physical origins of $\tilde{n}(\lambda)$ dispersions. For dielectrics, one useful model is the Lorentz , proposed by Dutch physicist Hendrik Antoon Lorentz. The model consists of a sum of so-called Lorentz oscillators, and can be expressed as follows [137, 139]:

$$\tilde{\varepsilon}_r(\omega) = \varepsilon_\infty + \sum_{j=1}^{N} \frac{f_j}{\omega_j^2 - \omega^2 - i\gamma_j\omega}$$

with each $j$ representing an oscillator. $f_j$ is the oscillator strength, $\omega_j$ is the energy (peak center) of the oscillator, and $\gamma_j$ is the full width half max (FWHM) linewidth. If a particular Lorentz model is able to account for all oscillators in the sample, then $\varepsilon_\infty$ (the real dielectric function at very high frequencies, "at infinity") is simply equal to 1. In a sense it should always be true that $\varepsilon(\omega = \infty) = 1$, but if one is only interested in correctly descibing a particular spectral window of the sample, then $\varepsilon_\infty$ can be set to non-unity as a way to capture the effect of oscillators at higher frequencies.

| | $\tilde{\varepsilon}_r(\omega) =$ | $f_j$ units | $\gamma_j$ units |
|---|---|---|---|
| Convention #1 | $1 + \sum_{j=1}^{N} \frac{f_j}{\omega_j^2 - \omega^2 - i\gamma_j\omega}$ | $eV^2$ | eV |
| Convention #2 | $1 + \omega_{p,m}^2 \sum_{j=1}^{N} \frac{f_j}{\omega_j^2 - \omega^2 - i\gamma_j\omega}$ | - | eV |
| Convention #3 | $1 + \sum_{j=1}^{N} \frac{f_j\omega_{p,j}^2}{\omega_j^2 - \omega^2 - i\gamma_j\omega}$ | - | eV |
| Convention #4 | $1 + \sum_{j=1}^{N} \frac{\omega_{p,j}^2}{\omega_j^2 - \omega^2 - i\gamma_j\omega}$ | - | eV |

Table 2.4: A summary of the various conventions used for Lorentz oscillators in the dielectric function $\tilde{\varepsilon}_r(\omega)$.

An important note is that when considering Re $[\tilde{\varepsilon}_r(\omega)]$ and Im $[\tilde{\varepsilon}_r(\omega)]$, they satisfy the Kramers–Krönig (KK) relations and thus are "KK consistent". KK consistency has to do with the fact that, the real and imaginary parts of the dielectric function Re $[\tilde{\varepsilon}_r(\omega)]$ and Im $[\tilde{\varepsilon}_r(\omega)]$ are related mathematically. By extension $n$ and $\kappa$ also are inter-related. There are some caveats however—for instance one must in principle know one or the other over a very broad spectral range (0 to "$\infty$" eV) in order to derive one from the other. That being said, not all dispersion models that are used are KK consistent. This is for a number of reasons. More information can be found in [137, 139].

Another important aspect is that, various conventions are used for the Lorentz model in the literature, which can be confusing. (For instance this means that oscillator strength values are not easily compared, and sometimes have different units.) Therefore, I have summarized them in Table 2.4.

The Lorentz model accounts for dielectrics, where charges are bound, i.e there is a bandgap with few free carriers. In metals, the Drude model (proposed by German physicist Paul Drude) can be used [137]. It accounts for the contributions of the free electrons. In fact the combined Drude–Lorentz model can account for both free and bound charge contributions. The model is derived in many standard texts [137, 139]. It can be expressed as

$$\tilde{\varepsilon}_r(\omega) = 1 - \frac{\omega_p^2}{\omega^2 - i\gamma\omega}, \qquad \omega_p^2 = \frac{n_e e^2}{\varepsilon_0 m_e}$$

where $\omega_p$ is the so-called **plasma frequency** (termed as such since the sea of free electrons in some metals behave as a gas and thus are a type of plasma since the particles making it up are charged). In fact, an even simpler model is to ignore the Coulomb scattering setting $\gamma = 0$ which gives

$$\tilde{\varepsilon}_r(\omega) = 1 - \frac{\omega_p^2}{\omega^2}$$

In the above case, we see that $\varepsilon_r$ is always real. We also see though that for $\omega < \omega_p$, $\varepsilon_r$ is $< 0$, and in fact it takes on quite significant negative values as frequency gets lower and lower and approaches DC. In fact the main signature of metallic behavior is a very negative number for the real part of $\tilde{\varepsilon}_r$. This results in a very large extinction coefficient $\kappa$ because of the relation $\tilde{n} = \sqrt{\tilde{\varepsilon}_r}$. Thus, we see that $\varepsilon''$ (imaginary part of $\tilde{\varepsilon}_r$) is not necessarily directly linked with $\kappa$.

At frequencies $\omega > \omega_p$, the metallic behavior starts to wear off and a metal behaves more like a dielectric. This point will become relevant later when exploring the origins of the BALM effect and the effect of using 450 nm wavelength vs. 650 nm wavelength.

The above represents the basic microscopic theories of the frequency dependent response of dielectrics and metals to an electric field. Some of these models are used later to describe the optical response of layers in the optical stack of IRM and BALM. Some other dispersion models will referenced as well accordingly in the text.

## Measurement techniques for optical properties

For many thin-film systems including for IRM and BALM, the values of the complex refractive index disperion $\tilde{n}(\lambda)$ are of paramount importance since it plays a role in determining the resulting reflectance. In some cases, even small changes in $n$ or $\kappa$ can have a significant effect. This is especially the case for $\tilde{n}_{\mathrm{MoS_2}}$ itself, and the Cr/Au (ARA) coating used in BALM.

Various techniques exist to measure $\tilde{n}(\lambda)$. The techniques used also depends on which frequencies are probed. For example at low frequencies, electrical spectroscopy can be used, while at infrared or optical regime then reflectometry and ellipsometry are common.

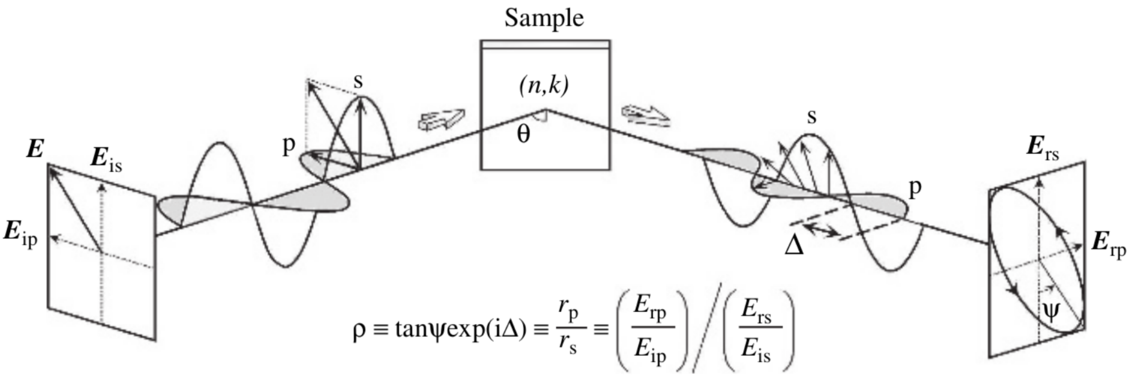

Figure 2.17: Principle of variable angle spectroscopic ellipsometry (VASE), reproduced from Fujiwara [138, p. 82].

Reflectometry has been around for a long time. The legacy approach requires computing a Kramers–Krönig (KK) integral [142, p. 117]. One such measurement pipeline is described in a 1959 paper [143] among others, where $\tilde{n}(\omega)$ was attained for a Ge crystal. The reflectance spectrum $|r(\omega)|^2$ is measured in a broad spectral range, in this case 1 to 10 eV. Then, using $r = |r|e^{i\theta}$ and Fresnel formulae, a KK integral for $\theta(\omega)$ is computed based on knowledge of

$|r|(\omega)$ and $\omega$, allowing finally conversion to $n(\omega)$ and $\kappa(\omega)$.

However, use of KK integrals on data requires a very broad spectral range, because of the nature of the integral and physical relation between $n$ and $\kappa$. There is a way out though (as discussed earlier), which is to add a real $\varepsilon_\infty$ to $\tilde{\varepsilon}(\omega)$ as a way of representing the effect of absorption processes outside the spectral window for the higher energies (which is what is meant by "$\infty$").

Finally, it should be noted that one can also perform reflectometry without any KK integrals. For example, if a KK-consistent dispersion model is used to fit the data (like a sum of Lorentzians), then the equations for Re and Im of $\tilde{\varepsilon}(\omega)$ are available in closed form and have KK-consistency built in [137] (although often it requires use of $\varepsilon_\infty$). This was done in several papers discussed later for 2D TMDs, including Li et al. [37] (Heinz group) for measuring $\tilde{\varepsilon}(\omega)$ of various TMDs and Yu et al. [144] where $\tilde{\varepsilon}(\omega)$ is measured for gated TMDs.

During the thesis, our collaborators from the *OptMatLab* in University of Genova used ellipsometry to measure $\tilde{n}(\lambda)$ for some of the layers in our optical stack. The principle of the setup is reproduced in Figure 2.17 from Fujiwara [138, p. 82]. The idea is to have a light wave reflect off of the sample and then measure $\rho$, defined as

$$\rho \equiv \frac{r_p}{r_s} = \frac{(E_p^r/E_p^i)}{(E_s^r/E_s^i)} \equiv \tan\Psi e^{-i\Delta}$$

where $r_p$ and $r_s$ are the complex reflection coefficients for $p$-polarized (TM) and $s$-polarized (TE) light. On the right-hand-side, the two ellipsometric parameters $(\Psi, \Delta)$ are the center-piece of ellipsometry. (Note that above I used the physics convention for phase. Many ellipsometry scientists prefer the optics/engineering convention which takes the form $\rho = \tan\Psi e^{i\Delta}$.)

Whenever $\rho$ is measured as a function of a range of wavelengths, the term spectroscopic ellipsometry (SE) is used. (There exist ellipsometers of just a single wavelength that for example have the main purpose of measuring a film thickness with well-known RI). Furthermore, when the angle of incidence (AOI) is varied in addition to the wavelength, it is called variable angle spectroscopic ellipsometry (VASE). Our collaborators from *OptMatLab* in general used VASE. Further aspects are elaborated later.

Now a final point is that, for both reflectometry and ellipsometry, there is a challenge when it comes to characterizing thin films, due to the coherent interferences that take place. The thin-film interferences, originating from the geometric aspect of the sample, make it more challenging to deduce the intrinsic optical response. In other words, differing between the "*sample geometry* and *sample material*" becomes the primary challenge when understanding the optics of thin films, as Stenzel put it [139, p. 5].

Yet, it can be overcome by use of Fresnel thin-film models discussed later, including Airy's recursive reflection formula and the transfer matrix method (TMM). However, due to reasons elaborated later, this does not always save the day. As explained later, for our own 2D $MoS_2$ which was characterized by *OptMatLab*, it was necessary to transfer it to a substrate which would remove the thin-film interference of the substrate—namely single-polished sapphire where light rays get diffused by the unpolished side to rid the system of interferences.

## Incoherent layers

So far, we only considered what happens when light encounters a single interface, where the two media surrounding it extend to infinity. Now let us consider a transparent slab of thickness $d$ and refractive index $n = 1.5$, surrounded by air ($n = 1$). There are two interfaces, at which light gets partially reflected and partially transmitted in both cases. Hence we have $(r_{12}, t_{12})$ and $(r_{23}, t_{23})$.

Now the question is, will the waves that get reflected and transmitted get added in a coherent superposition? Or will each ray be incoherent with respect to the other? This depends on a number of factors, including how $\lambda$ compares with $d$, the bandwidth $\Delta\lambda$ (temporal coherence) of the light, spatial coherence of the light, and rugosity of the slab.

Stenzel [139, p. 136] provides a great discussion on this point, including presenting transmittance data of a $d = 142$ $\mu$m glass slab for various bandwidths, $\Delta\lambda =$ 0.4, 1.2, 4.0 nm. The result has been reproduced in Figure 2.18. Upon inspection it is seen that there are three types of behavior: **incoherent**, **partially coherent** and **coherent**.

If the layer and conditions are such that the waves are added in a incoherent fashion, the layer is known as an incoherent layer. Mathematically this means adding the intensities of the light, whilst for the coherent case it is the fields/phases of the light that are added. The in-between case can be treated by the theory of partial coherence.

For the coherent case, the interference pattern is clearly seen in the data, corresponding to the peaks and troughs of constructive or destructive interference, while for the incoherent case it is constant. The mathematics for the incoherent glass slab is derived in [137, pp. 3–4] through

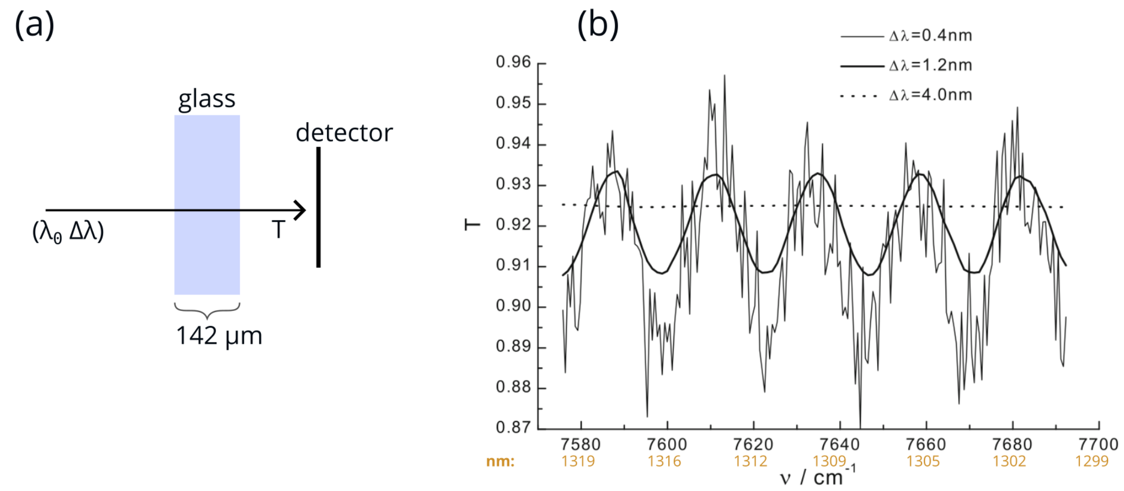

Figure 2.18: (a) Transmittance spectroscopy configuration of a transparent slab of 142 μm thickness, with wavelength and bandwidth as input parameters of a light ray. In (b), resulting transmittance spectra from Stenzel [139, p. 136] for differing bandwidths of $\Delta\lambda = 0.4, 1.2, 4.0$ nm. (and added labels converting $\nu$ [cm$^{-1}$] to $\lambda$ [nm])

an infinite sum. The in-between, partially coherent case, shows a hint of the pattern but it is “noisy”.

In this case, the thickness, wavelength, rugosity and temporal coherence are in such a way that changing the coherence length can cover the three cases. The temporal coherence length can be expressed as [139, p. 137–138]

$$t_{\text{coh}} = \frac{2}{\Delta\omega}$$

with associated bandwidth

$$\Delta\omega = \frac{2}{\Delta t_{\text{coh}}} = \frac{2\pi c}{\lambda^2}\Delta\lambda$$

For laser sources, which are usually highly coherent both temporally and spatially, interferences continue to take place even for very thick slabs. Coherence lengths can be on the order of centimeters or even meters.

In the thesis, the coherent case is of primary importance, with some incoherent used at times.

Treating of partial coherence can be quite complex and it is not explored in this thesis, although future work on how partial coherence may play a role in IRM and BALM optical response for the study of 2D and other materials would be of interest. For convenience, some papers are cited here which provide TMM-based implementations of partial coherence [145, 146, 147, 148, 149].

## Coherent layers: TMM and Airy's recursive formula

When the layers are coherent, the resulting superpositions are of the EM fields and not of the intensities. A derivation for the simplest case (not generalized) is found in [137].

It is useful though to have a mathematical formulation that can work for an arbitrary number of layers. There are two main approaches to a generalized form. The first which is more well-known is the so-called transfer matrix method (TMM) [90, p. 427] [150, 111]. I will not do a full derivation, but I reproduce the essential formulas below for normal incidence. Consider a coherent stack of $(n_j, d_j)$ where $j = 1 \ldots N$ and thus the initial and final semi-infinite media are $n_0$ and $n_{N+1}$. Now consider the matrix below

$$M_j = \begin{bmatrix} \cos\left[\beta_j\right] & -i\sin\left[\beta_j\right]/n_j \\ -i\sin\left[\beta_j\right]n_j & \cos\left[\beta_j\right] \end{bmatrix}$$

Here, $M_j$ is a matrix associated with the $j$'th layer in a coherent stack, and $\beta_j = k_0 d_j n_j$ is the so-called phase thickness of that layer (the physics phase convention was used above). Now consider the following multiplicative sum:

$$M = \prod_{j=1}^{N} M_j = \begin{pmatrix} m_{11} & m_{12} \\ m_{21} & m_{22} \end{pmatrix}$$

where $M$ is called the characteristic matrix. It turns out that the resulting reflection coefficient can be computed as follows:

$$r = \frac{m_{11}(n_0) - m_{22}(n_{N+1}) + m_{12}(n_0)(n_{N+1}) - m_{21}}{m_{11}(n_0) + m_{22}(n_{N+1}) + m_{12}(n_0)(n_{N+1}) + m_{21}}$$

Finally, it is worth noting that some authors prefer calling this simply the "matrix method", because the so called "transfer matrix" is actually used in a different type of system, according to [151].

The second method, which is less well-known by name, is via **Airy's formula** for recursive coherent reflections. Although the formula can be found in many places especially for a limited number of layers, it is usually given no name. However some texts such as P. Yeh's 1988 *Optical Waves in Layered Media* [152, pp. 86–87] as well as D. Ausserrée inventor of BALM [87] terms it "Airy's formula" because George Biddell Airy was the first to derive it in 1833.

For an arbitrary number of layers it takes the form [140, p. 187][139, p. 140]:

$$r_{012\ldots\ell(\ell+1)} = \frac{r_{012\ldots\ell} + r_{\ell(\ell+1)}e^{+2i\beta_\ell}}{1 + r_{012\ldots\ell}r_{\ell(\ell+1)}e^{+2i\beta_\ell}}$$

where $\beta_\ell \equiv k\tilde{n}_\ell d_\ell$ is the so-called **phase thickness** [138, p. 45] of the $\ell$'th layer. $\beta$ is thus the wavevector $k = 2\pi/\lambda$ multiplied by the complex optical path length (OPL) $\tilde{n}d$. (Note that in the engineering phase convention used by D. Ausserrée and others, the $+2i\beta$ above would be replaced by $-2j\beta$.)

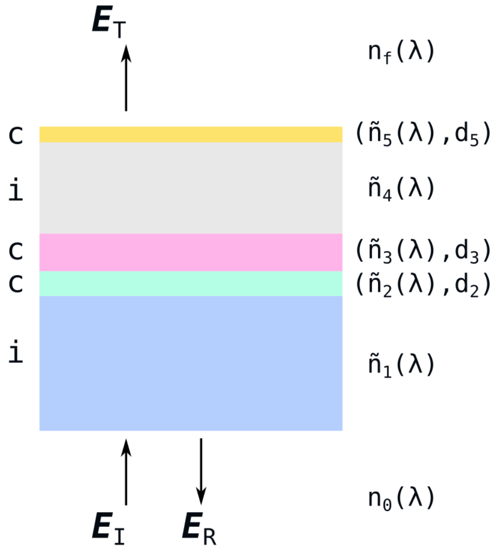

Figure 2.19: Example optical stack consisting of both incoherent ("i") and coherent ("c") layers. Only refractive index is an input for an incoherent layer, while coherent layers need both RI and thickness. Also note that the initial ($n_0$) and final ($n_\mathrm{f}$) media are not complex. This is true for the IRM/BALM systems considered in the thesis, and is important because mathematically things become more tricky when the initial or final medium is complex. The incident, reflected, and transmitted electric fields are also shown.

In some of the simulations, I make use of an implemention of Airy's formula in MATLAB by S. J. Orfanidis [140] (with the engineering phase convention, $\tilde{n} = n - j\kappa$). I also make use of a TMM Python implementation released by S. J. Byrnes [153] (with the physics convention, $\tilde{n} = n + i\kappa$). The latter TMM implementation includes the possibility to combine both coherent and incoherent layers, whilst the former is only valid for coherent layers.

In Figure 2.19, an example stack is given, consisting of both incoherent and coherent layers. It should also be noted that with regards to both the TMM and Airy's formula, additional mathematical difficulties arise if the incident or final semi-infinite media have a non-zero imaginary RI [153]. Fortunately, no such system is used in this thesis.

## Effect of incident angles

As was derived above, reflectance is a function of angle due to the nature of EM fields and their behavior at boundaries as derived by A. Fresnel. And, since objective lenses illuminate and collect across many angles, it is important to consider this aspect and to mathematically derive the weight of each angle for an illuminated and collected field of specular light rays.

In 2018, J. M. Katzen et al. (in F. Huang group) [67] provided a partial derivation of such a weight function in a way that is very clear, and furthermore relatively smooth to implement in code which I did for the simulations performed as discussed later in the text. Since only a partial mathematical derivation was provided in [67] I shall include a full version below to remove any ambiguity.

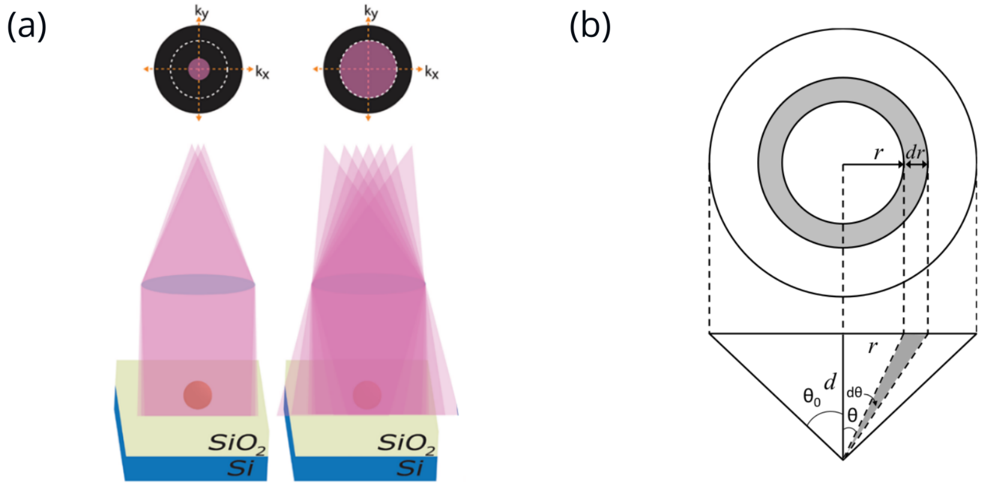

Figure 2.20: (a) From From Yurdakul et al. 2020 (Ünlü group) [97], Ünlü IRIS or my figure depicting the relationship between backfocal plane radius (INA) and resulting angular distribution of light beams. (b) Drawing from [67] showing geometry of incident rays and its mathematical decomposition.

In order to derive the weight function, consider the geometry of the microscope objective as shown in Figure 2.20, where (a) is reproduced from [97] and (b) reproduced from F. Huang group paper [67].

As can be seen, the rays originating from the back focal plane (BFP) of the objective behave as follows: the rays from the center have an incident angle of zero degrees, while the rays emanating away from the center of the circle have higher and higher incident angles. Upon inspection, it is evident that there are more rays coming from higher angles since it scales with the area of the incremented annulus.

The area of each annulus can written as $dA = 2\pi r\,dr$, and from the geometry we see that $r = d\tan\theta$, where $d$ is the distance from the BFP to the field plane. Thus,

$$dA = 2\pi\left(d\tan\theta\right)dr$$

Now, considering the tangent of $\theta + d\theta$, we see

$$d\tan\left(\theta + d\theta\right) = r + dr$$

Using a small angle approximation

$$\tan\left(\theta + d\theta\right) \approx \tan\theta + d\theta\sec^2\theta$$

we can simplify further to

$$dr = d\tan\left(\theta + d\theta\right) - r = d\tan\left(\theta + d\theta\right) - d\tan\theta$$

$$= d\left[\tan\theta + d\theta\sec^2\theta - \tan\theta\right] = d\left[\sec^2\theta d\theta\right]$$

Hence

$$dA = 2\pi d^2\tan\theta\sec^2\theta\ d\theta$$

The total reflectance at each angle $R(\theta)$ is given by

$$R(\theta) = \alpha|r_s(\theta)|^2 + (1-\alpha)|r_p(\theta)|^2$$

where $\alpha \in [0,1]$ deterimes the portion of rays which are $s$ (TE) polarized vs. $p$ (TM) polarized. If the polarization is random, which is typically a safe assumption if no polarizers have been placed in the light path, then $\alpha = 0.5$ so

$$R(\theta) = \tfrac{1}{2}\left(|r_s(\theta)|^2 + |r_p(\theta)|^2\right)$$

Now we need to integrate. We need to solve

$$\bar{R} = \frac{1}{A_0}\int_0^{\theta_0} R(\theta)\, dA = \frac{1}{A_0}\int_0^{\theta_0} R(\theta) 2\pi d^2 \tan\theta \sec^2\theta\, d\theta$$

The total area $A_0$ by itself would be

$$A_0 = \pi r_0^2 = \pi\left(d\tan\theta_0\right)^2 = \pi d^2 \tan^2\theta_0$$

We confirm also that the integral gives the same result:

$$A_0 = \int_0^{\theta_0} 2\pi d^2 \left[\tan\theta \sec^2\theta\right] d\theta = 2\pi d^2 \int_0^{\theta_0} \left[\frac{\sin\theta}{\cos^2\theta}\right] d\theta = 2\pi d^2 \left[\frac{\tan^2\theta_0}{2}\right] = \pi d^2 \tan^2\theta_0$$

Now we can write the integral with $R(\theta)$ and we have

$$\begin{aligned}\bar{R} &= \frac{1}{\pi d^2 \tan^2\theta_0}\int_0^{\theta_0} R(\theta)\; 2\pi d^2 \tan\theta \sec^2\theta\; d\theta \\ &= \frac{2}{\tan^2\theta_0}\int_0^{\theta_0} R(\theta)\;\tan\theta \sec^2\theta\; d\theta\end{aligned}$$

Now finally, since we assume random polarization we have that factor $1/2$ from $R(\theta) = \frac{1}{2}\left(|r_s(\theta)|^2 + |r_p(\theta)|^2\right)$. This gives us

$$\boxed{\bar{R} = \frac{1}{(\tan\theta_0)^2}\int_0^{\theta_0} \left(\,|r_s(\theta)|^2 + |r_p(\theta)|^2\,\right) \tan\theta\,(\sec\theta)^2\, d\theta} \tag{2.3}$$

Thus, the resulting weight function can be said to be

$$w(\theta) = \tan\theta(\sec\theta)^2 = \frac{\sin\theta}{\cos^3(\theta)}$$

It is useful to plot this weight function to get an idea of the influence of the angle. This has been done in (a) linear scale (b) log scale of Figure 2.21.

The range of angles of the plots range from 0° to 67°, the latter chosen because it is the $\theta_{\text{max}}$ of a NA$= 1.4$ oil immersion objective, the same used in our IRM/BALM setup. From the result, it is seen that in fact as expected the weight of higher angles are significantly higher than the lower angles. In fact, at $\approx 60°$ the weight is about 2 orders of magnitude greater than the

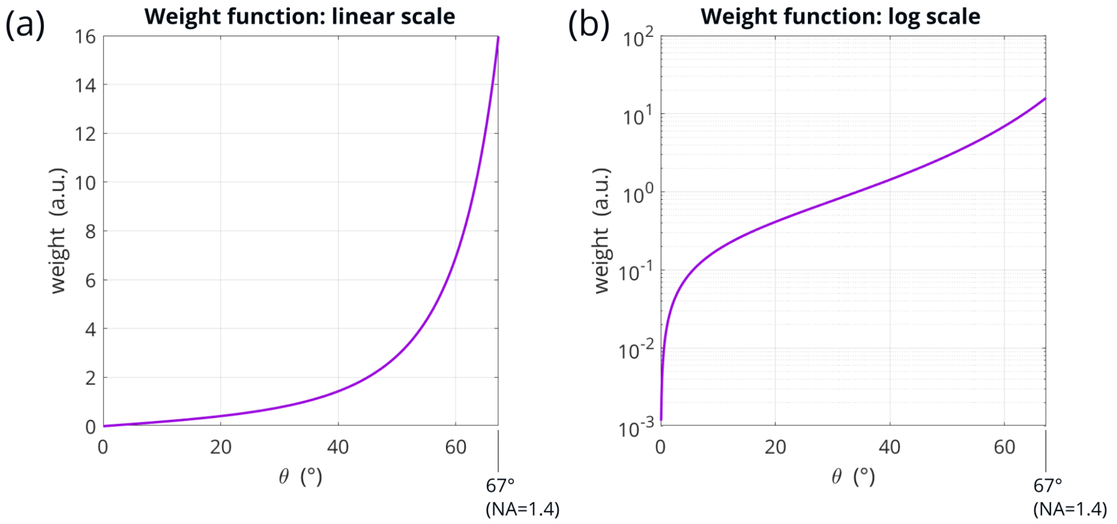

Figure 2.21: Resulting derived weight function plotted versus incident angle, in (a) linear scale and (b) log scale. The $x$-axis range maximum is that $\theta_{\text{max}}$ corresponding to an immersion oil objective of NA$= 1.4$ which is the one used in our IRM/BALM setup.

weights at $\approx 10°$. This has at times a significant effect on the resulting reflectance as will be shown in the Results section.

At this moment it is also useful to recall that the behavior of the NA$(\theta)$ function in air versus with oil immersion differs to some degree. The $\theta_{\text{max}}$ of 67° (for NA$_{\text{oil}} = 1.4$) is almost comparable to that of a NA$_{\text{air}} = 0.9$ objective, which has a $\theta_{\text{max}} = 64°$. This is due to the RI in the definition. The relation is clarified in Figure 2.22 with two y-axes, corresponding to air and oil case respectively. Still, a higher NA improves the resolving power due to how the mathematics works out.

Finally, it should be noted that various other papers have proposed weight functions. Some are presented with reasonable clarity and correctness, but at times without the full picture, or with limitations, or with mistakes.

In fact, a surprisingly large number of papers actually propose a Gaussian weight function, which would imply that $\theta = 0$ has the greatest weight, with lower weights for the higher angles. Some are cited here [154, 155, 156, 157, 158, 159, 160, 161]. There may be some logic to it in the first two papers [154, 155] because they utilize a laser in confocal scanning mode. Lasers do in fact have a Gaussian profile and thus it is probably correct. However, for the other papers [156, 157, 158, 159, 160, 161], they are in Köhler illumination mode and would have an identical optical geometry to the one described in Figure 2.20.

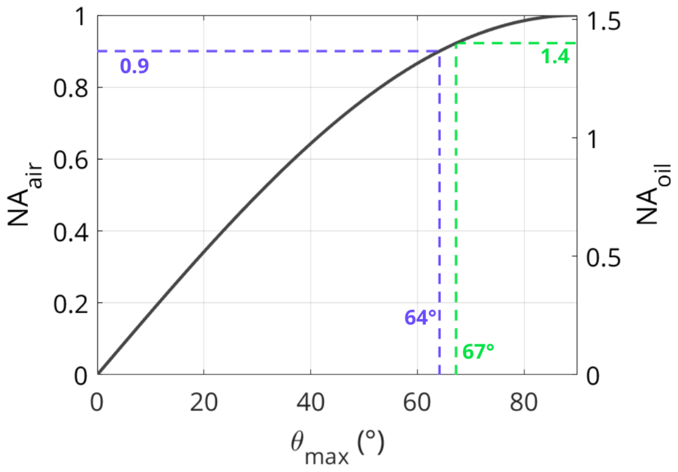

Figure 2.22: Plot depicting how NA values as a function of their $\theta_{\text{max}}$ differ for the air (left axis) versus oil (right axis) case where the former has $n = 1$ and the latter $n_{\text{oil}} = 1.518$. The cases of 0.9 and 1.4 for the former and latter are indicated.

In fact, F. Huang points out that in the literature, most of the weight functions proposed "are Gaussian weight functions of various forms", which "contradicts the results" of the earlier derived Equation 2.3, and that they are "inappropriate weight functions to calculate the average light reflectance measured by high-magnification objectives, which may be one of the reasons contributing to the notable discrepancy between experimental and theoretical result" [129].

Saigal et al. [162] also derived a weight function and tested it experimentally for graphene and 2D $MoS_2$. This weight function is derived as a discrete sum, exploiting the same geometrical considerations as for Equation 2.3, and to the the author's knowledge would yield identical results, if enough partitioned annuli are used in the sum.

A number of papers have had success in use of the weight function presented above in 2.3, including a series of papers by first and last authorships Y. Hattori and M. Kitamura [163, 164, 165, 166] (also discussed further in BALM section) among others.

## Temporal and spatial coherence

With regards to temporal coherence, there are two aspects at play. To address the first, consider a optical stack that has a few coherent films that are quite thin compared with the incident optical wavelength, say a few tens of nanometers. Let us assume that they also have negligible rugosity. Consider an incident beam of 10 nm bandwidth. The situation described is a decent recipe for a highly coherent case, in which fields are added in a superposition and not intensities.

For this situation however, the finite 10 nm bandwidth would still cover a spectral range that needs to be averaged over. This can be done with a simple integral proposed (among other places) in Hattori et al. [164] which takes the form

$$\bar{R}\left(\lambda_0\right) = \frac{1}{\lambda_{\mathsf{FWHM}}} \int_{\lambda_0 - \lambda_{\mathsf{FWHM}}/2}^{\lambda_0 + \lambda_{\mathsf{FWHM}}/2} \left( \left|r_s(\lambda)\right|^2 + \left|r_p(\lambda)\right|^2 \right) d\lambda \tag{2.4}$$

Here we can take the opportunity to note that if considered together with the effect of angle the reflectance can be formulated as follows [164]:

$$\bar{R}\left(\lambda_0\right) = \frac{1}{\left(\tan\theta_0\right)^2 \lambda_{\mathsf{FWHM}}} \int_{\lambda_0 - \lambda_{\mathsf{FWHM}}/2}^{\lambda_0 + \lambda_{\mathsf{FWHM}}/2} \int_0^{\theta_0} \left( \left|r_s(\theta,\lambda)\right|^2 + \left|r_p(\theta,\lambda)\right|^2 \right) \tan\theta \left(\sec\theta\right)^2 d\theta d\lambda$$

The former formula is tested later in the Results section. Now, let us consider the second situation as promsied above. Let's say that the stack is not favorable to coherent superpositions, but rather in the regime between incoherent and coherent. This situation may not be correctly described by Equation 2.4.

Now a few final remarks on spatial coherence. This type is related to the various aspects of INA and CNA described earlier. The theory of spatial coherence is also quite complex and has not been investigated so much in the context of IRM/BALM for 2D materials. Thus further research on these aspect would be logical. Some discussion of spatial coherence for IRM can be found in [110] among other sources.

# 2.3 . Results: IRM of $MoS_2$

## 2.3.1 . Experimental verification of contrast laws

The first order of things is to verify that contrast laws as derived earlier are met and behave as expected, and to get some sense of error bar. This involves a few aspects. The first is with regards how the detector is configured. The detector that is at the output of the IRM system can be a CCD or CMOS camera. Most Köhler illumination microscopes are designed such that the output diameter of the field image is not more than a few mm$^2$ in area. This is within typical ranges of CCD/CMOS sensor sizes.

The detector used throughout the thesis is a IDS UI-3880CP-M-GL Rev.2 (AB00854) which is of CMOS type and monochrome (grayscale, no RGB color). It has a detector of a size corresponding to the 1/1.8" standard (7.41 mm × 4.98 mm), with each pixel being 2.4 µm wide and totalling 3088 × 2076 px$^2$ (6.41 MP). The result for the setup is that multiple pixels span the optical resolution limit which is good, at about 30 px/µm = 3 px/100 nm where ≈ 500 nm is the optical resolution in our setup.

Now, an important aspect is that since the detector is measuring light intensity, it should be linearly proportional to exposure time. For images captured at different exposure time, the following relation must be satisfied:

$$\frac{I_1}{t_1} = \frac{I_2}{t_2} \qquad \Rightarrow \qquad I_2 = \left(\frac{t_2}{t_1}\right) I_1$$

This means that $I_2$ is related to $I_1$ by a multiplication factor which I define as $\alpha = t_2/t_1$, and not by an arithmetic operation of the form $I_2 = I_1 + \beta$ which is incorrect. This is a crucial point with regards to contrast.

Consider the multiplicative case, where resulting percent change contrast take the form

$$C_1 = I_1^{\text{obj}}/I_1^{\text{ref}} - 1, \qquad C_2 = I_2^{\text{obj}}/I_2^{\text{ref}} - 1$$

$$\Rightarrow \quad C_2 = (\alpha I_1^{\text{obj}})/(\alpha I_1^{\text{ref}}) - 1 \quad \Rightarrow \quad \boxed{C_2 = C_1}$$

It is seen that in the above contrast is invariant to exposure time. For the arithmetic case however, the result would be

$$C_2 = \frac{I_1^{\text{obj}} - I_1^{\text{ref}}}{I_1^{\text{ref}} + \beta} \quad \Rightarrow \quad C_2 \neq C_1$$

which is incorrect.

Yet another important aspect has to do with post-processing that sometimes is imposed by firmware or software. In photography, nearly all cameras apply a so-called gamma correction to the image such that $I_{\text{out}} = I_{\text{in}}^{\gamma}$ where $\gamma = 2.2$ is usually set. This results in a non-linear response curve of $I$ to exposure time. In fact, it is usually even more complicated than that because a piece-wise function is used, consisting of a linear slope for low grayscale values (called a "toe-slope") with the gamma transformation for higher grayscale values. This makes it so that a simple inverse transformation of $\gamma = 1/2.2$ is not possible. This problem was addressed in this work by the choice of iDS hardware and software. In the iDS *uEye Cockpit* software, the choice of "raw8" over "mono8" option ensured that the response is linear with no gamma transformation or other post-processing applied.

Now, let us again inspect $I^{\text{obj}}$ and $I^{\text{ref}}$ a bit closer. Their values for 8-bit grayscale images are in the range 0–255. In order for the contrast invariance to hold, it actually means that $\Delta I \equiv I^{\text{obj}} - I^{\text{ref}}$ would need to increase with exposure time. This may seem to violate something since the measured contrast is supposed to correspond to the "real" reflectance contrast

$$C_{\text{R}} = \frac{R_{\text{obj}}}{R_{\text{ref}}} - 1 = \frac{R_{\text{obj}} - R_{\text{ref}}}{R_{\text{ref}}} = \frac{\Delta R}{R_{\text{ref}}}$$

However, nothing is violated. Indeed, $\Delta R$ is constant, but $\Delta I$ is not. The latter must be variant in order for intensity contrast to remain constant.

Having addressed what the various expected trends should be, a series of images were taken at varying acquisition time of 2D $\text{MoS}_2$ on glass, in white light. The sample is shown in Figure 2.23(a). Multiple regions of interest (ROI) were defined to see the effect of nonhomogeneous illuminated field. In (b), grayscale intensity along with associated Weber contrast is plotted. It is confirmed that the theoretical contrast laws hold. In these white light conditions that 2D $\text{MoS}_2$ has around a 15% Weber contrast.

Figure 2.23(c) includes the contrast definitions of Weber, percent change and Michelson. As discussed in detail in the earlier section, the Weber and percent change contrasts are not

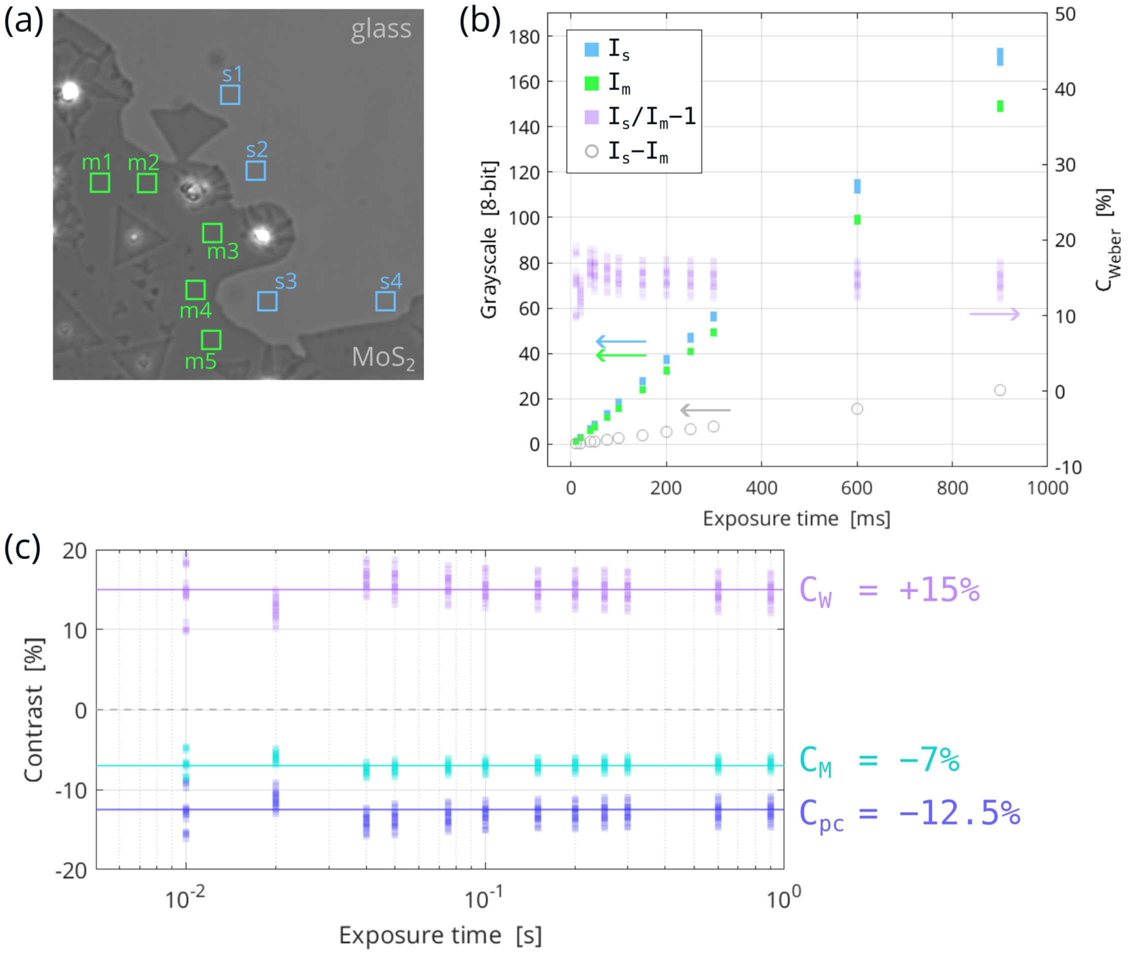

Figure 2.23: (a) White-light illuminated 2D MoS$_2$ on glass, with various squarare ROIs defined as shown. (b) Resulting grayscale and Weber contrasts plotted at varying explosure times. (c) Computed Weber, Michelson, percent change contrasts shown, which differ in value.

symmetric when the “object” (MoS$_2$) is darker than the reference (glass substrate). Again the significant difference in result of contrast definitions is also made manifest.

Finally, we see that across the tens of microns of the image, the choice of ROI does spread out a bit the points to something like a $\pm3\%$ which is reasonable. This can be further improved by background subtraction discussed in the next section.

## 2.3.2 . Background subtraction

In order to illustrate the principle of background subtraction, I present below Figure 2.24 which was taken of transferred CVD graphene, using a 550 nm bandpass.

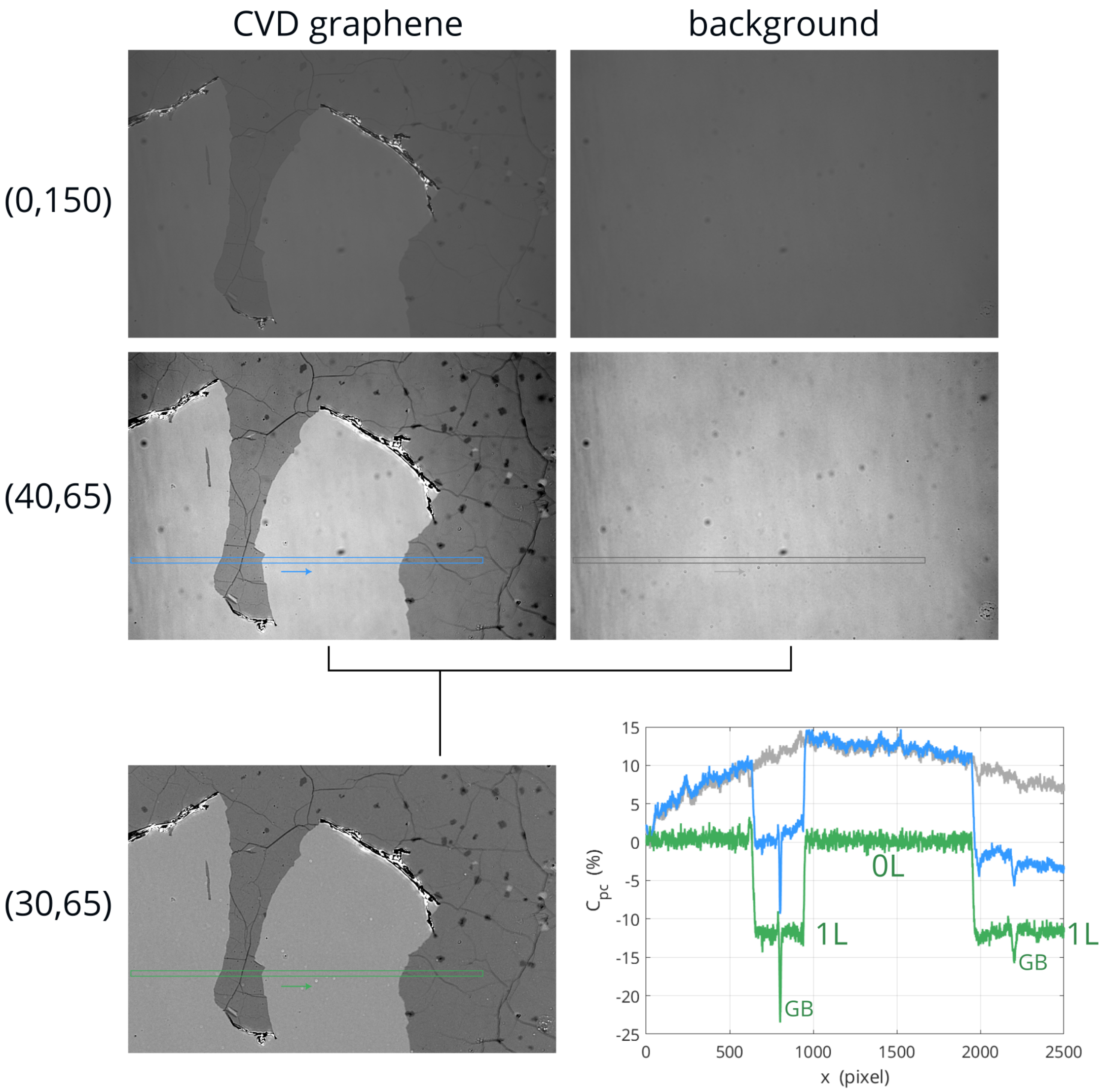

Figure 2.24: IRM micrographs using 550/10 nm bandpass filter of transferred CVD graphene and background, at 8-bit grayscale adjusted ranges of (0,150) top and (40,65) middle which improve visibility. Bottom right is a background-subtracted result with grayscale adjusted to (30,65). Plot indicates averaged line profiles as shown in the 3 neighboring micrographs. The green background-subtracted result is favorable since the field is non-unifom as seen by the gray curve and its effect on graphene contrast by the blue curve.

In the top micrographs, the sample (left) and background (right) are shown, and the 8-bit range was adjusted to (0,150). The grayscale was further compressed to the range (40,65) to improve visibility. It is seen that the background is rather textured, with various defects originating mainly from dust or dirt along the system of lenses. Furthermore the right and left corners of the field are visibly darker.

In the bottom left micrograph, the background has been subtracted. The grayscale again was adjusted, to (30,65) for better visibility. Clearly, it is visually more smooth, with less dirt/dust in the image. Averaged line ROIs were also defined as is visibly seen in each image. These are plotted in the bottom right. The background clearly takes a kind of arch, parabolic-like shape as was described by section 2.2.2 and Figure 2.12. Likely due to the aperture and field diaphragms not being perfectly aligned for this wavelength, among other factors.

When comparing the blue and green data it is also evident that the green data is a lot more uniform and clean. This means that in principle whenever possible the background subtraction should be used. As outlined before however it is not always practically feasible to do this. To minimize error, it is a good practice when computing contrasts to choose ROIs that are in close proximity, i.e. that the sample ROI is near the substrate ROI. In general, the nonuniform field is likely a major source of error bar, including the ones shown when testing the contrast laws in section 2.3.1.

## 2.3.3 . Optical stack

For IRM, the optical stack of concern consists of the layers as depicted in Figure 2.25 (a) and (b). As shown, there is no additional Fabry-Pérot layer present although there will be later on (Cr/Au and $AlO_x$) for BALM. A given ray of light thus emerges from the objective lens glass to the immersion oil, followed by the borosilicate glass coverslip, the $MoS_2$ and finally the top medium which can be air or another medium. In practice, a liquid is a convenient way to change $n_f$ as discussed later.

The immersion oil has a nominal refractive index (RI) of $n_{oil}$=1.518. This is the so-called "semi-infinite" incident medium for the ray, thus there are no interferences taking place here as the oil is hundreds of microns thick. Next comes the coverslip, which has a RI $\approx 1.5$. However, it is not exactly 1.5, and for that reason, it is important to measure the RI disperion of the glass. The coverslips we use are more specifically borosilicate glass, and they have a thickness of $\approx 170$ $\mu$m. This is the standard coverslip thickness to be used with oil immersion objectives, the so-called "No. 1.5" thickness. Our collaborators at the University of Genova measured the RI by spectroscopic ellipsometry, and the result is shown in Figure 2.26. As can be seen, it takes the values 1.545, 1.535, 1.529 at 450, 550, 650 nm respectively. This is fairly non-dispersive

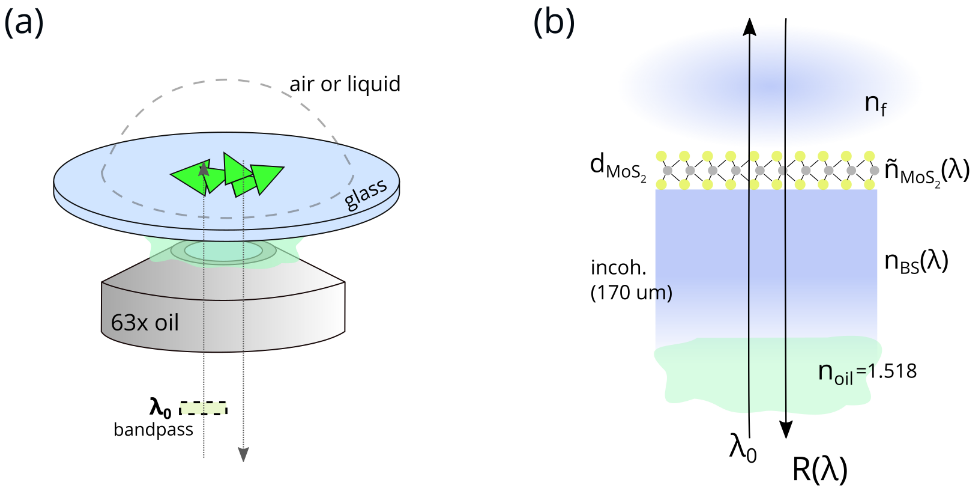

Figure 2.25: (a) Drawing of interference reflection microscopy (IRM) setup used with 2D $MoS_2$ as the sample. There is a bandpass, the oil immersion objective, borosilicate glass coverslip, $MoS_2$, and the possibility of changing the final interface by adding a liquid droplet or changing the gaseous environment. (b) Equivalent optical stack with parts labeled.

which is good. A Cauchy model was used which is appropriate since the glass has a $\kappa \approx 0$ in the optical regime since the nearest resonance (let's call it $\omega_0$) is farther away in UV, so $\omega_{\text{opt}} \ll \omega_0$ can be assumed.

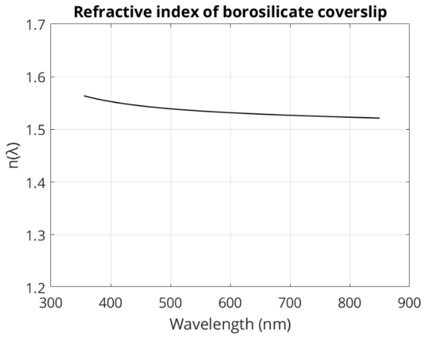

Figure 2.26: Measured refractive index dispersion of our borosilicate coverslip, from VASE ellipsometry data acquired and fitted by *OptMatLab* at University of Genova.

The other aspect about the coverslip is that it can probably be treated as an incoherent layer. It is $170\ \mu\text{m}$ thick, where $\lambda_0$ is around 0.3% of this. Using the Byrnes TMM package [153], I tested the effect of treating the coverslip as an incoherent layer with $n_{\text{oil}}$ as the incident medium. However, since the RI are so close it is negligible at least with regards to calculations of contrast for 2D $MoS_2$. Therefore, I in general assume the coverslip itself to be the semi-infinite incident medium. When considering a UV-Vis spectra of the coverslip (with other layers), treating the coverslip as incoherent is necessary since there the incident medium is air.

Regarding the final interface which also is semi-infinite, I call it $n_\mathrm{f}$. In air, it is unity, whilst for water it is $\approx 1.33$ at optical frequencies. The electrolyte DEME-TFSI which is discussed later has a RI around 1.4–1.5 [167].

As for the 2D $MoS_2$, it is certainly a coherent layer as its thickness is approximately $d_{\mathrm{MoS2}} = 0.65$ nm. Furthermore, it has a very high real RI $\approx$ 5, with significant extinction coefficient varying between 1–4. Furthermore, there are discrepancies in the literature as to the exact values, among other aspects that come into play, discussed in the next section. The $MoS_2$ is thus the main player dictating the reflectanece response in this system.

### 2.3.4 . Optical properties of TMD monolayers

In the optical stack of 2D $MoS_2$ on the coverslip substrate used in IRM, the optical properties $(n(\lambda), \kappa(\lambda))$ of the $MoS_2$ is critical. They play a significant role in the resulting reflectance response. Many papers have been published measuring the optical properties of 2D $MoS_2$ and other 2D TMDs. Some have been uploaded to the refractiveindex.org database [168], while for some I have used WebPlot Digitizer [169] to digitize the data.

In Figure 2.27, various $\tilde{n}(\lambda)$ from literature and from our own $MoS_2$ are shown, which will be elaborated in a moment. The black curve is our home-grown CVD $MoS_2$ as measured by Univ. of Genova, while the green is of purchased CVD $MoS_2$ from 2D SEMICONDUCTORS Inc. also measured by the same group, for comparison. The purple [37], orange [170] and red [171] curves are from the stated references.

The $\tilde{n}(\lambda)$ of various bulk TMDs were measured in 1979 by Beal et al. [17] using reflectometry. The first paper to the author's knowledge measuring $\tilde{n}(\lambda)$ of a $MoS_2$ monolayer was in 2010 [172]. Many tens of papers have been published since then. Not all could be covered here. Still there are some important points as there are significant variations in the measured $\tilde{n}(\lambda)$, so care must be taken to use appropriate values.

Some of the papers taking the reflectance spectroscopy approach include T. Heinz group in 2014 [37] (pink curve) and also Zhang et al. in 2015 [171] (red curve). These papers assume the 2D $MoS_2$ to behave as a finite thin film (slab) of thickness $d_{\mathrm{MoS2}} \approx 0.65$ nm.

However it is still debated in the literature whether treating 2D materials as "slabs" is appropriate, and if it is not better to treat 2D materials as pure 2D layers, called "sheet" models [173].

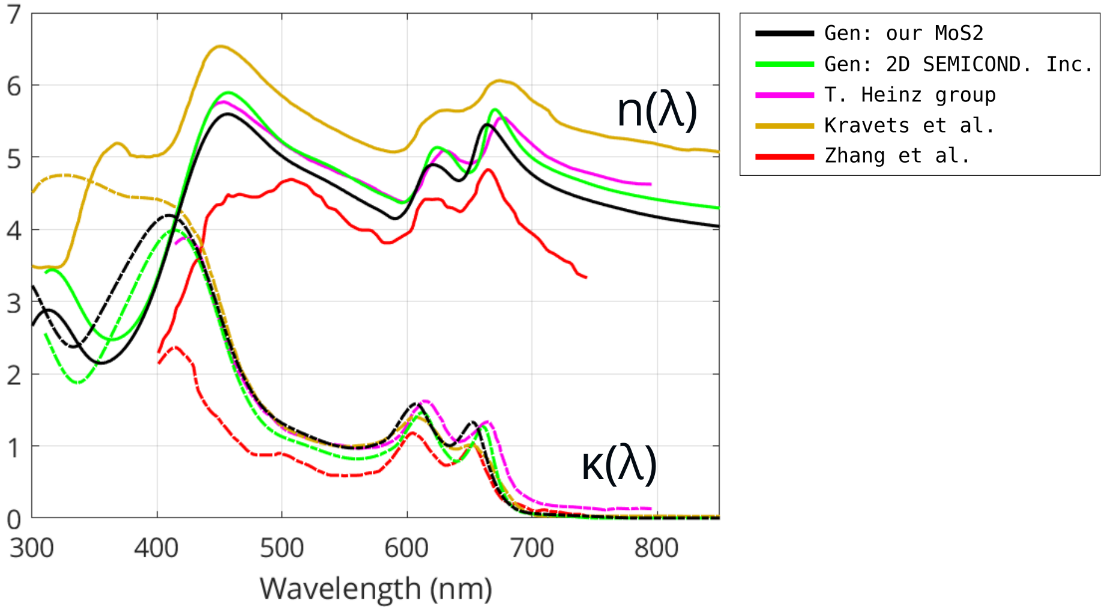

Figure 2.27: Real refractive index $n$ and extinction coefficient $\kappa$ dispersions of 2D $MoS_2$ acquired by various groups. The black and green curves were measured by our collaborators at University of Genova (hence "Gen"), for our in-house CVD $MoS_2$ and for a commercial CVD $MoS_2$ sample from 2D SEMICONDUCTORS Inc. The other data I digitized from [37] (T. Heinz group), and Kravets et al. [170], and Zhang et al. [171]. There is a degree of variation of measured $\tilde{n}$.

Morozov et al. [174] compared the approaches in 2015 by tandem reflectance, transmittance, absorptance measurements. A recent paper by Majérus et al. 2023 discusses various aspects of the two approaches and how they can be potentially reconciled [175]. Merano group has also provided various insights such as in 2021 [176].

Further research and literature is likely to emerge in the next few years to provide more insights as to which modeling approach is truly most accurate to the physical reality. In the meantime, it is the view of the author that the slab approach is reasonable. I say that because, as shown by our collaborators in *OptMatLab* at University of Genova, when comparing ellipsometry VASE data $(\Psi, \Delta) = f(\lambda, \theta)$ with the predictions of slab-based dispersion models for $(\Psi, \Delta)$, the match results in very low mean squared error (MSE).

Yet another aspect that comes into play is the role of anisotropy in the optical properties, for in-plane vs. out-of-plane components. Most early papers assumed isotropic optical properties, and there does not appear to be much recent literature on the anisotropy for single-layer TMDs. However there are recent publications measuring the anisotropy for bulk TMDs including $MoS_2$, from Volkov group in 2021 [177] and Shegai group in 2022 [178] for example, which are partially

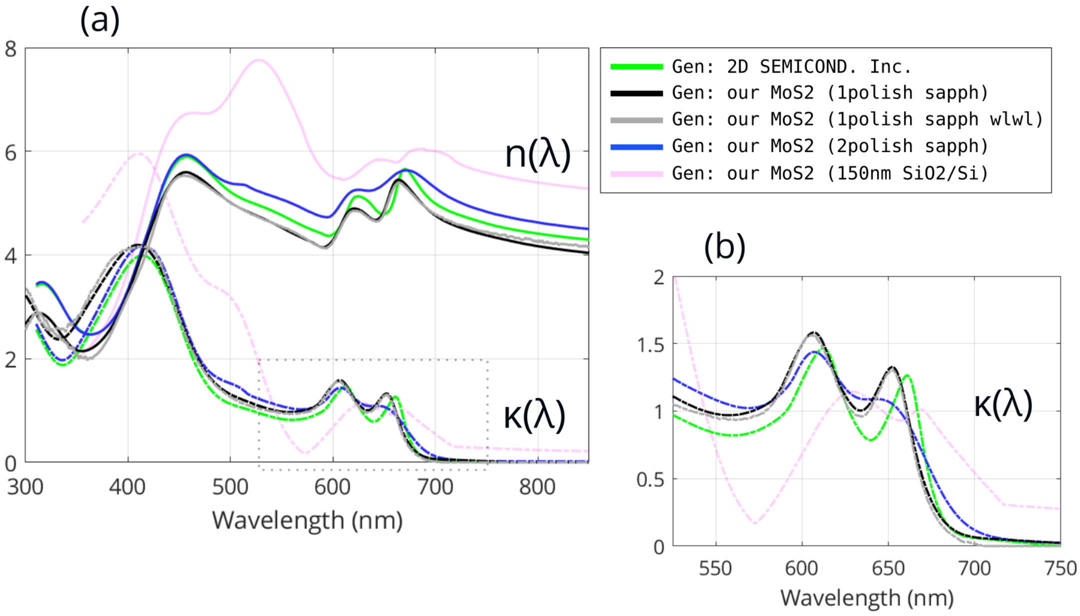

Figure 2.28: [Please see electronic version for better color rendering.] (a) Various 2D $MoS_2$ $(n(\lambda, \kappa(\lambda))$ data, (b) a zoom on the $\kappa(\lambda)$ data near the A and B exciton peaks. Green curve is CVD $MoS_2$ from 2D SEMICONDUCTORS Inc. The other curves are all from our same CVD growth of 2D $MoS_2$, but on different substrates, including 150 nm $SiO_2$/Si, double-polished sapphire, and single-polished sapphire i.e. with a rough backside. For the last case both a dispersion model fit and wavelength-by-wavelength result is shown, in which both are mostly similar which is a good sign.

reproduced in Figure 2.29. (See also [179].)

As was discussed in Chapter 1, there is also the important aspect of the stoichiometric form of a given 2D TMD. CVD $MoS_x$ versus $MoS_2$ are known to have differing optical properties, as was brought up. This is apparent even by taking RGB micrographs as shown by [64]. Thus, this also is a factor that can contribute to discrepancies between groups on measuring of optical properties. Environment and atmosphere also has an effect as was discussed.

Thus, if at all possible, **it is important to measure the optical properties of one's own in-house CVD $MoS_2$ if the optical response in a thin-film system like IRM is to be simulated with good accuracy**. Fortunately this was possible thanks to the collaboration with *OptMatLab* from University of Genova, Italy. One representative CVD growth at LICSEN was diced into multiple pieces for characterization.

The actual growth substrate was $\approx 150$ nm a-$SiO_2$/Si. Other pieces were transferred first onto a double-polished sapphire substrate, followed by transfer to a single-polished sapphire substrate (so one side is rough). Chronologically this was done as such to improve the quality of the ellipsometry data. Because of the $SiO_2$ FP layer, the $\Psi, \Delta$ was masked by the $SiO_2$ resonances

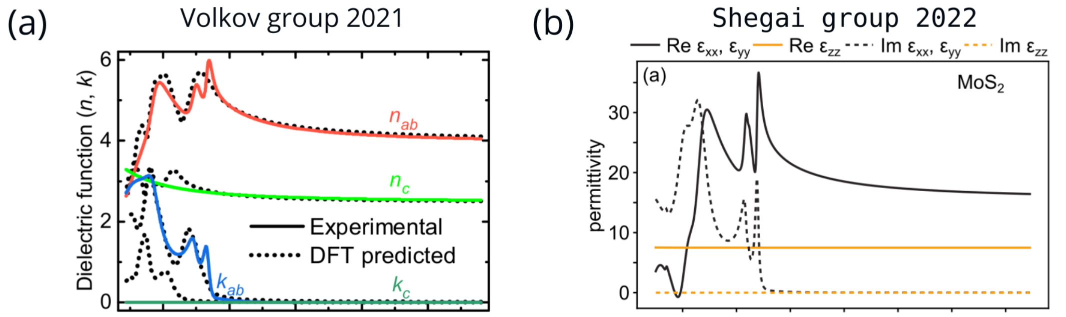

Figure 2.29: Recent literature on in-plane vs. out-of-plane optical properties of bulk $MoS_2$, from (a) Volkov group 2021 [177] and (b) Shegai group 2022 [178].

and thus the resulting $(n(\lambda), \kappa(\lambda))$ were unreliable. It has been reproduced in Figure 2.28 in faint pink. Next since double polished thick sapphire was available, a transfer was done followed by characterization. The quality of the attained $\Psi, \Delta$ were improved and are shown in blue, also in (b).

The advantage of the double-polished sapphire, is that it is an optically incoherent layer with no FP resonance and thus less intrusive on the $MoS_2$ response. Yet, the incoherent reflections on the back of the substrate actually were still obstructive enough to motivate a transfer onto single-polished sapphire. For this sample, the back-reflections could be ignored, resulting in even cleaner data. These are shown in black and gray in (b). The gray data is a so-called wavelength-by-wavelength (wlwl) fit, which means that no dispersional model is used to fit the data but that the MSE at each point is minimized.

For the black curve, it is the result of a fitting with a Kramers-Krönig consistent dispersion model, consisting of six PSEMI-Tri oscillators, in the same way as described in the supplementary document of [180]. It is a good sign that both the disperion model fit and wlwl fit essentially gave the same result.

It is seen from the Figure 2.28(b) as well as the zoomed in (c) that the substrate used in the ellipsometry measurements has a significant impact on the resulting $\tilde{n}(\lambda)$. This is in addition to the many other factors that can influence RI like the ones mentioned previously. It is thus not surprising that values available in the literature are so varied, and again is a testament to the need for characterizing the RI of one's materials. Thus, we now are armed with accurate $\tilde{n}(\lambda)$ for the in-house grown CVD $MoS_2$ that we produce, as well as the possibility to compare with other measured disperions from the literature.

## 2.3.5 . IRM contrast for $MoS_2$ in air, water, and DEME-TFSI

First let us consider the simulated percent change contrast ($C_{\mathrm{pc}}$) using different $\tilde{n}(\lambda)$ values from literature, for the cases of air ($n_{\mathrm{f}} = 1.0$) and water ($n_{\mathrm{f}} = 1.33$) at the final interface (see Figure 2.25 for a drawing of the stack). For now, normal incidence is assumed, with bandwidth not being taken into account. The results are shown as Figure 2.30.

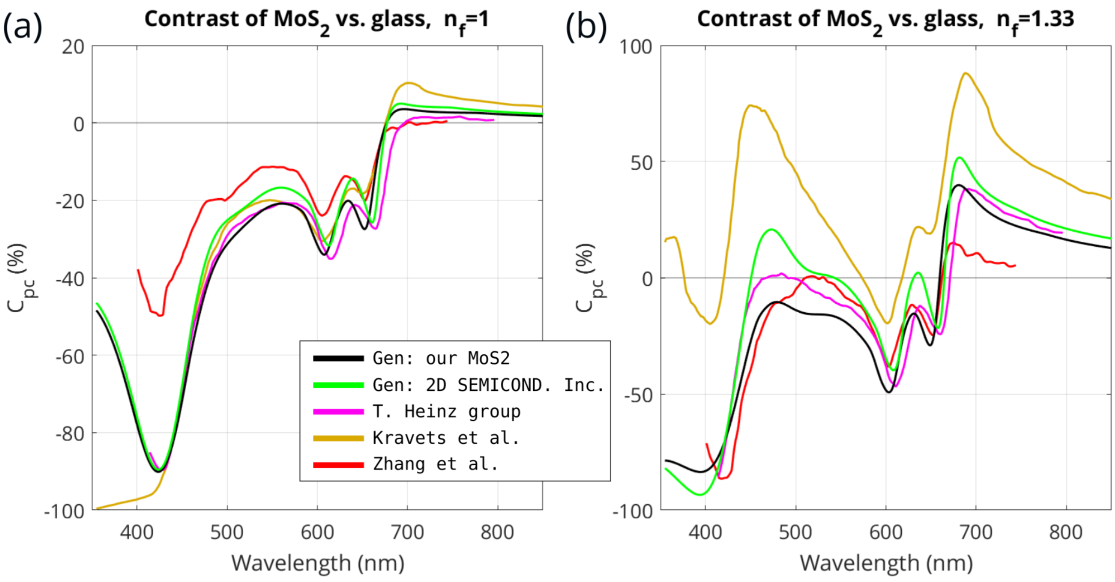

Figure 2.30: Simulated percent change contrast of 2D $MoS_2$ versus glass substrate in an IRM configuration, with (a) air as the final interface ($n_f = 1.0$), and (b) water ($n_f = 1.33$), computed for various $\tilde{n}(\lambda)[MoS_2]$ data, showing that it is important to have reliable $\tilde{n}(\lambda)$ for one's own in-house CVD $MoS_2$.

For the air case (a), it is seen that the contrasts are mostly negative across all optical frequencies, where 400 and 450 nm bandpass filters appear to be good choices for best vertical resolution. It is also seen that depending on the $\tilde{n}(\lambda)$ used for $MoS_2$, the results are quite varied, where the red Zhang et al. [171] is especially an outlier. At around 425 nm for instance, there is a difference of $\approx$ 40% between the Zhang data and the other.

The most significant discrepancy across all across the curves at least for the air case appears to be near the bandgap at the A and B exciton energies. This in some sense is expected because it is especially the exciton/trion weights that are sensitive to the various aspects of growth, environment, etc and thus would differ among various measured $\tilde{n}$.

For the water case, various observations can be made. The first is that the curves have greater variation than in the air case. The reason for this is likeley related to the substrate reflectance, which is the divisor when the contrast $C_{\text{pc}} = R_{\text{MoS}_2}/R_{\text{substr}} - 1$ is computed. In air, $R_{\text{substr}} \approx 4\%$ because of the $\approx 1.5/1.0$ interface, whilst in water the interface is $\approx 1.5/1.33$ resulting in $R_{\text{substr}} \approx 0.36\%$ (more than one order of magnitude lower). It is seen that greater positive contrasts are expected at around 700 nm, with very steep reflectivity changes both at around 660 nm and 450 nm. In this simulation the orange Kravets et al. [170] data, is the more deviatory.

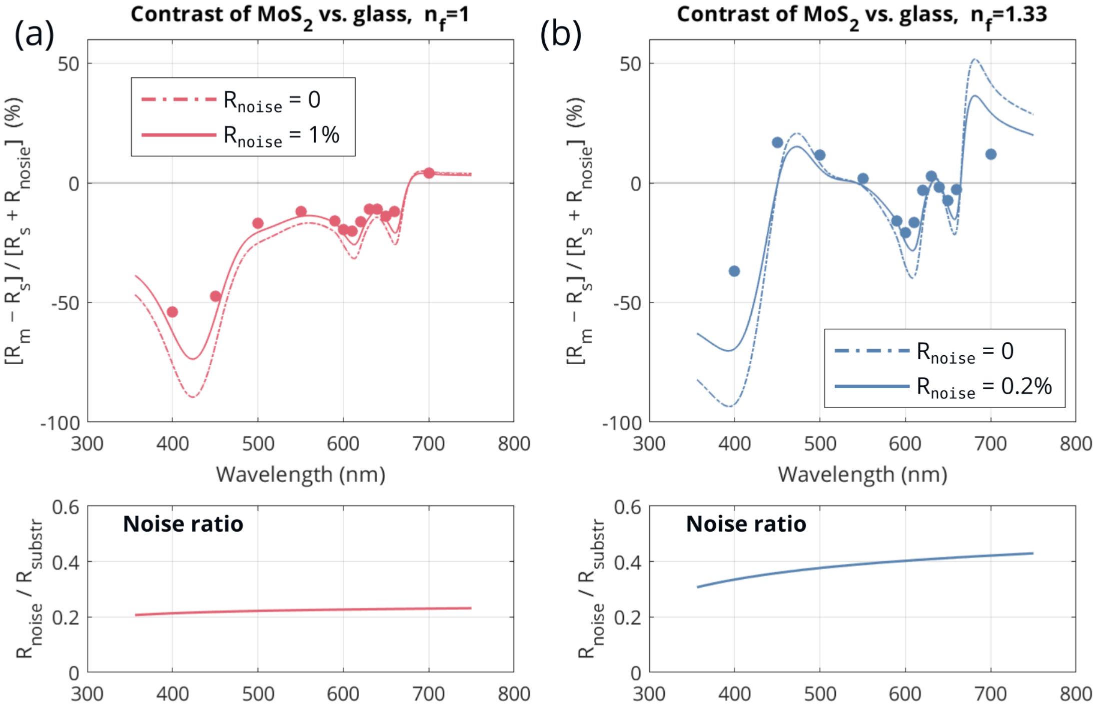

Figure 2.31: Data and simulation of optical contrast for 2D $MoS_2$ vs. IRM glass substrate, in air ($n = 1.0$) and in water ($n = 1.33$). Effect of optical noise (stray rays) in the system shown. Since the inclusion of optical noise matches the better data, it is one possible explanation as to the actual contrasts being lower than a zero-noise simulated response.

Now, how do these compare with data? In Figure 2.31, corresponding data and simulations are shown. The data were collected by using 13 different bandpass filters, each of 10 nm bandwidth. They include 400, 450, 500, 550, 590, 600, 610, 620, 630, 640, 650, 660, 700 nm. Essentially, the data are obtained by taking images one by one, changing the filters for each image. Some of these images are shown in 2.32(b). Then, using ImageJ code, rectangular regions of interest (ROI) are defined—one ROI for a substrate portion of the image, and one ROI for a monolayer $MoS_2$ portion. This is reproduced in 2.32(a) for one of the images. The ROI size in this case was set to $50 \times 50$ px$^2$, and the 8-bit average of each ROI is extracted automatically for each image. Finally the experimental contrast is computed for each of the filters.

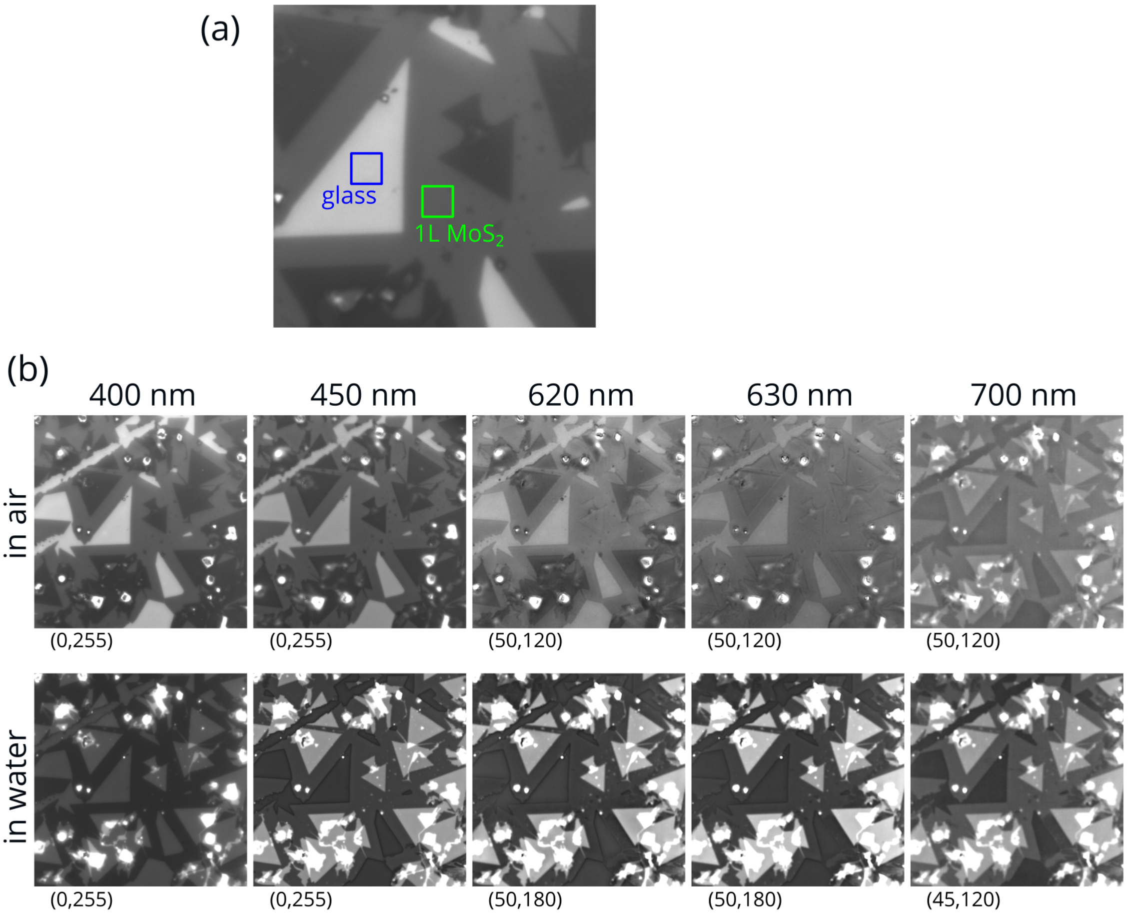

Figure 2.32: IRM micrographs taken at 13 wavelengths, with 5 of them reproduced in (b) as shown, some of which have an adjusted grayscale for improved visibility. In (a) the two defined ROIs are shown and labeled.

Notice that this particular sample has a variety of nice and well-contrasted bilayers as well. This is discussed in a later section.

The dash-dot lines in Figure 2.31 are the percent change contrasts $C_{\text{pc}}$. Upon a first inspection, it is clear that **there is a reasonable agreement between the experimental and simulated contrasts**. One pattern however is that the simulated contrasts are expected to be higher across the whole range. One possibility that explains this is that the presence of stray rays in the optical system contribute noise that function to lessen the measured contrast. Therefore, it is a good opportunity to test whether use of the $C_{\text{pc}}^{\text{noise}}$ function that was derived in section 2.2.3 can explain what is going on. This is what is shown by the solid lines in the plots. For air, $R_{\text{noise}}$ was set to 0.01 (1%) while for water it was set to 0.002 (0.2%). What matters more in the end though is the ratio $R_{\text{noise}}/R_{\text{s}}$ since

$$C_{\text{pc}}^{\text{noise}} = \frac{C_{\text{pc}}}{1 + R_{\text{noise}}/R_{\text{s}}}$$

It is seen that this results in divisions spanning 1.2–1.4 in the simulated contrasts as shown in the Figure. Overall, since the coverslip substrate dispersion is not highly significant, the noise ratio does not vary significantly across the optical frequencies.

Now, it is of interest to explore what the resulting contrast spectrum would look like for other values of $n_{\text{f}}$. This can be a powerful thing because it is a way to tune the contrast. Inspection of Figure 2.32(b) indeed shows that at some wavelengths, switching from air to water completely reverses the sign of the contrast for instance.

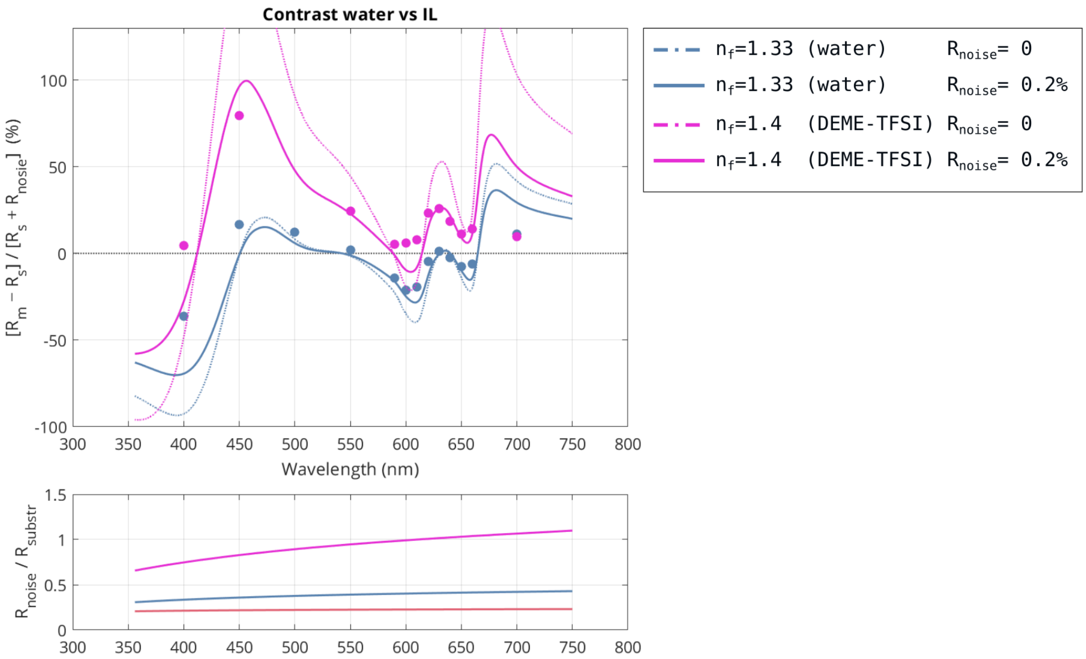

Figure 2.33: Data and simulations (normal incidence) of 2D $MoS_2$ versus glass in IRM configuration for the cases of water ($n_{\text{f}} = 1.33$) and DEME-TFSI ionic liquid ($n_{\text{f}} = 1.4$) at the final interface. The simulation trend mostly matches the data, and is improved by including the effect of stray light noise which could be one origin of the contrast data being reduced compared with the simulation.

In Chapter 3, an ionic liquid is used for gating. This liquid (DEME-TFSI) happens to have a RI higher than water, at somewhere between 1.4–1.5 [167]. Thus it is a good moment to compare contrasts spectrum for water vs. IL. Results are reproduced in Figure 2.33. As a first remark, it is seen that the simulations and experimental contrasts do shift in towards the good direction, i.e. more positive overall when compared with water.

Secondly, again the effect of noise is included for the solid line. For $n_\mathsf{f} = 1.4$ which results in substrate reflectance of $\approx 0.12\%$ which causes values to be even more blown up than in the water case. If this could be acheieved in practice it would be amazing since values of $C_\mathsf{pc} = 177\%$ would be attained at 450 nm. However the noise is possibly an actor to the watered-down contrast, resulting in the $C_\mathsf{pc} \approx +80\%$ measured contrast at 450 nm. It could be though that noise does not play a role and that the angle distribution is the main actor, which is explored in section 2.3.7. Nevertheless, this is very high and in fact the highest reported for IRM ever for $MoS_2$, to the author's knowledge.

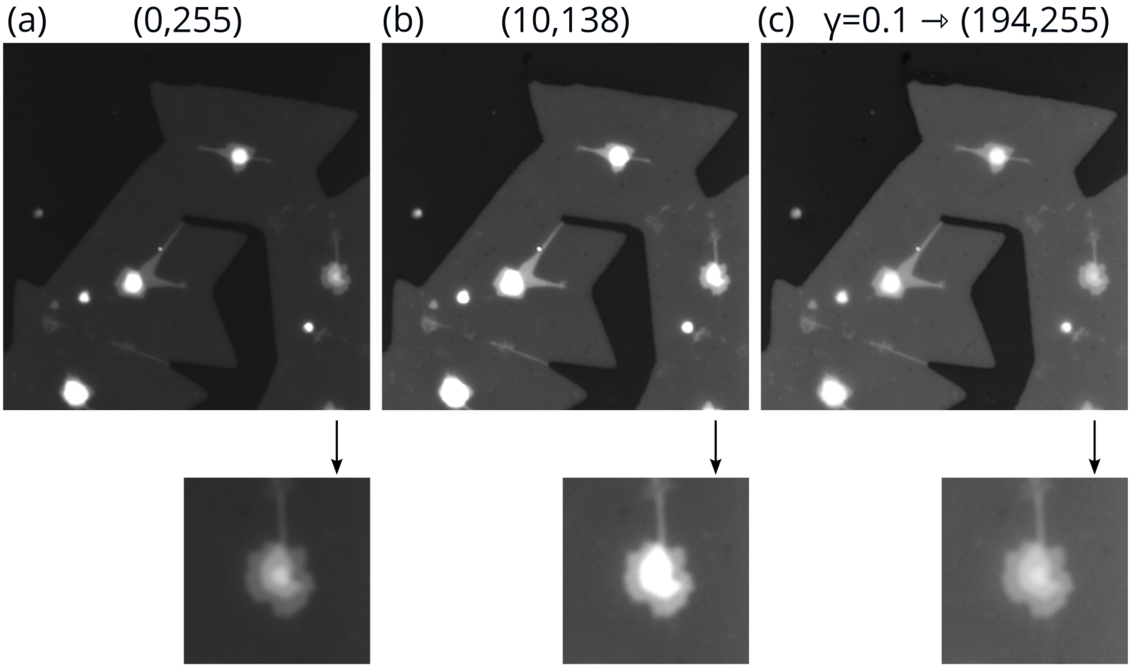

Figure 2.34: [Please see electronic version for better rendering.] (a) $\lambda_0 = 450/10$ nm micrograph of $MoS_2$ on glass with ionic liquid DEME-TFSI at the final interface ($n_\mathsf{f} \approx 1.4$), with no post-processing. (b) Grayscale adjusted to (10,138). (c) Gamma transformation of $\gamma = 0.1$ applied followed by grayscale adjustment (194,255). The last image shows best visibility of topography due to less saturation thanks to the gamma transformation. These results represented the highest contrast attained for 2D $MoS_2$ during the thesis, at around $C_\mathsf{pc} = 80\%$.

The 450 nm micrograph associated with this high $+80\%$ contrast is shown in Figure 2.34. In (a) is the raw 8-bit image with no adjusted grayscale range is shown. In (b) the grayscale has been adjusted to improve the visibility. As mentioned with the earlier example, the simple post-processing step of adjusting the grayscale after acquiring the image is a powerful and simple way to improve visibility. Finally, in (c), two processing steps were applied. The first is to impose a $\gamma = 0.1$ gamma transformation which takes the form

$$I'(x, y) = 255 \times \left( \frac{I(x, y)}{255} \right)^{\gamma}$$

followed by a grayscale adjustment. This gamma transformation is particularly useful here, because some of the topographical features near the nucleation sites are very close to saturation such that without gamma (like in (b)) features get saturated.

The error was also computed for this contrast (in the same manner described later in section 2.8.2) resulting in $C_{\text{pc}} = 80.1 \pm 3.7\%$.

### 2.3.6 . Influence of bandwidth

Thus far, zero bandwidth was assumed in the simulations. However, as previously stated, the bandwidth of the color filters used are 10 nm, which could have an effect on resulting contrasts. This is because the incident/reflected light will in fact feel an average of the various $\tilde{n}(\lambda)$ dispersions in the stack. The effect of the averaging is explored in this section.

Before diving in however, it should be noted that the following does not address the effect of partial coherence. As stated earlier, for some thin-film systems the bandwidth of the light affects whether the layer behaves as a coherent, partially coherent, or incoherent layer which was summarized in the example of Figure 2.18. This is especially true for films that are close in thickness to the wavelength of the light, say around 500 nm. As the $MoS_2$ is 0.65 nm in thickness, it is probably safe to assume that it will behave as a coherent layer even for a wide bandwidth like 50 nm.

Now, having clarified this point, an integral as described in Hattori et al. 2021 [164] is used, reproduced below:

$$\bar{R}\left(\lambda_0\right) = \frac{1}{\lambda_{\text{FWHM}}} \int_{\lambda_0 - \lambda_{\text{FWHM}}/2}^{\lambda_0 + \lambda_{\text{FWHM}}/2} \left( \, |r_s(\lambda)|^2 + |r_p(\lambda)|^2 \, \right) d\lambda$$

After implementing this in code using the trapezoidal rule, the same stacks in air and water were computed, for the bandwidths 0, 10, 30, 50, 100 nm. The results are shown in Figure 2.35, where parts (a) and (b) are for the air case whilst (c) and (d) is for water.

It is seen that from 0 to 10 nm bandpass in each of the cases, the effect is minimal. It is thus safe to assume that not taking into account bandwidth is okay for the 10 nm case. However,

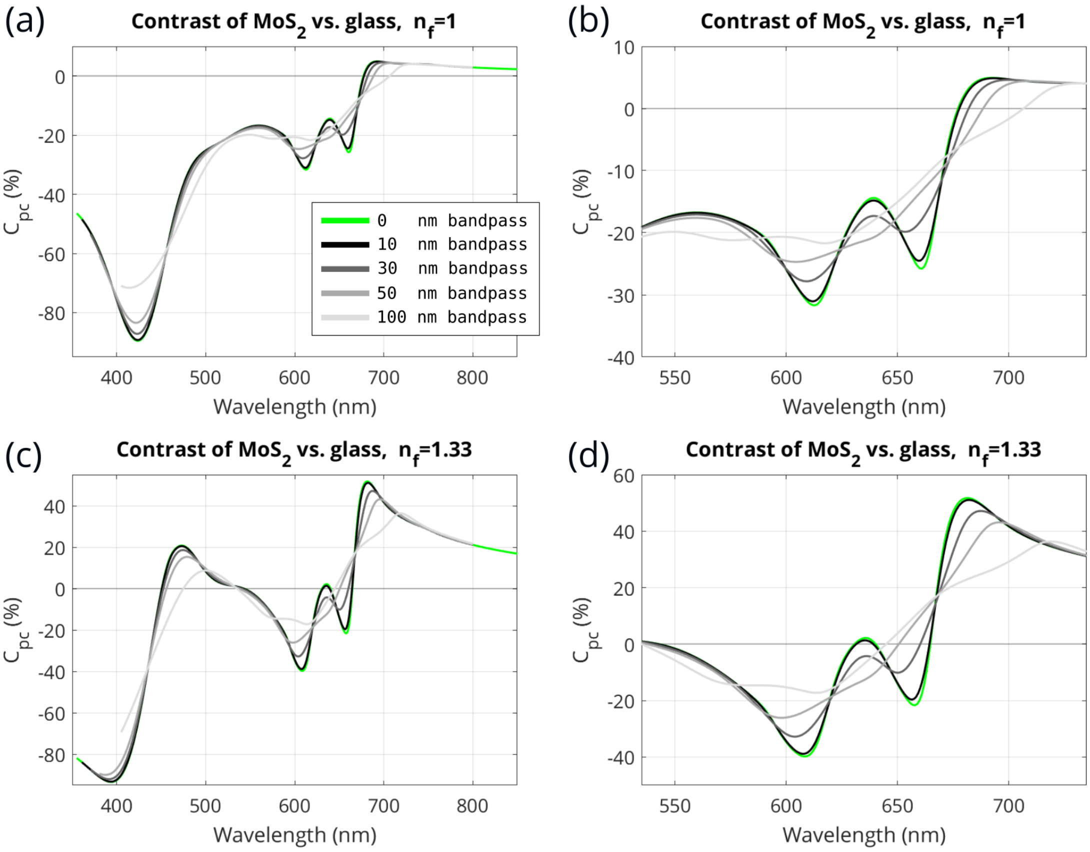

Figure 2.35: Effect of bandwidth on resultant percent change contrast curves for 2D MoS$_2$ on glass in IRM configuration, for the cases of (a) air and (b) water at the final interface. In (b) and (d) respective zooms on the data near the A and B excitons are shown.

for 30 nm the contrast does suffer. It can also be seen that it is at the points of high second derivative where the effect is most pronounced.

## 2.3.7 . Influence of angle

It is now of importance to assess the influence of angle. As was derived and discussed in in 2.2.4, the angle theoretically have a significant effect especially because of the higher weight on annuli corresponding to higher angles. As plotted in Figure 2.21(b), angles near 67° (corresponding to the $\theta_{\text{max}}$ of the NA$= 1.4$ oil objective) should have two orders of magnitude weight compared with 10° incident angles.

In Figure 2.36 the effect of angle is explored, both WITH and WITHOUT the weight function, which is useful in order to see what effect is to do with incident angle versus what is due to the influence of the weights. (a) and (b) show the simulated reflectance spectrum response with and without the weight respectively, whilst (c) and (d) are the corresponding percent

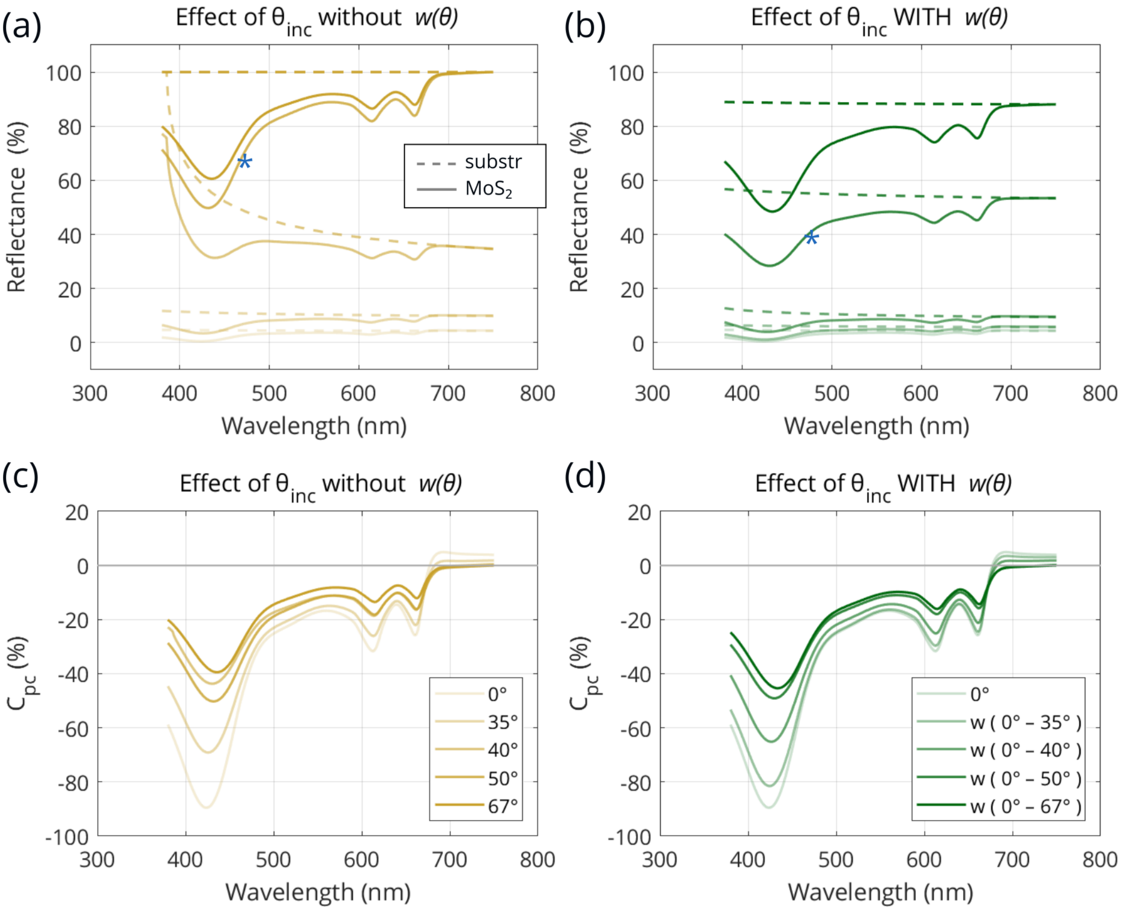

Figure 2.36: Effect of incident angles on (a,b) Reflectance and (c,d) percent change contrast for 2D $MoS_2$ and glass substrate in IRM configuration in air. (a) and (c) is the result at one incident angle at a time, while (b) and (d) includes the integral of the weight function in the range from 0° to the specified angle, where the highest angle case of 0° to 67° corresponds to the NA$=1.4$ oil immersion objective used in the thesis. The blue star "*" aids the eye to find the corresponding curves.

change contrasts. Note that the curve opacity indicates the angle (or range of angles for weighted case). The blue stars in (a),(b) also aids the eye to find corresponding curves and their differences.

The first observation that can be made from (a) is that the reflectances are increasing significantly both for substrate and $MoS_2$ as the incident angle(s) are increased. This is actually expected, and is not due to any exotic property of the $MoS_2$ since the simple transparent glass substrate is behaving in a similar fashion. The main mechanism to the increased reflectivities is attributed to fundamental principles of optics having to do with the Fresnel equations for $r_s$ and $r_p$. The geometry and boundary conditions of the fields start to approach a total-internal-reflection (TIR) condition occuring at a critical angle $\theta_c$, which for a glass/air interface takes the form

$$\theta_c = \arcsin\left(\frac{n_{\text{air}}}{n_{\text{glass}}}\right)$$

and has a value of 41.8° for a 1.5/1.0 interface. This explains why the third orange curve $\theta_{\text{inc}} = 40^\circ$ has a more radical shape for the substrate. At 370 nm the TIR conditions are already met at 40° due to the dispersion of this glass (Figure 2.26), whilst not yet for the values towards the red part of the specturm. Then, for the 50° and 67° the substrate reflectance is exactly 100% for all optical frequencies.

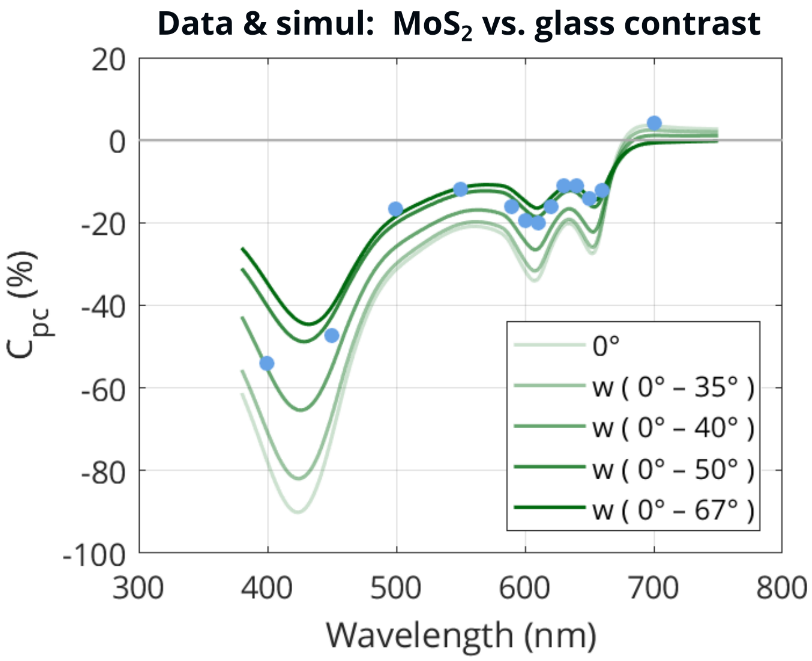

Figure 2.37: Data (same as before) of 2D $MoS_2$ vs. glass in IRM configuration, and simulated curves with angular weight function for various angle ranges. $\tilde{n}(\lambda)[MoS_2]$ is from our home-grown CVD $MoS_2$.

Now, commenting on (c) and (d), it is seen that as expected the inclusion of the full range of angles illuminated by the objective, with weights, serves to bring down the reflectances, which is expected since the weights shift away from the TIR conditions. An interesting aspect to consider at this point is to compare these results with the contrast data from before, which is done in Figure 2.37.

It is seen that since the inclusion of angles and weights has the effect of lowering the overall contrast, bringing it closer to the data. Thus, it is possible the the noise approach explored earlier is actually not the best physical description, and that rather the effect of angles would serve to explain the data vs. simulated results.

Now, in theory, it is the $w(\theta)$ from 0°–67° that should be used for the NA$= 1.4$ objective since its $\theta_{\text{max}} = 67°$. However, as discussed previously there are various factors that influence what the true NA of the system is. For starters, the series of micrographs was acquired with the aperture iris slightly closed beyond the objective's pupil diameter. This is usually recommended as a way to improve contrast however it theoretically reduces the INA and CNA to the likes of 1.3 or 1.2. The other aspect is that the visible aperture iris diameter is changing with field iris diameter. I close the field iris as much as possible to reduce stray light (optical noise), and then stop down the aperture iris to the visible 4/5 of the BFP. Also, it is possible that as the rays are relayed throughout the optical system, some of the lenses are cutting out the large NA rays which would reduce the effective INA/CNA. Overall though, the relatively close match between simulation and data when taking the angles into account is a good sign and acheivement of the thesis work.

Ultimatily, one could also do Fourier imaging of the aperture plane in the collection end of the optics. This would allow also to study the effects of $s$-polarized and $p$-polarized light separately. A recent paper from A. Canales et al. 2023 (Shegai group) actually does this for multi-layered $MoS_2$ in what is essentially also an IRM configuration.

### 2.3.8 . IRM of particles on $MoS_2$

One sample of 2D $MoS_2$ became "decorated" with nanometric, sub-µm and µm-sized particulates and defects by accident during an experiment. This sample is thus ideal for exploring the $z$-focus sensitive contrast exhibited by such particles given the diffuse waves that back-scatter from them as was covered in section 2.2.2

In Figure 2.38, a $z$-focus "scan" at 450 nm wavelength is shown at three different foci, $Z^0$ being the most in focus while $Z^-$ and $Z^+$ constitute negative and positive change of the stage. In (b) a zoomed in portion near the top of the triangular flake is shown, with a $y$ line profile is defined where the percent change contrast is shown in (c). As expected based on section 2.2.2, the particle completely inverts its contrast from $Z^-$ and $Z^+$, with a approximately $-12\%$ and $+8\%$ respecively which is quite significant. Notice though that the monolayer itself where light specularly bounces off does not have this change in contrast.

In collaboration with the Molecular Systems and nanoMaterials for Energy and Health (SyMMES)

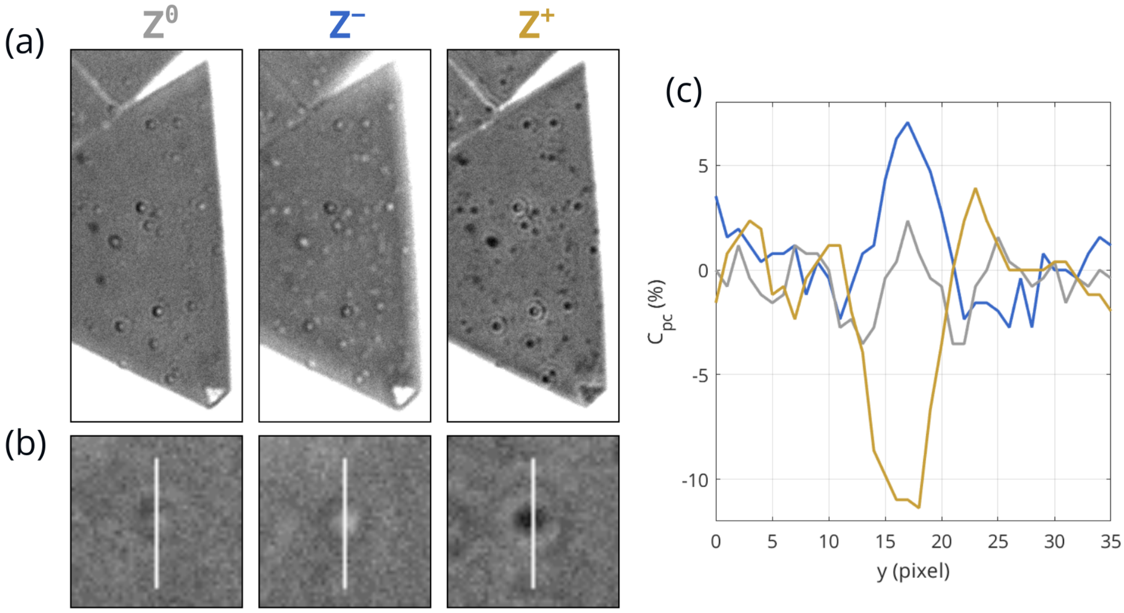

Figure 2.38: (a) Three micrographs of 2D $MoS_2$ that has various nanometric and µm-sized particulates on it, taken at differing $z$-focus including $Z^0$, $Z^-$, $Z^+$. Each image was using 450/10 nm filter and adjusted grayscale (42,62) which saturates the substrate intensity. (b) Zoomed in portion on one of the particulates near the top of the triangle, with indicated line profiles in the $y$-direction. (c) Corresponding profiles plotted as contrasts with respect to the monolayer.

laboratory in Grenoble, a sample of $MoS_2$ was functionalized with 6 nm cubic $CsPbBr_3$ perovskite nanocrystals by D. Aldakov and co-workers. IRM/BALM micrographs were attained before and after at two different $z$-focus points at 450 nm. The results are shown in Figure 2.39, with the left column being before functionalization, and right column after. This preliminary result confirms that such nanocrystals can be resolved to some extent via IRM/BALM especially by adjusting $z$-focus and tuning the field and aperture diaphragms for improved visibility.

The two above preliminary results of nano-structure systems on 2D $MoS_2$ show the potential of characterizing such systems. It also highlights the general utility of IRM given the high contrasted result.

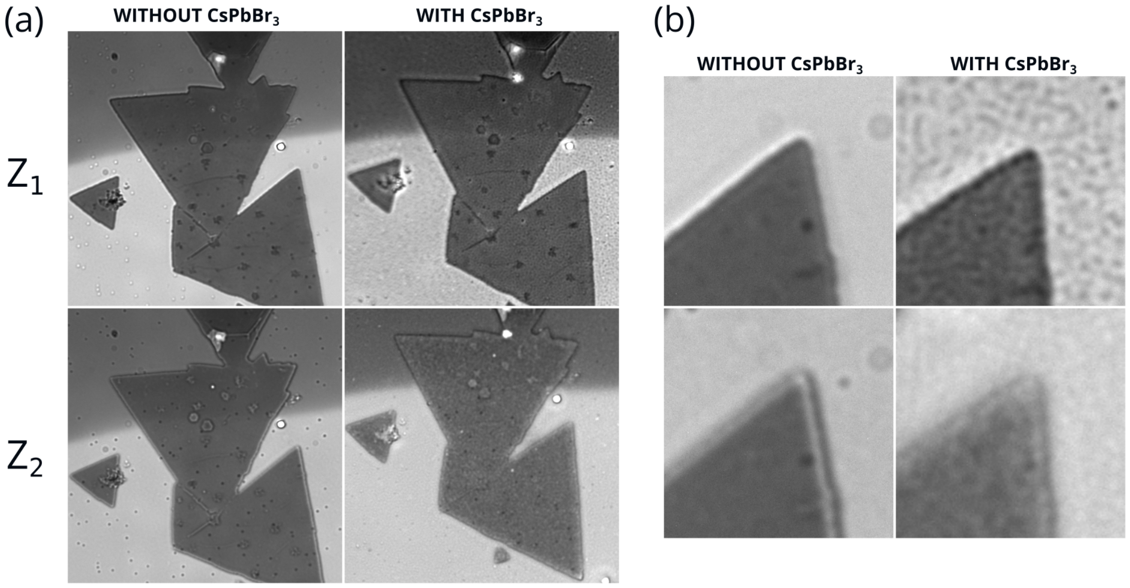

Figure 2.39: Left column: IRM images at two different $z$-focus points $Z_1$ and $Z_2$ at 450 nm of 2D $MoS_2$, partially on glass and partially on 0.5/3 nm Cr/Au. Right column: after functionalization with 6 nm cubic $CsPbBr_3$ perovskite nanocrystals, by the Molecular Systems and nanoMaterials for Energy and Health (SyMMES) laboratory.

# 2.4 . Results: IRM of $MoS_2$ and $WSe_2$ bilayers

## 2.4.1 . $MoS_2$: 2H vs. 3R contrast

As was previously introduced in Chapter 1, the topic of homobilayer stacking order in TMD crystals is an active area of research. The most common stacking orders are of the types 2H and 3R. For CVD-synthesized TMDs that are triangular in shape, it is the case that for 2H, the bilayer triangle is stacked in a manner opposite to the monolayer, whilst for the 3R case it is aligned.

However, for some growth conditions, the distribution of crystal mono- and bi-layers are such that it can be difficult to distinguish the stacking order. Therefore, any technique that can help distinguish this is of value. Now, because of inter-layer coupling between the first and second layer, this gives rise to an interlayer coupling phonemonon for the excitons, which means that the dielectric function is different at some wavelengths depending on the nature of the stacking. This has been measured and addressed in some publications, such as by X. Marie group in Toulouse and collaborators [181], which shows differing reflectance spectra for 2H vs. 3R for $MoS_2$ homo-bilayers.

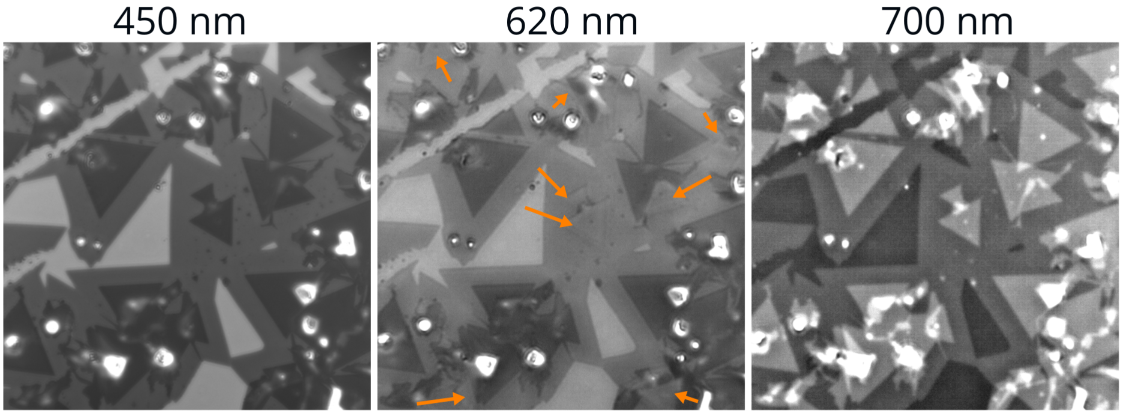

Figure 2.40: Three IRM micrographs at three different wavelengths, of CVD $MoS_2$ that consists of monolayers and both 2H (AB) and 3R (AA) stacked bilayers. It is seen that while at 450 and 700 nm the various bilayers have the same contrast, the 620 nm case has differing contrast for 2H bilayers (labeled with orange arrows), while the 3R bilayers remain darker.

Differing reflectance spectra should mean that IRM micrographs taken at certain wavelengths could potentially help distinguish the stacking, possibly with higher contrast than with a normal reflectance microscope. This was found to be the case based on filter series data that I acquired with IRM in 2022, for a CVD $MoS_2$ growth that had non-trivial stacking orders. The result is shown in Figure 2.40 for three wavelengths, each with 10 nm bandwidth (this is from the same data series as the one presented in Figure 2.32). It is seen that for 450 and 700 nm, the various bilayers in the micrograph have the same contrast. But, for the 620 nm case, there are two strikingly different contrasts for the various bilayers, as indicated by the orange arrows.

It is safe to conclude that the darker bilayers in the 620 nm micrograph are of 3R type since the bilayer has the same orientation as the monolayer, while the bilayers with orange arrows are of 2H type, which is corroborated by the $MoS_2$ bilayer near the center of the image, which points in the opposite direction of its monolayer. Although it is obvious by the direction of the near center bilayer that it is 2H, it is less obvious for most of the bilayers indicated by the orange arrows, which have a more random shape and orientation. It is therefore clear that IRM can be a powerful tool in such a situation for distinguishing the stacking order, without having to scan any probe or Raman laser spot for example, to differentiate the stacking order.

An experiment of somewhat similar yet different character was published in January 2023 [182], where color filters in a microscope were used to distinguish bilayers that were grown versus manually stacked. At some wavelengths, in their case 450 nm, the contrast was different for those two types of stacking. This is partially attributed to a possible insulating gap between the mono and bilayer for the manually stacked case.

## 2.4.2 . WSe$_2$: 2H vs. 3R contrast

IRM contrasts at multiple wavelengths were also investigated for the case of WSe$_2$ homobilayers. This material was grown using a CVD process by collaborators at the Centre for Nanosciences and Nanotechnologies (C2N).

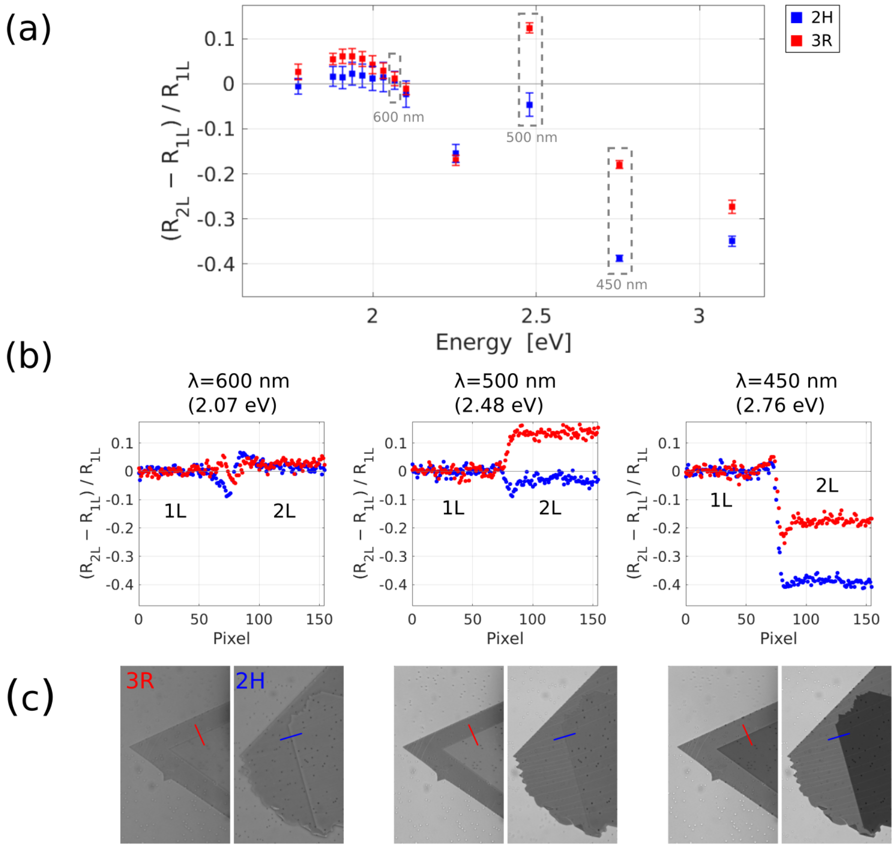

Figure 2.41: IRM data of CVD WSe$_2$ grown at C2N Mat2D group, which consists of both 3R bilayers and 2H bilayers. The IRM spectra were taken at 13 bandpass filters, with the resulting fractions of bilayer versus monolayer plotted in (a). The micrographs and line profiles for the 600, 500, 450 nm cases are shown in (b) and (c). It is clear that the bilayers have drastically different contrasts for the 500 and 450 nm case, while it is similar at other wavelengths such as 600 nm. This data was published in 2023 [27].

In the collaboration, various properties of 2H and 3R homobilayers of WSe$_2$ were characterized experimentally by different partners, including by Raman, photoluminescence, angle-resolved photoelectron spectoroscopy (ARPES), and finally by IRM optical contrast spectoroscopy, the last of which I executed, the results of which are reproduced in Figure 2.41. This work resulted in a co-publication [27].

The main purpose of the IRM data in this case was to test whether at certain wavelength there would be a significant difference in contrast between the different bilayers. This was expected based on prior reflectance spectrographs reported for $WSe_2$ homobilayers by McCreary et al. 2022 [183] and other published works. The IRM results indicated that indeed this was the case, and most significantly at 500 nm (2.48 eV) and 450 nm (2.76 eV). This would have been expected for the different stacking orders 2H and 3R which have different intercoupling between the layers. At some wavelengths, as indicated in (a), the contrast is mostly similar, while at some wavelengths the contrast is significantly different (as indicated). The most striking differences are included in (b) and (c) where the former contains line profiles of the corresponding micrographs in (c).

In particular, the 500 nm case is interesting because in that case the bilayer contrasts switches sign with respect to the monolayer, meaning there is a striking difference which can allow fast and efficient stacking order detection by IRM, in widefield, without scanning.

## 2.5 . BALM background & theory

Having covered theoretical and experimental results of interference reflection microscopy (IRM) of 2D materials with a focus on mono- and few-layered $MoS_2$ crystals, the next order of things is to cover the BALM related efforts and contributions of the thesis.

The next few sections are concerned with theoretical and historical background of BALM. This is followed by results and findings regarding the characterized optical properties of the BALM stack and insights into BALM itself. The section concludes with $MoS_2$ samples studied via BALM.

### 2.5.1 . BALM background

In 2014, Dominique Ausserée (Université du Mans / CNRS) and co-authors introduced an optical micro-interferometry technique based on what they termed an “anti-reflecting absorbing” (ARA) layer, via a publication in the *Journal of Nanomedicine & Nanotechnology* [88].

The setup essentially consists of an IRM microscope, with an ARA layer on the coverslip substrate being the active component. The ARA layer is nanometeric gold, i.e. a few nanometers of evaporated Au on top of the coverslip, with an extra sub-nm Cr layer as adhesive for the Au. They found that such a layer (thin Cr/Au), at some specific thicknesses and wavelengths while illuminated from the glass backside, exhibits anti-reflection properties due to interference effects—meaning it results in a reflectance that is less than that of the bare substrate. This is a useful discovery as it means that this nanometric gold (ARA layer) can serve both as a Fabry-Pérot (FP) resonator, thus enhancing contrast for various types of samples, while at the same time serving as a conducting electrode for various *in situ* experiments that involve application of a bias, such as in electrochemistry. The FP interference effect for this system was demonstrated in the 2014 paper [88] by a plotting of simulated contrast. Furthermore, in the paper its utility in studying local electrochemical phenomena is explored, where a voltage is applied to the ARA layer to achieve a redox reaction and analyzing the local changes with diffraction-limited resolution.

In 2016, at the *229th ECS Meeting*, S. Campidelli (LICSEN), D. Ausserrée (Université Le Mans / CNRS), and co-authors introduced the term “backside absorbing layer microscopy” (BALM) to describe the technique, the first time this term is used to the author’s knowledge.

At this conference, the utility of BALM for studying graphene oxide (GO) and its *in situ* chemical modification was presented. This work culiminated in a 2017 publication in [87], where it was demonstrated that GO and a chemically reduced graphene oxide (rGO) could be distinguished with very high contrast using BALM. Furthermore, 2D $MoS_2$ was shown to exhibit high contrasts as well. Some specific examples of the *in situ* modification of GO was also demonstrated, with good vertical resolution. Figure 2.5 from an earlier section reproduced some of these results.

Ph.D. student Kévin Jaouen at LICSEN contributed further developments to BALM in 2016–2019, with a focus on tandem BALM and electrochemical voltammetry curves for graphene oxide [13]. Some of this work was also published in 2019 [184], which among other things demonstrated the utility of an additional coherent optical layer on top of the BALM/GO stack in improving contrast.

F. Kanoufi group and collaborators also have published a number of studies using BALM for electrochemical studies, some of which are cited here [185, 186]. They also have performed studies using IRM (with a transparent conducting ITO layer as the working electrode) [124].

Ausserrée and collaborators have contributed various developments. This includes a 2020 publication [187] which presents a formula that according to the authors provides a more universal character among other advantages, in the context of BALM reflectance curves and associated changes in reflectance due to any arbitrary sample $(\tilde{n}, d)$. This was demonstrated for the case of tethered bilayer lipid membranes grafted on a BALM coating in a 2021 publication [188], and also in a recent 2023 publication with hBN [189].

Now, it is important to spend some time covering other published works that also have explored the utility of gold (or other metal) thin-films as optical FP layers for various applications. Some of them resemble the concept of ARA layer and BALM, whilst others are less close to those core principles.

The first case of interest involves not gold films but instead semi-infinite planar gold, and thus is not in direct resemblance to BALM. The research is from the Tokyo Institute of Technology, based on a series of papers by K. Kajikawa and H. Mihara and collaborators [190, 191, 192, 193, 194]. In their work, they exploit what they term "anomalous reflection" (AR) of gold, for optical sensing. The anomalous behavior which they are referring to is the fact that towards blue wavelengths, the extinction coefficient of gold is largely reduced and thus the gold starts to behave more like a dielectric causing a reduction in reflectivity. This is a well-known behavior of gold and is the reason it has its “gold color” as opposed to being silverish. It is the same phenomenon which makes the BALM principle work better at blue wavelength ($\sim$ 450 nm) rather than red wavelgnths ($\sim$ 650 nm), discussed later. Their earliest paper is from 2003 [190], followed by additional sensing-related results [191, 192] including in imaging mode in 2009 [193]. The group also explored more complex optical stacks such as a metal–insulator–metal (MIM) for improved detection sensitivity [194].

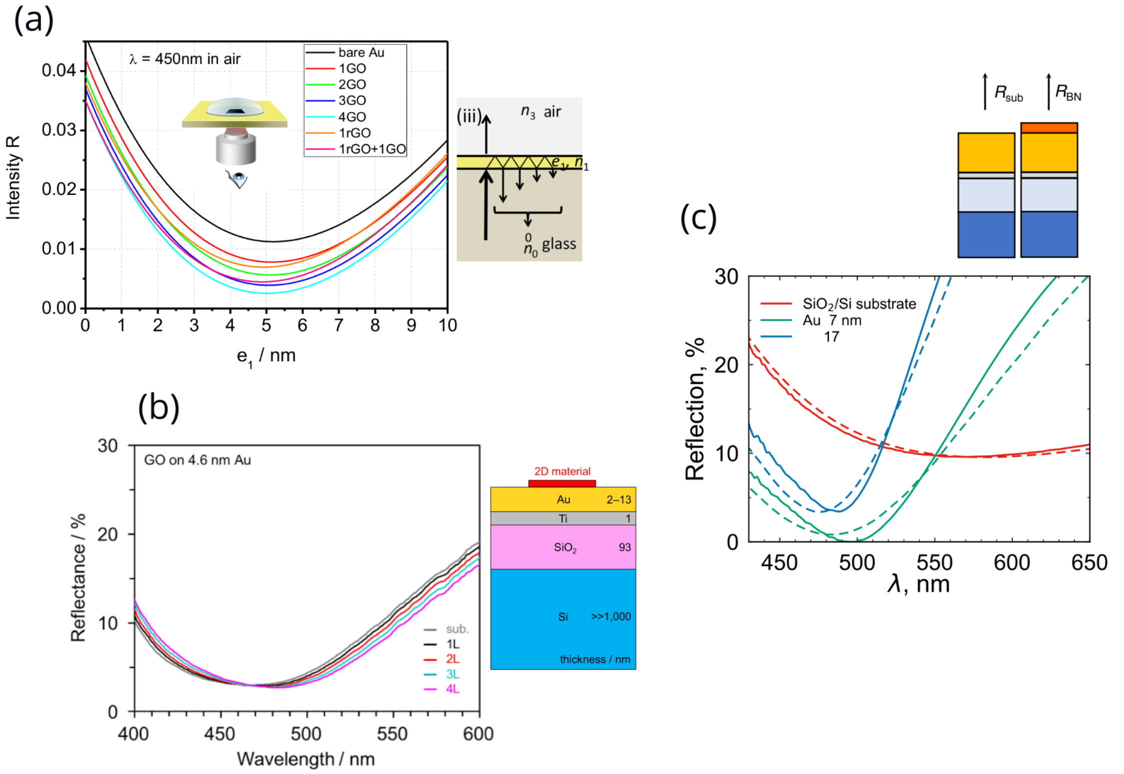

Figure 2.42: (a) From [87], the anti-reflection effect of a thin gold coating on glass in the IRM configuration revealed by plotting reflectance versus gold thickness. (Graphene oxide layers are also included but less relevant here.) (b) From [132] (F. Huang group), anti-reflection behavior of 1/4.6 nm Ti/Au on SiO$_2$/Si. (c) From [164], anti-reflection behavior of thin Au on SiO$_2$/Si, with the 7 nm Au case showing a particularly low reflectivity.

F. Huang and collaborators published several papers also exploiting both semi-infinite gold and thin gold films, for contrast improvement of 2D materials. The case of graphene on semi-infinite gold was published in 2018 [67], showing contrast improvement at some wavelengths. In 2020 thin Au films between 2–13 nm on $\approx$ 90 nm SiO$_2$/Si (with Ti as adhesive layer) were used for improving contrast of graphene and GO [132], and for MoS$_2$ a similar structure was also used with Au film thicknesses in the same range, published in 2020 [131]. F. Huang presented additional insights on contrast theory of 2D materials in [129]. Some of the results from [132] are reproduced in Figure 2.42(b).

Researchers from Kobe University by Y. Hattori, M. Kitamura and collaborators also published several papers that in fact leverage gold films as opposed to semi-infinite gold [163, 164, 165]. Their system consists of 7 nm Au (with Cr as the adhesion layer) on top of an $SiO_2$/Si substrate among others. The reflectance spectrum of this system is reproduced in Figure 2.42(b) from a 2021 paper [164]. It is seen that a near-zero reflectance is acheived around $\sim$ 500 nm. Using this FP system they were able to image hBN with very good contrast. They also studied in 2023 Au oxidation by exposure to UV ozone with a mask, measuring and simulating the changes in contrast [165]. Finally, they also studied the sensitivity of a (thin Au)/$SiO_2$/Si system to adsorbed alkanethiol in 2021 [163].

Thus, we see there are a few notable examples in the literature exploring the use of metallic Fabry-Pérot films for various purposes in optics and improvement of contrast of 2D and other materials. Their use has a lot of potential and remains still relatively unexplored, which in part motivated this thesis work. It is also a good moment to note the work of Kats et al. 2013 [195], where the authors explore the use of thin metallic films as a means to produce colors. The authors emphasize the utility of a non-zero extinction coefficient in metallic FP films. The more typical dielectric FB films which have $\kappa = 0$ suffer from the constraint that the thickness must be on the order of wavelength (so hundreds of nm for optical) in order to have the interference fringes appear. This is rooted in the 0° or 180° phase restriction upon Fresnel reflection. The $\kappa \neq 0$ condition makes it so that with a few nanometers strong interference effects can be produced. This insight is also at the heart of the BALM effect.

## 2.5.2 . BALM formulas

For transparent Fabry-Pérot (FP) layers, a simple formula can be derived that states which combination of thickness and wavelength results in the most destructive interference conditions. It is quite intuitive. Say you have two semi-infinite media of RI $n_0$ and $n_{\mathsf{f}}$ with a FP film $(n_{\mathsf{AR}}, d_{\mathsf{AR}})$ in the middle. Then, interference minima are found for the condition [140, pp. 167–170]

$$n_{\mathsf{AR}} d_{\mathsf{AR}} = \begin{cases} \frac{1}{4}\lambda, \frac{3}{4}\lambda, \frac{5}{4}\lambda, \ldots, & n_0 < n_{\mathsf{AR}} < n_{\mathsf{f}} \\ \frac{1}{2}\lambda, \frac{3}{2}\lambda, \frac{5}{2}\lambda, \ldots, & n_0 < n_{\mathsf{AR}} > n_{\mathsf{f}} \end{cases}$$

In the former case, it is the so-called "quarter-wave layers" which meet the criteria of the optical path length (OPL) $n_{\mathsf{AR}} d_{\mathsf{AR}}$ being at a minimma. This applies often for anti-reflective (AR) coatings on eyeglasses for example. However if $n_{\mathsf{AR}} < n_{\mathsf{f}}$ it is a half-wave layer which results in destructive interference. This is the case for suspended soap films. Furthermore, it can be derived that the most ideal RI value for a quarter-wave layers is [140, pp. 167–170]

$$n_{\mathsf{AR}}^2 = n_0 \, n_{\mathsf{f}}$$

The reason for this case-condition is the previously mentioned phase of the light upon reflection, in Equation 2.2.

For BALM ARA layer, D. Ausserrée derived formulae as well which rely on some approximations. They take the following form [87], for the $\tilde{n} \equiv n - j\kappa$ convention:

$$d_{\mathsf{ARA}} = \frac{\lambda}{4\pi} \frac{(n_0 - n_{\mathsf{f}})}{n_{\mathsf{ARA}} \kappa_{\mathsf{ARA}}}$$

and

$$n_{\mathsf{ARA}}^2 - \kappa_{\mathsf{ARA}}^2 = n_0 \, n_{\mathsf{f}}$$

They are not used explicitly in this thesis since the full parameter space is explicitly computed via simulations, but are stated for completeness, and for improved physical intuition of the system.

### 2.5.3 . BALM vs. SPRi

At this point it is a good moment to discuss briefly surface plasmon resonance imaging (SPRi) because it has some similarities to BALM, although at the end of the day it is still quite different. A comparison is illustrated in Figure 2.43.

Surface plasmon resonance is the effect where $p$ polarized light at a specific angle (and wavelength) couples with charge on the surface of a metal, for the stack $n_{\mathsf{i}}/\tilde{n}_{\mathsf{metal}}/n_{\mathsf{f}}$ where the condition $n_{\mathsf{i}} > n_{\mathsf{f}}$ must be met. The resonance is because of a strong coupling between the electromagnetic wave of light with surface plasmons (charge), which form a type of polariton called a surface plasmon polariton (SPP). This results in a change of dispersion relationship of the light.

Due to the strong coupling, there is a high sensitivity to refractive index changes $\Delta n_{\mathsf{f}}$ because

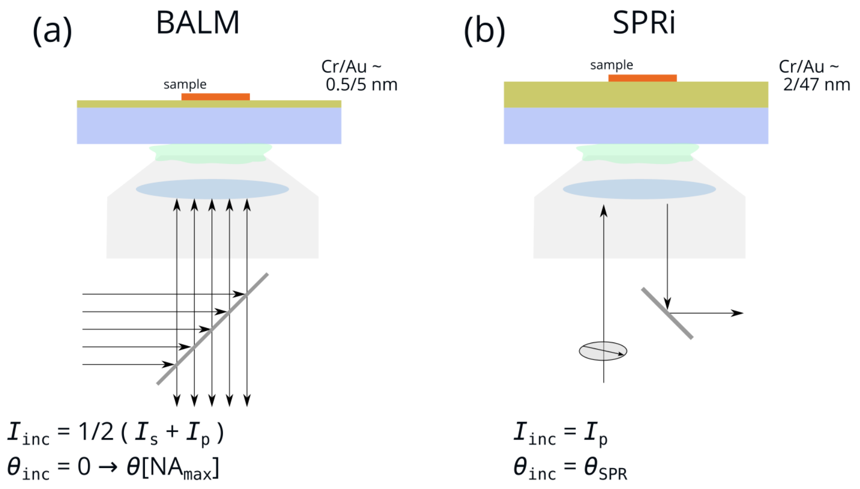

Figure 2.43: Comparison of BALM vs. SPRi in (a) and (b) respectively.

the angle at which the resonance occurs ($\theta_{\text{SPR}}$) is sensitive to any small change. This has led to SPR sensors which are used both commercially and in research for many applications [196, 197, 198, 199]. Now, one way to turn SPR sensing into SPR imaging is to exploit the relationship between BFP annulus and incident angle. That is, one can focus the light source at a specific radius of the BFP. Furthermore, one can construct the optical elements such that the incident angle can be tuned.

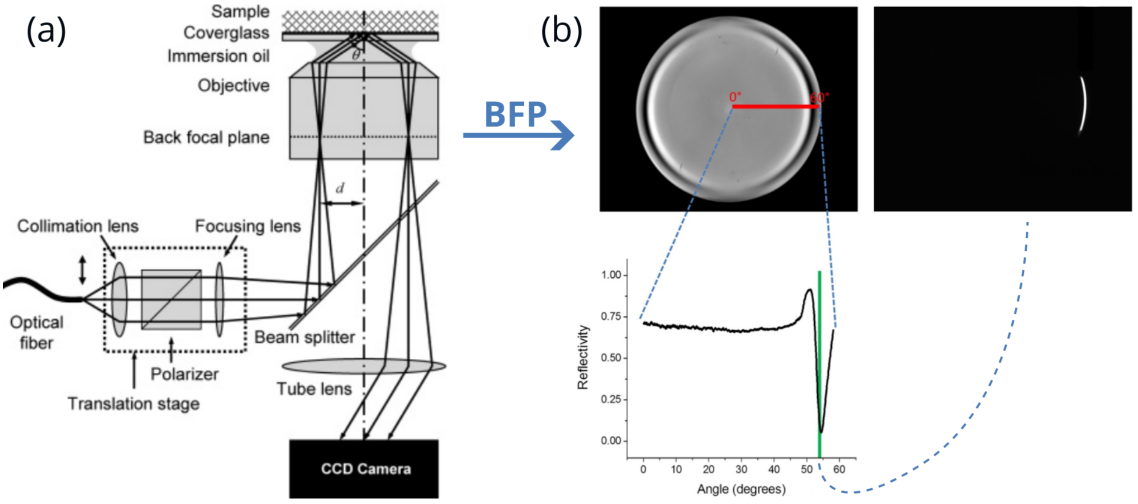

Figure 2.44: (a) From [200], diagram of SPRi setup. (b) From [201], back focal plane (BFP) configuration to control incident angle for best SPR response.

This was done for instance in Huang et al. 2007 [200], with their setup reproduced from the paper in Figure 2.44(a). Figure 2.44(b) is from a different publication, Peterson et al.

2014 [201], where the back focal plane (BFP) was imaged and it is seen that the there is the characteristic dip in reflectivity around 53.5°, which in turn is then used to illuminate the sample. Recall that there is the relationship $r = f \sin \alpha$ between annular radius and incident angle. This is the relationship being exploited. Another difference with BALM is the Cr/Au thickness, which happens to work well at a combination of around 2/47 nm for SPRi, which is quite different from the 0.5/5 nm used in BALM. There is also the fact of sending only $p$ polarized light, while in BALM the incident light is randomly polarized as covered in 2.2.4.

All in all there are thus various differences between BALM and SPRi. Since a wide range of both $s$ and $p$ polarized light is used in BALM, probably the effect of SPR at $\theta_{\text{SPR}}$ consitutes a weak contribution. In principle it would be interesting though to test via simulation and experiment whether the SPR has an important effect on the BALM data though. Finally, it should be noted that in [188] the authors did compare to some extent BALM and SPR, but not SPRi in the sense described here. (The authors mention they are using SPRi but that HORIBA system [202] is not the same as described here.)

# 2.6 . Results: BALM stack optical properties

## 2.6.1 . Optical properties: Au and Cr

Before diving into the basics of the typcial response of a BALM stack, it is important to cover aspects of the optical properties of Cr and Au which form the essence of the stack, being the "anti-reflection absorbing" (ARA) layer.

The values of $\tilde{n}_{\mathrm{Au}}(\lambda)$ and $\tilde{n}_{\mathrm{Cr}}(\lambda)$ are of great importance because even a small variation in their values can have a significant effect. This is especially due to the RI being complex, as transparent films are more tolreant to small thickness variations.

Although Au and Cr have been measured and calculated by various techniques in the literature, in practice the way they are evaporated actually can cause significant variations in their properties. This fact was echoed for example in a *Perspective* from 2015: *Plasmonic Films Can Easily Be Better: Rules and Recipes* [203]. In the perspective, the authors lament that researchers in plasmonics lack experience in deposition methods to produce good quality metal films. They show for instance how the rate of deposition significantly affects resulting optical properties, sometimes even by 150% for the real part of the dielectric function, at some wavelengths.

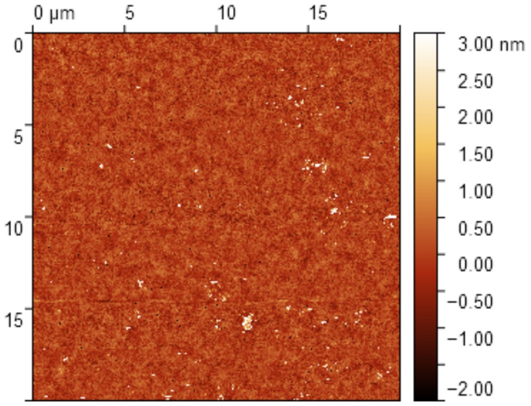

RMS ~ 0.5 nm

Figure 2.45: AFM image of 0.5/5 nm Cr/Au acquired *OptMatLab* at University of Genova. Field is 20×20 µm with 3 nm height colorbar. Resulting RMS was measured to be 0.5 nm.

Another aspect has to do with the fact that the typical thickness of the Au layer used in BALM is very low, around 5 nm. In this regime from say 2–10 nm the microstructure can differ quite a bit. This was investigated to some extent by the group from Kobo University mentioned earlier, in which they show the microstructure evolution as measured by SEM, for 7 nm vs. 12 nm films, as well as the change in sheet resistance [164, 163].

Thus the best practice is to actually measure the optical properties of the in-house evaporated BALM ARA (Cr/Au) films used. Fortunately this was possible thanks to the collaboration with *OptMatLab* at the University of Genova that are experienced with VASE ellipsometry measurement and analysis. To the author's knowledge, this is the first time that the optical properties of Cr/Au are measured and applied for a home-grown BALM experiment, as previously published BALM research makes use of existing literature values for the $\tilde{n}(\lambda)$.

The films are deposited here at LICSEN using thermal physical vapor deposition (PVD). Coverslips are mounted into the PVD chamber upside-down and pumped down to around $2 \times 10^{-6}$ mbar. Then, a high current is applied to a tungsten crucible containing pellets, one for Cr and one for Au. The resulting microstructre was measured by *OptMatLab* via AFM and is reproduced in Figure 2.45. The resulting RMS was measured to be around 0.5 nm, which is fairly acceptable and means that the film can be treated as planar and diffuse reflections are minimal.

Now, a factor of importance has to do with the effect of ambient oxygen on the films. Although Au is inert thanks to its high work function and is less readily forming $\mathrm{AuO_x}$, it is not so for Cr which easily forms $\mathrm{CrO_x}$ upon exposure to air. Furthermore, Au cannot be evaporated onto the coverslip without Cr because, it forms nanoparticles of Au with a completely different microstructure and optical properties compared with when the adhesive Cr layer is used. This makes it more challenging to disentangle the effect of Cr vs. Au on the resulting ellipsometric (or reflectance) response.

Indeed, experimentally when I tested evaporating Au by itself, it resulted in a blue film which easily peels off, the color due to the localized SPR. For Cr, ultra-thin films of 0.1, 0.5, or 1 nm were essentially transparent (thus a more oxidized form of $\mathrm{CrO_x}$), whilst 3 nm or thicker consisted both of the underlying unoxidized Cr plus the $\mathrm{CrO_x}$ forming as a capped layer preventing further oxidation deeper into the Cr.

Most of ARA layers we used consisted of nominal thicknesses of 0.5/5 nm Cr/Au. Anything thinner than 0.5 nm Cr is pushing the limits of the needed adhesive function of the Cr for the Au. For the latter, 5 nm is also a good compormise because the film needs to be conductive enough to be used as a gate electrode, but not too thick as to reduce the anti-reflective "BALM effect".

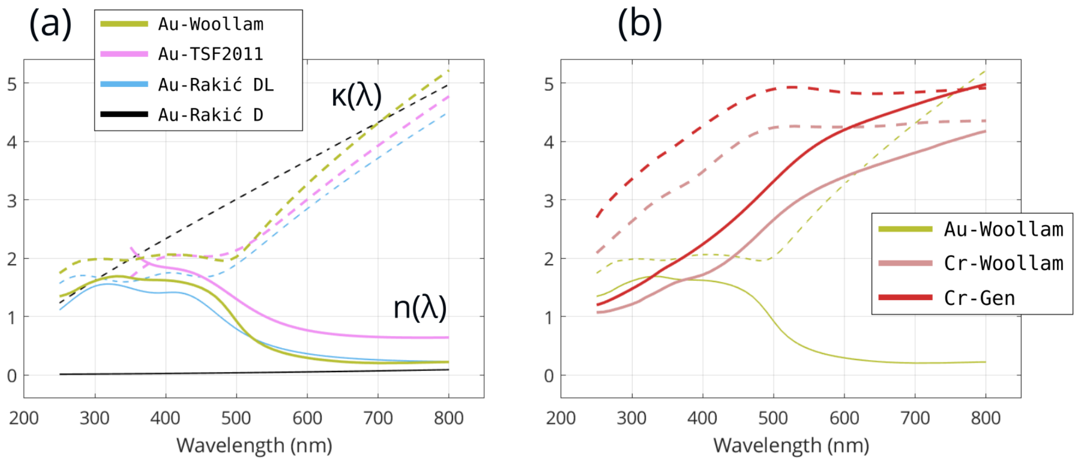

Figure 2.46: (a) Complex refractive index of Au according to 4 datasets as indicated in Table 2.6. (b) Complex refractive index of Cr per Table 2.6.

To disentangle the two, three substrates consisting of nominal thicknesses 0.1/5, 0.5/5, 3/5 nm of Cr/Au were prepared and sent to *OptMatLab*. Varying the Cr thickness while keeping Au constant allowed disentangling the effect of the two. It was found that, for Au, the optical properties from the J.A. Woollam database provided an accurate desciption of the VASE ellipsometric response. This was based on a number of factors, notably the fact that when fitting ($\Psi$,$\Delta$) for the 0.1/5 nm case the $\tilde{n}_{\text{Au, Woollam}}$ alone provided a reasonable fit (with MSE around 7.7). This is a very good sign because it means that the Au films produced by our PVD method are not radically different from "textbook bulk gold" even when being as thin as 5 nm. Then, based on further analysis it was found that the Cr optical properties however were differing from that of the J.A. Woollam database to some degree. Thus *OptMatLab* calculated new values for the Cr layer produced by our PVD method. This means that while the Au optical properties are typical, the Cr differ. This is not too surprising since as mentioned it is difficult to know the degree to which the Cr gets oxidized during evaporation. As the Cr films are quite thin, even thinner than the Au, there is also the possibility that a differing microstructure is the main mechanism giving rise to differing optical properties. (The group from Kobo University discussed earlier also used Cr as an adhesive layer, but conjectured that their Cr layer was $\text{CrO}_x$ and took on a non-dispersive $\tilde{n}_{\text{Cr}} \approx 2.0 + 0.5i$ at optical frequencies.)

The resulting measured $\tilde{n}(\lambda)$ for Cr and Au are shown in Figure 2.46 with the "Au-Wollam" and "Cr-Woollam" corresponding to the values from J.A. Woollam database, and "Cr-Gen" being the newly calculated Cr used for "our PVD Cr". Additionally, other $\tilde{n}(\lambda)$ dispersions were explored in the thesis, especially before having access to the measured results by *OptMatLab*. This includes Au values from a 2011 paper in the journal *Thin Solid Films* by L. Gao, F. Lemarchand and M. Lequime [204]. Thus this dataset (which is available at the RI database [168]) is nicknamed "Au-TSF2011". In the paper the authors explored gold films at low thicknesses in particular, including at 3.96 nm, and thus seemed an appropriate starting point. Yet, somehow our PVD Au did not have as high values for the real part $n(\lambda)$ at optical frequencies.

Furthermore it is of interest to compare the measured $\tilde{n}(\lambda)$ of Au to a simple dispersion model. Now, a variety of disperion models have been proposed for gold, some more true to the real physical mechanisms than others. Here I explored both a Drude–Lorentz and a pure Drude dispersion model, which are more classical and simple. As we shall see, these models allow us to explore some of the physical mechanisms underlying BALM. Rakić et al. 1998 [205] provided parameters for such a Drude–Lorentz and Drude model for Au, which B. Ung et al. 2007 [206] conveniently implemented in MATLAB code. A table of the parameters as stated by Rakić et al. [205] are reproduced in Table 2.5.

| | $\omega_j$ (eV) | $f_j$ (unitless) | $\gamma_j$ (eV) |
|---|---|---|---|
| Drude | 0 | 0.760 | 0.053 |
| Lorentzian 1 | 0.415 | 0.024 | 0.241 |
| Lorentzian 2 | 0.830 | 0.010 | 0.345 |
| Lorentzian 3 | 2.969 | 0.071 | 0.870 |
| Lorentzian 4 | 4.304 | 0.601 | 2.494 |
| Lorentzian 5 | 13.32 | 4.384 | 2.214 |

Table 2.5: Drude-Lorentz parameters for gold according to A. Rakić 1998 [205].

Note that [205, 206] use the (Drude–)Lorentzian convention #2 of the ones listed earlier in Table 2.4. Thus it is of the form:

$$\varepsilon_r(\omega) = \varepsilon_\infty + \omega_p^2 \sum_j \frac{f_j}{\omega_j^2 - \omega^2 - i\omega\gamma_j}$$

In this case $\varepsilon_\infty = 1$ and plasma frequency of Au taken as $\omega_p = 9.03$ eV. Now, for convenience, the various $\tilde{n}(\lambda)$ values and models stated so far and further used below are summarized in Table 2.6, including the "short name" by which I will be referring to these models in the text and figures.

| **Short name** | **Source** | $d_{Cr}$ / $d_{Au}$ (nm) | $\tilde{n}_{Cr}$ | $\tilde{n}_{Au}$ | **MSE** |
|---|---|---|---|---|---|
| Au-Woollam | J. A. Woollam [207] | 0 / $d_{Au}$ | - | Woollam [207] | - |
| Au-TSF2011 | 2011 paper in *Thin Solid Films* [204] | 0 / $d_{Au}$ | - | TSF2011 3.96nm | - |
| Au-Rakić-LD | 1998 paper by Rakić [205] | 0 / $d_{Au}$ | - | Drude-Lorentz | - |
| Au-Rakić-D | 1998 paper by Rakić [205] | 0 / $d_{Au}$ | - | Drude | - |
| CrAu-GenMain | Univ. of Genova ellipsometry | 0.5 / 4.9 | new | Woollam [207] | 18.4 |
| CrAu-GenAlt | Univ. of Genova ellipsometry | 0.7 / 4.9 | Woollam [207] | Woollam [207] | 19.0 |

Table 2.6: Cr/Au parameters

Some further comments about the measured Cr/Au dispersions are needed here. As was mentioned, the Cr optical properties (as well as for Au) are to some extent dependent on thickness. Thus in theory the ellipsometric fits that led to $\tilde{n}_{\text{Cr, new}}(\lambda)$ with a particular thickness combination does not necessarily apply to other ranges of thicknesses. In fact, the primary Cr/Au result, which I will refer to as "CrAu-GenMain" (with "Gen" being short for "Genova" where the analysis was done), yields an MSE of 18.4 only for the thickness combination 0.5/4.9 nm. In fact, an alternative combination which consisted of using the J.A. Woollam values for both Cr and Au was tested, but necessitated an increase of Cr thickness to 0.7 nm for the MSE to be acceptable. This gave a slightly higher MSE of 19.0 however. This result is termed "CrAu-GenAlt" and I will compare it with the main result. In the end, the resultant thickness and dispersions are a reasonable and acceptable starting point for BALM simulations, especially as it is the first time a BALM substrate is characterized by ellipsometry to the author's knowledge. In the text, the use of Au without Cr in simulations is explored (with comparisons with Cr included when appropriate) because it is the Au that is the essence of the BALM optical response.

Now, a first consideration for the Au is to plot the complex relative permittivity

$$\tilde{\varepsilon}(\omega) = \varepsilon'(\omega) + i\varepsilon''(\omega)$$

for each of the four Au dispersions listed in Table 2.6. The main reason to do this is that, considering only the complex RI $\tilde{n}(\lambda) = n(\lambda) + i\kappa(\lambda)$ actually hides some of the intrinsic behavior. Recall that absorptance and loss are dictated by the imaginary part of $\tilde{n}$ which is $\kappa$ (where $\alpha = (4\pi/\lambda)\kappa$). There are two mechanisms however that can cause an increase in $\kappa$: the first is an increase in the imaginary permittivity $\varepsilon''$, while the second is for the real permittivity $\varepsilon'$ to be $< 0$ since $\tilde{n} = \sqrt{\tilde{\varepsilon}}$ results in the square root of a real negative number.

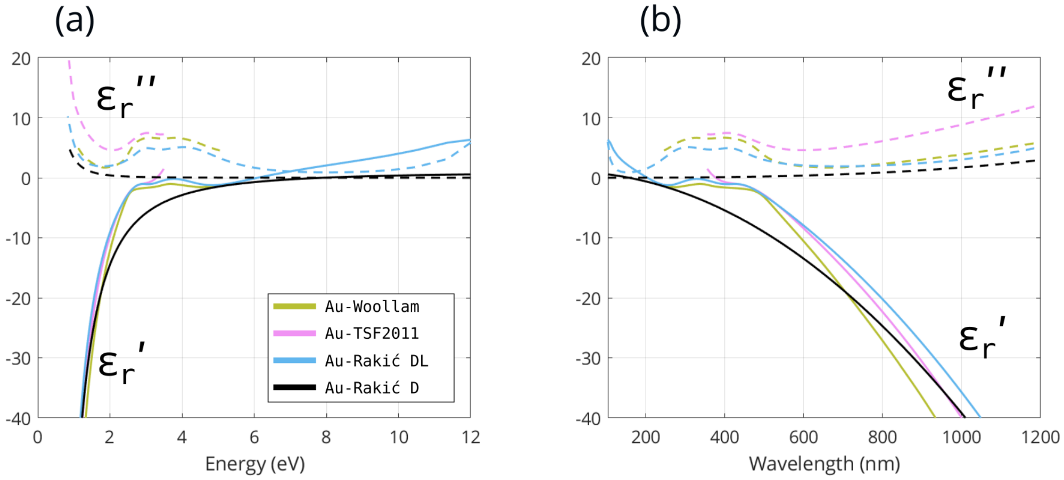

Figure 2.47: Real and imaginary dielectric function $\tilde{\varepsilon}_r = \varepsilon_r' + i\varepsilon_r''$ of Au for 4 different datasets as summarized in Table 2.6, as a function of energy (a) and wavelength (b).

The real permittivity being less than zero ($\varepsilon' < 0$) is in fact the primary signature behavior of a metal, i.e. the expected response of a free electron gas to an AC electric field. In fact, as was recollected before, the simplest model for the AC response of a metal ignores electron scattering in the lattice and is of the form

$$\tilde{\varepsilon}(\omega) = 1 - \frac{\omega_p^2}{\omega^2}, \qquad \omega_p^2 = \frac{n_e e^2}{\varepsilon_0 m_e}$$

which makes $\varepsilon_r(\omega)$ entirely real with no imaginary part. The version with scattering included is

$$\tilde{\varepsilon}_r(\omega) = 1 - \frac{\omega_p^2}{\omega^2 - i\gamma\omega}$$

This is the version also included in Figure 2.47 as "Au-Rakić D" and is thus the Drude model of the above formula. The "Au-Rakić DL" is for the Drude–Lorentz version as reproduced above.

There are a couple of take-aways from studying the Au relative permittivity of Figure 2.47. The first is that overall the various models mostly have the same trends, with no radical outliers, although there are some important differences. Notably, towards the blue part of the spectrum the Drude version is a lot farther from unity than the other models.

The reason the DL and other models are closer to unity around 450 nm is because of the interband transitions (Lorentz oscillators) that start to dominate at that wavelength (recall Table 2.5). Now, if it were not for the interband transitions, the metal would only start to behave as a dielectric around the plasma frequency $\omega_p$ which is 9.03 eV for gold far into the UV, because that is around where $\varepsilon'$ would cease to be negative but positive again.

The interband transitions thus are responsble for bringing $\varepsilon'$ closer to unity much earlier at the blue wavelengths, making the gold more transparent there. This is the same phenomenon discussed before of the "anomalous reflectivity" as described by the group at Tokyo Institute of Technology [190].

The above analysis and discussion is the first time to the author's knowledge that the physical mechanisms behind BALM are elaborated, with the comparison of Drude vs. Lorentzian contributions to the anti-reflection effect and the other aspects mentioned and thus is a contribution of the theis.

### 2.6.2 . Optical properties: $\mathrm{AlO_x}$

In addition the the Cr/Au ARA layer which forms the essence of BALM, it is also possible to add other coherent layers on top of (or actually even before) the ARA layer itself. This can in some cases be of interest. The addition of layers to the BALM stack was explored to some extent by K. Jaouen, V. Derycke, and co-authors in 2019 [184], in the context of graphene oxide imaging.

In the thesis $\mathrm{AlO_x}$ was explored to a significant degree for a few reasons. The first being that it can be used as a dielectric to gate $\mathrm{MoS_2}$ with the ARA acting as a back-gate. This is discussed more in depth in Chapter 3, along with how charge imaging can be done in that configuration. Even by itself though, $\mathrm{AlO_x}$ is of interest in terms of an optical layer, potentially improving contrast at a desired wavelength based on its thickness and optical properties.

Attaining an insulating and non-absorbing $\mathrm{AlO_x}$ was very difficult and took a lot of tailoring of our process. We use thermal PVD with a set partial pressure of $\mathrm{O_2}$ in the chamber, combined with pulsing a thin film of Al at a time. It is thus a CVD-like process.

For similar reasons why it is of importance to measure the optical properties of the Cr and Au layers, it is also important if possible to have the $\mathrm{AlO_x}$ measured. Furthermore, resultant

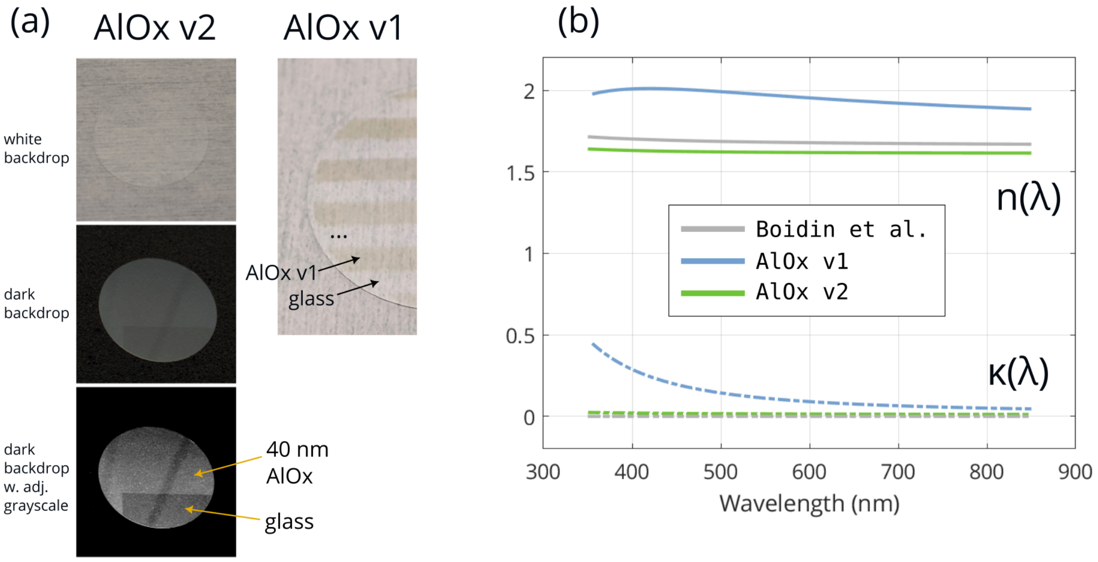

Figure 2.48: (a) Pictures of both v1 and v2 AlO$_x$. The v2 is improved and transparent and thus less visible hence the black backdrop and grayscale adjustment of the image to be able to see it. The v1 was more visible but slightly conducting and more absorbing. (b) AlO$_x$ v1 and v2 optical properties measured by *OptMatLab* at University of Genova, showing how v1 has an absorption tail while v2 does not. Also in the result comparing with Boidin et al. 2016 [208] which is similar to v2 result.

optical properties can be compared with the literature, and here I shall compare with Boidin et al. 2016 [208]. Amorpous $Al_2O_3$ (or AlO$_x$ since it may not be fully stoichiometric) is in theory transparent at optical frequencies and thus the extinction coefficient $\kappa$ should be $\approx 0$.

In practice however, the first version of our AlO$_x$ process (referred to as "v1") was not oxidized enough and thus had an absorption tail, as measured and confirmed through VASE ellipsometry by *OptMatLab* with the complex RI plotted in Figure 2.48(b). Further improvements to the process led to more transparent AlO$_x$, yielding the result shown by the green curve, referred to as "v2". This version is quite close to that obtained by Boidin et al. For gating and use as a capacitive dielectric, it is of courrse the v2 that is desired. However, optically there is not any particular reason for one to be intrinsically better. For some optical stacks, the v1 could actually be desired. In fact, Figure 1.13 had a 20 nm v1 AlO$_x$ dielectric on top of the Cr/Au 0.5/3 nm ARA, and displays a remarkable contrast.

Figure 2.48(a) are pictures of the v2 and v1. The v1 is easy to see by eye thanks to the absorption tail, while the v2 required a black background and adjusted grayscale as shown.

# 2.7 . Results: BALM optical response

## 2.7.1 . BALM stack normal incidence

In the previous section on the optical properties of Au and Cr, some aspects as to the mechanisms of BALM were addressed. The next step is to consider what is the basic optical reflectance response of a BALM stack. The anti-reflective absorbing (ARA) layer is at the heart, and thus it makes sense to first consider the reflectance and contrast curves as a function of gold thickness, and second as a function of optical wavelengths.

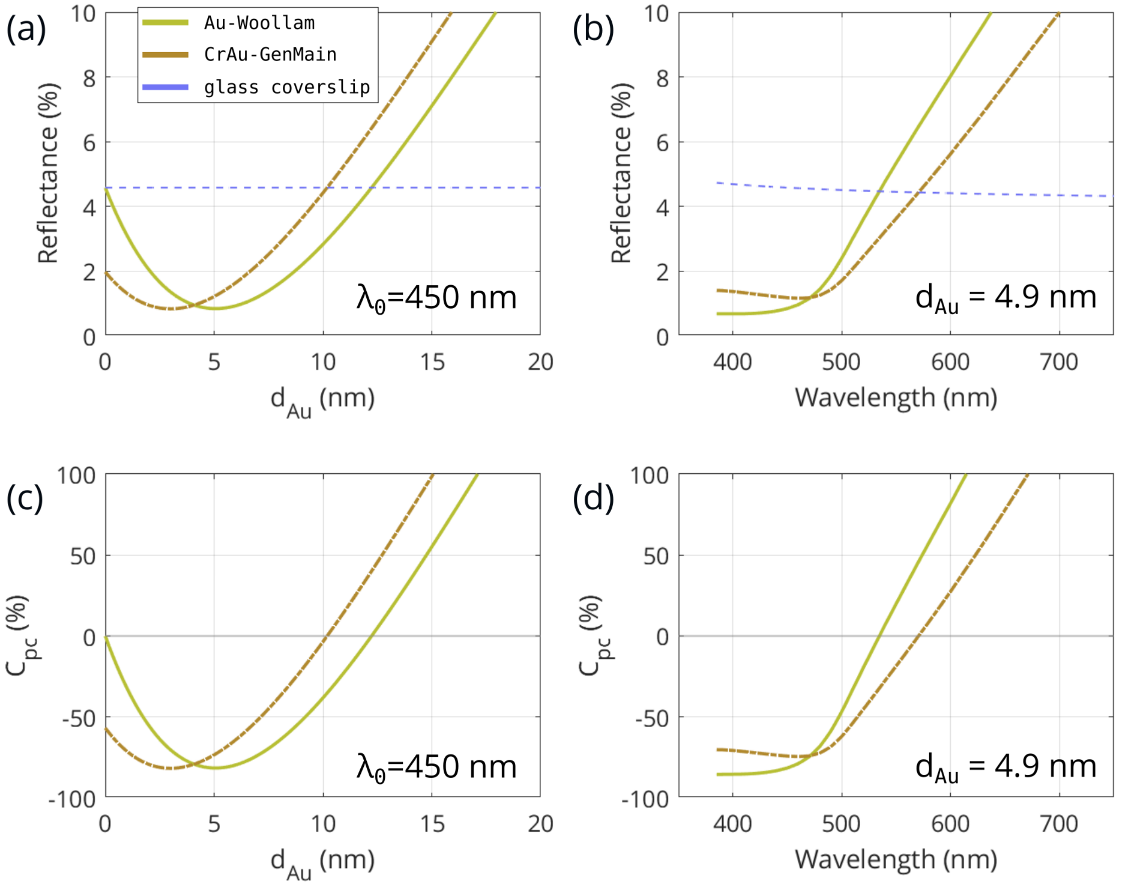

Figure 2.49: (a,c) Reflectance and percent change contrast of a BALM ARA layer at 450 nm normal incidence. The Au-Wollam case alone differs a bit from the CrAu-GenMain, the latter of which is in theory closer to reality. The trend is the same however, with a anti-reflection minima around 3–5 nm Au. (b,d) Reflectance and percent change contrast of ARA versus glass coverslip, as a function of wavelength, where Au thickness was set to 4.9 nm. This shows that blue wavelengths have more of an anti-reflection effect.

The results for normal incidence are shown in Figure 2.49. In (a) and (b) the reflectances are plotted, both using the "Au-Woollam" case (with 0 nm Cr), as well as using the "CrAu-

GenMain" parameters, meaning with 0.5 nm Cr and $\tilde{n}_{\text{Cr,new}}(\lambda)$ and Au Woollam dispersion on top. The bare glass coverslip reflectance is also shown. Corresponding percent change contrasts $C_{\text{pc}}$ of ARA versus glass coverslip are in (c) and (d). For the effect of $d_{\text{Au}}$ the wavelength is kept fixed at 450 nm. When the effect of wavelength is explored in (b) and (d) then the Au thickness is set to 4.9 nm, because it is a resasonable thickness as we shall see and also is the exact parameter used in the CrAu-GenMain fitting.

Upon inspection of the curves it is seen that the effect of the Cr is indeed significant and is playing a role in the resulting reflectance and contrast. Yet, the trends overall are similar of course and the Au is the center-piece here. We see that 5 nm thick Au seems to be a optimal choice for the "Au-Woollam" case while for the real stack it is closer to 3 nm. Yet, in general I use a nominal evaporation of 0.5/5 nm Cr/Au as it is a robust bilayer which is not too resistive which we found to be the case at times for 0.5/3 nm for example.

Regarding (b) and (d), it is seen that indeed towards the blue spectrum is more optimal as in fact theoretically the anti-reflective properties are not present beyond around 550 nm towards the red end of the spectrum. This again echos the notion of gold's anomalous reflectivity [190] in the blue wavelengths which has a less "metallic" response due to the interband transitions discussed earlier. Yet, this could be an issue if the gold's anti-reflection properties are desired in red wavelengths (which in fact is relevant for Chapter 3). One solution, discussed later on, is the addition of another coherent dielectric on top of the ARA layer.

Now, another point is that the optimal anti-reflection for the ARA layer is not necessarily always desired. If the goal is to attain optimal contrast of a particular sample $(\tilde{n}, d)$, then the resultant contrast depending on the sample thickness and RI will determine what the optimal conditions are. Furthermore, if sample's change in optical properties $(\Delta n, \Delta \kappa)$ (or change in thickness) are the suject of interest, the "static" optimal contrast is not the priority, but rather the optimal change in contrast ($\Delta C_{\text{pc}}$ or $R_{\text{pc}}$) with respect to a change in optical properties and/or thickness.

Having covered the basic "BALM curve", it is of interest to explore the $C_{\text{pc}}$ vs. $d_{\text{Au}}$ for the other dispersions outlined in Table 2.6, as well as for other wavelengths. The former is done in Figure 2.50(a), at 450 nm wavelength, for the cases "CrAu-GenMain", "CrAu-GenAlt", "Au-Woollam", "Au-TSF2011", "Au-Rakić DL", "Au-Rakić D". The first case of interest is to compare the Drude version of Rakić with the Drude-Lorentz version. We see that considering purely the Drude version does not result in anti-reflection behavior.

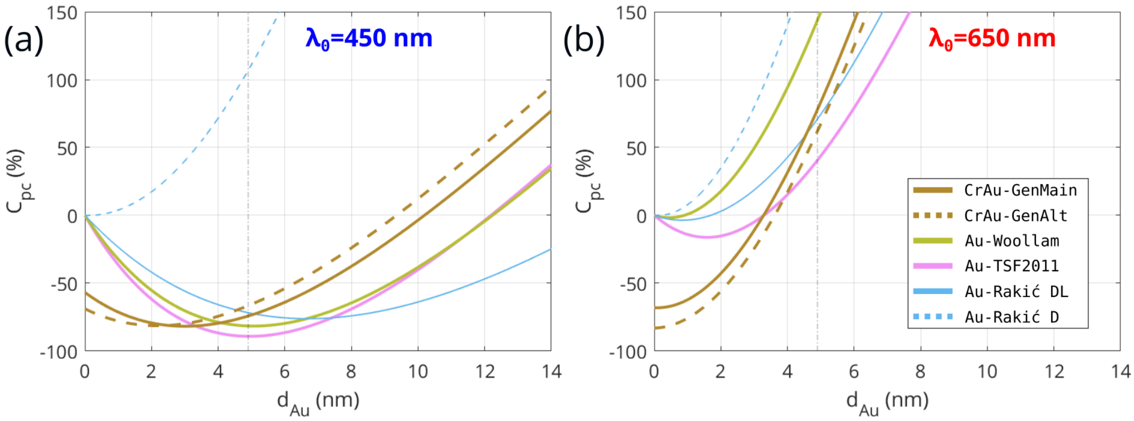

Figure 2.50: Percent change contrast versus Au thickness for various data sets, and at (a) 450 nm and (b) 650 nm incident wavelength.

Thus, it is not purely the metallic property of Au that is necessarily the secret ingredient to the BALM anti-reflection effect. In fact it is found that the interband transitions, that *together* with the Drude part play the critical role in resulting in the anti-reflection effect. This is the first time the Drude and DL parts of Au are separated out in this way to explain the physical origins of the BALM anti-reflection effect, and thus this result represents a contribution put forth by this thesis.

Next we see that the other various curves show some differences which, again as before differ significantly enough to be important. The DL model for instance predicts a minimum anti-reflection condition at around 7 nm while the measured system (CrAu-GenMain and Alt) predict 3 nm to be opimal. This is a significant difference. It is also reassuring to see that GenMain and GenAlt do not differ astronomically. A vertical line at 4.9 nm is included since this is essentially what was mostly used experimentally (see electronic version for better visibility). In the early part of the thesis however, 3 nm was explored for a bit as well.

Figure 2.50(b) is for the case of 650 nm wavelength. As expected from the BALM stack spectrum shown earlier of Figure 2.49(b), the anti-reflection effect is not quite as present at this wavelength, with the exception of the "Au-TSF2011" case. The "Gen" cases though imply that less than 4 nm actually would result in an anti-reflection condition in the red wavelengths.

and that what's happening with Au is that the interban d transp bring the real eps r closer to 1 faster than the plasma frequency can, and that is what contributes to the balm effect happenign at optical frequencies (blue).

## 2.7.2 . BALM: effect of angle

Having investigated the normal incidence cases, it is of relevance to see what the effect of angle would be, especially since theoretically with the NA$= 1.4$ oil immersion objective the range of angles should span 0°–67° with great weight placed on higher angles as was derived in section 2.2.4. To the author's knowledge, no extensive investigation as to the effect of angle on the BALM effect has been reported thus far, and thus these result consistute a contribution to the understanding of BALM.

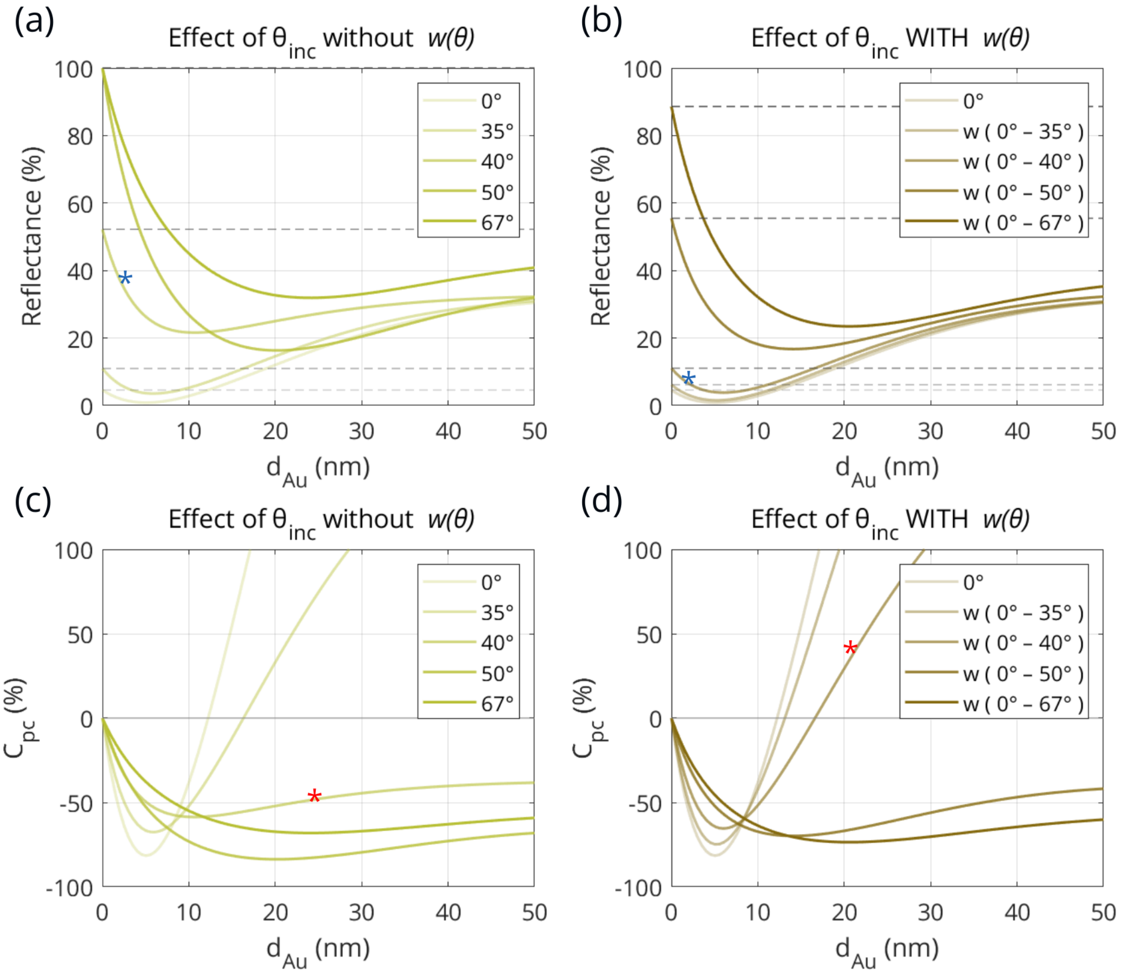

Figure 2.51: Effect of angle on the BALM reflectance curves (for the case $\lambda = 450$ nm). Note that 67° corresponds to $\theta_{\text{max}}$ of $\text{NA}_{\text{oil}}$=1.40. (a) Reflectance without weight function, computed as $R_{\text{ave}}(\theta) = \frac{1}{2}\left(R_s(\theta) + R_p(\theta)\right)$, and (b) reflectance with weight function $w(\theta)$. (b) and (d) are performed with the full weight function from 0° up to specified angle. The blue star helps the eye find corresponding curves from the left column.

The effects of $\theta_{\text{inc}}$ are shown in Figure 2.51, both without and with the weight function $w(\theta)$, where (a) and (b) show reflectance response while (c) and (d) show $C_{\text{pc}}$ response. It is useful to compare with and without weight function in order to see what is a result of the angle and what is a result of the weights.

The $\theta$ values included are 0°, 35°, 40°, 50°, 67°. The first general observation of (a) is that indeed the angle has a significant effect on resulting reflectances (as was the case with IRM in Figure 2.36). However again this is a result of Fresnel conditions and not anything particular to this BALM stack. Thus it is of use to consider the $C_{\text{pc}}$. Before doing so, it is worth noting the expected trend of the weight function in (b) "slowing down" the tendency towards ultra-high reflectance, which is due to the weights at lower angles, even though the weights are significantly higher at high angles still they will shift the curve to some extent.

In (d), which represents the "real" system in question, it is seen that for 0°, 35°, 40° the trend is similar to the one of normal incidence, showing an anti-reflection response from about 0–10 nm thickness. However, interestingly for 0°–50° and for full NA=1.4 i.e. 0°–67° it is theoretically the case that the anti-reflection behavior is preserved for a wide range of thickness including up to 50 nm even. When comparing with (d), it is interesting to study the 40° case (which is also labeled by the star "*"). We see that again the weights across all angles preserve the "normal BALM trend" more than the single angle. It shall be of interest to see how this compares with experimental data which is discussed later.

### 2.7.3 . BALM + $\text{AlO}_\text{x}$ reflectivity

At this stage the previously mentioned additional $\text{AlO}_\text{x}$ coherent layer and its potential utility is addressed. As a first step, the characteristic $C_{\text{pc}}$ BALM curve is simulated again, with three different thicknesses of $\text{AlO}_\text{x}$, including 20, 30, 40 nm. The case is considered for two wavelengths, 450 nm and 650 nm, the results of which are included respectively in (a) and (b) of Figure 2.52, for normal incidence.

In (a), it is seen that actually adding the $\text{AlO}_\text{x}$ reduces the anti-reflecting property, with the exception of the first 20 nm case which lowers it. However, at 650 nm, the added $\text{AlO}_\text{x}$ actually significantly improves the anti-refelctive property, where $C_{\text{pc}} \approx -100\%$ for the 40 nm case! This is an important result, because as mentioned before, the red end of optical spectrum is where the BALM anti-reflection effect was suffering. This will be of use in Chapter 3 where 650 nm wavelength must be used in order to do the charge density imaging. Results involving the $\text{AlO}_\text{x}$ contrast response are are also compared with experiment in a later section. The thicknesses 20, 30, 40 nm are shown in simulation because that is in the ballpark of what

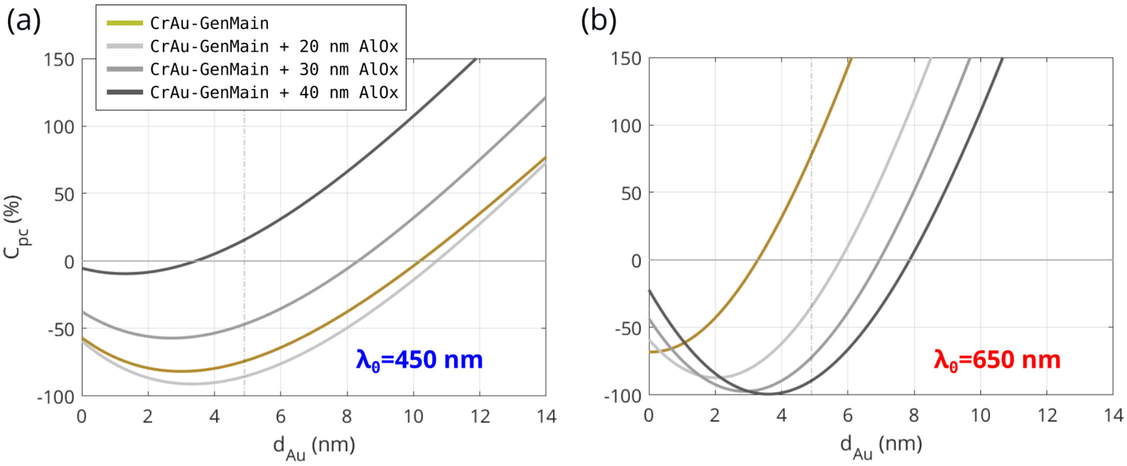

Figure 2.52: Effect of percent change contrast versus gold thickness, for an added layer of $AlO_x$ at thicknesses of 20, 30, 40 nm, in air, for (a) 450 nm and (b) 650 nm. The latter shows an improved anti-reflection effect while the former not for 30 and 40 nm.

practically we can grow in the lab.

## 2.7.4 . UV-Vis transmittance BALM stack

We acquired various UV-Vis transmittance spectra of coverslip/Cr/Au (ARA) as well as coverslip/$AlO_x$, as well as comparison via simulation using the $\tilde{n}(\lambda)$ measured by *OptMatLab*. This provided a cross-check on the ellipsometry data. In one experiment, 3 coverslips were prepared as shown in Figure 2.53(a), with varying Cr thickness of the ARA layer (Cr/Au). 5 nm of nominal thickness was evaporated for the gold while the underlying Cr layer was varied as 0.1, 0.5, 3 nm. The samples were characterized and led to the VASE ellipsometry fits of “CrAu-GenMain” and “CrAu-GenAlt” as are described in Table 2.6.

Data were acquired for the configuration shown in 2.53(b), where I built a stack using S. J. Byrnes TMM Python code [153] consisting of the incoherent coverslip, and the coherent Cr/Au layers. The data result and simulation result (using both CrAu-GenMain and CrAu-GenAlt) are shown in 2.53(c).

The match between data and simulation is quite good, and interestingly both “main” and “alt” versions match pretty well for this particular system. Still, their differences could be more pronounced in other optical stacks including the full BALM stack with $AlO_x$ and $MoS_2$ and thus the “main” version is used in the other simulations.

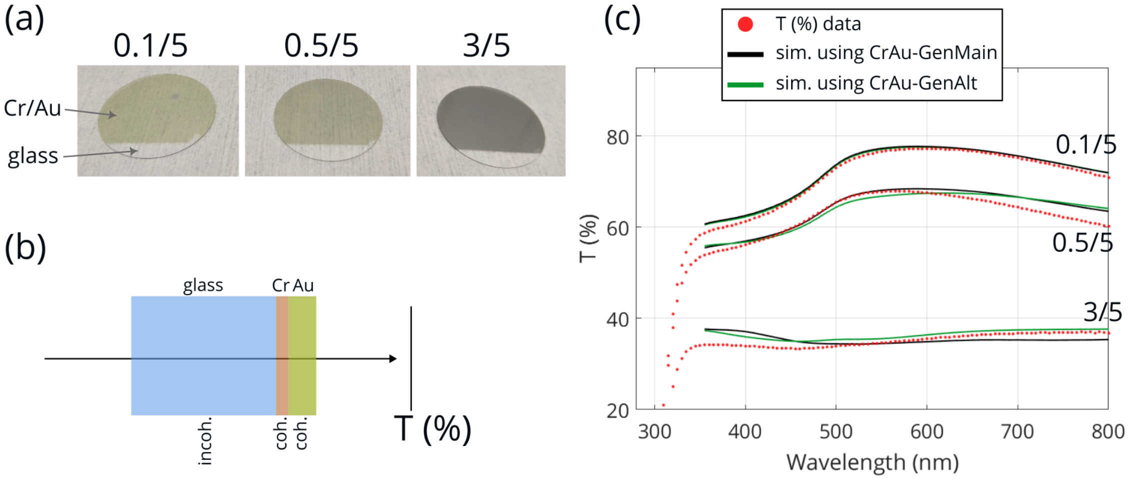

Figure 2.53: (a) Three coverslips with Cr/Au ARA layers consisting of 0.1/5, 0.5/5, 3/5 nm. (b) Transmittance spectroscopy configuration and stack used in simulation where the coverslip is an incoherent layer, with Cr and Au as coherent layers. (c) Resulting data, and fits using the CrAu parameters outlined in Table 2.6.

In Figure 2.54 data and simulations of the transmittance spectrum was again performed for both $AlO_x$ v1 and v2. The former is the version that was slightly conducting and absorbing and thus visible as seen in (a) right-side, while the improved v2 $AlO_x$ on the left-side is more transparent and completely insulating, requiring use of a dark background and adjusting the grayscale of the image.

The data and simulation are a little bit off although the trend is the same. This could be that the $AlO_x$ we produce does not have fully consistent optical parameters, varying slightly with each evaporation. It could also be that the thickness is not completely consistent. Although some $AlO_x$ step-heights were measured by AFM to confirm the thickness, not all could be measured. Overall though, the result is a good sign and mostly consistent with the ellipsometry data. A thicker $AlO_x$ in the 100s of nm would have been ideal to measure by transmittance spectroscopy because multiple undulations of the interference pattern would show up, instead of a single curve.

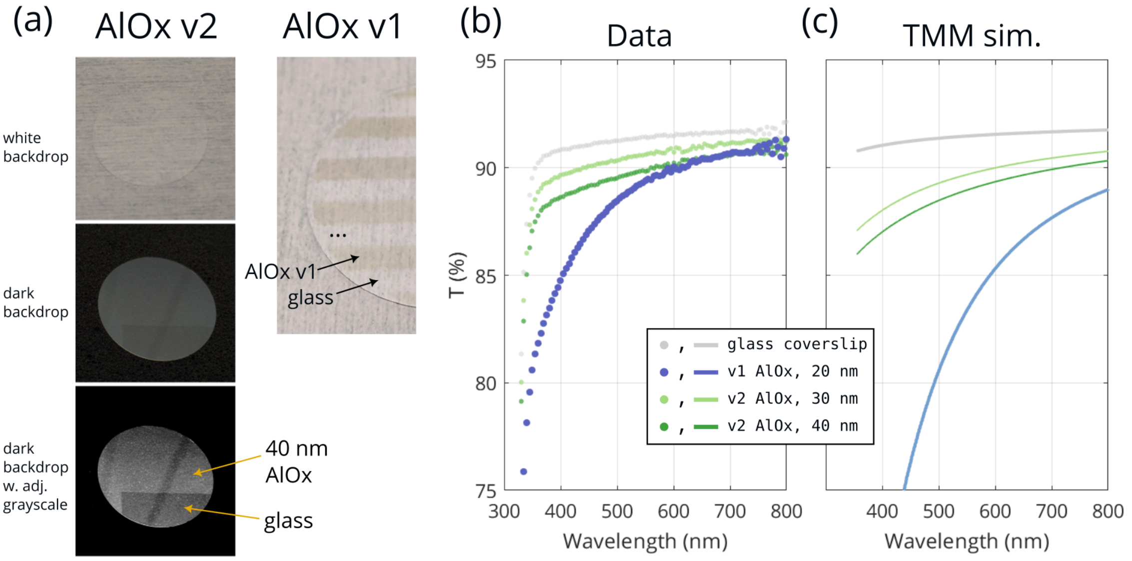

Figure 2.54: (a) Pictures of substrates with v2 and v1 $AlO_x$ vs. glass coverslip. The v2 is more faint since it is nice and transparent and insulating, requiring grayscale adjustment of the image to see it clearly. The v1 was more absorbing and conductive, and thus more easily visible. (b) Data and TMM simulation of transmittance spectrum. The data and theory match reasonably well, although the latter seems to overshoot a bit.

# 2.8 . Results: BALM of $MoS_2$

## 2.8.1 . $MoS_2$ on ARA

The first question to consider is whether there is any condition in which an ARA layer is helpful for improving contrast of $MoS_2$ vs. ARA. In this context it is also important to explore the effect of angle, which as discussed so far can have an important impact.

In Figure 2.55, the percent change contrast of 2D $MoS_2$ vs. ARA was simulated as a function of (a,c) wavelength (for 4.9 nm Au thickness) and (b,d) Au thickness (for 450 nm light), in air. In (a,b) the "Au-Woollam" is utilized for the ARA layer and in (c,d) the "CrAu-GenMain" is utilized for the ARA layer (see Table 2.6). Recall that the latter is in theory closer to the real system. For each plot, the weight function over a different range of angles is explored (recall section 2.2.4 for derivation and discussion). In theory the $0^\circ - 67^\circ$ weight (or $0^\circ - 50^\circ$ weight) should be close to reality since in general the aperture diaphragm (INA) was only slightly closed beyond the entrance pupil of the objective. However as previously discussed the off-alignment of optical elements as well as the non-uniformity of the bulb among other factors can change the result.

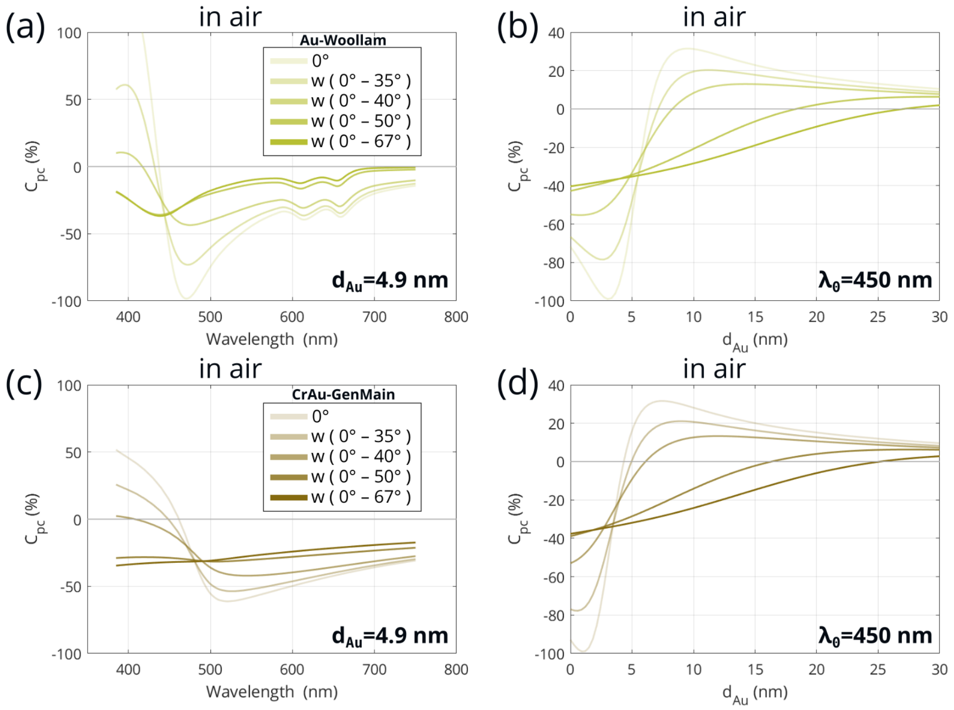

Figure 2.55: Simulated contrasts for 2D $MoS_2$ on top of a BALM ARA layer, all in air, with (a,c) being as a function of wavelength for Au thickness 4.9 nm while (b,d) are as a function of Au thickness for 450 nm light. In all cases the weight function of angles is computed as shown. Top row is using "Au-Woollam" model for ARA layer while bottom row is using "CrAu-GenMain" for the ARA layer.

Upon investigation of the plots, it is seen that first of all there is a significant difference between the use of Au-Woollam and CrAu-GenMain. This again highlights the importance of characterizing the ARA layer optical properties and thickness. It can be seen that at certain wavelength and thickness combinations, $MoS_2$ could be well contrasted, but the results are not very impressive.

In Figure 2.56 the same was done but with water at the final interface. Among various results it can be seen that for 450 nm, there appears to be a favorable condition at 450 nm wavelength, with about 2 or 3 nm of Au thickness.

Experimentally, one sample among others was imaged as reproduced in Figure 2.57, at 450 nm wavelength. This ARA thickness was about 0.5/3 nm, close to the favorable conditions described in the previous paragraph. Now, a number of observations can be made in this figure, which is quite ideal because the bottom half is the glass coverslip and thus an IRM image, while the top half is an ARA layer and thus a BALM image. First we see that the ARA layer is exhibiting the anti-reflection effect since it is darker than glass. This is expected. Then,

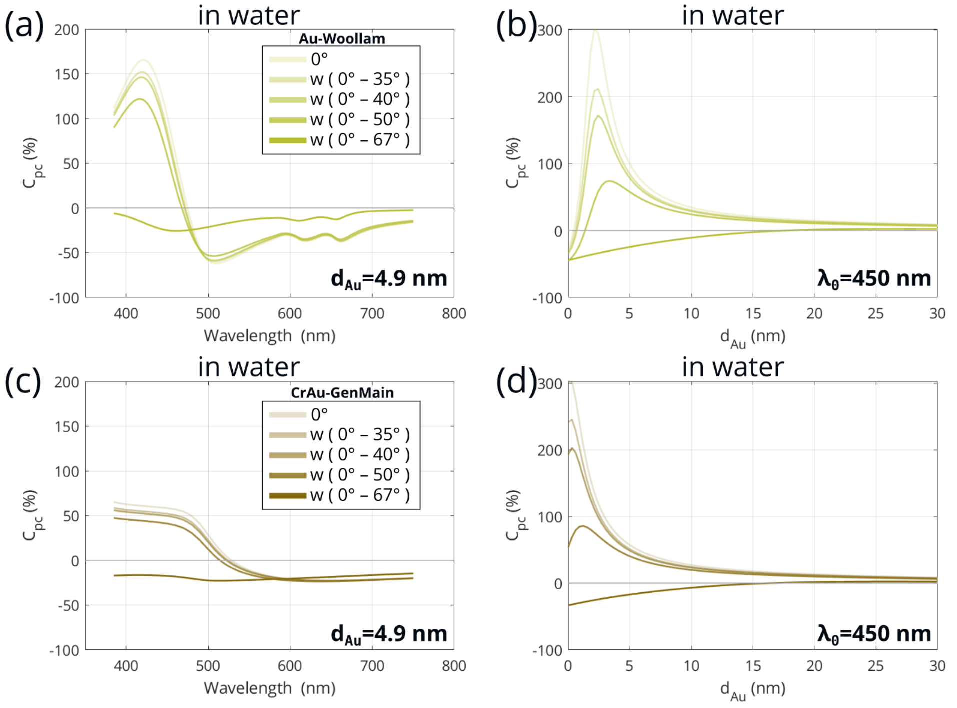

Figure 2.56: Same as Figure 2.55 but with water ($n_f = 1.33$) at the final interface instead of air.

we notice that in the IRM case the (negative) contrast is more favorable in air than in water. However for the ARA case, the $MoS_2$ has a much more favorable contrast in water, as was just discussed above.

The experimental contrast of $MoS_2$ vs. ARA in water is about 34% in the raw 0–255 grayscale image. As usual as with almost all grayscale images in the thesis, the grayscale was altered for better visibility. This actually changes the contrast, so in this case the contrast is improved to 135% in fact. However this is not any violation of physical laws and indeed some information is "lost" during such a transformation. Still, the post-grayscale adjustment step certainly dramatically improves the quality and visibility in many cases—as one would adjust any colorbar appropriately for a any given dataset.

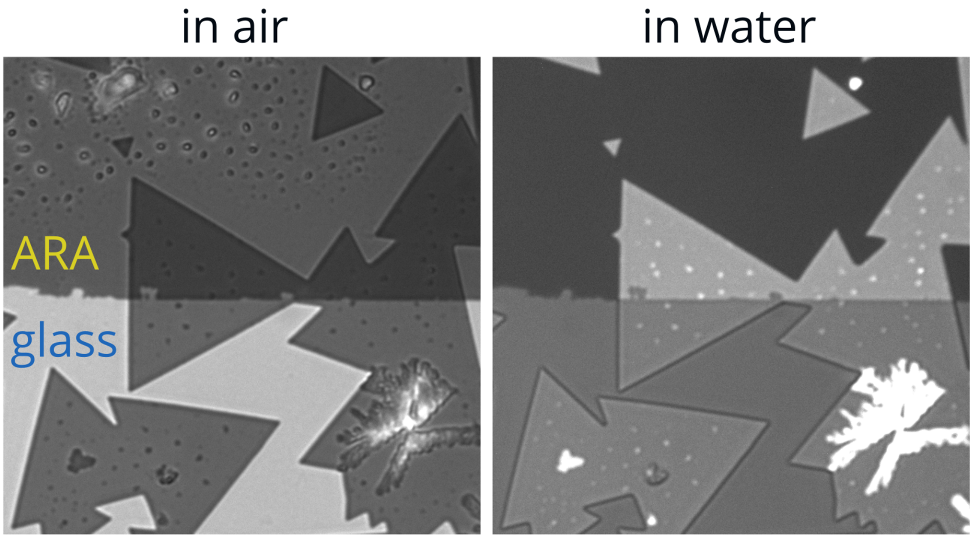

(34,113) (30,66)

Figure 2.57: Micrographs of 2D $MoS_2$ that were transferred on top of an interface of glass and a 0.5/3 nm Cr/Au ARA layer. Bottom half thus is an IRM image while top half is a BALM image. Both images are taken with a 450 nm bandpass, with left image in air and grayscale adjusted to 34–113, while right image is in water with grayscale adjusted to 30–66. The latter image results in improved BALM contrast while the former image is better suited for IRM contrast.

## 2.8.2 . $MoS_2$ on alumina/ARA

Although a deeper exploration of optical response of $MoS_2$ on a pure ARA layer could have been explored, the timeline and priorities of the thesis required a lot of $AlO_x$+ARA related work. As mentioned previously this system was especially important for the context of Chapter 3. This section is dedicated to contrast response of both $MoS_2$ on ARA/$AlO_x$ as well as the contrast response of just ARA on $AlO_x$.

A sample consisting of a nominal 0.5/5 nm Cr/Au ARA layer, with a nominal 40 nm $AlO_x$ layer was realized. 2D $MoS_2$ was transferred last. Micrographs were attained at 13 bandpass filters, with the source micrographs reproduced in Figure 2.58, including 3 square ROIs defined as shown.

It can be seen that the contrast is varying at the various optical wavelengths, both for the ARA layer itself as well as for the $MoS_2$. The ROI contrast results are summarized in Figure 2.59 together with simulations. (a,c) is the ARA vs. $AlO_x$+glass contrast spectrum while (b,d,) is the 2D $MoS_2$ vs. ARA+$AlO_x$+glass contrast spectrum. In the top (a,b) curves are computed for normal incidence at varying $AlO_x$ thickness as shown, with "CrAu-GenMain" used for the

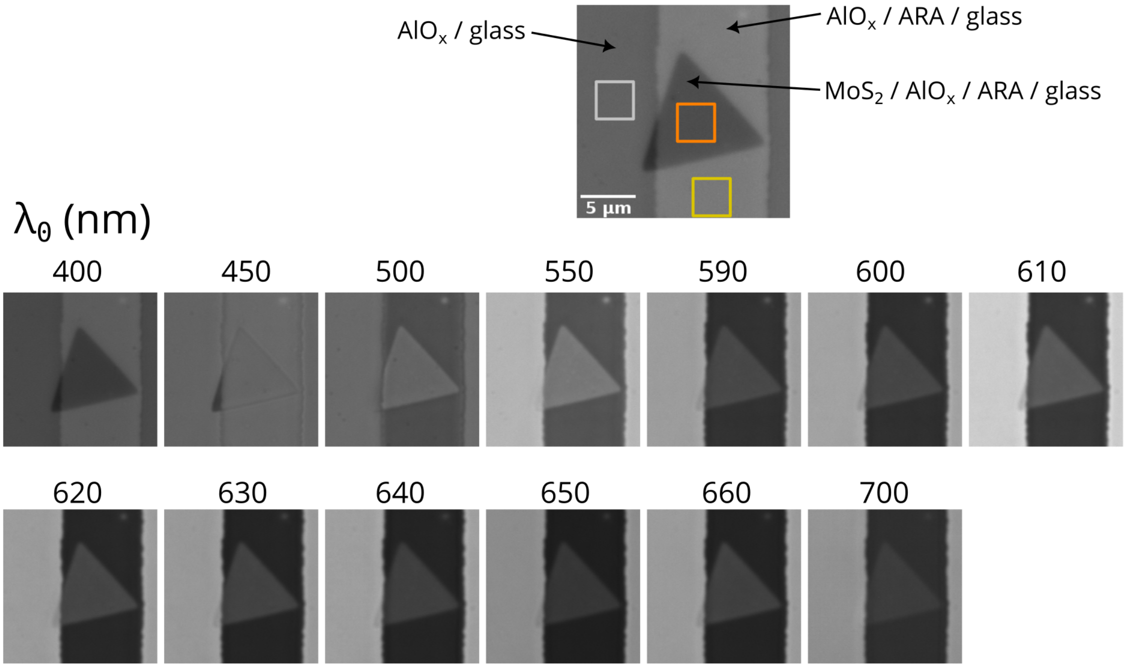

Figure 2.58: 2D MoS$_2$ flake sitting on nominal 40 nm AlO$_x$on Cr/Au ARA of 0.5/5 nm. Top: labeled micrograph and 3 ROIs defined. Bottom: 13 bandpass filter series with no grayscale adjustment (hence range 0–255).

ARA layer. The 30 nm case shows the most dramatic result, while 40 and 50 nm lessen the contrast in both cases. In (c,d) the angle weight function was used for the ranges shown.

In this particular case, it seems the 50 nm case with 0° – 35° range provides a reasonable fit for both the ARA and MoS$_2$ cases. This is quite off from the expected result. What seems to be clear is that some combination of thickness (or $\tilde{n}$) error together with effect of angle would explain the experimentally obtained result, in addition to possible noise of stray light rays. The simulated response is in some ways reproducing the correct trends, but still wildly off in some cases. This again is a testament to the complexity in the optical stack and of simulating the experimental conditions. This provides a start and further work would be needed to understand the experimental optical contrast response.

Now, considering the actual contrast values, it is seen that the 630 nm case resulted in the highest contrast, at $78.9 \pm 3.3$ % (or $\approx$ 79% as stated in the abstract). This was computed based on standard error propagation used for divided quantities, in the form $\delta C = \sqrt{(\delta m/m)^2 + (\delta s/s)^2}$. The raw 8-bit data in this case was $m = 66.223 \pm 1.318$ and $s = 37.016 \pm 0.974$. The resultant error bar is consistent with the previous discussion of error discussed in section 2.23. This is a high contrast, although the plot predicts that hundreds

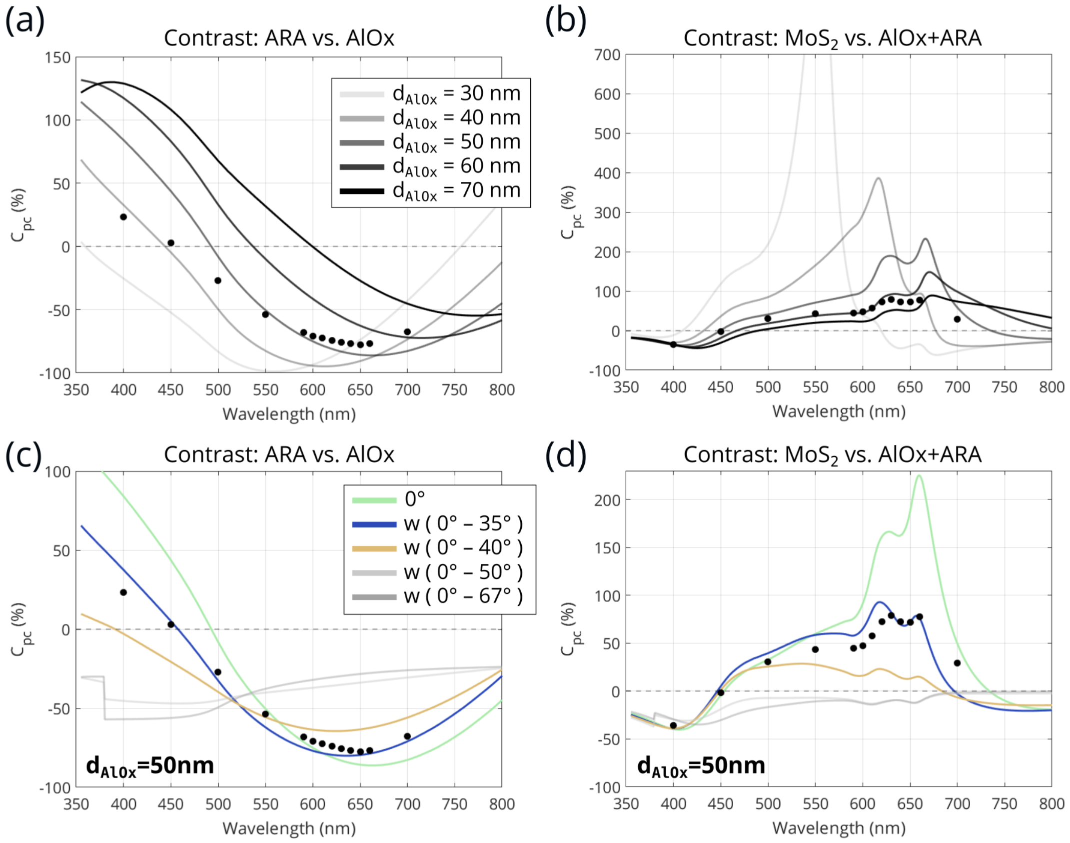

Figure 2.59: Data and simulation of contrast for (a,c) ARA vs. $AlO_x$ and (b,d) 2D $MoS_2$ vs. $AlO_x$+ARA. In (a,b) normal incidence is used, with varying $AlO_x$ thickness as shown. In (c,d) effect of weighted angles are shown, for the case of 50 nm $AlO_x$ thickness.

of percent contrast should be possible at some $d_{AlO_x}$ especially if the INA is lowered (this would lower the lateral resolution however). Further simulation would aid in find an even more resonant FP condition though at certain ARA and $AlO_x$ thicknesses and wavelength, even for high angles.

It could also be envisaged that the $AlO_x$ layer be evaporated on top of the 2D TMD. This would result in a differing optical response which could potentially be favorable and tuned for resonance. In addition, the $AlO_x$ could serve as a capping layer, protecting the 2D TMD from its environment. This was for example demonstrated in 2017 [209] for the case of ultra-thin black phosphorus and a 1 nm $AlO_x$ cap. Such a cap would also result in less degradation over time and pretect it from potential adsorption of ambient water and hydrocarbons as discussed in section 1.1.7.

This concludes Chapter 2, which began with background on optical microscopy techniques used to study 2D materials, followed by theory and background of IRM and BALM, and finally multiple sections of results of data and simulations were presented. In the results, $MoS_2$ was the main focus in the context of IRM and BALM, with some sections devoted exclusively to the BALM optical stack, and also to a few other 2D materials including bilayer systems. Various take-aways and perspectives are further detailed in the *Conclusions & perspectives* section at the end of the thesis.

# Chapter 3

# Charge density imaging of $MoS_2$ devices by IRM and BALM

This chapter begins with basic theory of charge accumulation in 2D semiconductors. Then, some background and principles of field-effect transistor (FET) devices are covered, including the case of 2D $MoS_2$ FETs. Then, conventional state of the art techniques for both static and *in operando* studies of 2D $MoS_2$ FETs are presented, especially the case of kelvin probe force microscopy (KPFM). This is followed by literature on studying charge density via optical systems, as well as the mechanisms behind the gate-tunable complex refractive index of 2D TMDs. After then introducing modulation depth definitions, the first Results section is presented.

The majority of the Results focus on IRM-mode liquid electrolyte gated capacitors and FETs of 2D $MoS_2$ that were realized experimentally. The work culiminated in an article which is under review at the time of this writing [210]. Electrical characterization and (macroscopic) transmittance spectra during gating are also covered. Following this, the final section is presented which consists of a preliminary study of BALM $MoS_2$ FETs in solid-state (dry) configuration. The thin Cr/Au ($\approx 0.5/5$ nm) anti-reflective absorbing (ARA) layer is used as a back-gate, with $AlO_x$ acting both as a dielectric and additional optical layer, the thicknesses of which can be tuned to acheive Fabry-Pérot (FP) resonance. It should be noted that the BALM FET system with its large number of process steps is very complex with a lot of failed samples along the way. Thus the BALM FET results are only preliminary and further work is needed to complete it.

# 3.1 . Background & theory

## 3.1.1 . Charge accumulation in 2D semiconductors

The density of states (DOS) of electrons in a semiconductor depends on its dimensionality, and takes the form [211]:

$$\begin{aligned}
\rho^{3\mathsf{D}}_{\mathsf{c,\ DOS}} &= \frac{1}{\sqrt{2}}\left(\frac{m_e^*}{\pi\hbar^2}\right)^{3/2}\sqrt{E_F - E_{\mathsf{c}}} \\
\rho^{2\mathsf{D}}_{\mathsf{c,\ DOS}} &= \left(\frac{m_e^*}{\pi\hbar^2}\right)\sigma(E_F - E_{\mathsf{c}}) \\
\rho^{1\mathsf{D}}_{\mathsf{c,\ DOS}} &= \left(\frac{m_e^*}{2\pi\hbar^2}\right)^{1/2}\frac{1}{\sqrt{E - E_{\mathsf{c}}}}
\end{aligned}$$

where $m_e^*$ is the effective electron mass, $E_F$ is the Fermi level, and $E_{\mathsf{c}}$ is the conduction band minimum (CBM). In the 2D case, $\sigma$ is a step function and thus $\sigma = 1$ for $E_F \geq E_{\mathsf{c}}$. Thus we can set it to 1 for further calculations.

The electron number density $n_e$ can be expressed as [212]:

$$n_e = \int_{E_c}^{\infty} \rho_{\mathsf{DOS}}(E) f_{\mathsf{FD}}(E) dE$$

where $f_{\mathsf{FD}}$ is the Fermi-Dirac statistical distribution which electrons follow since they are Fermions of half-integer spin 1/2. Solving this integral leads to [212]:

$$\boxed{n_e = \rho^{2\mathsf{D}}_{\mathsf{DOS}} k_B T \ln\left[1 + e^{-(E_{\mathsf{c}} - E_F)/(k_B T)}\right]}$$

and

$$\boxed{E_F - E_{\mathsf{c}} = k_B T \ln\left[e^{n_e/\left(\rho^{2\mathsf{D}}_{\mathsf{DOS}} k_B T\right)} - 1\right]}$$

We now have a relationship between $n_e$ and $E_F - E_{\mathsf{c}}$ for a 2D semiconductor. Now, a few points need to be made, before further discussing the nature of the relationship, which is plotted in Figure 3.1.

The units of $n_e$ as one would expect depend on the dimensionality. In 3D vs. 2D it is thus cm$^{-3}$ and cm$^{-2}$ respectively. Also, note that it is easy to convert to electron charge density $q_e$ where $q_e = n_e e$ where $e \approx 1.6 \times 10^{-19}$ C. Because of the simple conversion I use "charge density" to refer both to $n_e$ and $q_e$. To get a feeling for numbers, an $n_e$ of $10^{13}$ cm$^{-2}$ is on the high side and is in the regime of the ON-state of a 2D MoS$_2$ FET. This corresponds to

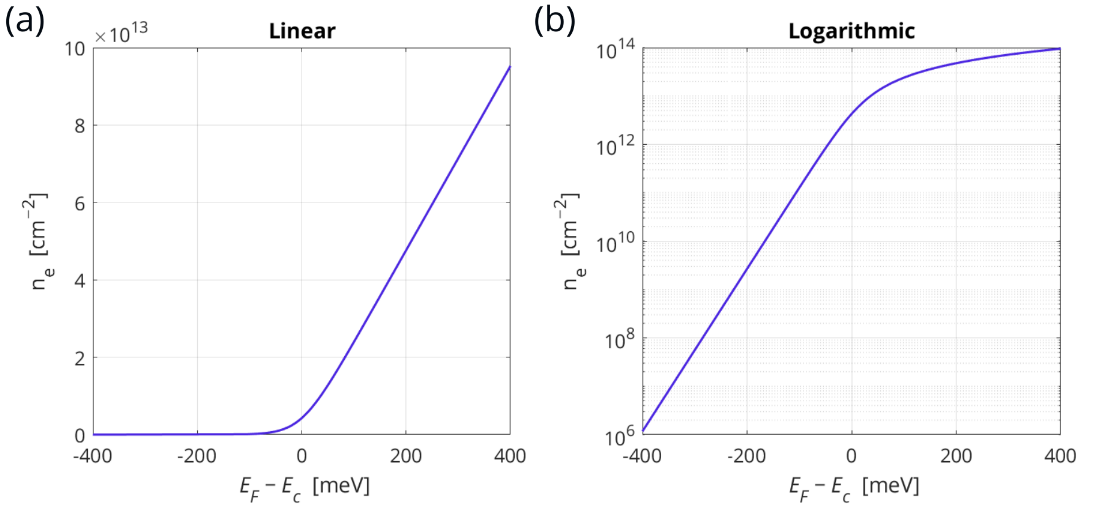

Figure 3.1: Relationship between $n_e$ and $E_F - E_c$ at room temperature $T = 300$ K in (a) linear scale and (b) log scale.

$q_e = 1.6$ µCcm$^{-2}$.

Now, regarding the relationship between $E_F$ and $n_e$, their non-trivial relationship in a 2D semiconductor is important. It is interesting to note that in graphene, which is a semi-metal, the relationship between the two is simply linear [213]. Not for 2D $MoS_2$ however.

The Fermi level $E_F$ is trivially related to the work function (WF), using relations between bandgap $E_g$, conduction band minimum $E_c$, valence band maximum $E_v$, electron affinity $\chi_e$ and vacuum energy $E_{\text{vac}}$. As discussed later, WF measurements by kelvin probe force microscopy (KPFM) is the conventional way to measure *in operando* (*in situ*) and *ex situ*. This will be an important point as to it means that in operando $MoS_2$ FET studies by KPFM has direct access to WF and not $n_e$ but relies on some theoretical model to attain $n_e$, while other techniques may or may not be more or less directly coupled with $n_e$.

Now, let us turn to how Fermi level (and $n_e$) can be tuned in a 2D semiconductor, via a capacitively coupled gate. Although FET devices and gating is discussed in the next section it is relevant to address certain additional points here first.

How does one accumulate charges in a semiconductor material? This can be acheived by constructing a capacitively coupled metal plate under or above the semiconductor separated by a dielectric/insulator. An electrical connection must be made to the metal plate and the semiconductor. For the latter, a metal is usually evaporated directly on top of the semiconductor, allowing an electrical connection to it (this introduces some challenges discussed later because it forms a so-called "Schottky barrier").

Once that is done, metal wires connected to the semiconductor and metal plate are connected to an external voltage source unit (VSU), from which "bias" is applied. By convention, the semiconductor is usually grounded, while the external bias, which is the "gate voltage" $V_{\mathsf{GS}}$ in this case, is applied on the metal plate. This means that a $V_{\mathsf{GS}}$ above the threshold voltage ( $V_{\mathsf{TH}}$) discussed in a moment, will cause electrons to accumulate in the semiconductor, whilst a voltage $V_{\mathsf{GS}} < V_{\mathsf{TH}}$ below threshold will cause electrons to be depleted.

An important quantity in the system is the capacitance of the dielectric (often called "oxide" even if it is a non-oxide dielectric), which takes the form $C_{\mathsf{ox}} = \frac{\varepsilon_s \varepsilon_0 A}{d_{\mathsf{ox}}}$ where $\varepsilon_s$ is the static dielectric constant so $\varepsilon_s = \varepsilon_r(\omega \approx 0)$, $\varepsilon_0$ is the free space permittivity, $A$ is area and $d_{\mathsf{ox}}$ is the thickness of the oxide. In general though, it is more useful to consider capacitance per unit area, which often is denoted by the lowercase where $c_{\mathsf{ox}} = \frac{C_{\mathsf{ox}}}{A} = \frac{\varepsilon_s \varepsilon_0}{d_{\mathsf{ox}}}$ (it is usually clear from the context whether it is per unit area or not). Now, in fact there exists a simple relation between $n_e$ and $V_{\mathsf{GS}}$ which is:

$$n_e = c_{\mathsf{ox}} \left( V_{\mathsf{GS}} - V_{\mathsf{TH}} \right) / e$$

This is sometimes denoted $n_{\mathsf{ox}}$ because it is $n_e$ when considering the oxide capacitance as being the sole or at least primary contribution to the capacitance. There is in fact another capacitance that can play a role in low- dimensional materials: the quantum capacitance (or chemical capacitance), $c_{\mathsf{q}}$. When one plate of a capacitor has a limited density of states, this can alter the possibility for the gate to freely accumulate an arbitrary charge density through the simple relation above. In place, the total capacitance corresponds to two contributions, $c_{\mathsf{ox}}$ and $c_{\mathsf{q}}$, in series, so that the smallest of both dominates. $c_{\mathsf{q}}$ is strongly potential-dependent and would have a significant impact in the deep OFF state where its value is very low. Conversely, $c_{\mathsf{q}}$ is high in the ON-state and its impact there remains limited up to relatively high electron densities. A particularly thorough discussion of the impact of $c_{\mathsf{q}}$ in 2D TMD FET can be found in [212]. In this thesis, XRM proves to be mostly interesting to observe the ON state of FETs and thus the effect of $c_{\mathsf{q}}$ was ignored. Yet, in the future it would be of interest to take $c_{\mathsf{q}}$ into account and determine whether it plays a significant role in these specific systems, especially in the sub-threshold regime.

### 3.1.2 . FET devices

Before covering the basics of FET devices in general and the case of a 2D TMD FET device, I shall cover some history on the matter. The first 2D $MoS_2$ FET, to the author's knowledge, was realized in 2005, shown in the previously mentioned PNAS paper [1], however only a limited part of the transfer characteristic was measured. The 2010 Heinz group paper mentioned earlier [16] includes a transfer characteristic over a broader voltage range, which shows clearly that the 2D $MoS_2$ is behaving $n$-type. In 2011, the group of Andras Kis published data of a high-performing 2D $MoS_2$ FET [15]. In the work, a bottom and top gated device was realized using $HfO_2$ as a high-$\kappa$ dielectric ("$\kappa$" here refers to the static permittivity $\varepsilon_s$). The device performance was shown to be promising and exhibiting high mobility (although possibly not as high as claimed, as elucidated by a *Comment* [214] and *Reply* [215].) A. Kis claims they made the "first monolayer $MoS_2$ transistor" [216].

Since then, a lot of work has been done to investigate its device physics and improve performance. In fact, 2D semiconductors may be used in future semiconductor nodes, as indicated by the involvement and interest of major semiconductor companies such as TSMC [18] and Samsung Electronics [19]. 2D semiconductors are strong candidates for a list of reasons. One of the main advantages is the capability for high gating efficiency and thus great electrostatic control of the channel. Historically, in silicon technologies, one of the leaps following optimization of the gate dielectric, was the introduction of FinFETs. In this geometry, silicon fins were realized which improved gating efficiency. Another development was silicon-on-insulator technology to reduce body effects, again for improved electrostatic control. However thinning of silicon has limitations, and thus a 2D 3-atom or 1-atom thick semiconductor would have an optimally scaled channel thickness.

Let us now turn to some basic aspects of field-effect transistor (FET) devices and how they work. They are essentially variable resistors which are controlled by a third voltage called the "Gate". The two leads of the resistor are the "Source" and "Drain". The source is grounded while the drain is the point where the positive voltage is applied (for $n$-type FETs). The source lead is the "source of electrons" which then "fall down the drain", hence the terminology.

The physical mechanism is that the electric field created by the gate voltage (across the gate dielectric) is what turns the resistor more "ON" or "OFF", hence the term "field-effect". The active part of the device is thus the resistor (called the "channel"), which is made of a

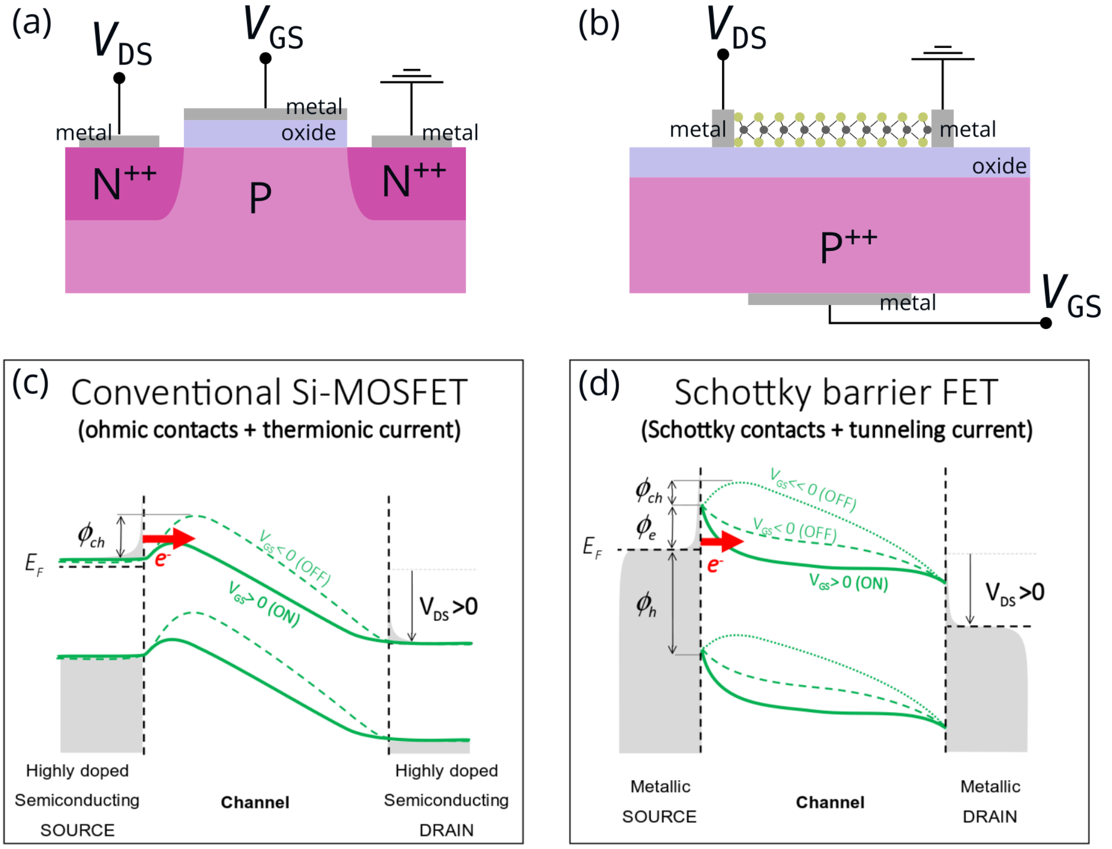

Figure 3.2: (a) Conventional N-type silicon MOSFET and (c) associated band diagram and behavior. (b) Typical N-type 2D $MoS_2$ FET which is a type of Schottky FET, with associated (d) band diagram and behavior.

semiconductor material. The presence of the field has the effect of *bending* the energy bands of the semiconductor. Equivalently, the bands can be thought of as static, with instead the Fermi level being the one *bending*. I shall use the latter version mostly throughout the text.

In general, if the Fermi level is close to the conduction band (at $V_{\text{GS}} = 0$), the channel behaves as $n$-type (*n*egative carriers), while if it is close to the conduction band, it is $p$-type (*p*ositive carriers). FETs can be constructed to operate either in "accumulation mode" or "depletion mode" or "inversion". In accumulation mode, the gate voltage is used to accumulate charge carriers, while in depletion mode, the gate voltage is used to deplete the channel of charge carriers. Inversion is when the gate voltage is applied such that the carrier opposite the type of the channel is made to accumulate (for example, if the channel is $p$-type, then $n$-type carriers are made to accumulate). This mode requires strong band bending, but is in fact very common for silicon-based FETs.

A conventional silicon metal-oxide-semiconductor field-effect transistor (MOSFET) is shown in

Figure 3.2(a). The "MOS" refers to the vertical stack of metal, oxide, semiconductor seen below the gate lead $V_{\text{GS}}$. (Note that the insulator between gate and semiconductor does not have to be an oxide. For this reason, the alternative name "MISFET" is sometimes used.) The depicted MOSFET operates in inversion. The substrate is $p$-doped, which is acheived done by diffusing atoms of one less valence electron than silicon, like boron. (For $n$-doping one can diffuse phosphorus.) Since the channel is $p$-doped, one might imagine that a hole current can be made to flow from source to drain (and further amplified by applying $V_{\text{GS}} < 0$) but no, because the shown highly degenerately doped $n^{++}$ silicon on each source and drain side results in an energy barrier (PN junctions). This is by design. The barrier is in fact further raised with $V_{\text{GS}} < 0$. For $V_{\text{GS}} > 0$ the Fermi level gets raised and raised until inversion of the channel so that $n$-type carriers (electrons) can flow (and the barrier between the formed $n$ channel and $n^{++}$ is thus low). This design results in a very high ON-OFF ratio of the source–drain current $I_{\text{D}}$. Another point is regarding the metal/$n^{++}$ junction on each of the source and drain sides. MOSFETs are highly engineered to attain a ohmic behavior at the contact.

Now let us consider the device in Figure 3.2(b) which is a typical geometry for a 2D TMD FET. $p^{++}$ silicon is used as the back-gate, chosen as such because this degenerately doped silicon is very conductive, almost like a metal. On top is a thermally grown $\text{SiO}_2$ oxide, with the 2D TMD on the surface. Drain and source are contacted using lithography and evaporating metals.

This geometry is usually called the "thin film transistor" geometry. If 2D $\text{MoS}_2$ is used as the channel, which is $n$-type, then a positive $V_{\text{GS}}$ turns it more ON (accumulating electrons) while a negative $V_{\text{GS}}$ turns it more OFF (depleting the channel of electrons). The behavior described in the previous paragraph is represented schematically in Figure 3.3(a) (where I partly used the results from [15]). Since as mentioned this "variable resistor" is being made more or less resistive, it can be said to be in an "OFF" state when $I_{\text{D}}$ is low while in an "ON" state when $I_{\text{D}}$ is high.

The sweep of $I_{\text{D}}(V_{\text{GS}})$ is called the "transfer characteristic". This term is linked with "transconductance" which is defined as $g_m \equiv \frac{\text{d}I_{\text{D}}}{\text{d}V_{\text{GS}}}$ (also called "mutual conductance" hence the subscript "$m$") which is at the heart of a transistor device. A high transconductance means a large gain in terms of being able to switch from a lower to higher $I_{\text{D}}$ with a smaller change in $V_{\text{GS}}$. It has the same units of condutance and is reported in milli-Siemens (mS). Since a gate can so significantly alter current, the transfer characteristic is often reported in both linear scale as in 3.3(a) and log

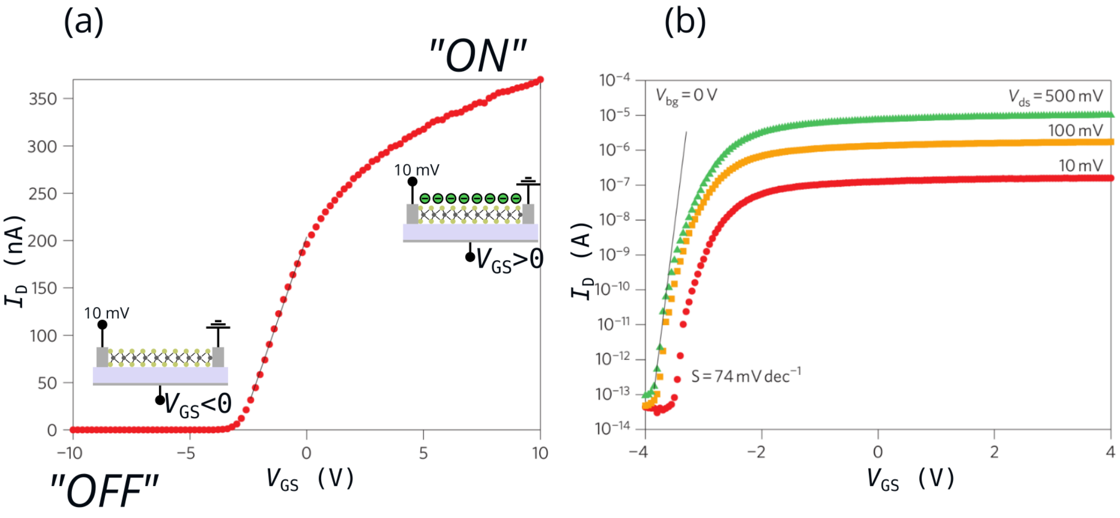

Figure 3.3: From [15], with added labels and drawings to illustrate working principle of $n$-type 2D MoS$_2$ FET. In (a) is the linear transfer characteristic, where a negative $V_{\mathrm{GS}}$ results in depleting the channel of electrons hence turning the device more "OFF", while a positive $V_{\mathrm{GS}}$ accumulates electrons in the channel, turning it more "ON". (b) is a log-scale transfer characteristic from [15] during top-gating, where the sub-threshold slope was found to be 74 mV/dec.

scale, which was reproduced in 3.3(b) also from [15]. In this particular case a so-called ON-OFF ratio of $\sim 10^8$ was acheieved since the off-state current is $\sim 10^{-13}$ A while the on-state current is $\sim 10^{-5}$ A.

While the $g_m$ slope is used in the linear scale and typically reported right about threshold ($V_{\mathrm{TH}}$), another relvant quantity is the **sub-threshold slope**, which is the slope ($S \equiv \frac{\mathrm{d}V_{\mathrm{GS}}}{\mathrm{d}I_{\mathrm{D}}}$) in log scale in the sub-threshold region towards the deep OFF state, in units milli-Volts per decade (mV/dec). In the example of Figure 3.3(b), $S = 74$ mV/dec was found by the linear fit shown in the sub-threshold region. Finally there is also the $I_{\mathrm{D}}(V_{\mathrm{DS}})$ sweep which is called the "output characteristic". This sweep among other things reveals the nature of the contacts, whether they are ohmic or exhibit Schottky diode behavior.

Now, a few considerations related to band diagrams and related topics are covered. Consider Figure 3.2(c). Here, the gate-controlled charge modulation along the channel leads to the modulation of the potential barrier $\phi_{\mathrm{ch}}$ within the silicon channel. This barrier thus controls the current flow. TMD-based transistors have transfer and output characteristics ($I_{\mathrm{D}}(V_{\mathrm{GS}})$ and $I_{\mathrm{D}}(V_{\mathrm{DS}})$) that bear similarities with those of Si-MOSFETs. Their operation principle is however different.

The TMD transistors studied in this thesis are Schottky-barrier transistors. As can be seen in Figure 3.2(d), at positive gate bias, electrons are similarly accumulated in the channel as for conventional MOSFETs but electrons from the source need to tunnel through the Schottky barrier (of height $\phi_e$) at the metal/semiconductor interface to enter the channel, which degrade the performances. At moderate negative gate bias, the width (not height) of the Schottky barrier increases which blocks electron injection at the source and thus turns the device OFF. A small residual current can still flow: the one that is thermally activated above the barrier. At more negative gate bias, an additional barrier $\phi_{\text{ch}}$ in the channel is formed, which reduces the OFF-state current even further.

It is important to note that if the Schottky barrier height is high (which is the case when no special care is taken in the engineering of the metal-TMD contact), $\phi_e$ alone is sufficient to bring the OFF-state current to the detection limit of our equipment. It is safe to assume, that our gold-connected $MoS_2$ FETs are operated in a regime where both the ON and OFF states are limited by tunneling through $\phi_e$.

The origin and nature of Schottky barrier height (SBH) in typical 2D TMD FETs including 2D $MoS_2$ FETs are to some degree understood although results and analysis vary in the literature. There are three main considerations. The "intuitive" picture is that the barrier is related to the difference between metal work function with the semiconductor valence or conduction band energy, the former if hole injection is desired and the latter for electron injection. Schulman et al. [217] suggest this picture, plotting a linearly correlated SBH to metal WF. Other groups such as Kim et al. [218] found the so-called Fermi level pinning as the main mechanism, meaning that states are pinned due to interfacial effects no matter what metal work function is used. Finally there is the aspect of the nature of how the metal is deposited as explained by Liu et al. [219] among others. All in all SBH engineering and research in 2D semiconductors is a hot topic and of central importance.

### 3.1.3 . Capacitor based devices

Aside from FETs, capacitor geometries consisting of just source and gate are widely used in many types of devices. 2D TMDs have found themselves the subject of many such studies. Thus they are covered here because charge density imaging for capacitive devices has very high relevance.

Electro-optic modulators (EOM) are an instance where capacitive geometry is used. EOMs are devices that allow modulation of intensity or phase of a light beam via an electrical input.

The most commonly deployed today are based on lithium niobate [25] and are at the heart of fast data transfer speeds in fiber optic networks. 2D TMDs have emerged as candidates for EOM [24], in part due to their impressive attainable modulation depths, where by the real and imaginary parts of their refractive index can be tuned by 200% in some cases [220], with 6 dB of modulation demonstrated in some configurations [170].

Redox electrodes in electrochemistry also use a capacitive geometry, whereby TMDs have been demonstrated as strong candidates for some types of reactions [44, 43].

Other capacitve devices have been used for tunable lenses [6] and beam-steering [26] and tunable mirror [5].

### 3.1.4 . State of the art: Charge density imaging via scanning probe microscopies

An important aspect of understanding the functioning and operation of FETs is the channel voltage profile, $V_{\text{ch}}(x)$, and its evolution upon applied drain and gate voltages [221, pp. 212–213][222]. The profile can be measured experimentally by kelvin probe force microscopy (KPFM), which has an AFM-like scanning probe tip that measures work function (WF) at each point (instead of or in addition to height topography).

Various groups have performed *in operando* measurements of WF for $\text{MoS}_2$ FETs upon application of drain and gate voltages, which is discussed below. It is also possible to measure the surface current profile (SCP) by conductive AFM (C-AFM) and microwave impedance microscopy (MIM). Finally scanning gate microscopy (SGM) can be used to locally gate the channel and study its effects.

#### KPFM: static

The principle behind KPFM is to apply a voltage at the tip that nullifies the potential of the surface WF. Thus one attains the so-called contact potential difference (CPD) or $V_{\text{CPD}}$ which is the raw signal. To get the absolute WF one must calibrate to a known metal WF like Au. Often groups report simply the $V_{\text{CPD}}$ especially if the main interest are changes in WF as opposed to exact WF values. Since the early days of KPFM various improvements have been made and in fact the working principle is a bit more complex, consisting of both dc and ac voltages and use of lock-in amplifiers to improve sensitivity to WF changes [224]. A simplified schematic of the

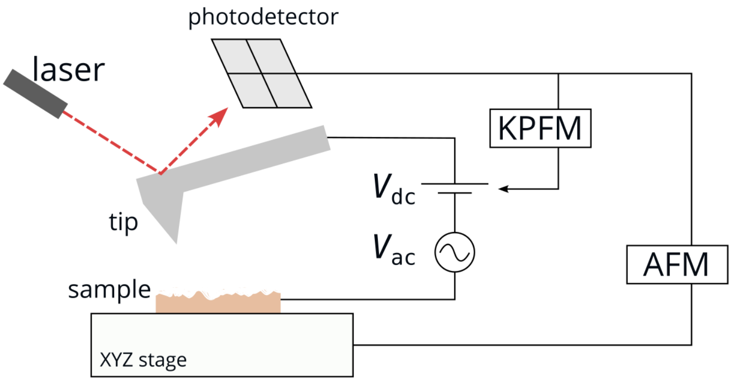

Figure 3.4: Schematic of kelvin probe force microscope (KPFM) which measures work function (WF) profile $\varphi(x, y)$. Many setups such as this one can also perform atomic force microscope (AFM) images in addition to WF. (Diagram inspired by [223].)

setup is illustrated in Figure 3.4.

A lot of useful information can be attained by performing KPFM scans of 2D TMDs in a "static" configuration, i.e. not in an operating device configuration (*in operando*). For instance a 2013 paper [226] studied how trapped charges in commonly used substrates for 2D materials ($SiO_2$ and hBN) would act as substrate-induced doping. The authors converted WF to 2D charge densities of the surface, estimating that for $SiO_2$, trapped charges result in electron densities varying from $0.24$ to $2.7 \times 10^{11}$ cm$^{-2}$.

The effect of trapped charges in the substrate is highly significant and a lot of work has focused on studying the effect it has on various 2D materials. For instance, for a given 2D TMD, the trapped charges effectively are applying a "gate" and has the effect of shifting the threshold voltage $V_{\text{TH}}$ of a 2D TMD FET, even before any external $V_{\text{GS}}$ has been applied.

The WF of a TMD depends on a number of factors, including the substrate, the number of layers, the stacking order, the ambient conditions (temperature, pressure), the presence of any adsorbates or absorbates, and others. Performing an anneal can also change WF. Some of these effects are beautifully demonstrated in a 2017 conference paper [225]. Some of the results have been reproduced in Figure 3.5. In (a), an AFM and KPFM image are shown side-by-side. Various observations can be made: it is seen that grain boundaries have a different WF from the monolayer, the bilayers also have a different WF, and other layers show variations in WF even though the topography is the same. In (b), the group show the effect of annealing before and after.

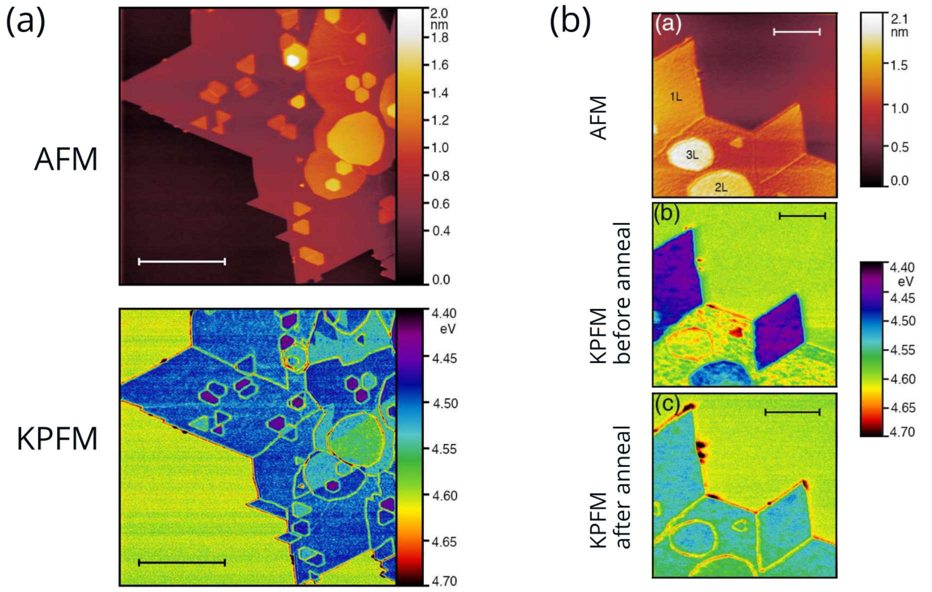

Figure 3.5: Reproduced from [225]. (a) AFM and KPFM of a CVD-grown $MoS_2$ consisting of mono-, bi- and multi-layers, grain boundaries and other topographies. (b) AFM and KPFM of CVD $MoS_2$ before and after annealing in vacuum.

Varying the CVD growth conditions can also have an effect on the WF landscape. This was shown for example in Senkić et al. 2023 [55], with two of the KPFM images reproduced in Figure 3.6, for the growth temperatures (a) 800°C and (b) 900°C. In both cases, various inhomogeneities can be seen both inside the flake and in particular a differing WF near the edges.

Finally there is a range of literature of KPFM based modalities where modifications are made for specialized or improved data acquisition. One such mode was used in a study published in 2023 by A. Arrighi et al. 2023 [228] of which I am a co-author. In this work, CVD $MoS_2$ grown at LICSEN was investigated. A mode was developed where KPFM data was free of electrostatic force contribution. The paper provides some insights on topographic and work function inhomogeneities of CVD grown $MoS_2$.

## KPFM: *in operando*

Although the static KPFM is useful in many ways, it takes to acquire *in operando* KPFM data to understand how the gate and drain in a FET impact WF in the channel, among other aspects of device physics. An early paper on this topic is from 2013 for a bilayer $MoS_2$ FET [229]. The group of Yossi Rosenwaks has published a number of papers on *in operando* KPFM of $MoS_2$

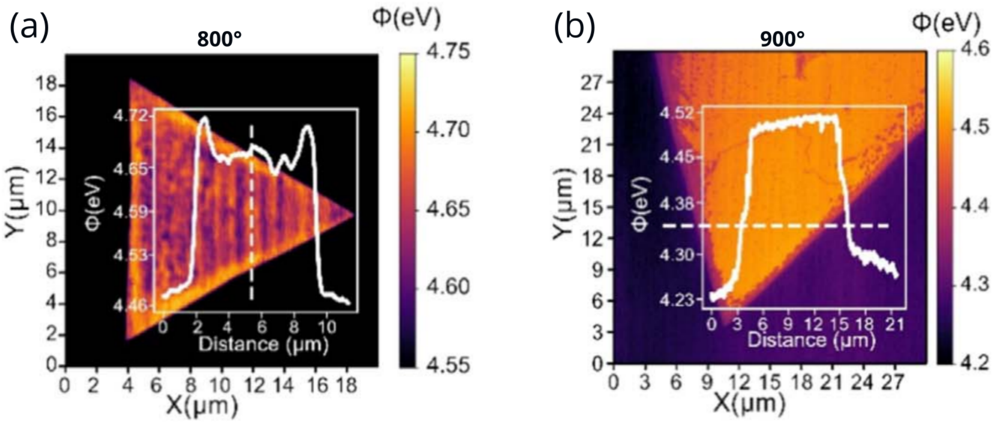

Figure 3.6: From Senkić et al. 2023 [227]. KPFM images of CVD 2D $MoS_2$ flakes grown at (a) 800°C and (b) 900°C. Various inhomogeneities in the work function are seen, including within the flake but also a clear trend of edge effect as well.

FETs.

In Dagan et al. 2019 (Rosenwaks group) [230], the WF difference ($V_{\text{CPD}}$) was acquired *in operando* for a monolayer exfoliated $MoS_2$ FET (and for a range of multi-layers). The results are reproduced in Figure 3.7(a), where in this case it is quite clean and linear from drain to source, with a drain-dependent Schottky barrier height on both the drain and source side. In the paper they also are able to estimate the layer-dependent variation in charge density. For a monolayer they found a variation of 1.2 to 2.3 $\times 10^{12}$ cm$^{-2}$.

In Vaknin et al. (Rosenwaks group) 2020 [231], the group explores how Schottky barrier height on the source side of an $MoS_2$ FET is lowered by an "image force", which they are able to quantitatively estimate using a model. Other studies by this group exploring in operando $MoS_2$ FETs are found in [233, 234, 235]. In these Rosenwaks papers the profiles are mostly clean.

Matković et al. 2020 [232] studied 1-dimensional profiles of $MoS_2$ FET *in operando*. Among various aspects of this work, the effect of a channel containing wrinkles is studied. These wrinkles introduce resistances, this is reproduced from their paper in Figure 3.7(c) where both AFM and KPFM profile is shown in the same plot. In (d) the group shows a channel without wrinkles.

Regarding acquisition of $(x, y)$ *in operando* $MoS_2$ FET KPFM images, the literature is relatively limited. The 2013 paper mentioned earlier though [229] shows nice $(x, y)$ images, as reproduced

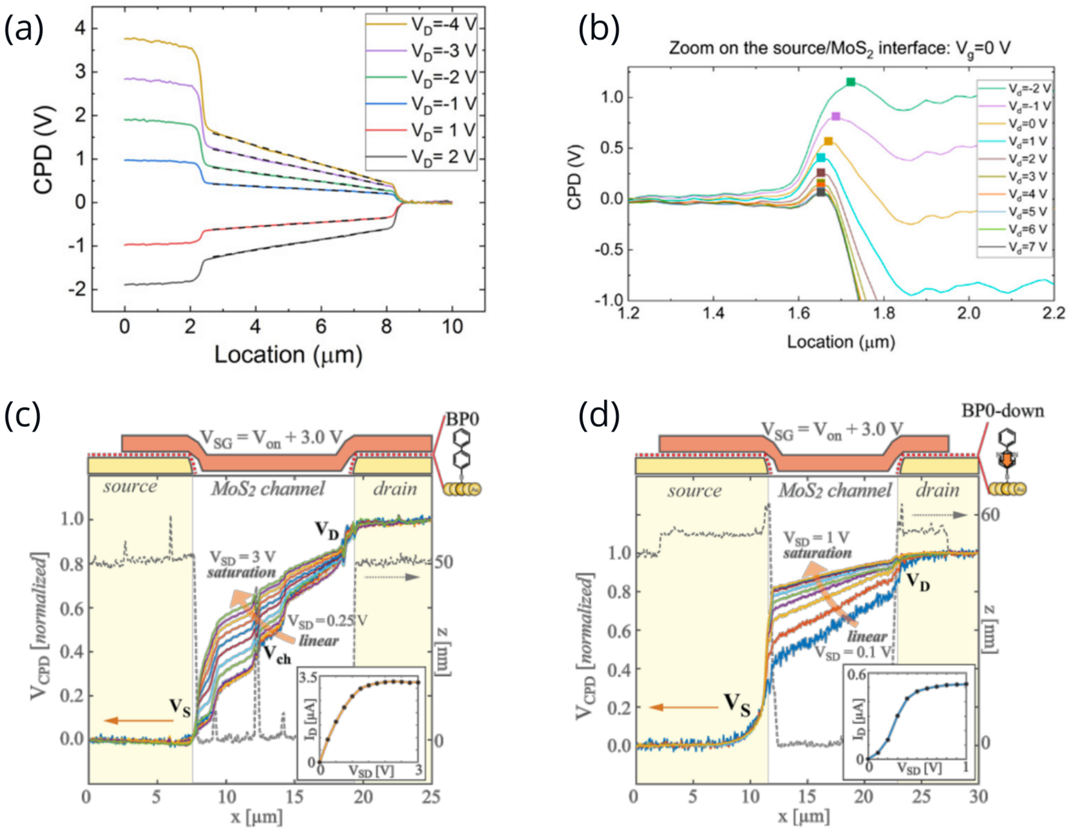

Figure 3.7: (a) From [230] (Y. Rosenwaks group), *in operando* KPFM line profiles of 2D MoS$_2$ FET at different drain voltages. (b) From [231] (Y. Rosenwaks group), *in operando* KPFM revealing effect of drain on Schottky barrier at the source side of 2D MoS$_2$ FET. (c,d) both from [232], including both AFM and KPFM scans *in operando* in each case. The former case shows the effect of wrinkles in the channel, causing potential drops and introducing resistances. Latter case is more linear.

in Figure 3.8(a) which show an AFM scan and KPFM at drain voltages of $0$ and $-5$ V. Here inhomogeneities in the channel can be seen, including the two particulates and also variations in the monolayer itself. Noyce et al. 2020 [237] is a more recent example, and also Aslam et al. 2022 [236]. The latter paper showcases KPFM of *in operando* single crystal nanoribbon MoS$_2$ FETs. One image is reproduced in Figure 3.8(b). In the article, averaged line profiles are also included from drain to source, where in one case node features in the nanowire channel can be seen to affect the channel potential profile.

## CAFM, MIM, SGM, EFM

Conductive AFM (CAFM) is also a useful means to study *operando* behavior of MoS$_2$ devices, in its ability to map current (A), which in some cases can be converted to conductivity (S/m).

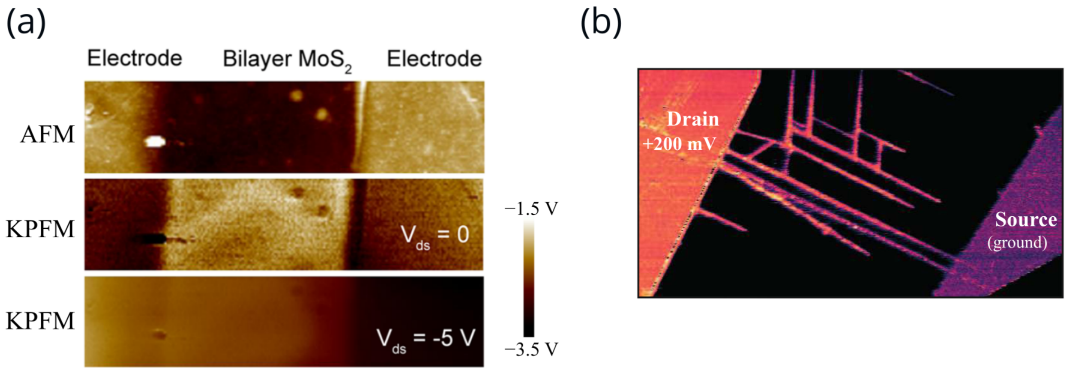

Figure 3.8: (a) From [229], AFM and KPFM $(x, y)$ scans at two drain voltages. Some inhomogeneities in channel are seen. (b) From [236], nanowire $MoS_2$ FET *in operando* KPFM.

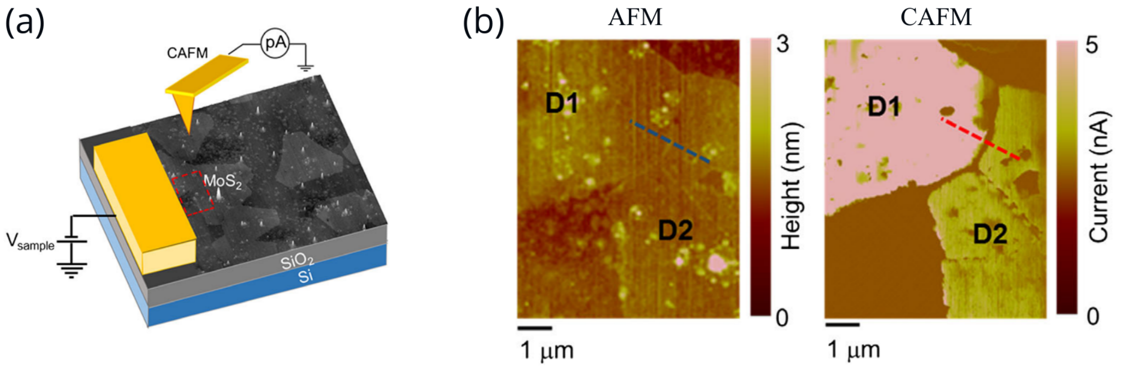

Figure 3.9: From [238] (Roccaforte group). (a) Drawing of CAFM experiment with optical micrograph of sample. (b) AFM (left) and CAFM (right) scan of inter-connected 2D $MoS_2$ domains. Reveal a large grain boundary resistance of about 428 MΩ.

Among other teams, the Roccaforte group has published several papers mapping $MoS_2$ devices by CAFM. One of them is from F. Giannazzo et al. 2020 [238], where some data is reproduced in Figure 3.9. In (a) a schematic of the setup is shown with an optical micrograph of a resistor sample between two connections one being the tip. In (b) on the left is an AFM image while on the right is a CAFM image. In this case it is clearly seen that the grain boundary has a significant resistance which causes a drop in current from regions D1 and D2. They estimate $R_{\text{GB}} \approx 428$ MΩ in this particular case. This result is interesting because later with XRM / IRM configuration we observe resistive grain boundaries having an effect on the charging of capacitors.

Another powerful scanning probe technique for measuring local current density is microwave

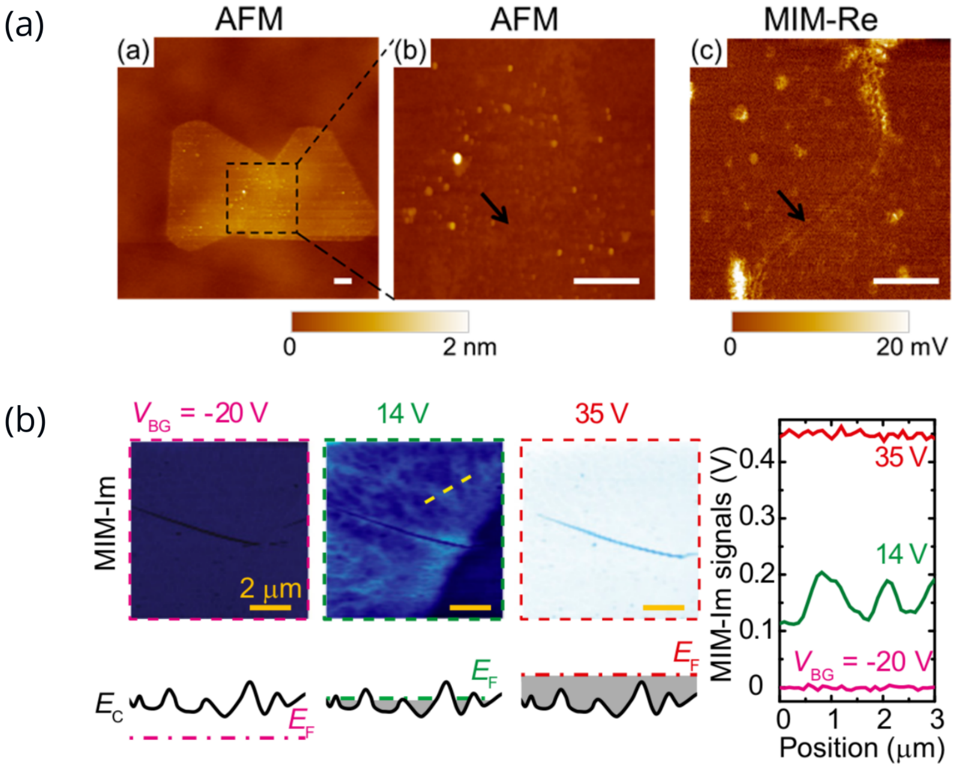

Figure 3.10: (a) From Y. Liu et al. 2014 [42], AFM and MIM-Re scans, with the latter revealing a grain boundary. (b) From [239], MIM-Im signal of capacitive *in operando* 2D $MoS_2$, where the center data at 14 V reveals $E_c$ inhomogeneities due to the Fermi level being near the conduction band edge. Line profiles in right plot.

impedance microscopy (MIM) [240] which makes use of microwave coupling between tip and sample. Liu et al. 2014 [42] showed for example how a grain boundary is revealed by MIM, as reproduced in Figure 3.10(a) which shows both AFM and the real part of the MIM signal. (The same group also used MIM to study thermal oxidation of a TMD [241].)

Wu et al. 2016 studied the local conductance landscape of *in operando* $MoS_2$ capacitors [239], some data of which is reproduced in Figure 3.10(b). In particular, the authors reported how the variations in local conductance landscape is very pronounced at certain voltages while being invisible in others. They explain this based on the Fermi level position—if it is close to $E_c$ then the local $E_c$ variations are visible while if it is above or below, the variations are not seen, as shown in (b). This is an interesting result, and we believe to have observed a similar effect as is discussed in a later section. The same group also studied gated TMD heterostructures using MIM in 2019 [242]. Finally there is also Alam et al. 2020 [243] who acquired *in operando* MIM data of TMD FETs *in operando*, providing insights on transistor and amplifyer device performance via the technique.

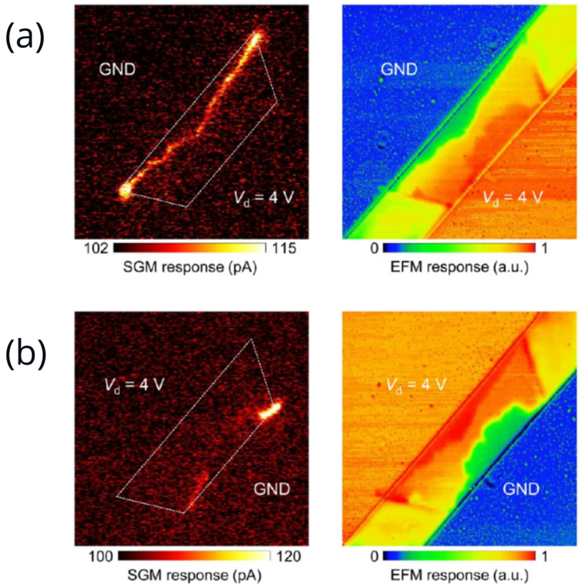

Figure 3.11: From [244], Scanning gate microscopy (SGM) and electrostatic force microscopy (EFM) *in operando* images of a 2D $MoS_2$ FET, with (a) and (b) being of swapped polarities.

Scanning gate microscopy (SGM) and electrostatic force microscopy (EFM) also enable local study *in operando* of TMD devices. M. Matsunaga et al. 2016 (Aoki group) [244] explored this, some data of which is reproduced in Figure 3.11. This particular device had by design a portion of the channel that was strained. (a) and (b) include SGM and EFM images for each polarity. When doing these types of in operando studies, it is in general useful to explore how swapping source and drain polarity has an effect, as there is often an asymmetry which can then be deterimed. I used the polarity switch in experiments shown later.

Based on the above, it is clear that the scanning probe techniques of KPFM, CAFM, MIM, SGM, EFM can be powerful tools for both static and *in operando* research of 2D TMDs and their device configurations. The main limitation with all of these is the throughput and scanning nature. As we shall see, optical configurations for *in operando* charge density imaging can be used in widefield and thus attain higher throughputs, which is a significant advantage. Importantly, a low throughput does not only mean longer acquisition time. In addition it forces to use static bias for duration that favor charge trapping in defect sites (in particular in the dielectric) so that the system under consideration sverely evolved as it is studied.

Although they too will have some drawbacks that the scanning probe microscopies do not have, in the end having multiple complimentary techniques is desired.

### 3.1.5 . State of the art: Charge density imaging of 2D TMDs using optics

In terms of optical techniques, much of the early literature that investigated local (µm-resolved) imaging of charge density in 2D materials made use of Raman and photoluminescence (PL) spectroscopies. Such results from literature were reproduced and discussed in Chapter 1. One paper of interest that should be added involves PL imaging of $MoS_2$ at a gate bias in an electrolyte, namely Tezuka et al. 2020 [245]. In their paper a decaying of PL intensity is seen in the direction away from the electrode.

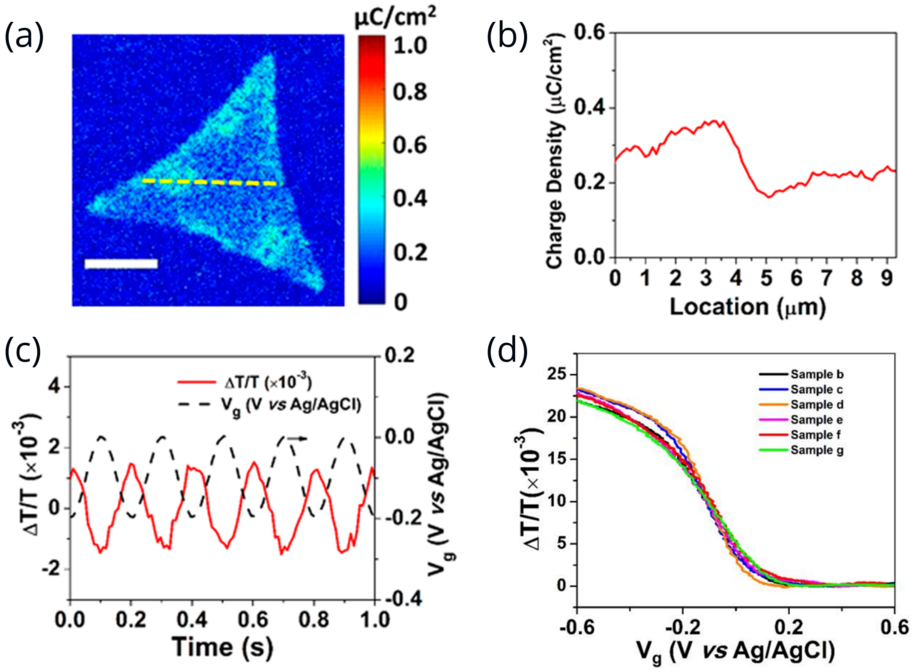

Figure 3.12: All from Hao Zhu et al. 2019 [246]. (a) Charge density image of a 2D $MoS_2$ flake lying on ITO, being gated via an electrolyte. Inhomogeneities in charge density can be seen, and further so in the (b) line profile. In (c) gate cycling is shown, with the $\Delta T/T_0$ signal showing stable cycling over time. (d) $\Delta T/T_0$ signal plotted as a function of bias, for multiple different samples. There is a linear regime of the response between around $-0.2$ and $+0.1$ V.

Now, in terms of converting an optical reflectance or transmittance image to charge density, the first such case to the author's knowledge is Hao Zhu et al. 2019 [246]. The basic principle is to use a bandpass near one of the exciton energies where it is known that charge and optical properties are correlated, which is discussed in detail in the next section.

Zhu et al. use a 655/15 nm bandpass with a trans-illumination optical microscope. They transferred CVD-grown 2D $MoS_2$ to an ITO-covered slide. They use 0.1 M $NaF_{(aq)}$ electrolyte, with a capacitance they estimate as 3.5 µF/cm$^2$. They measure $\Delta T/T_0$ of the 2D MoS$_2$ upon gate cycling. In their particular case, the signal is quite small though, and they had to use FFT post-processing of the data to de-noise the results.

In some regimes of the gating, the response of $\Delta T/T_0$ versus applied bias (and thus of $\Delta q$ using $\Delta q = c\Delta V$) is linear. Hence, in this regime, the authors propose to compute a simple constant of proportionality between the $\Delta T/T_0$ and $\Delta q$, which they call $\alpha$. This thus takes the form $\Delta T/T_0 = \alpha\Delta q$.

Some results from their paper is reproduced in Figure 3.12. In (a), the computed charge density image is shown, revealing some inhomogeneities. A line profile is taken as indicated in (a) and shown in (b). In (c) an example of their cycling is shown, and plotted as a function of bias in (d). In their setup a negative bias is accumulation (opposite the typical convention in FETs). It is clear that in depletion the response is flat while towards accumulation bias there is a response, where a portion of it is linear as descrbied earlier. The authors also test the effect of altering the frequency of cycling in the range of 5 to 20 Hz. Furthermore they use it as a sensor for molecules, and also compare the results with SPRi.

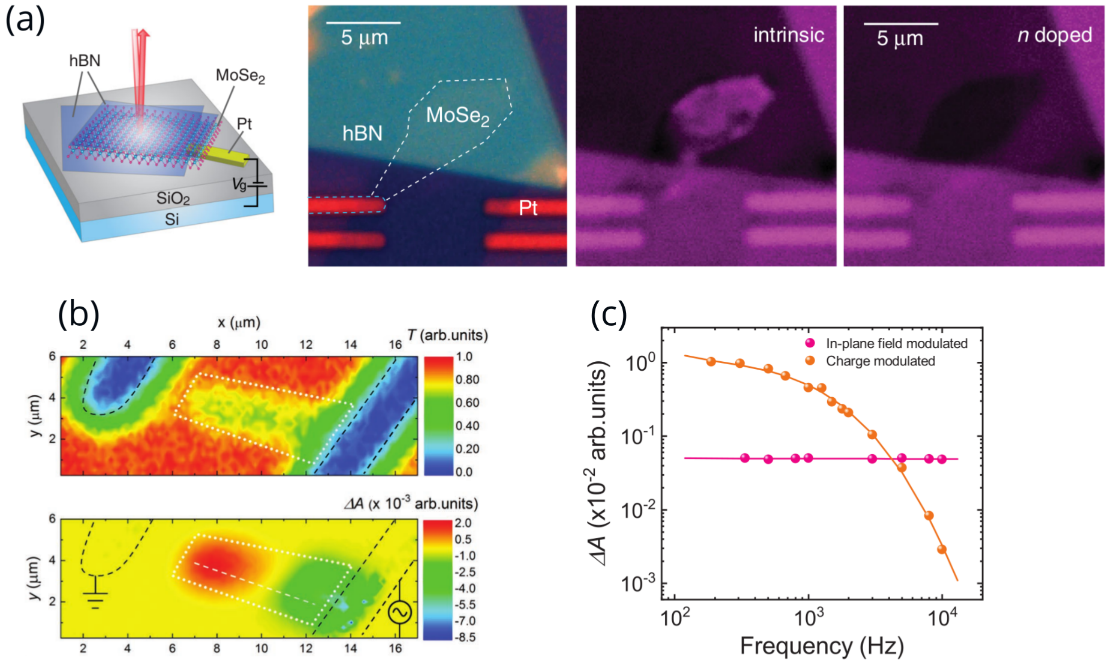

Figure 3.13: (a) From Scuri et al. 2018 [247], 2D MoSe$_2$ encapsulated by hBN, and gate modulated, with reflectance micrographs revealing a significant change in reflectance due to correlation between charge density and optical properties. (b) From Vella et al. 2021 [248], transmittance (top) and $\Delta A$ absorptance change during ac operation of 2D MoS$_2$ FET, attributed to a Stark effect. (c) Also from [248], a deconvolution between charge and field modulated optical properties, thanks to frequency dependence of the former and not the latter.

Overall the work is impressive, setting precedent for charge density imaging using the gate-dependent exciton of a TMD. Yet, there is a lot more to be explored, especially in the context of FET devices, and also more typical capacitor geometries where the semiconductor sits on a dielectric—here the flakes are sitting on the electrode itself. The same group also published another study in 2022 [249], using a total internal reflection (TIR) microscope, doing more sensing of molecules and proteins using the 2D $MoS_2$. In 2022, another group, Zhao et al. [250] also acquired charge images via an SPRi microscope, also using a linear relation between percent change reflectance and gate applied bias. Scuri et al. 2018 [247] studied the gate-dependent reflectance of $MoSe_2$ encapsulated in hBN. In one of their figures, they include reflectance micrographs at differing gate voltages, which shows a significant modulation of the $MoSe_2$ flake. This is reproduced in Figure 3.13(a).

Finally, the work of Vella et al. 2017 [251] and 2021 [248] stands out in the discussion. This group used electro-absorption (EA) spectroscopy (also known as Stark spectroscopy), to image $\Delta A$ of 2D $MoS_2$ FETs during gating at both dc and ac fields. One result is reproduced in Figure 3.13(b) from [248]. In fact they also were able to de-convolute the two mechanisms that can cause a change in $\tilde{n}(\lambda)$ which include charge and field, the latter attributed to the Stark effect. This is seen from the result reproduced in Figure 3.13(c). The topic of charge versus field driven modulation of $\tilde{n}(\lambda)$ is addressed in the next section.

### 3.1.6 . Gate-dependent refractive index in 2D $MoS_2$

As we shall see, the charge imaging via IRM and BALM, which we term eXciton reflection microscopy (XRM), is based on the change in optical properties near exciton energies due to charge density. This effect has been studied relatively extensively in the literature. In 2012, Mak et al. [252] with J. Shan, T. Heinz and co-authors measured the absorption $A$ of 2D $MoS_2$ upon gating. They appear to be the first to propose the physical mechanism, attributing the change in absorption to a shift in spectral weight from neutral exciton ($X^0$) to charged exciton ($X^-$) during accumulation. This is reproduced in Figure 3.14(a).

In 2015, Mukherjee et al. [253] also measure $A$ at different gate voltages, comparing it with [252]. In later work in 2019, Kravets et al. [170] measure the complex refractive index at different gate voltages using ellipsometry. The results are reproduced in Figure 3.14(b). I digitized this data to use in simulations, covered later.

Yu et al. 2017 [144] measured gate-dependent refractive index of monolayer $WS_2$ which is

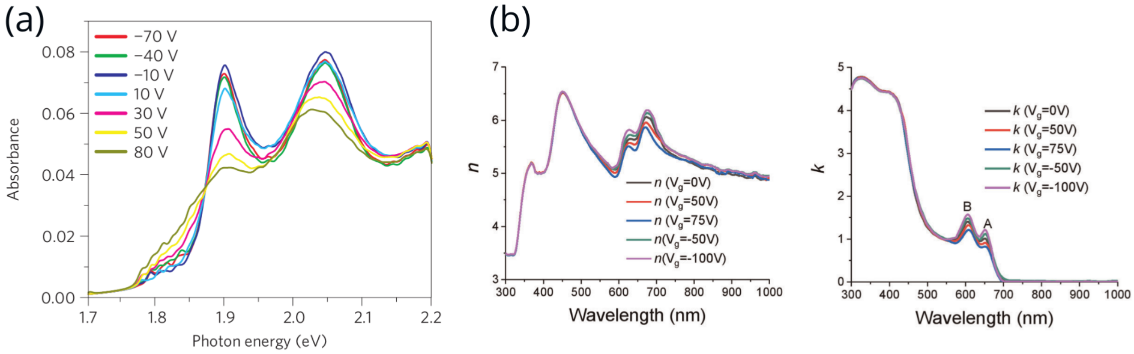

Figure 3.14: (a) From Mak et al. 2012 [252] (Heinz group), gate-dependent absorptance of 2D MoS$_2$. (b) From Kravets et al. 2019 [170], $n(\lambda)$ and $\kappa(\lambda)$ of 2D MoS$_2$ measured at different gate, via ellipsometry.

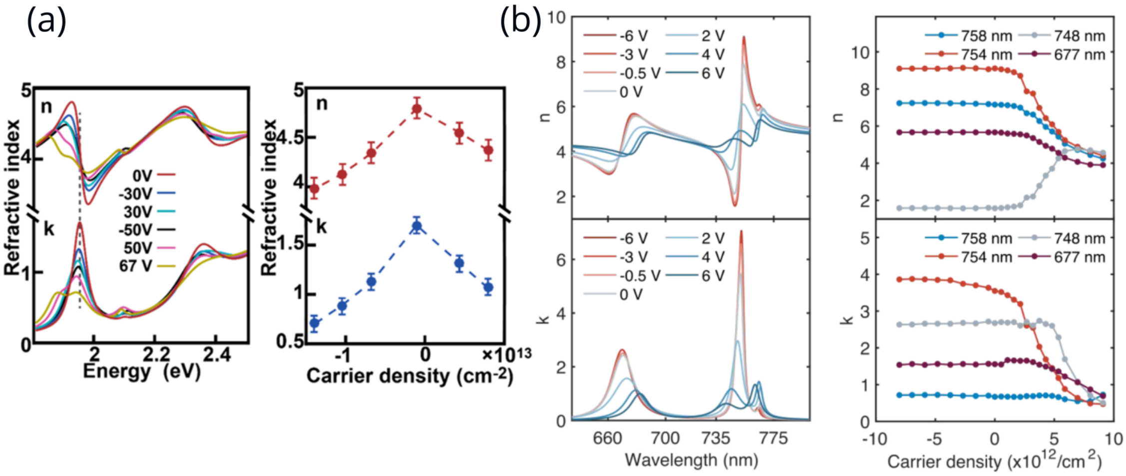

Figure 3.15: From Yu et al. 2017 [144], gate dependent refractive index $\tilde{n} = n + i\kappa$ of 2D WS$_2$. (b) From M. Li et al. 2021 [220], gate dependent RI of MoSe$_2$ encapsulated in hBN.

ambipolar, using reflectometry. They fit the results nicely with a a multi-Lorentzian model, including a $\varepsilon_\infty$ term. Some results are shown in Figure 3.15(a), where we see that it is on the order of several units of $10^{12}$ cm$^{-2}$ that changes in charge density that result in the modulation of $\tilde{n}(\lambda)$ near exciton energy.

Two papers from 2017, Back et al. [5] and Scuri et al. [247] (the latter mentioned earlier) explore 2D MoSe$_2$ encapsulated in hBN showing a significant modulation of 200 to 300% in $n$ and $\kappa$ at some wavelengths. Li et al. [220] studied this system in 2021, some results of which are reproduced in Figure 3.15(b). The carrier density changes are of similar proportion, several units of $10^{12}$ cm$^{-2}$ as in Yu et al. In the range explored in (b), the MoSe$_2$ is behaving as $n$-type, which is why at negative carrier density there is no hole accumulation and thus $(n, \kappa)$

are staying constant, behaving "intrinsically".

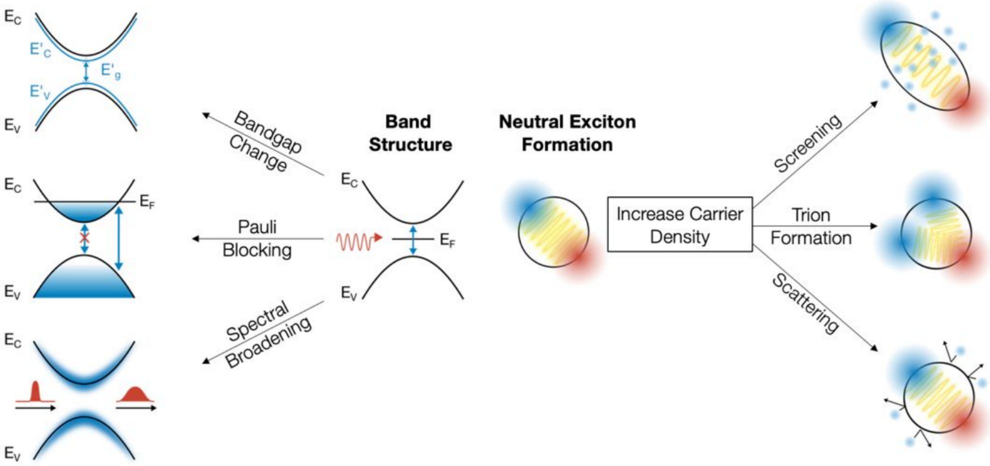

Figure 3.16: From M. Li et al. 2023 [26], a drawing summarizing the physical mechanisms giving rise to the gate dependent optical properties of 2D TMDs.

Regarding the physical mechanism, as touched on earlier it seems that the charge-driven modulation is the main one while a Stark effect is weaker. Within the charge related mechanisms, there are typically three mechanisms which are stated [144, 26] which include trion formation, screening and Coulomb scattering, which in turn result in bandgap change, Pauli blocking, and spectral broadening. The effects are nicely summarized in a drawing from [26] reproduced in Figure 3.16. In this particular paper, the authors also state: "*We note that there are also other effects that are typically observed in 2D semiconductors such as Stark shift where a vertical electric field can cause a reduction of the bandgap and red-shift the absorption peak. However, we believe this is a very weak effect in our gating scheme where a pure vertical displacement field in absence of doping does not exist.*" The discussion on the field (Stark) contribution versus charge contribution is rather limited, although the previous Figure 3.13(c) shows how [248] deconvolved the two effects by measuring the frequency dependence.

Other papers exist on the topic. From an applications perspective, its use for electro-optic modulators (EOM) could be attractive [25], as explored for example in [24]. Due to their tunable refractive index, metalenses with tunable focal distance was shown in 2020 [6] and a more recent example from 2023 of steering a laser beam reflecting off of a 2D TMD at an angle was demonstrated [26].

## 3.1.7 . Modulation depth definitions

There are different ways to define the attained modulation depths, i.e. the extent to which reflectance (in this case) is changed upon application of $V_{\mathsf{GS}}$. Percent change is one way to quantify it, as

$$\mathsf{MD}_{\mathsf{pc}} \equiv \frac{\Delta R}{R_{m,0}} = \frac{R_{m'} - R_{m,0}}{R_{m,0}} = \frac{R_{m'}}{R_{m,0}} - 1$$

where $\times 100$ is implied if "%" is used. Above I use $R_{m,0}$ to mean the $\mathsf{MoS}_2$ reflectance at $V_{\mathsf{GS}} = 0$ V, and $R_{m'}$ to mean the $\mathsf{MoS}_2$ reflectance at some applied bias. The above definition is the one I use mostly throughout the text. I also drop the "$m$" subscript for brevity, so I just write $\Delta R/R_0$. Also, as I shall discuss later, I do not always use the reference $R_0$ to be the $V_{\mathsf{GS}} = 0$ case. This is a relevant point because if the 0 V case is not depleted enough it can be more logical to use the most depleted case as the reference.

Another option can be to use the change in contrast, so

$$\mathsf{MD}_{\Delta C} \equiv \Delta C = \left(\frac{R_{m'}}{R_s} - 1\right) - \left(\frac{R_{m,0}}{R_s} - 1\right) = \frac{R_{m'} - R_{m,0}}{R_s} = \frac{\Delta R}{R_s}$$

where $R_s$ is the substrate reflectance. One could also imagine computing the percent change of the percent change contrast,

$$\mathsf{MD}_{\Delta C/C_0} \equiv \frac{\Delta C}{C_0} = \frac{\frac{R_{m'} - R_{m,0}}{R_s}}{\frac{R_{m,0} - R_s}{R_s}} = \frac{R_{m'} - R_{m,0}}{R_{m,0} - R_s} = \frac{\Delta R}{R_{m,0} - R_s}$$

however this version is not very useful.

In the context of electro-optic modulators (EOM) among others, it is common to report in decibel (dB) [24]. Since reflectance/intensity is a power quantity, it takes the form

$$\mathsf{MD}_{\mathsf{dB}} \equiv 10 \log_{10}\left(\frac{R}{R_0}\right)$$

(Recall, that for field quantities like pressure, dB takes the form $\mathsf{dB}_{\text{field quant.}} \equiv 10 \log_{10}(p^2/p_0^2) = 20 \log_{10}(p/p_0)$, where it takes 20 dB to effect a $\times 10$ change, while for power quantities it is more intuitive in that 10 dB is a $\times 10$ change.)

To convert between $\mathsf{MD}_{\mathsf{dB}}$ and $\mathsf{MD}_{\mathsf{pc}}$, one simply can do some algebra and get

$$\mathsf{MD}_{\mathsf{pc}} = \left[10^{\frac{\mathsf{MD}_{\mathsf{dB}}}{10}} - 1\right] \times 100$$

Finally, there is the possibility to explore the reflectance difference. Consider the following definition:

$$\mathsf{MD}_{\Delta R} = \Delta R = R_{m'} - R_{m,0}$$

In principle there is no problem with this but in practice there is. The measured signal is always the grayscale intensity

$$\Delta I = I_{m'} - I_{m,0}$$

and in fact, the grayscale difference is not universal and will depend on the exposure time. Earlier it was shown (in Figure 2.23(b)) that the grayscale difference $I_m - I_s$ actually increases with exposure time, and it is no different when considering the grayscale difference $I_{m'} - I_{m,0}$.

However, the percent change version is universal, where

$$\Delta R / R_0 = \Delta I / I_0$$

hence its preferred use. However, there is one advantage of using the grayscale difference which has to do with reduced noise.

# 3.2 . Results: $MoS_2$ devices studied by IRM

## 3.2.1 . Principle of charge density imaging by XRM

First, I shall introduce a complete broad strokes overview of charge density imaging with IRM, which we refer to as eXcitonic reflection microscopy (XRM) due to the central aspect of the exciton–charge density correlation. Then, I shall go into more details in the next sections. Consider the following capacitor system. A Cr/Au film of approx. 0.5/3 nm thickness was evaporated with a shadow mask. Then, CVD $MoS_2$ was transferred. Some systems of flakes landed at the edge of the Au/glass interface. First let us consider images in air using the 450 nm filter which was shown in previous sections to generally maximze contrast for 2D $MoS_2$. The result is shown in Figure 3.17 on the left. The flakes are visible with $C_{\mathsf{pc}} = -46\%$ contrast, with various different adlayers visible. The inter-connected network consists both of triangle-shaped domains on the left and pentagram-shaped domains on the right.

However, as explained previously, a wavelength in the red near exciton wavelength is necessary in order to perform the charge density imaging. Also, an electrolyte is needed in order to perform capacitive charging with a gate voltage. For this sample, $10^{-1}$ M NaCl was used, and thus dropped on top of the substrate and then a counter electrode placed in the liquid. Thus, changing both the wavelength to 650 nm and the RI at final interface $n_{\mathsf{f}}$ to 1.33, which impacts the contrast.

While 450 nm gave $C_{\mathsf{pc}}$ of $-46\%$, the latter case only has about $-1.5\%$ contrast for the monolayer, which is very small, as seen on the right-hand-side of Figure 3.17. However because the adlayers are more contrasted, and because of diffraction at the edges, the eye manages to reconstruct the flakes, especially with help of the grayscale adjustment shown in the bottom image. Yet, it is by no means an optimal contrast, but it is not of much consequence, because 450 nm in air can be used for best visibility, while the 650 nm filter together with electrolyte is used for the charge density (XRM)imaging mode.

Now, the next step is to apply a gate bias. This will cause a reflectance change since there is a correlation between charge density and optical properties and thus with reflecitvity. For the capacitor in Figure 3.17, $V_{\mathsf{GS}}$was ramped at $+400$ mV/s while recording a video at 2 frames-per-second (fps). The raw result for the frames at $t = 0$ s (0 V), $t = 3.5$ s (1.4 V) and $t = 4.5$ s (1.8 V) are shown in Figure 3.18(a), while in (b) the grayscale is adjusted. It is clearly seen

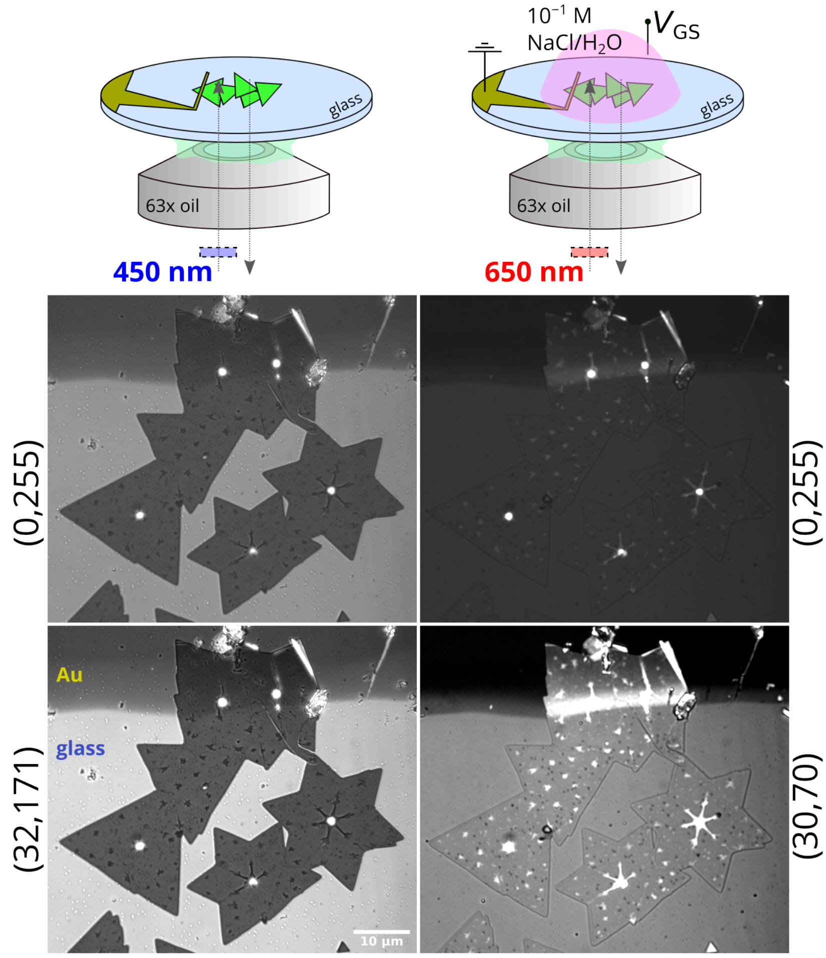

Figure 3.17: Interference reflection microscopy (IRM) micrographs of a 2D MoS$_2$ network in air at 450 nm (left) and after adding NaCl$_{(aq)}$ electrolyte at 650 nm, with adjusted grayscale values in the bottom row. Note that the 450 nm case has a intrinsic contrast of $-46\%$ while the 650 nm has an intrinsic contrast of $-1.5\%$.

that the 2D MoS$_2$ gets brighter. **From these frames, the percent change reflectance for each pixel is computed**, via an ImageJ Java PlugIn developed by the author. The result is shown in (c), where the "Fire" lookup table (LUT) available in ImageJ was used as the colorbar (adjusted to 4–20% range in this case). That means that the top 1.4 V image of 3.18(c) $\Delta R/R_0$ image was computed as

$$\Delta R/R_0[1.4\ \mathrm{V}] = \left(\frac{R_{1.4\ \mathrm{V}}}{R_{0\ \mathrm{V}}} - 1\right) \times 100\%$$

and the bottom 1.8 V image of 3.18(c) computed as

$$\Delta R/R_0[1.8\ \mathrm{V}] = \left(\frac{R_{1.8\ \mathrm{V}}}{R_{0\ \mathrm{V}}} - 1\right) \times 100\%$$

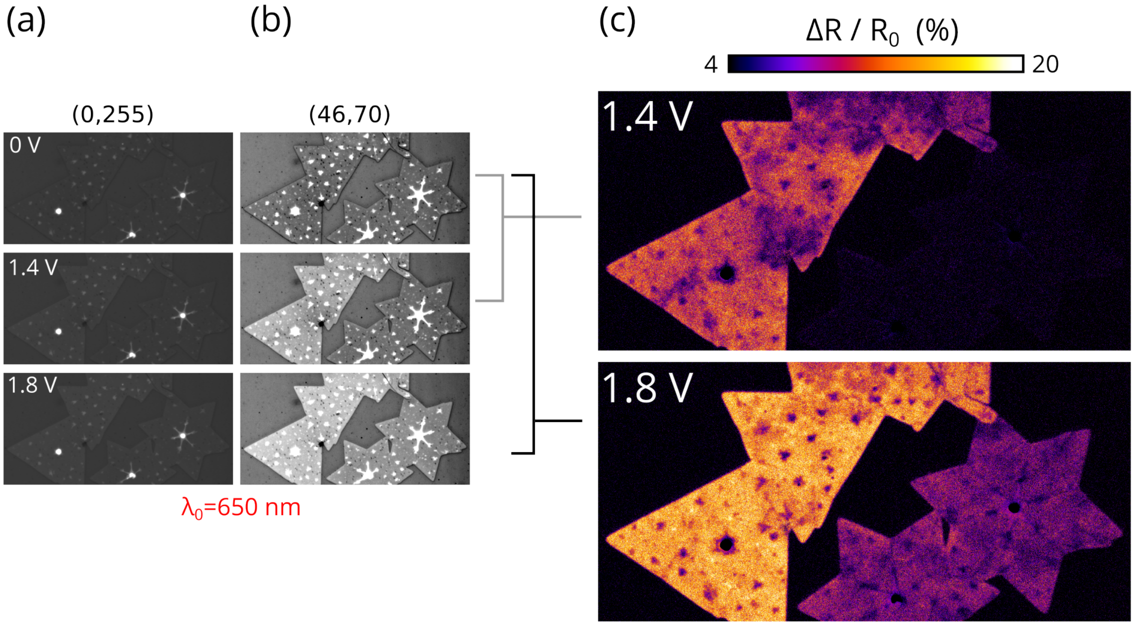

Figure 3.18: Principle of eXcitonic reflection microscopy (XRM). Raw reflectance micrographs at 0, 1.4, 1.8 V in (a), and adjusted grayscale in (b) where the network is getting brighter upon gating. In (c), the percent change reflectance was computed for each pixel with the 0 V image used as reference, as indicated by the lines. Colorbar is called "Fire" and was set from 4 to 20 %. In this particular experiment, various inhomogeneities can be seen, as well as different parts of the network charging at different rates.

**In the rest of the Chapter 3 this is how the percent reflectance change ("charge") images are computed and thus it is important to make note of that here**.

Various interesting observations can be made from this, notably the presence of inhomogeneities as well as delays in the pentagram part of the network. These results are discussed in a later section in detail.

### 3.2.2 . Capacitive charging with NaCl/$H_2O$

Chronologically, the electrolyte NaCl/$H_2O$ was the first explored in the thesis. Mainly this was because of its simplicity, accessibility, and high capacitance. Usually the concentration was set to $10^{-2}$ or $10^{-1}$ M.

M. Khademi et al. [254] measured the electrical double-layer capacitance ($C_{\mathrm{EDL}}$) of NaCl/$H_2O$ as a function of concentration. They found that for $10^{-2}$ and $10^{-1}$ M concentrations, the capacitances are around 8 and 10 μF/cm$^2$ respectively. These are very high values (compared with for example 150 nm $SiO_2$ oxide which has a capacitance of 0.023 μF/cm$^2$). This means that even within ≈ ± 3 V, it is possible to sweep the entire transfer characteristic. The main

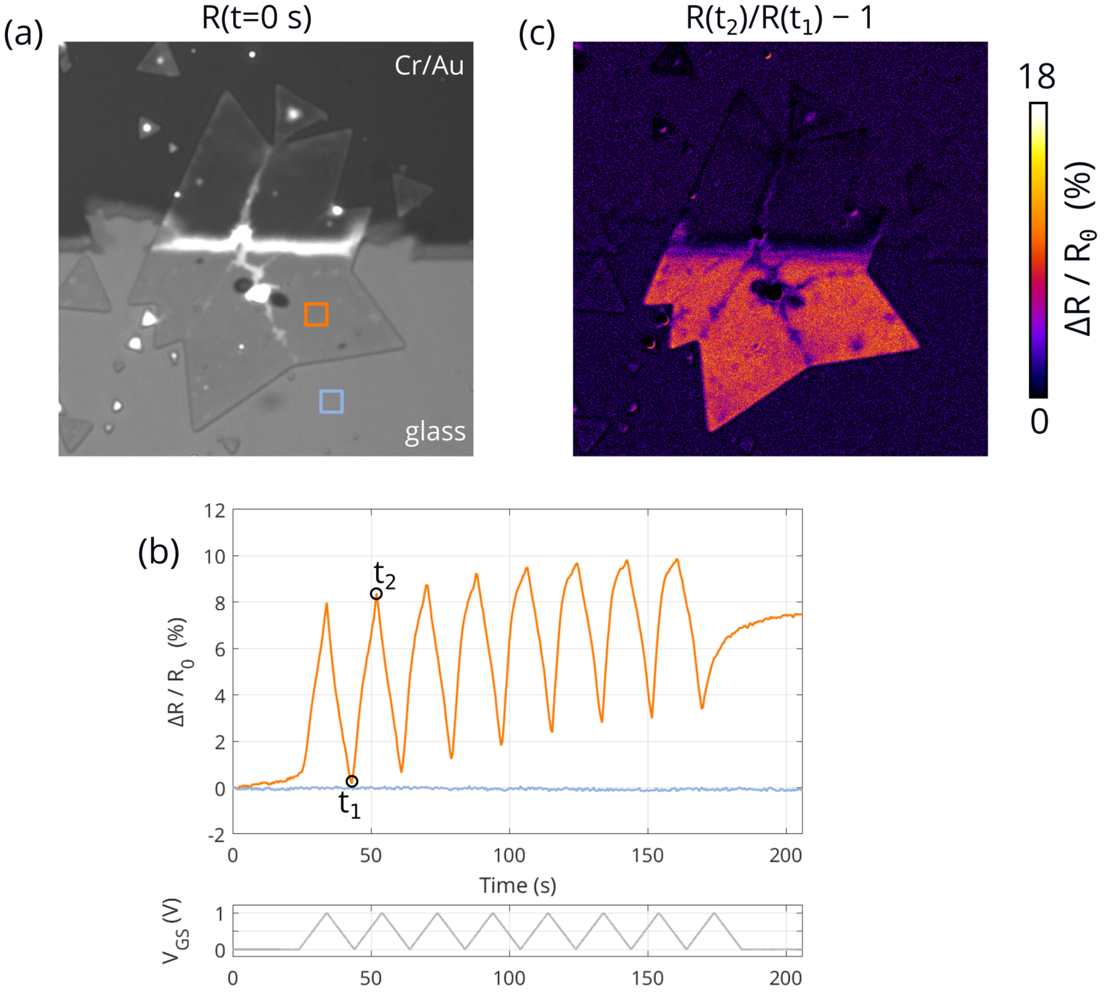

Figure 3.19: (a) a 650 nm IRM micrograph of a 2D $MoS_2$ flake with $NaCl_{(aq)}$ electrolyte added, and two ROIs defined. (b) Result of 2 fps video during cycling of the gate between 0 and $+1$ V at 100 mV/s over a total of 8 cycles, for the orange and blue ROIs, and applied $V_{GS}$ at the bottom. (c) $\Delta R/R_0$ image using reflectance images at $t_1$ and $t_2$ as indicated in (b).

potential issue with electrolyte gating though is the possibility for electrochemical reactions taking place, which can alter the material properties. Thus, it is always safer to use as small voltage range as needed. Despite care in the applied potential, we found that the NaCl/$H_2O$ seems to be causing significant non-reversible effects, which are discussed further in a moment.

Consider the capacitor shown in Figure 3.19(a). This is a 650 nm micrograph (grayscale 30–120), with two regions of interest (ROI) defined as shown by the $50 \times 50$ px$^2$ squares. The orange ROI is situated on the monolayer while the blue ROI is on the glass. The gate bias was then swept between 0 and $+1$ V at 100 mV/s over a total of 8 cycles. Resulting percent changes for each ROI are plotted in (b), with the applied $V_{GS}(t)$ below the plot.

Upon first inspection, it is seen that the blue ROI is staying constant, while the orange ROI is reacting somewhat in sync with the gate. This is a good sign and is what was expected. A charge image was then computed, shown in (c) using $R(t_1)$ and $R(t_2)$ as indicated in (b). From the plot and image it is seen that the monolayer region has about 8 % modulation with a good signal-to-noise ratio. The $\sim$ 1–2 µm sized grain boundaries and other adlayers however do not react so much, which is expected, because it is the monolayers that have a the strong gate-dependent excitons/trions, and not so much the ill-defined adlayers. On the monolayer, slight inhomogeneities can also be made out. Such monolayer inhomogeneities may correspond to variations in charge in the susbtrate, which is investigated deeper in a different experiment (see Figure 3.22).

Now, upon further inspection, it can be seen that the orange ROI is not perfectly in sync with the gate, and the phase is lost after a few cycles. Furthermore, there is a "left shoulder" for each orange peak that becomes more and more prominent over time. Finally, there is the obvious trend that the monolayer reflectance is not returning back to its initial reflectance $R_0$ when $V_{\text{GS}} = 0$. In fact, even when the cycling is stopped, the reflectance curve drifts upward, opposite the direction of the initial $R_0$. Thus, it appears that the monolayer is possibly being altered over time electrochemically. It could also be that charges are being trapped in the system, for example in the borosilicate substrate or in $\text{MoS}_2$ defect states, which shifts the zero-bias charge. This is discussed further later.

A similar gate cycling was performed on this device at 450 and 550 nm, as a falsification test. It is expected that the optical properties are not gate-dependent at these wavelengths, and it is thus an appropriate test to see whether the 650 nm reflectance changes indeed can be attributed to capacitive charging, instead of some other process that could give rise to reflectance changes, such as the differing RI of the electrical double layer (EDL) above the $\text{MoS}_2$. The result was that no modulation was detected at all for 450 and 550 nm. Further falsification tests are presented later.

## Charging hysteresis in NaCl/$\text{H}_2\text{O}$ capacitors

A different sample was tested also with $10^{-2}$ M NaCl/$\text{H}_2\text{O}$ electrolyte, but gated at very small voltages, oscillating between 0 and 0.1 V at a rate of 20 mV/s. This particular system was in fact particularly sensitive to applied bias, which probably is because of the high quality of this particular CVD growth. Many of the triangular monolayers have a very sharp and defined shape which is correlated with high quality growth.

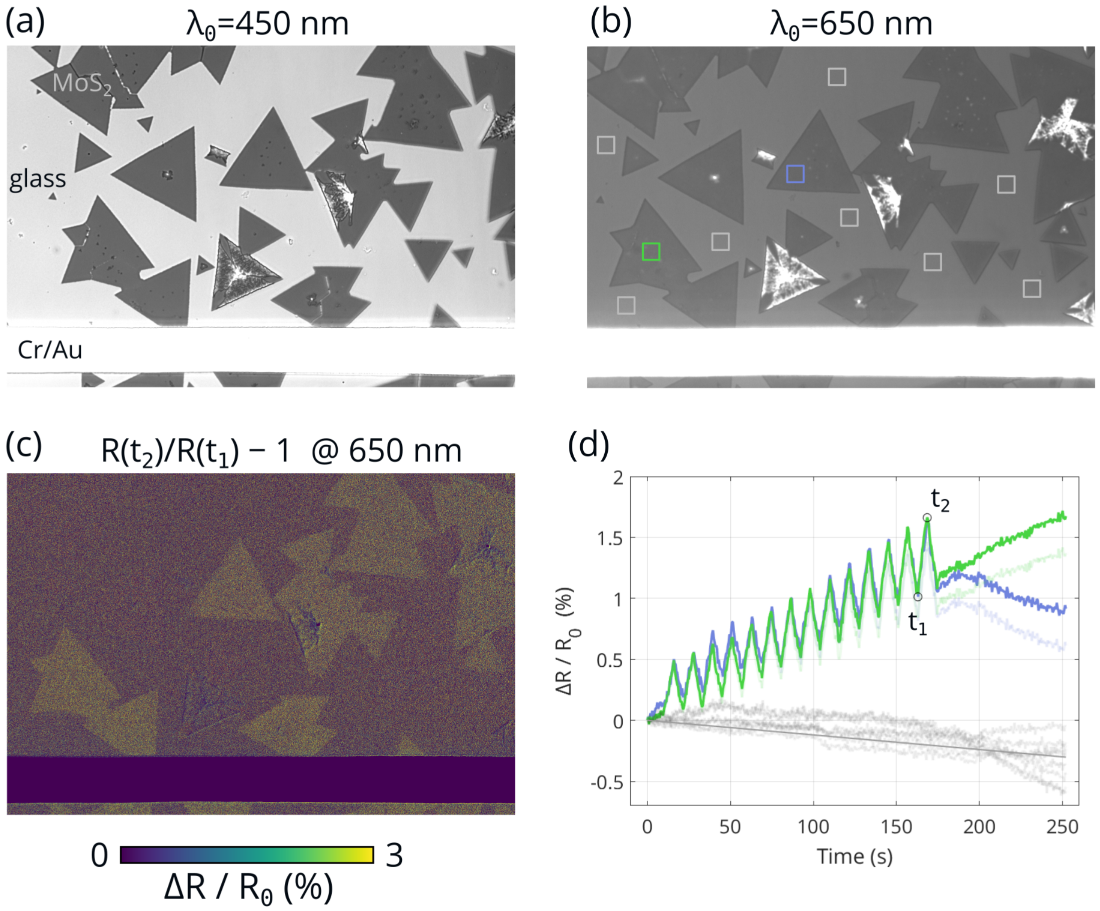

Figure 3.20: (a) IRM micrograph at 450 nm in air of 2D $MoS_2$ high-quality flakes some of which are connected to a Cr/Au electrode. (b) 650 nm IRM micrograph after adding $NaCl_{(aq)}$ electrolyte, with multiple ROIs defined. In (d) the result of ROI percent reflectance change is plotted during cycling. The result showed a rare drift of substrate which was corrected for in the $MoS_2$ ROI data as shown, with the faint color being the raw data. In (c) a $\Delta R/R_0$ image is shown using $t_1$ and $t_2$ indicated in (d). The (c) image reveals which $MoS_2$ crystals are actually connected and being charged.

A micrograph at 450 nm in air was first taken for good contrast and visibility of the sample, shown in Figure 3.20(a). Then, the filter was swapped for 650 nm for the charge imaging (XRM) mode. A still image before gating is shown in 3.20(b), with various square ROIs defined. The green one is on a monolayer close to the electrode, while the blue one is an a monolayer farther away that is only connect via an elaborate network of other monolayers connected back to the electrode. Finally multiple ROIs were defined on the substrate.

In 3.20(c) a charge image is shown from one of the cycles, from the reflectances as indicated by $t_1$ and $t_2$ in (d). The first striking result from (c) is that it is immediately apparent which monolayers are connected to the electrode and which are not. In (d), we see that the blue and green ROIs are reacting with the applied gate somewhat in sync, as last time. In this particular case, the substrate ROI also had a slight drift, possibly due to the bulb slowly wanning in intensity due to aging. A line was fit and the background made flat (raw data for $MoS_2$ are the very faint blue and green). In general, we do not detect any significant substrate drift, although in this particular experiment it was the case, hence the correction.

Again, as in Figure 3.19, there is a drift in the monolayer reflectance. There is also an interesting behavior at the point where the cycling is stopped $\sim$ 175 s. The monolayer closer to the electrode is continuing to drift while the one far away seems to be decaying to its original state. Whatever the exact case, it is evident that even at very small voltages of 0.1 V, some permanent highly hysteric behavior is present. This lead us to change to a more standard electrolyte used for gating as explained later.

## Tungsten vs. Au micromanipulator tips

In the previously shown experiments, gold tips were used for both micromanipulators. We found early on that this is actually an important factor as the type of tip was found to have an influence. In particular it was the case for tungsten (W) micromanipulator tips, which are very common.

Recall that on the substrate itself, it is Cr/Au making contact with the $MoS_2$. Now, what was found, is that using a tungsten tip actually resulted in an effective gating of the $MoS_2$. The reason for this has to do with the difference in work function between Au and W, which results in a potential difference being applied even when both micromanipulators are kept grounded. This is the same principle behind the voltaic pile, where A. Volta stacked metals of differing WF separated by electrolyte to generate a potential difference. The results are shown in Figure 3.21 (same sample as was shown in Figure 3.20).

This means that gold tips should be used if one does not desire the tips to apply an effective gate potential. Yet, this could be an interesting application to this 2D $MoS_2$ IRM sensing platform, as a metal work function measuring device. That is outside the scope of this work however.

## Charging delays

At this stage it is a good moment to investigate deeper the results that were briefly introduced in Figure 3.18. As was stated, this experiment is a one-way gate ramp at $+400$ mV/s, filmed at

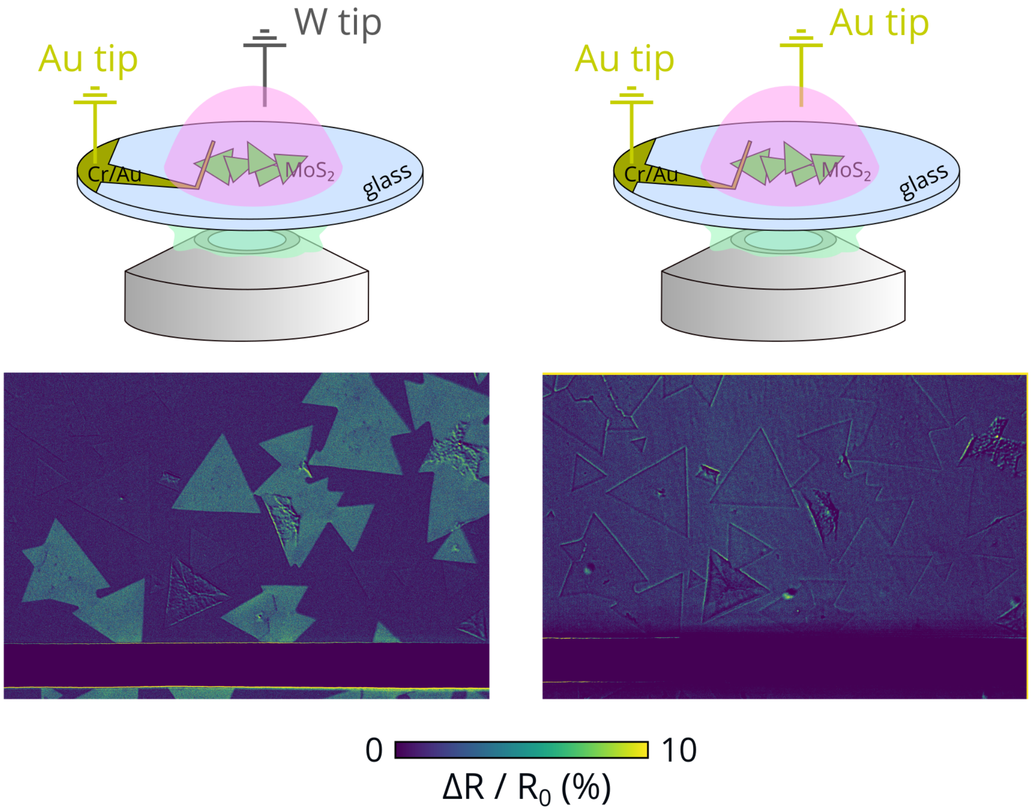

Figure 3.21: The same device as Figure 3.20. Two micromanipulators were grounded, but a tip changed for tungsten (W) for the left column. This reveals that due to the work function difference of the metals, a potential difference is formed, similar to the principle behind a voltatic pile consisting of different metals separated by electrolyte. The response is significant, at several percent.

2 fps. This was done partly due to the fact that there is not a good stability for the NaCl/$H_2O$ electrolyte over multiple cycles (as discussed in the previous sections), and thus a single ramp can convey some interesting results. Furthermore the concentration used in this case was on the higher side ($10^{-1}$ M) which increases the gating efficiency.

In Figure 3.22(a) a 650 nm micrograph is shown (grayscale 0–150), with 4 different square ROIs defined, including the gray one near the electrode (refer back to Figure 3.17 to see the electrode), two ROIs on the triangle-shaped domains (orange and pink) and one on the pentagram domain (blue). The resulting ROI percent reflectance response is shown in (b) as a function of time (bottom axis) and gate bias (upper axis). Corresponding effective charge density images are shown in (c) as a film reel for the frames at 0, 1.5, 2.0, 2.5, 3.0, 3.5, 4.0, 4.5 s which correspond to 0, 0.6, 0.8, 1.0, 1.2, 1.4, 1.6, 1.8 volts of bias. Note that for the first half, a grayscale LUT from 2–5 is used while for the second half the Fire LUT is used in the range 4–20. This was done for better visibility as it is impossible to see the early charging

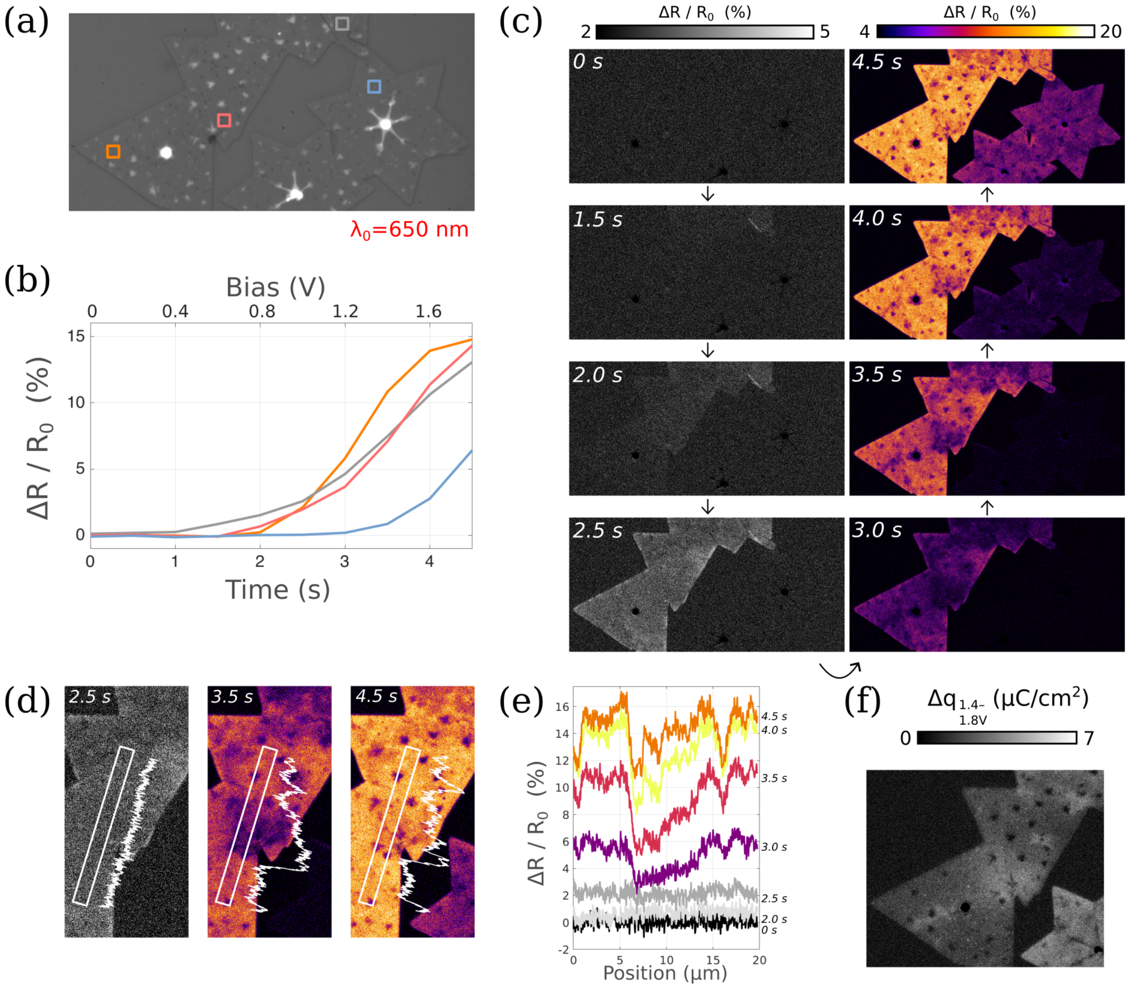

Figure 3.22: (a) Schematic of interference reflection microscope (IRM) with a CVD MoS$_2$ electrolytic capacitor as the system under study. (b) IRM 8-bit micrograph at 450 nm (grayscale range 32–171) in air, showing strong negative contrast of $C \approx 46\%$. (c) Micrographs at 650 nm (range 46–70) in the presence of an electrolyte ($10^{-1}$ M NaCl$_{(aq)}$) and for different applied gate voltages: 0, 1.4 and 1.8 V. (d) False color images of percent change in reflected light, at 1.4 V (upper panel) and 1.8 V (lower panel) using the 0 V image in (c) as reference. Images in (d) directly map the electron density evolution from 0 at 1.4 V, and 0 to 1.8 V, respectively.

without this adjusted LUT and range in the first half.

From the ROI responses in (b) as well as from the film reel in (c), various observations can be made. The first most obvious result is that not all of the domains are reacting at the same rate. The left domains (triangle-like) react first, with the right domains (star-like) react with about a $\sim$ 1.5 s delay. This is evident both from the reel and ROI curves. Most likely, this delay can be attributed to a highly resistive node at the upper star domain, which would cause a resistive delay in this effective RC circuit.

This is intersting because this type of sub-second charging delay is too fast to have been noticed by conventional techniques like KPFM which would need several minutes per scan. Furthermore, if one would be performing capacitive spectroscopy [255] in say MHz range, if one had assumed that the whole surface area of the $MoS_2$ capacitor was reacting the same way, the parameters extracted from the capacitance spectroscopy would be off. A similar principle would hold true when estimating mobility in a FET where the channel surface area is an input parameter.

The role of inter and intra flake resistance is further conveyed by examining the gray, pink, orange, blue ROIs, which react to the bias in that order. The gray ROI, being closed to the electrode, is especially apparent including at the 1.5 s frame where it lights up first, having the least resistive path from the electrode.

Now, it is also apparent that there is some degree of inhomogeneity on the monolayers themselves, which are more visible on some frames compared to others. This is made apparent by taking averaged line ROIs as shown in 3.22(d) for the 2.5, 3.5, 4.5 s frames. While 2.5 s is flat, the 3.5 s is especially contrasted, exhibiting a “valley” of charge, whilst the 4.5 s frame is again more flat. Further profiles are plotted in (e) together with the (d) profiles.

Charge inhomogeneities are common in 2D materials, often resulting from trapped charges in the substrate, or adsorbates. This results in µm-sized variations in the conduction band energy $E_\mathrm{c}$. A significant literature exists that analyze such $E_\mathrm{c}$ variations by Raman and photoluminescence spectroscopies [54, 256], along with scanning probe techniques covered earlier.

The fact that the 3.5 s frame reveals the inhomogeneity valley with such clarity is likely tied to the Fermi level being near the conduction band edge, similarly to the drawing in Figure 3.10(b) from [239] described earlier. The result showcases how XRM the widefield sub-second throughput data has its utility of revealing such charge inhomogeneities in a relatively straightforward manner.

Finally, there is the aspect of converting the percent change in reflectance $\Delta R/R_0$ to change in charge density $\Delta q$. To do this, the model proposed by Zhu et al. [246] was used, of the form $\Delta R/R_0 = \alpha\Delta q$. The orange ROI was used for the fit since it is on a smooth part of the monolayer and with less lag to the applied gate compared with other domains. The slope was found to be $\approx 2.0 \times 10^4$ cm$^2$C$^{-1}$, based on use of the capacitance for $10^{-1}$ M NaCl/$H_2O$ according to [254]. Thus a $\Delta q$ image was calculated for the charging window 3.5–4.5 s (1.4–1.8 V). In this particular window, it is seen that the “valleys” from before appear brighter in (f), which makes sense because since the charge tends to get homogeneous in the

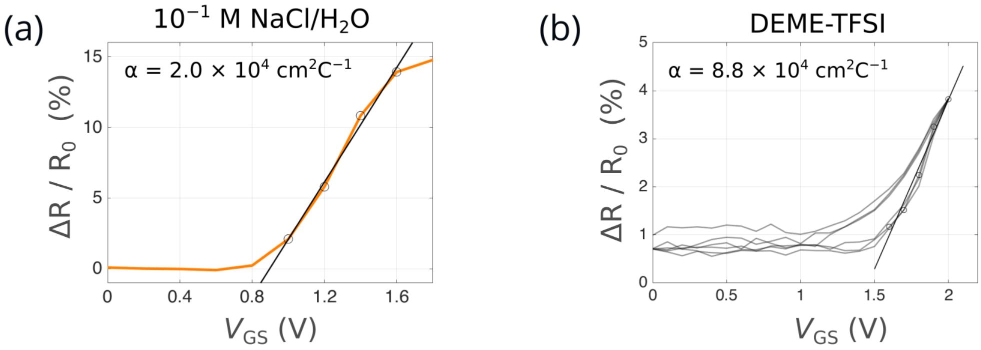

Figure 3.23: Linear fits of $\Delta R/R_0$ vs. gate bias, above threshold ($V_{\text{TH}}$), to extract the $\alpha$-parameter used in the main text for the electrolytes (a) $10^{-1}$ M NaCl$_{\text{(aq)}}$ and (b) DEME-TFSI.

high accumulation regime, the initially depleted puddles experienced a stronger evolution in that charging window.

## 3.2.3 . Capacitive charging with DEME-TFSI

### Stability of DEME-TFSI

Having now explored multiple capacitive cases for the NaCl/$H_2O$ electrolyte, the use of diethylmethyl(2-methoxyethyl)ammonium bis(trifluoromethylsulfonyl)imide (DEME-TFSI) is presented next. Chronologically it was used after the NaCl/$H_2O$ experiments, since we found the stability to multiple cycles of gating to be much improved with this ionic liquid.

The stability is evident in the capacitive cycling in Figure 3.24. The capacitive device is shown with the 450 nm filter in (a) where the best contrast is, after adjusting gamma to 0.05 followed by 225 to 255 grayscale adjustment, for improved visibility. Then the 650 nm filter is used for the charge density imaging, the $t = 0$ frame of which is shown in (b), with two ROIs defined, one on the monolayer (green) and one on the substrate (gray). The gate was then cycled five times between 0 and 2 V in a linear fashion, and the resulting percent change reflectance is shown in (c). It is evident that the cycling is a lot more stable compared with the NaCl/$H_2O$ electrolyte where there was significant drift over multiple cycles as was shown in Figures 3.19 and 3.20. (In this particular experiment there is a drift appearing at 60s which shifts both curves upwards. It appears to be due to the lateral XY drift of the stage in this case.) In 3.24(d) a percent change reflectance image (and thus charge density image) is computed for the times $t_1$ and $t_2$ indicated in (c).

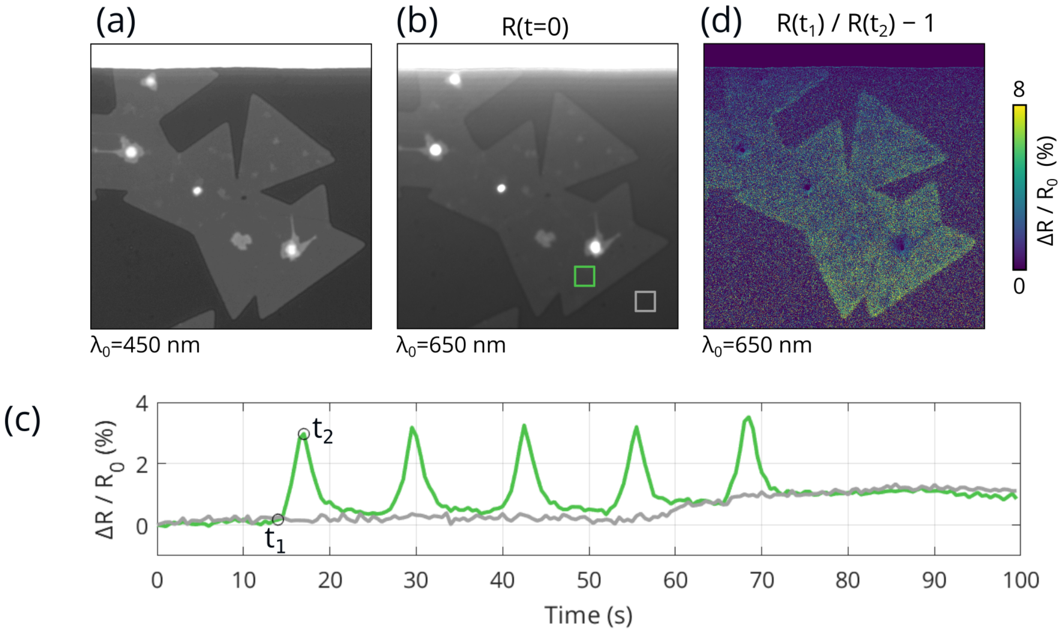

Figure 3.24: (a) 450 nm micrograph, adjusted using $\gamma = 0.05$ and grayscale (225,255). (b) 650 nm micrograph with grayscale (0,150), and two ROIs defined. (c) Resultant percent change reflectance versus time, showing stable cycling response. (d) $\Delta R/R_0$ image computed using $t_1$ and $t_2$ from (c).

## XRM control experiment

Now, throughout the thesis the 650 nm filter was typically used for the charge density imaging, for various reasons. This includes the fact that it enables comparing with the previously mentioned literature that explores charge imaging via the gate-dependent RI of $MoS_2$ [246, 249], and also that it should be quite near the peak of the A exciton. However, in theory there could be advantages to other filters, for example if the wavelength lies in a slope of improved sensitivity between change in $(n, \kappa)$ and IRM/BALM reflectance. Furthermore, it is important to do control experiments to see that significant reflectance changes are not taking place at other wavelengths where optical properties should not be affected by charge density.

Such a control experiment was performed using DEME-TFSI. Namely, to apply a 2 V gate voltage at 12 different bandpass filters, including 400, 450, 550, 590, 600, 610, 620, 630, 640, 650, 660, 700 nm, all with 10 nm bandwidth. The result is shown in Figure 3.25, where (a) contains the resulting $\Delta R/R_0$ images where the minimum intensity was used as the reference to better visualize the magnitude of the change, and in (b), the zero volt case was used as reference, with the ROI result from the rectangles defined in (c). The result corroborates the $\Delta R/R_0$ to the excitonic effect, since two peaks can be seen corresponding to the A and B

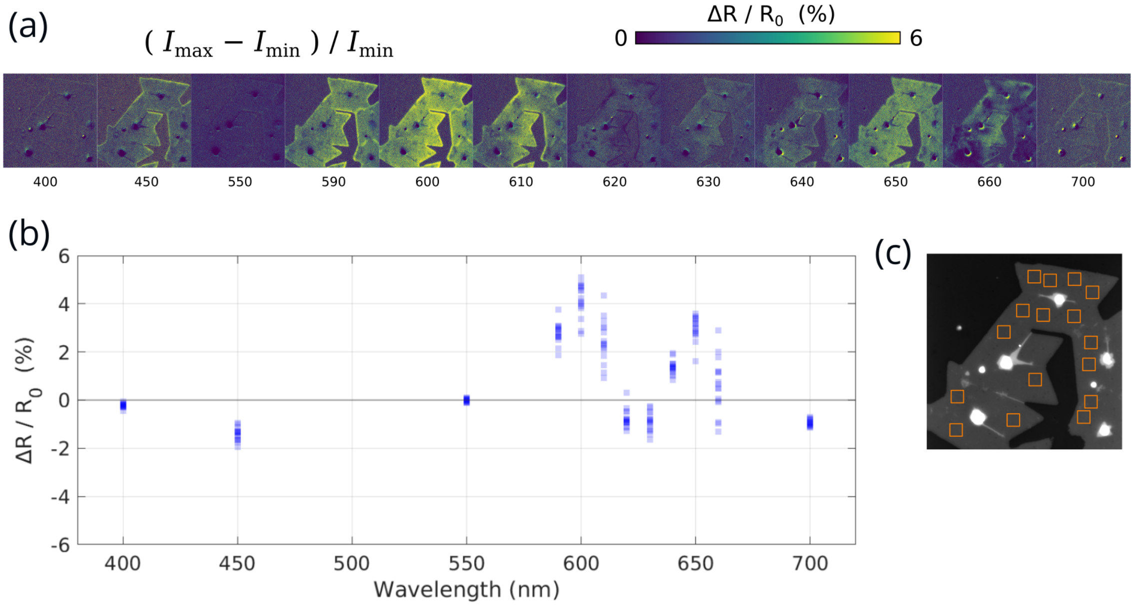

Figure 3.25: (a) $\Delta R/R_0$ response (using minimum intensity $I_{\text{min}}$ as reference) at 12 different bandpass filters of 10 nm bandwidth. (b) Corresponding $\Delta R/R_0$ (with $R(0\,\text{V})$ as reference), for all ROIs defined in (c).

excitons, whilst the effect is less prevalent at other wavelengths, for example completely absent at 550 nm. To the author's knowledge, this is the first time that such charge/reflectance images are measured at multiple bandpass filters in the optical regime, as prior literature utilized mainly a single bandpass for the charge imaging mode [246, 249, 250]. Interestingly, there is some moderate modulation happening at 450 nm. The reason for this is not clear. However it could be related to the fact that the real part of $\tilde{\varepsilon}(\omega)$ has a longer tail far away from the frequencies where the modulations are happening and that the modulation has an interferometric resonance there.

It should also be noted that some wavelengths like 660 nm exhibit a lot of variation across the surface, which is apparent both in the plot in (b) and visually in (a). It could be that 660 nm is more sensitive to local variations in charge. It would be of high interest to explore this further. As this finding came late in the thesis, 650 nm was the main focus in order to compare with literature results [246, 249] as well as being able to compare across many different experiments.

### 650 vs. 660 nm filter

The potential of 660 nm was explored to some extent however although further work would remain to understand why and how it is different from 650 nm filter. There are in fact two aspects related to 660 nm which motivates its potential. The first one is the one previously described, where the $\Delta R/R_0$ images upon gating exhibit a lot more spatial variations compared with the 650 nm case. The second finding, is that even without gating, variations across a flake can in fact be discerned.

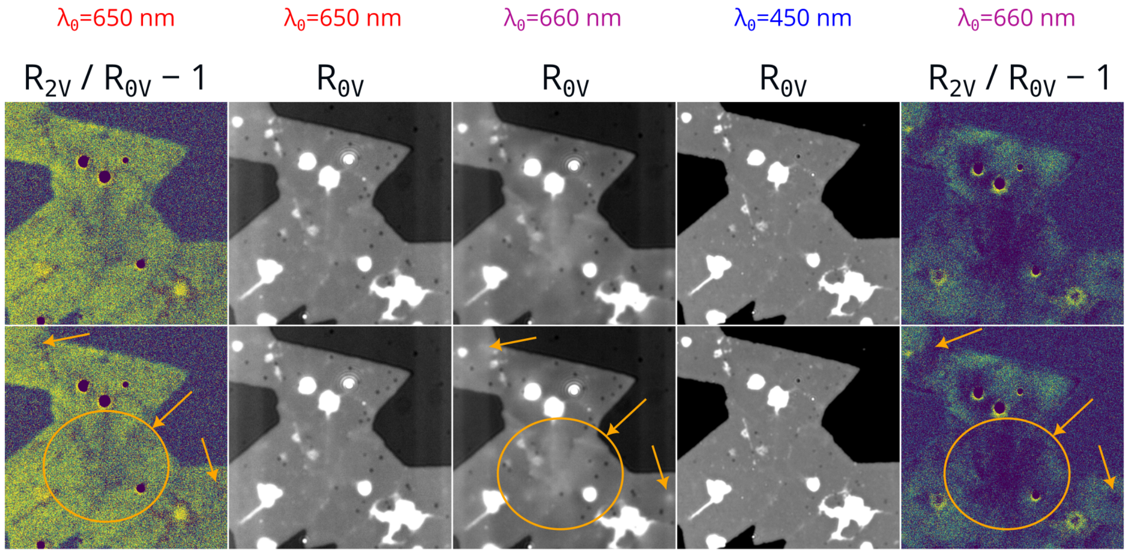

Figure 3.26: Left-most and right-most are $\Delta R/R_0$ images at 2 V gate at 650 and 660 nm bandpass filters respectively. Three middle images are with zero bias (with adjusted grayscale), for 650, 660, 450 nm. Arrows and circles indicate that grayscale inhomogeneities can be seen with 0 V 660 nm center image, as also seen clearly in the left-most and right-most gated responses. This means 660 nm is a wavelength whereby the local charge landscape may be visible without needing to apply a gate. The grayscale inhomogeneity is completely absent in the 450 nm case.

Consider Figure 3.26. Here, the same flake was imaged at 0 V for the cases 450, 650, 660 nm. Also, the $\Delta R/R_0$ at 2 V cases are shown for 650 and 660 nm. When comparing the 450 and 660 case, it is clear from the indicated orange arrows how there are inhomogeneities visible only in 660 that are not at all visible with 450 nm (the 650 nm has a faint hint of those inhomogeneities as well). Upon gating, the indicated inhomogeneities are even more visible with the 660 nm case, and also slightly better visible for the 650 nm case. It would seem logical that indeed the 660 nm static image is revealing local variations in static charge density. This is a significant finding because it means that in these IRM conditions in widefield with the proper band filter one can visualize variations in charge in a 2D TMD without more sophisticated techniques like Raman or KPFM. To the author's knowedge this is the first time such a finding is reported.

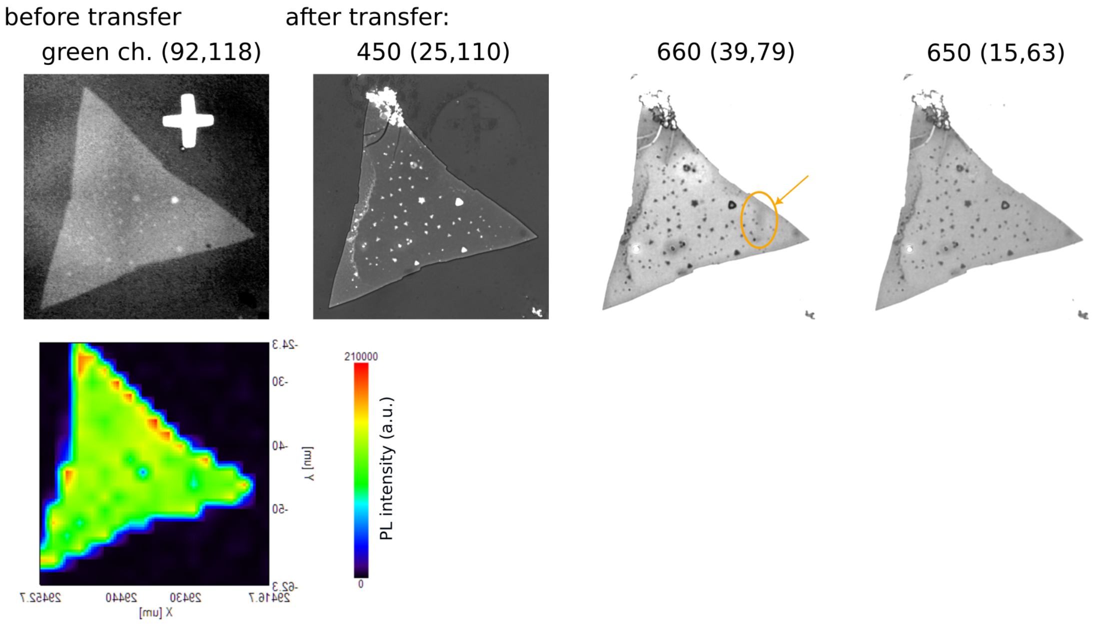

Figure 3.27: CVD $MoS_2$ flake grown at LICSEN, imaged before transfer in top left, where green channel at adjusted grayscale is shown. PL intensity map (bottom left) also acquired. After transfer to ARA substrate, IRM/BALM images were acquired at 450, 660, 650 nm, and grayscale adjusted. Orange arrow indicates a grayscale inhomogeneity that is visible in 660 nm but not 450 nm.

A second investigation of the 660 nm case is reproduced in Figure 3.27. The first micrograph is the flake on $SiO_2/Si$ in white light, where the green channel was taken and adjusted. The next three micrographs are after transfer to a BALM ARA substrate, at wavelengths 450, 660, 650 nm with adjusted grayscale. Finally the photoluminescence map (previously shown in Figure 1.16) taken by *OptMatLab* is reproduced. Again an orange arrow indicates a grayscale variation which is absent in the 650 case. It is interesting to see if a Raman and or/PL map would reveal the same inhomogeneity as one revealed by a 660 nm micrograph. It is difficult to say for this particular case, but further study of this would be very revealing and of interest to the 2D material community. Finally, this is a good illustration of improved visibility/contrast that is possible via IRM/BALM compared with the white light micrograph from a conventional upright reflection microscope. The adlayers are much more visible and better resolved (including additional defects due to imperfect transfer in this particular example).

# 3.3 . Results: $MoS_2$ FET electrical measurements

Before diving into charge imaging of FETs, it is of relevance to present electrical characterization that was performed with the ionic liquid DEME-TFSI. For that purpose, an interdigitated FET configuration was realized for 2D $MoS_2$ on $SiO_2/p^{++}$-Si. This geometry makes it so that the current is dominated by $MoS_2$ channel resistance instead of being majorly shorted across the electrolyte. An SEM micrograph of the device is shown in Figure 3.28(a).

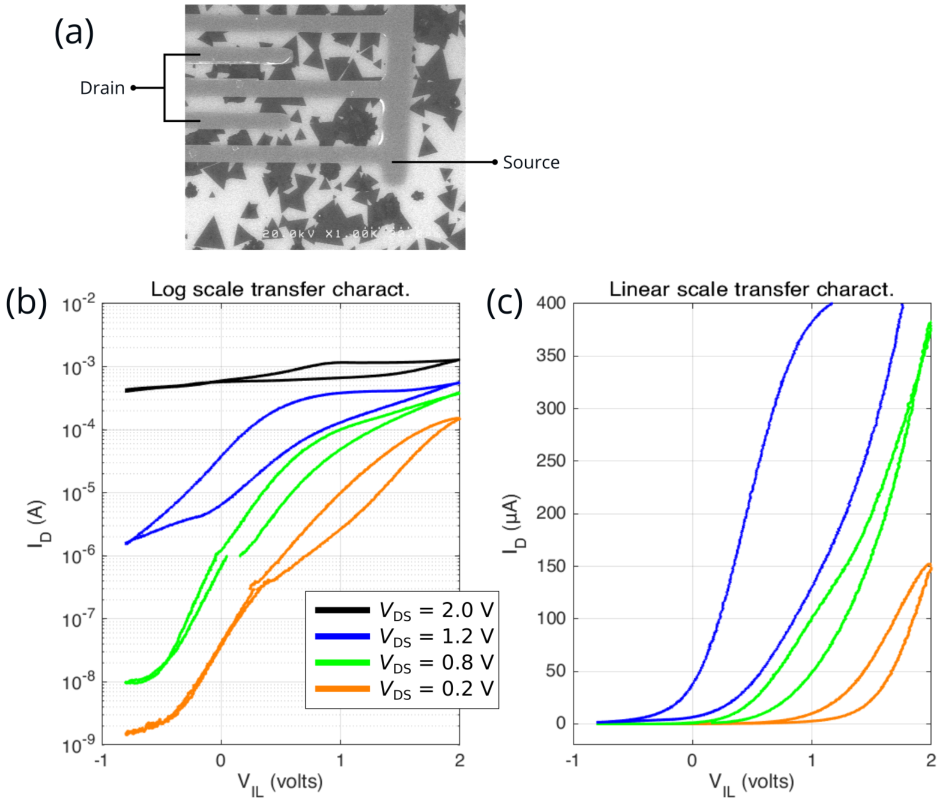

Figure 3.28: (a) SEM micrograph of a 2D $MoS_2$ FET on 150 nm $SiO_2$/Si, consisting of inter-digitated source and drain. (b) Log-scale and (c) linear-scale transfer characteristic with ionic liquid (IL) top-gate, with varying $V_{DS}$ as indicated.

The gate-sweep transfer characteristic was then attained, as shown in log an linear scale in (b) and (c) respectively. The green and orange curves were acquired in two steps to adjust the current amplifier gauge so as to better measure the small current in the OFF-state. At $V_{DS} = 0.2$ V the ON-OFF ratio is about $10^5$ which is quite good, and notice this is attained within the narrow range of $-1$ to $+2$ V gate swing, thanks to the high gating efficiency of the ionic liquid. At higher drains the ON-OFF ratio is significantly reduced, and in fact the drain itself is turning the channel ON.

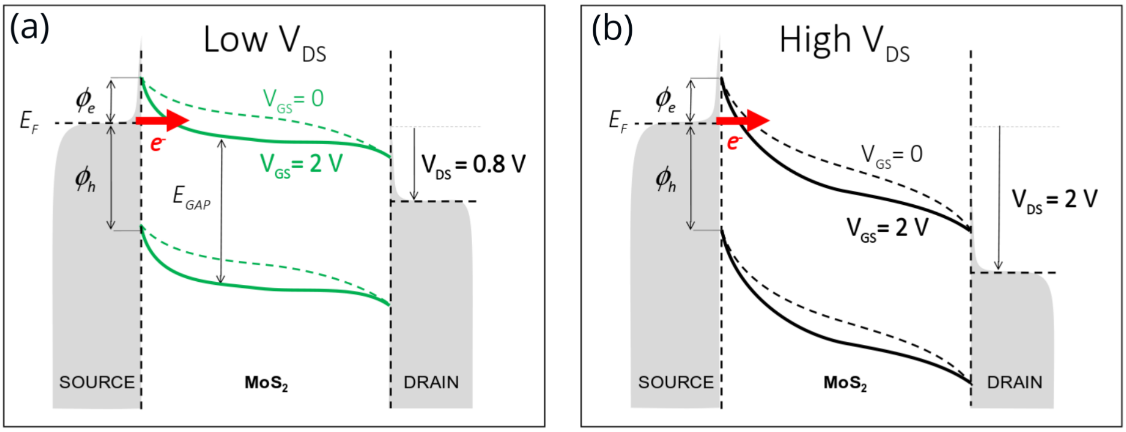

Figure 3.29: Band diagrams for (a) low $V_{\mathrm{DS}}$ and (b) high $V_{\mathrm{DS}}$, which explain the physical origin of Schottky barrier FET behavior.

This is due to what can be termed drain induced barrier thinning (DIBT), as opposed to a different yet related phenomenon called drain induced barrier lowering (DIBL) in conventional silicon MOSFETs (DIBL is not relevant here for Schottky barrier FETs). The effect of $V_{\mathrm{DS}}$ on the ON-OFF ratio in Schottky barrier FETs is illustrated in Figure 3.29. At low and moderate $V_{\mathrm{DS}}$, for example at $V_{\mathrm{DS}}$=0.8 V corresponding to the green curve in Figure 3.28 and the (a) part of Figure 3.29, $V_{\mathrm{DS}}$ has no impact on the band bending profile close to the source contact, where electron injection occurs. The switching is thus classically controlled by the gate potential alone, which in such Schottky barrier FET controls the Schottky barrier transparency at the source (as discussed earlier with Figure 3.2 in section 3.1.2).

Conversely, at high $V_{\mathrm{DS}}$, for example for $V_{\mathrm{DS}}$=2 V corresponding to the black curve in Figure 3.28 and the (b) part of Figure 3.29, the drain bias has a very strong impact on the band bending profile all the way to the source side. By thinning the Schottky barrier at the source, $V_{\mathrm{DS}}$ is able to turn the FET ON even at $V_{\mathrm{GS}}$=0. As $V_{\mathrm{DS}}$ is increased, the gate is progressively losing its control over the device switching and the ON-OFF ratio is lost. At the same time, this strong impact of $V_{\mathrm{DS}}$ is accompanied by a strong shift of the threshold voltage ($V_{\mathrm{TH}}$) as clearly observed in the linear scale transfer characteristics of Figure 3.28(c). Note that this discussion will be very important when observing in operando by XRM the charge density evolution in FET as a function of both $V_{\mathrm{DS}}$ and $V_{\mathrm{GS}}$.

For the later conversions from $\Delta R/R_0$ to $\Delta q$, it is important to estimate the capacitance of this ionic liquid. In the literature, a variety of values have been reported. One paper from Perera et al. 2013 [257] reported $C_{\mathsf{IL}} = 1.55$ µF/cm$^2$. Hu et al. 2017 [167] measured the frequency-dependent capacitance from $10^{-2}$ to $10^6$ Hz. For 1 Hz they measured $\sim$ 1.6 µF/cm$^2$ while it could go up to 4 µF/cm$^2$ for $10^{-2}$ Hz (beware there is a typo in their plot in SI it should be µF not mF).

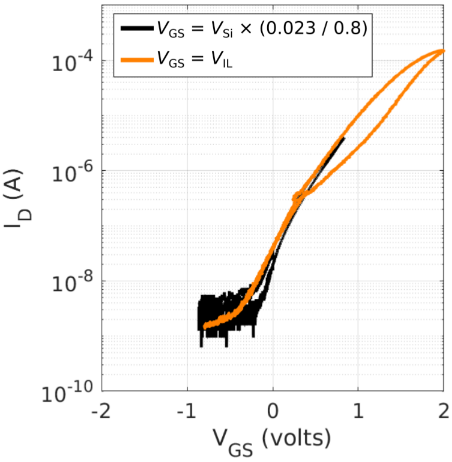

Figure 3.30: Overlay of the transfer characteristics of the same MoS$_2$ FETs controlled by the DEME-TFSI ionic liquid (IL) gate (orange) and by the 150 nm SiO$_2$/Si back-gate (black). The black curve was multiplied by a factor 0.023/0.8 which results in an estimate for the electrical double layer (EDL) capacitance $C_{\mathsf{EDL}}$.

To estimate the capacitance, gate sweeps were performed both with the ionic liquid as well as with the well-defined solid-state backgate of 150 nm SiO$_2$/Si. Since the static permittivity of amorphous SiO$_2$ is $\varepsilon_s = 3.9$, then

$$C_{\mathsf{SiO_2}} = \frac{\varepsilon_s \varepsilon_0}{d_{\mathsf{SiO_2}}} = \frac{3.9\varepsilon_0}{(150\ \mathrm{nm})} = 0.023\ \mu\mathrm{F/cm}^2$$

$C_{\mathsf{IL}}$ can then be estimated by overlaying the transfer characteristic of both cases and multiplying $V_{\mathsf{Si}}$ by a factor that reveals $C_{\mathsf{IL}}$:

$$V_{\mathsf{IL}} = \frac{C_{\mathsf{SiO_2}}}{C_{\mathsf{EDL}}} V_{\mathsf{Si}} = \frac{0.023}{C_{\mathsf{EDL}}} V_{\mathsf{Si}}$$

Based on this exercise, it was found that in this case $C_{\mathsf{IL}}$= 0.8 µF/cm$^2$ provides a reasonable overlay, as shown in Figure 3.30.

# 3.4 . Results: FET operation with DEME-TFSI

Having covered the superior stability of capacitive gating in DEME-TFSI electrolyte when compared with NaCl$_{(aq)}$, I now shall cover IL-gated FET studies that were performed with XRM.

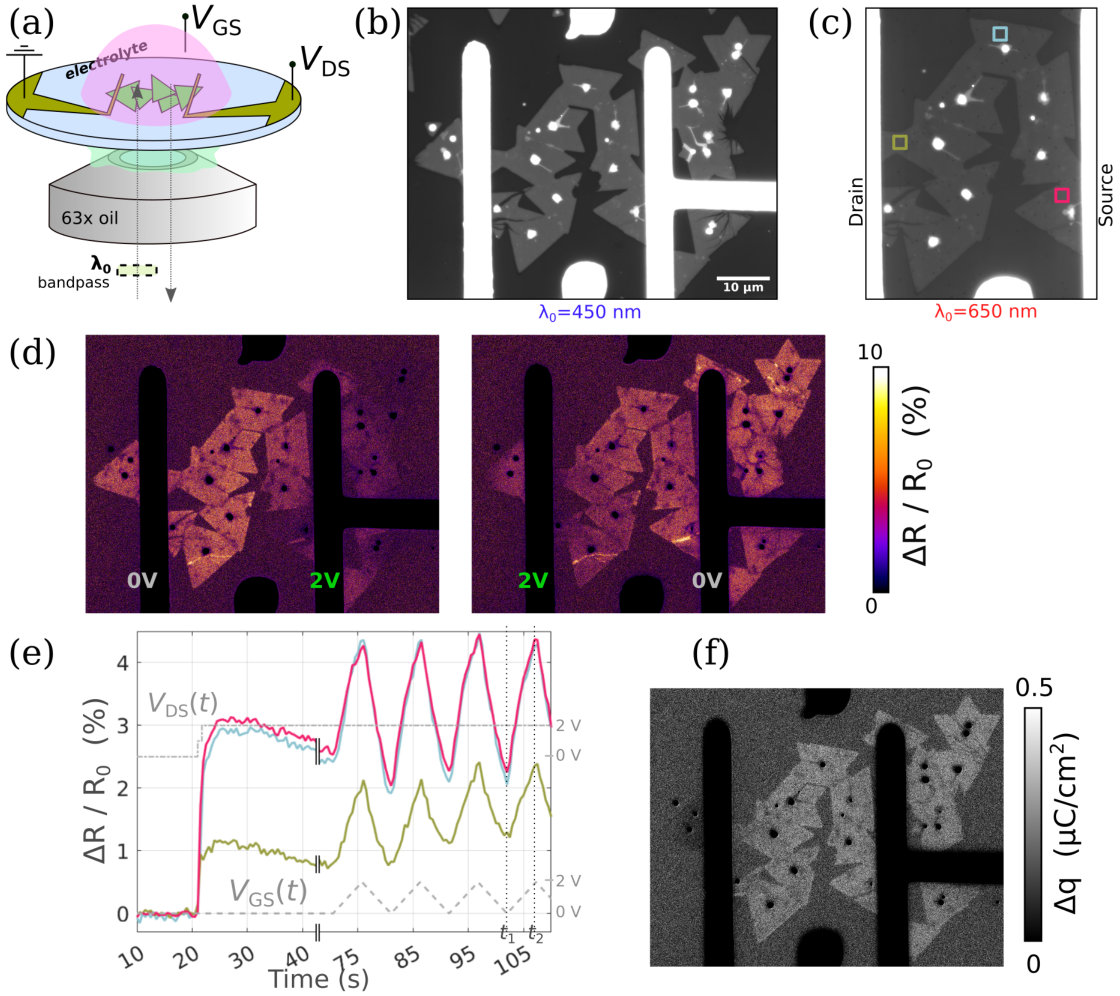

Figure 3.31: (a) Drawing of IL-gated MoS$_2$ FET coupled with IRM. (b) 8-bit micrograph (0–200 range) at 450 nm with electrolyte added, resulting in a high contrast $C = +98\%$. (c) 650 nm (0–255 range) with ROIs indicated, for XRM. (d) Percent change reflectance images for $V_{\mathrm{DS}} = 2$ V applied first on the right electrode (left panel) and then on the left electrode (right panel). (e) ROI reflectance changes as a function of time and bias. The applied $V_{\mathrm{DS}}$ and $V_{\mathrm{GS}}$ are indicated on the right $Y$-axis. (f) $\Delta q$ CDP computed for the time range $t_1 = 102$ s to $t_2 = 107$ s using $\alpha = 8.8 \times 10^4$ cm$^2$C$^{-1}$.

An IL-gated FET was realized in the configuration shown in Figure 3.31(a). A 450 nm micrograph is shown in (b) which was taken after the DEME-TFSI IL was added.

As discussed earlier the contrast attained with this ionic liquid is at 450 nm is the most optimal, with a value of $C_{\text{pc}} = 98\%$ for the monolayer. In (c) a 650 nm micrograph is shown, which is suitable for the XRM mode for charge density imaging. Three ROIs are defined as shown by the colored squares, including close to the source, close to the drain and in the central part of the channel. The channel consists of interconnected crystalline monolayer $MoS_2$ domains separated by grain boundaries.

As a first test, a drain bias of 2 volts was applied on the right electrode with the source and gate held at 0 volt. The same was then repeated with the drain and source swapped. The percent change in reflectivity was computed for both cases and is shown in 3.31(d). Clearly, there is a strong charge accumulation in the channel associated with a significant charge gradient from source to drain in a decreasing fashion. This is the expected behavior for a Schottky-barrier FET in the ON-state. Note that while $V_{\text{GS}}$=0 in this particular case, the use of a high drain bias (2 V) is sufficient to turn the transistor ON, as confirmed by the electrical measurements from Figure 3.28.

To further illustrate the technique, a video was recorded at 2 fps where a drain bias of 2 V is applied at $t = 20$ s and held constant, while the gate is swept multiple times between 0 and 2 V at 400 mV/s starting at $t$ =70 s. The reflectance change extracted from the 3 ROIs indicated in Fig. 3(c) is plotted as a function of time in (e) using the t=11 s frame as the reference $R_0$. (Also, the right-most image of (d) corresponds to $\Delta R/R_0[t = 22.5 \text{ s}]$ of this video). The plot first confirms the formation of a charge density gradient from source to drain when $V_{\text{DS}}$=2 V is initially applied (the red curve corresponding to a three time stronger contrast compared to the green curve). It also indicates that the charge density in the center of the channel (blue curve) is mostly following the one on the source side, as expected in such FET in the ON-state. Then, once the gate bias is swept, the contrast is clearly modulated. This way of extracting data from an XRM experiment allows directly assessing: (i) the respective efficiency of $V_{\text{DS}}$ and $V_{\text{GS}}$ in fixing the charge density at any point along the channel, (ii) the stability of the charging/discharging upon multiple $V_{\text{GS}}$ sweep cycles, (iii) the evolution of the charge density when both $V_{\text{DS}}$ and $V_{\text{GS}}$ are kept constant. For example, one can observe a slow decay of the charge density in the 25 s to 65 s time range. This expected behavior is similar to the decay of the ON-state current observed in electrical measurements at fixed bias for all types of nanomaterial-based FETs. It is related to the progressive trapping of charges either in defects of the material channel itself, or in the gate dielectric or in adsorbed molecules.

Such charge trapping leads to the commonly observed hysteresis in the $I_D(V_{DS})$ characteristics present in virtually all $MoS_2$-FET studies, when $MoS_2$ lies on $SiO_2$ or other dielectrics with a significant density of shallow trap states. Finally, the third way of extracting data from XRM videos consists in computing $\Delta q$ maps in particular bias ranges. (f) displays such a $\Delta q$ map extracted from one of the gate sweeps (0 → 2 V) between $t_1$ =102 s and $t_2$ =107 s (marked with dotted lines in (e)) obtained using an alpha value of $\alpha = 8.8 \times 10^4$ cm$^2$C$^{-1}$. Based on this, the near-drain (green) ROI experiences a $\Delta q$ of $\sim$ 0.12 µC/cm$^2$ in this time range, whilst the channel center (blue) and near-source (red) both experience $\Delta q$ of $\sim$ 0.24 µC/cm$^2$ ($\sim$ $1.5 \times 10^{12}$ electrons/cm$^2$).

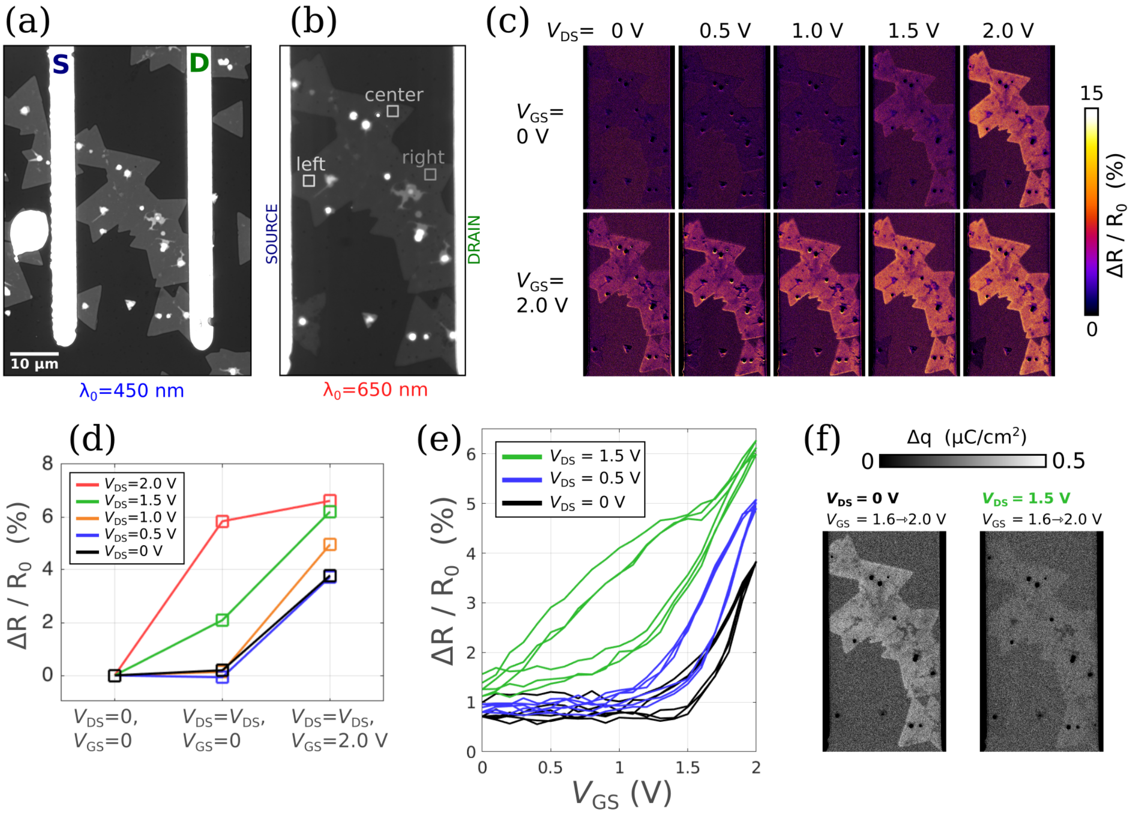

Figure 3.32: (a) IRM 8-bit micrograph (range 0–150) at 450 nm with electrolyte, of an FET device, and (b) at 650 nm (range 0–255) with 3 ROIs defined. (c) Effect of drain and gate biases on $\Delta R/R_0$ for drain values 0, 0.5, 1.0, 1.5, 2.0 V and gate values of 0 V (upper row) and then 2.0 V (lower row), with (d) corresponding plot for the ROI defined at the center of the channel. (e) Reflectance change vs. gate voltage. (f) Charge density images generated using $\alpha = 8.8 \times 10^4$ cm$^2$C$^{-1}$ in $V_{GS}$ window 1.6 to 2.0 V.

In Figure 3.31, a 2 V source–drain bias was used for clarity due to its strong impact on the reflectivity. It is however an unconventionally high $V_{DS}$, able to turn ON the device even at $V_{GS}$=0. FETs are more commonly operated at low to moderate $V_{DS}$ so that the gate bias dominates the control of the charge in the channel. Thus, the next portion will focus on XRM across a range of $V_{\mathrm{DS}}$, and how it can be used to directly visualize this $V_{\mathrm{DS}}$, $V_{\mathrm{GS}}$ competition for control of the channel charge.

To that end, a second FET device was realized, shown in Figure 3.32(a) at 450 nm with high contrast. (b) is taken at 650 nm, the compatible wavelength for XRM condition, with 3 ROIs defined, situated near source, near channel center and near drain. Voltages of $V_{\mathrm{DS}}$=0, 0.5, 1.0, 1.5 and 2.0 V were explored for the drain. For the gate, a maximum of $V_{\mathrm{GS}}$=2 V was applied for each case. Micrographs of reflectivity change corresponding to these ten ($V_{\mathrm{DS}}$, $V_{\mathrm{GS}}$) conditions are shown in (c). The $V_{\mathrm{DS}}$=0 to $V_{\mathrm{DS}}$=1 V cases correspond to typical n-type FET operation with little charge in the channel for $V_{\mathrm{GS}}$=0 and strong electron accumulation observed at $V_{\mathrm{GS}}$=2 V. Increasing $V_{\mathrm{DS}}$ to 1.5 V and eventually 2 V induces electron accumulation even at $V_{\mathrm{GS}}$=0 (as discussed earlier for Figure 3.31). Unsurprisingly, combining $V_{\mathrm{DS}}$=2 V and $V_{\mathrm{GS}}$=2 V leads to the maximum charge density in the channel. This is in close agreement with typical electrical measurements of $\mathrm{MoS_2}$-FETs using such ionic liquid as gate electrolyte, as exemplified in the electrical characteristic from Figure 3.28.

To quantify this balance of $V_{\mathrm{DS}}$ vs. $V_{\mathrm{GS}}$ efficiency in fixing the charge, the response at the center ROI are plotted in Figure 3.32(d). The other ROIs along with other data are shown in Figure 3.33. The ability to isolate any ROI along the channel is of significant utility of XRM, allowing for CDP analysis at any ($V_{\mathrm{DS}}$, $V_{\mathrm{GS}}$) polarization point and any position along the channel.

Next, the results of the videos taken at $V_{\mathrm{DS}}$ = 0, 0.5 and 1.5 V while the gate was swept back and forth from charge depletion ($V_{\mathrm{GS}}$=0 V) to charge accumulation ($V_{\mathrm{GS}}$=2 V), at a rate of 200 mV/s, are presented. The reflectance change is plotted as a function of time in 3.33(c) and as a function of $V_{\mathrm{GS}}$ in 3.32(d). Interestingly, these optical $\Delta R/R_0(V_{\mathrm{GS}})$ curves bear strong similarities with conventional electrical transfer characteristics $I_{\mathrm{D}}(V_{\mathrm{GS}})$. In particular, they both allow extracting the gate efficiency above the threshold voltage (in the form of a transconductance for electrical measurements or here, in the form of a "trans-reflectance") and to assess the level of trapped-charge related hysteresis, when alternating the gate sweep direction. Yet, reflectivity intrinsically contains two unique features: (i) since charge is measured in place of current, data can be collected at $V_{\mathrm{DS}}$=0V, in the absence of current flow, (ii) in place of a global current as the only observable, reflectivity is measured locally so that inhomogeneties in the channel are directly mapped. As already observed in the case of capacitors in Figure 3.22,

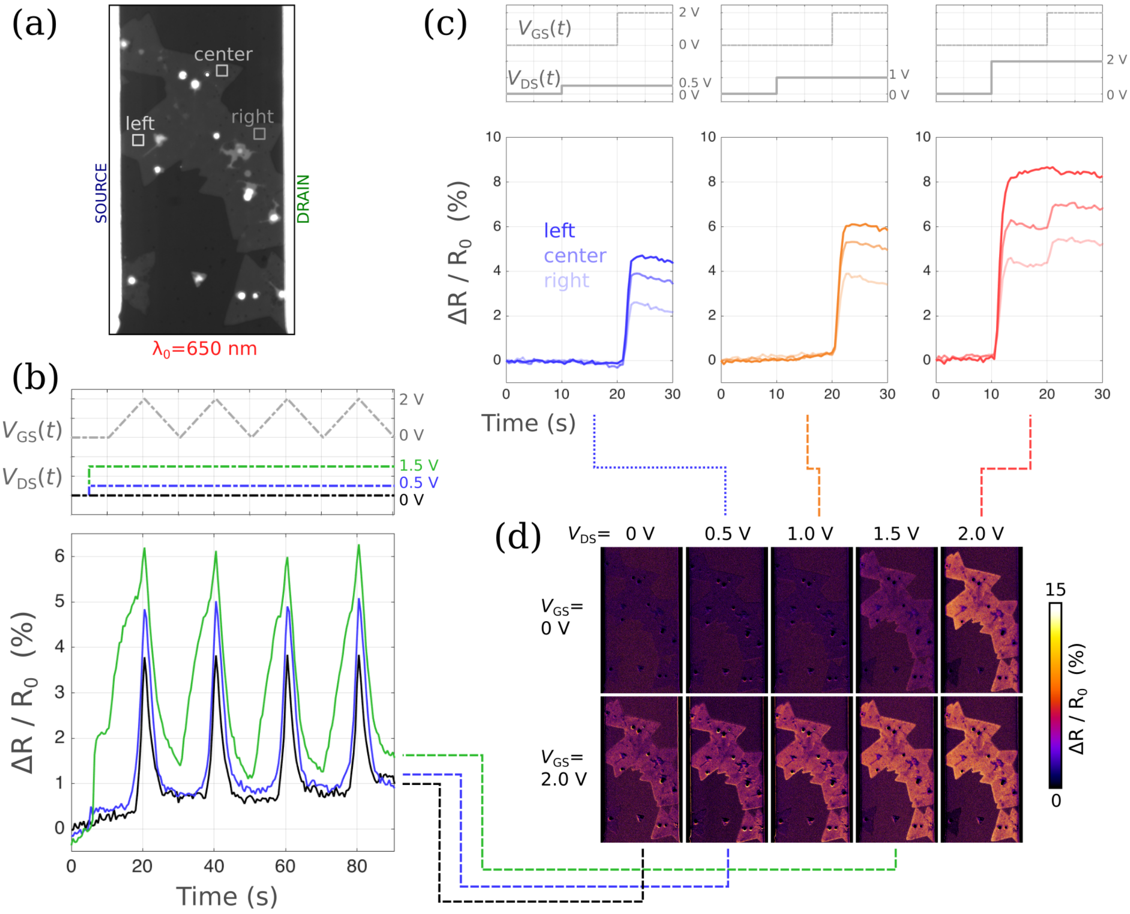

Figure 3.33: (a) ROIs of 1.47 × 1.47 $\mu$m$^2$ at left, center and right areas along the channel. (b) Top: schematic of the applied $V_{\mathrm{DS}}(t)$ and $V_{\mathrm{GS}}(t)$ for the cases $V_{\mathrm{DS}} = 0, 0.5, 1.5$ V. Bottom: $\Delta R/R_0$ versus time. (c) Top: Schematic of the applied $V_{\mathrm{DS}}(t)$ and $V_{\mathrm{GS}}(t)$ for the cases $V_{\mathrm{DS}}$ =0.5, 1.0, 2.0 V, with (middle) the corresponding 2 fps percent change reflectances and (bottom) the corresponding $\Delta R/R_0$ charge density images.

not all the flakes are identically well connected so that the effective channel can significantly differ from the geometrically defined one.

Finally, using the $V_{\mathrm{DS}}$=0 case (black curve in (e)) as a reference, the alpha parameter was fitted and found to be $\alpha = 8.8 \times 10^4$ cm$^2$C$^{-1}$ shown in the earlier Figure 3.23(b). Using this, CDP images were generated and are presented in 3.32(f) for the gate bias range 1.6–2.0 V (time range 38.5–40.5 s) for the case of $V_{\mathrm{DS}}$=0 (left) and $V_{\mathrm{DS}}$=1.5 V (right). They indicate that the gate is altering the CDP to a lesser extent at $V_{\mathrm{DS}}$=1.5 V when compared with $V_{\mathrm{DS}}$=0 V, in that regime. This is in agreement with the increased impact of the drain in fixing the charge when the transistor is operated at high $V_{\mathrm{DS}}$. Note that the left map of 3.32(f) (obtained at $V_{\mathrm{DS}}$=0) corresponds to a gate bias swing starting at 1.6 V. This bias also corresponds to the threshold voltage of the reflectivity change (as seen from the black curve in (e)). It is thus reasonable to consider this $\Delta q$ map to be simply a $q$ map (the charge at $V_{\mathrm{TH}}$ being negligible compared to the charge in the ON-state).

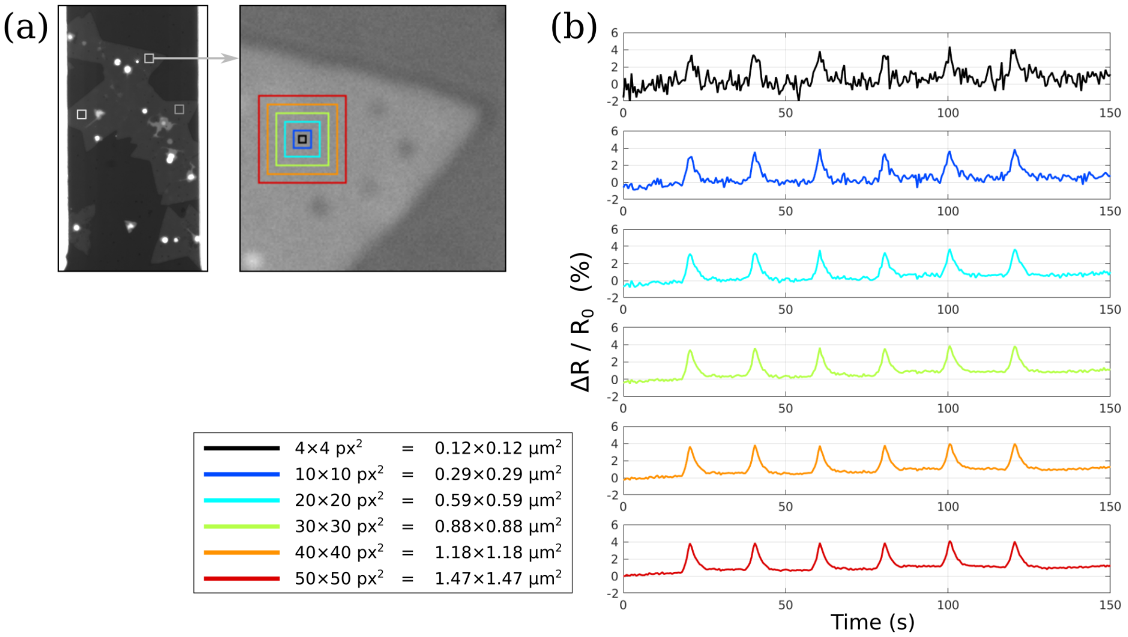

Figure 3.34: Effect of size of ROI, tested for the cases indicated in (a) in the center of the channel (grayscale is 0–100 for top image). (b) $V_{\mathrm{GS}}$ was oscillated between 0 to 2 V at 200 mV/s, and resulting percent change reflectance curves are shown, with pixel and µm areas indicated in legend.

As one of the main assets of XRM is its capability to map charge density evolution along the channel, one important aspect concerns the size of the ROI which is required to correctly extract device parameters. To explore this point, we calculated $\Delta R/R_0$ for a range of ROIs that vary in size but are centered at the same point, where a gate was swept back and forth to capacitively charge and discharge the monolayer $\mathrm{MoS_2}$. The time-dependent traces were thus plotted for 6 ROIs that vary from $50 \times 50$ pixels ($\sim 1.47 \times 1.47$ µm$^2$) down to $4 \times 4$ pixels ($\sim 0.12 \times 0.12$ µm$^2$), shown in Figure 3.34. We found that the gate modulation effect is still easily distinguishable from the noise even down to the smallest ROI, whilst $10 \times 10$ pixels ($\sim 0.29 \times 0.29$ µm$^2$) can be considered the lower limit of usable signal to extract the "trans-reflectance" mentioned earlier.

# 3.5 . Results: Transmittance spectra during gating

Transmittance spectra during gating were acquired. A sample was prepared consisting of inter-connected CVD 2D $MoS_2$ monolayers, where on the denser side a shadow mask was used to evaporated Cr/Au. The beam in the UV-Vis transmittance spectrumeter is about 7 mm in height and 1 mm in width.

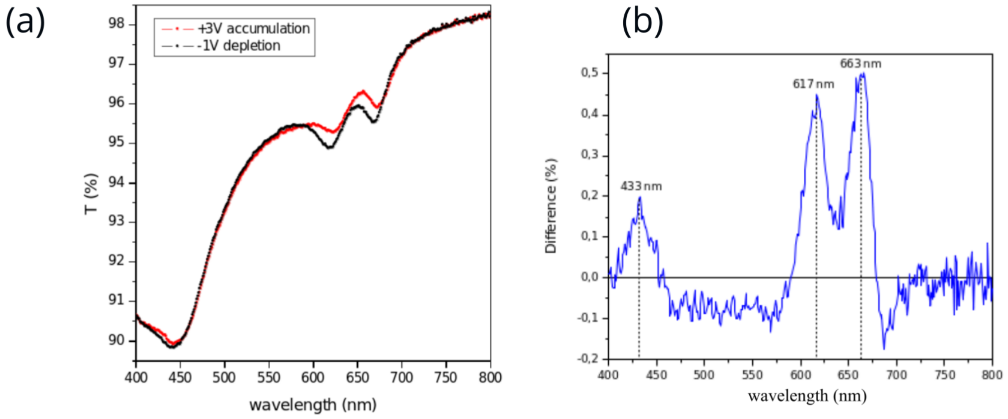

Figure 3.35: (a) Transmittance spectrum of 2D $MoS_2$ at DEME-TFSI gated values of $-1$ V (depletion, black) and $+3$ V (accumulation, red). (b) Difference of curves in (a), showing maxima at 663 nm (A exciton) and 617 nm (B exciton). Some modulation also takes place around 433 nm.

In Figure 3.35(a) a UV-Vis transmittance spectrum is shown of the inter-connected 2D $MoS_2$, at gate voltages of $-1$ V (depletion) and $+3$ V (accumulation). In (b) the difference between the two is plotted. From these results, it is reassuring that primarily the modulation that does occur in the optical properties is indeed near the two excitonic energies. In this particular case the maxima of modulation take place at 617 nm and 663 nm. These maxima would not necessarily be the same in the IRM/BAIM configuration due to the reasons explored earlier such as the distribution of angles, the optical properties of each layer of the optical stack, and so on. Nevertheless this information is useful. There is also a peak around 433 nm, which recalls the slight modulation seen at 450 nm in Figure 3.25. It could be associated with the C exciton or other phenomena. Further investigation would be needed to determine its origin.

Further data was taken at additional voltages between $-1$ and $+3$ V at steps of 0.5 V as shown in Figure 3.36(a). To get an idea of the behavior as a function of voltage, the wavelengths of

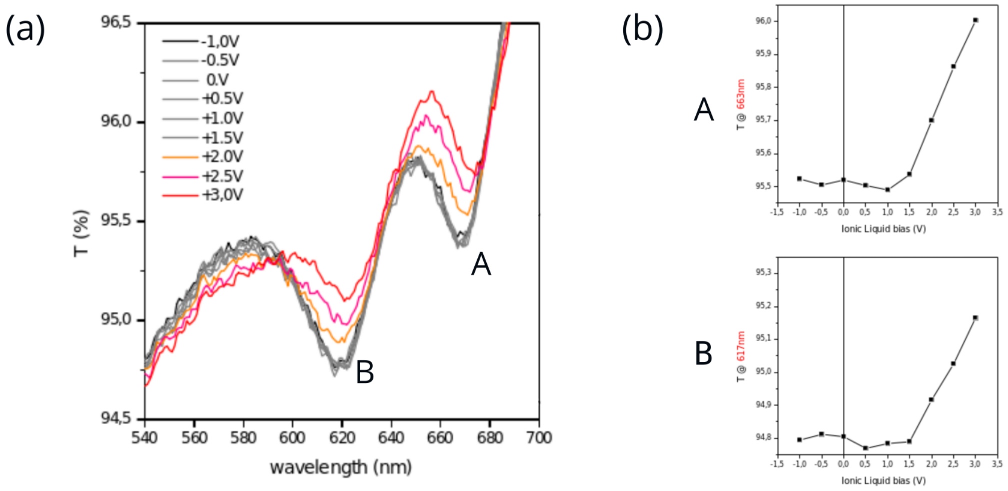

Figure 3.36: (a) Transmittance spectra at 9 different gate voltages via DEME-TFSI ionic liquid, with A and B excitons labeled. (b) Result plotted as a function of gate voltage for the wavelengths 663 nm (A exciton) and 617 nm (B exciton).

663 and 617 nm were chosen from the A and B excitons respectively, as shown in (b). From these results it is seen that only at $1.5$ V and above does a modulation actually start to take place. This is where the shift in spectral weight from neutral exciton to trion starts to become significant [252]. It is also indicative of a $V_{\mathrm{TH}}$ value that is probably greater than 0, consistent with the electrical measurements discussed earlier.

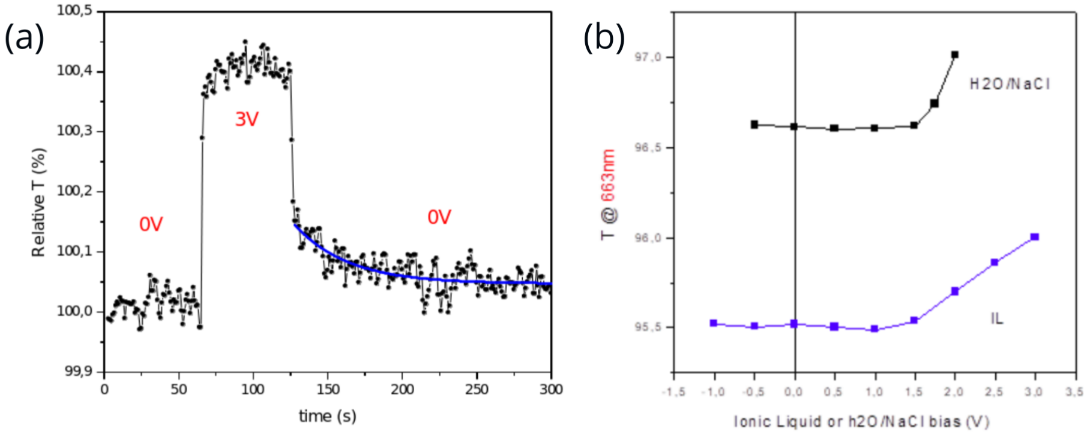

Figure 3.37: (a) Relative $T$(%) measured as a function of time at 663 nm (A exciton), where gate was pulsed to $3$ V and then back to 0 V. The result reveals a decay on the order of seconds/minutes. (b) $T$(%) response versus gate for both DEME-TFSI ionic liquid and for $\mathrm{NaCl_{(aq)}}$ electrolyte.

Pulses as a function of time were also explored, which are shown in Figure 3.37(a). From these results, the pulse up to 3 V from 0 V results in a near immediate response at the sub-second time-scale. However when pulsing back to 0 V, there is a slow decay which appears on the order of minutes. This seems to indicate a trapping/detrapping mechanism of charges induced by the gating, most probably in the dielectric under the $MoS_2$.

In Figure 3.37(b), a result for 663 nm is also reproduced using the $NaCl_{(aq)}$ as well as the DEME-TFSI IL. It is seen that the response for the $NaCl_{(aq)}$ is steeper, which is consistent with its higher capacitance [254] discussed earlier.

# 3.6 . Results: $MoS_2$ devices studied by BALM

As discussed previously, it would be of high interest to attain a charge density imaging configuration based on XRM for 2D $MoS_2$, using a more conventional solid-state FET configuration, and furthermore with a BALM optical stack. A solid-state configuration is more "classical" and would allow for measuring the current–voltage characteristics while simultaneously imaging the charge. Furthermore, as covered before the Cr/Au ARA layer can double as both a FP resonator and a back-gate, while $AlO_x$ is used as a dielectric and also FP resonator.

## 3.6.1 . Microfabrication steps

In order to microfabricate capacitive and FET devices consisting of the $\sim 170\ \mu m$ glass coverslip, the Cr/Au anti-reflective absorbing (ARA) layer, a dielectric layer of $AlO_x$, and finally the 2D $MoS_2$ with micro/nano-fabricated metal contacts on top, a complex series of steps had to be developed and realized.

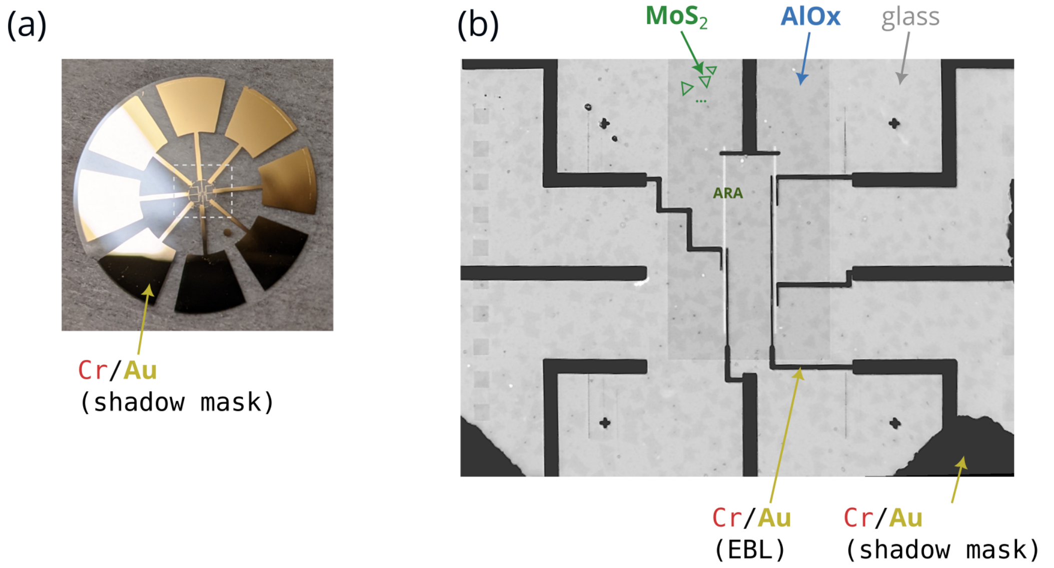

Figure 3.38: (a) Representative glass coverslip substrate (24 mm diameter), where multiple process micro(nano)fabrication steps have been performed. The macroscopic electrodes are acheived via a shadow mask and thermal PVD. (b) Optical micrograph at 4x magnification, with grayscale inverted for improved visibility. Various features labeled, including the electron beam lithograph (EBL) pattern for the Cr/Au electrode extensions that serve as source/drain, the $AlO_x$ dielectric for solid-state capacitive coupling, and the transferred 2D $MoS_2$.

The process begins by evaporating 8 thick macroscopic Cr/Au pads using a shadow-mask that I designed in FreeCAD and had laser-cut by a contractor. The shape is such as to form a ciruclar pattern as shown in Figure 3.38(a). This is the macroscopic cm/mm-scale part. Then, 3 layers of resist are spun and baked, one of which is conducting so as to allow for use of electron beam lithography (EBL) on insulating glass, which is very challenging. A pattern is then designed consisting of 8 extensions of the macroscopic electrode to a smaller field. This is followed by development, Cr/Au deposition, and lift-off. These extensions can be seen in the optical micrograph of Figure 3.38(b), in black. This micrograph had its grayscale inverted for better visibility which is why the thick Cr/Au is black instead of white.

The same 3 layers of resist are then again spun and baked. A pattern is drawn for the Cr/Au 0.5/5 nm ARA part of the stack. After exposition, development, evaporation, lift-off, the sample is cleaned using reactive ion etching (RIE) for 90 seconds. We tested that this indeed improves cleanliness of the sample, and it does not significantly affect the ARA layer. The ARA can be seen in white in 3.38(b) (again inverted from gray). Then 3 layers of resist are again spun, followed by a EBL window for the $AlO_x$ layer. After development, the $AlO_x$ is deposited (usually either 30 nm or 40 nm) using a thermal evaporator, with a tailored partial pressure of $O_2$ in the chamber.

Attaining of a proper insulating $AlO_x$ was extremely challenging as mentioned before, and took a lot of tries to get right. The "v1" $AlO_x$ was slightly conducting and had the absorption tail mentioned. The "v2" however was much improved and transparent and insulating. After another RIE, 2D $MoS_2$ is transferred, using a OM-aided technique that I developed that allows multiple transfer attempts of the film, leveraging the thin water layer between film and substrate. After drying the transfer, again 3 layers must be spun. Finally an EBL pattern is drawn to obtain usually several capacitors and FETs. Many samples had a faulty dielectric at the end and were unusable, or plagued by other issues. Some capacitors were realized however that allowed XRM imaging. One FET was realized which initially was working but later was disabled due to a channel failure. More work is needed to finalize the FET portion.

## 3.6.2 . Capacitive gating

In Figure 3.39 a $MoS_2$ capacitor device is shown, where (a) is a micrograph at 550 nm wavelength and adjusted grayscale (25,100). First it is seen that the ARA+$AlO_x$ part is darker compared with the glass (which also has the same transparent $AlO_x$ on top), which makes sense, based on the anti-reflection effect predicted earlier for 40 nm $AlO_x$on 0.5/5 nm Cr/Au ARA. In this case the Cr/Au contact to the $MoS_2$ is on the glass (+$AlO_x$) part of the substrate, instead of on top of the dielectric on top of the ARA back-gate! This was done because often putting the metal contact on top of the $\mathrm{AlO_x}$/ARA created a easy leak or easy break-down that shorted the source to the gate.

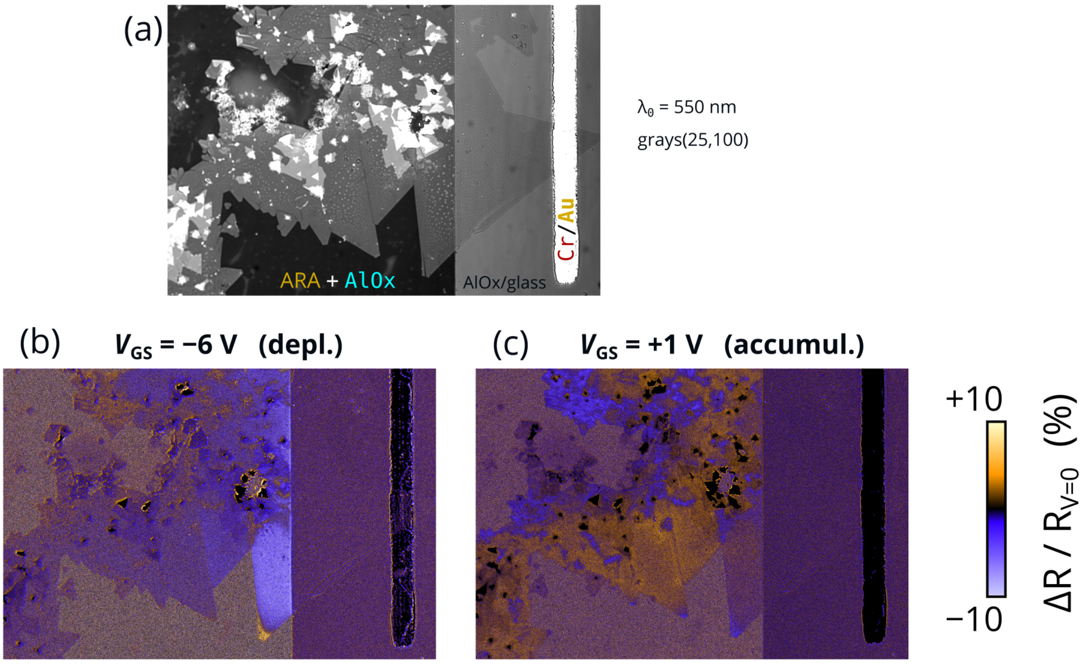

Figure 3.39: (a) Optical IRM micrograph at 550 nm with adjusted grayscale (25,100). Labeled areas include the glass/$\mathrm{AlO_x}$ substrate, the 0.5/5 nm Cr/Au anti-reflective absorbing (ARA) layer with 40 nm $\mathrm{AlO_x}$ dielectric on top, the $\mathrm{MoS_2}$, and finally a thicker 10/80 nm Cr/Au for the source lead.

In Figure 3.39(b) and (c) $\Delta R/R_0$ images were computed using $R(0\text{ V})$ as the reference. In (b) a depletion voltage of $-6$ V was applied while in (c) an accumulation voltage of $+1$ V was applied. For the colorbar, a LUT called "ICA" (in ImageJ) was chosen in order to clearly illustrate the positive versus negative percent reflectance change, where orange is positive, blue is negative, and near-black is close to zero. The result is a bit unexpected—not all monolayers are reacting in the same way. The large monolayer near the edge seems to potentially be more "on" at zero volts (perhaps it has a negative $V_{\mathrm{TH}}$), which would explain why it responds upon depletion.

Other monolayers do not change so much. On accumulation, the large monolayer seems "already accumulated" while other monolayers still had room for accumulation. It is difficult to interpret exactly the results, but it is a starting-point of the BALM charge density imaging for sure.

A video was also taken for this device at 2 fps, where a depletion of $-6$ V was applied as a pulse at the $t$ =10 s mark, and then back to zero at $t = 45$ s. Results are shown in Figure 3.40. In (a), a 650 nm micrograph is shown with one ROI defined, (b) is a $\Delta R/R_0$ image,

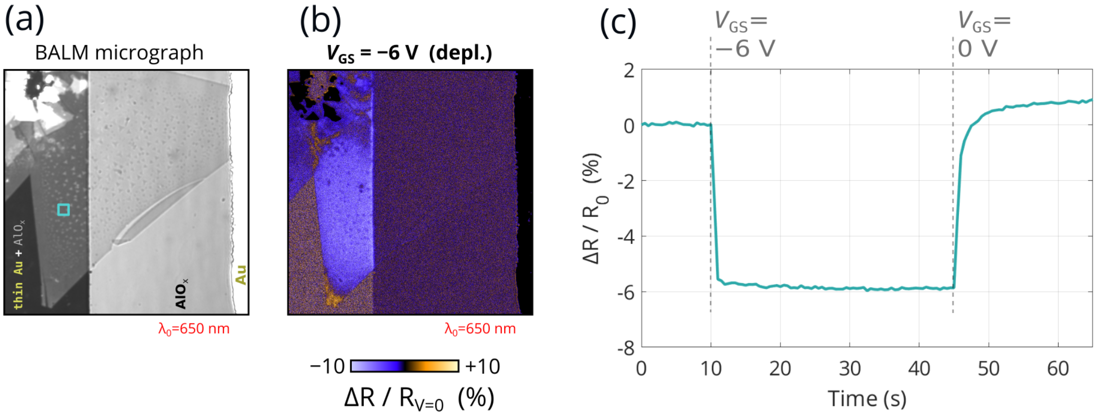

Figure 3.40: (a) BALM micrograph at 650 nm with one ROI defined. (b) A $\Delta R/R_0$ image showing effect of depletion. (c) Plotted ROI percent reflectance change vs. time of a 2 fps video where gate was pulsed to $-6$ V at $t = 10$ s followed by a pulse back to 0 V at $t = 45$ s.

and (c) is a plot of $\Delta R/R_0$ versus time. One result that is evident is that the initial depletion pulse responds very fast, at sub-second after the pulse, while back to zero there is a slower decay over multiple seconds. This would be consistent with charge trapping in the dielectric which is an effect near-ubiquitous in FETs which gives rise to hysteresis in the electrical transfer characteristic as well. Figure 3.40(c) highlights an advantage of dry state devices as in IL-gated devices both mechanisms occur at the same time scale.

Furthermore, a near $-6\%$ of modulation is attained, which is a decent modulation depth, illustrating that with a relatively low depletion voltage a significant signal is attained and thus charge sensitivity is appreciable. As before, there is also the advantage of widefield here and high 2fps throughput and local mapping of the charge in real time. Some variations in profile across the monolayer is also seen.

A different capacitor device was realized on the same substrate (thus same CVD $MoS_2$ growth and same dielectric $AlO_x$ deposition) and is shown in Figure 3.41. The micrograph in (a) was taken at 650 nm with no grayscale adjustment. In this case, $-6$ V depletion bias was explored, as well as a $+3$ V accumulation bias. The center and right $\Delta R/R_0$ images in (b) uses 0 V as reference as was done in Figures 3.39 and 3.40. In the left-most image though the $-6$ V was used as depletion with the $+3$ V computed. The results indicate variations across the monolayers, which is due to reasons not fully known. It could be due to variation of $V_{\text{TH}}$ across the monolayers due to a substrate doping landscape. It could also be that this particular CVD growth gave monolayers with varying stoichiometry across different flakes. The bilayers are also

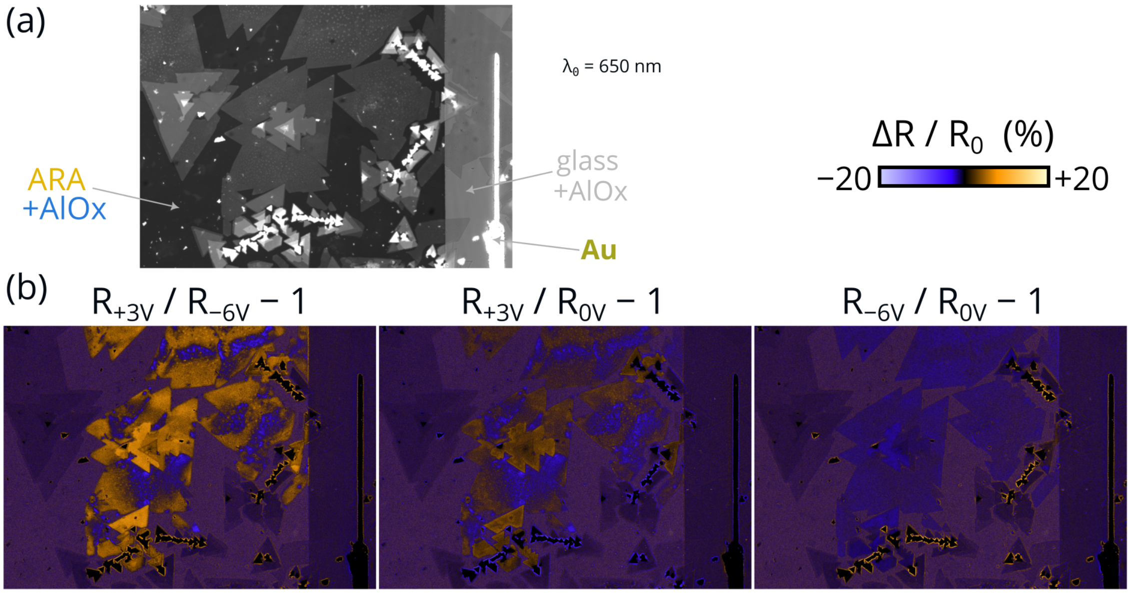

Figure 3.41: (a) 650 nm micrograph with no grayscale adjustment (0,255), of a BALM $MoS_2$ capacitor device, with the various parts labeled. (b) Reflectance change response for $+3$, $-6$, 0 V gate, using 0 V as reference for the right and center images, while left image uses fully depleted as reference for the accumulation image.

seen to react, consistent with gate-dependent bilayer response related to inter-layer exciton dynamics as explored among others by Peimyoo et al. 2021 [258]. Further experiments would be needed to further understand this system.

### 3.6.3 . Preliminary $MoS_2$ BALM FET

A FET device on a different substrate was realized and almost worked. This substrate also consisted of a 40 nm $AlO_x$ deposition, with 0.5/5 nm Cr/Au ARA , and a different CVD $MoS_2$ batch transferred to it. A 450 nm micrograph is shown in Figure 3.43(a). At this stage, the channel had already "burnt up" somehow on the right side, while on the left side there was still access to the gold contact. A 650 nm micrograph is shown in (b), with various components labeled and a scalebar.

Notice that as before with the capacitor example, although the 450 nm is ideal for the non-ARA portion, it is actually quite bad in terms of contrast in ARA portion. The 650 nm though is providing great static contrast ($C_{\text{pc}} \approx +47\%$). The device was then gated between $-6$ and $+6$ V in a linear fashion, at a rate of 1 V/s, with 4 fps used. Double the frame-rate than previous experiments could be used in part thanks to the high mentioned positive contrast on the ARA/$AlO_x$ BALM stack which allows for a shorter acquisition time.

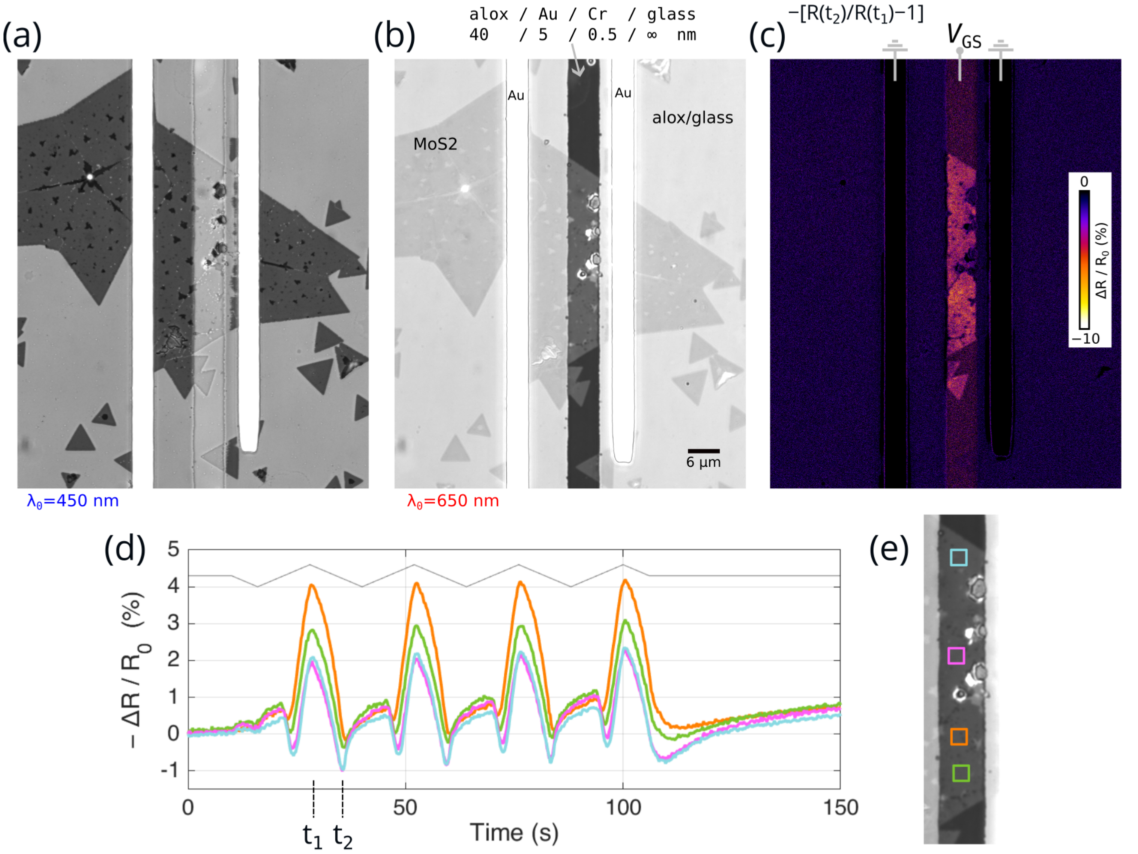

Figure 3.42: (a) 450 nm micrograph of BALM $MoS_2$ FET device. The channel on the right has been destroyed at this point, so only capacitive gating was possible. (b) 650 nm micrograph with parts labeled. Notice the $MoS_2$ over the ARA back-gate is much more easily seen at 650 nm in this case. (d) Resultant $-\Delta R/R_0$ for the ROIs defined in (e) at 4 fps, during gate cycling at 1 V/s between $-6$ to $+6$ V. In (c) a $-\Delta R/R_0$ image is computed using $t_1$ and $t_2$ as labeled in (d).

A rate of $1$ V/s was used. The resulting reflectance change (multiplied by $-1$) for ROIs defined in 3.42(e) are shown in 3.42(d). In the IRM FET data on glass, accumulation always made the $MoS_2$ brighter. Here however, it is the opposite, and thus for clarity the sign is inverted. One $-\Delta R/R_0$ image from $t_1$ and $t_2$ (see (d)) is shown in 3.42(c). This particular "charge density image" shows a somewhat although not completely smooth modulation across the flake. As seen by the different ROIs there are some differences along the channel.

Now, as before, it is of interest to plot the ROI reflectance response as a function of gate voltage. This has been done in Figure 3.43, where the ROIs are reproduced in (a) again for clarity, with the orange ROI plotted ($\times[-1]$) in (b), and the orange, green, pink ROIs in (c). (The cyan ROI was excluded because it was very similar to the pink one). Again there is a resemblance to a transfer characteristic, where the major modulation is happening in the accumulated state. A hysteresis effect is noticed as well which likely is due to trapping in the

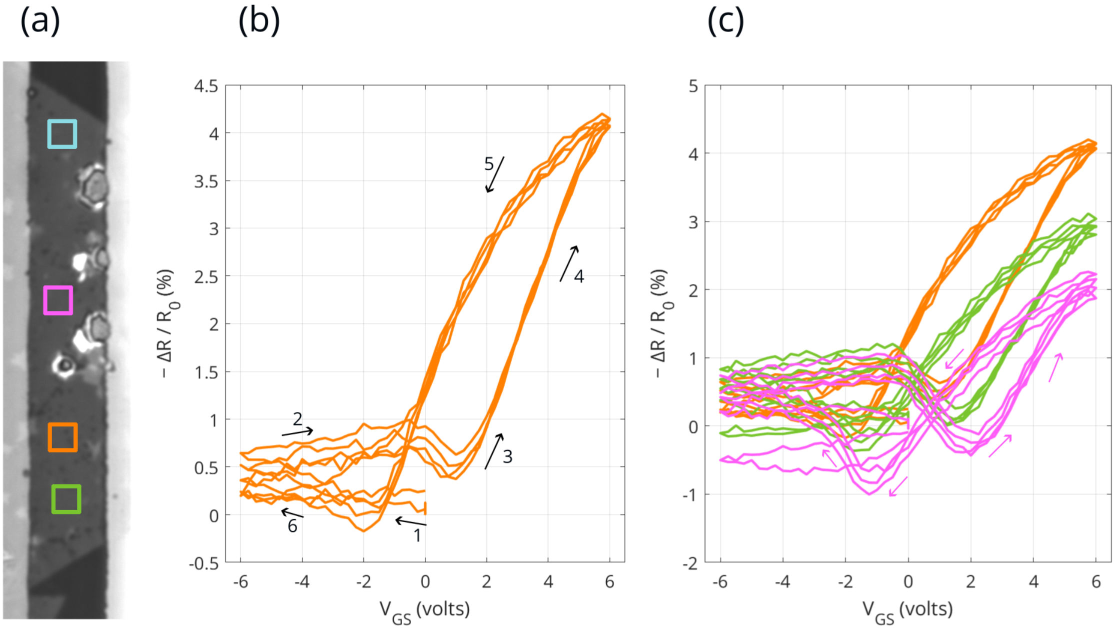

Figure 3.43: (a) ROIs defined in channel. (b) Resultant $-\Delta R/R_0$ for orange ROI plotted versus $V_{\mathrm{GS}}$ from data in Figure 3.42. Time sequence of curve labled from 1 to 6. (c) Orange, green, purple ROIs.

dielectric. Furthermore, the 3 ROIs appear to have differing "reflectance thresholds", especially the pink case. This demonstrates the potential of using this BALM stack to study 2D MoS$_2$ FETs in operando. The next step, if the FET had not busted, would have been to perform voltage sweeps at different drain, and to evaluate the drain vs. gate competition, as was done for the IL-FET earlier.

In fact, prior to mounting this sample to the microscope, the three FETs on this sample were tested electrically at low voltages. This is likely when FETs were busted, or possibly due to electrostatic discharge during handling of the sample. Anyway the electrical measurements of one of the FETs of the sample are shown in Figure 3.44(a). Here $I_{\mathrm{D}}$ is shown as a function of time, where first $V_{\mathrm{DS}} = 0.4$ V was applied, followed by depletion ($-1$ V), accumulation ($+1$ V), depletion ($-1$ V) via $V_{\mathrm{GS}}$. The response is typical of that of $n$-type MoS$_2$ showing that the FET was indeed alive at the time.

During acquisition of the $-\Delta R/R_0$ video discussed in Figures 3.42 and 3.43, the leakage current between gate and source $I_{\mathrm{GS}}$ was measured. The result is shown in Figure 3.44(b). It is seen that during the depletion the current was low while the current is responding during accumulation. This makes sense because since the metal is not on the dielectric, it is the 2D MoS$_2$ semiconductor through which the current is leaking—and this resistor changing as the

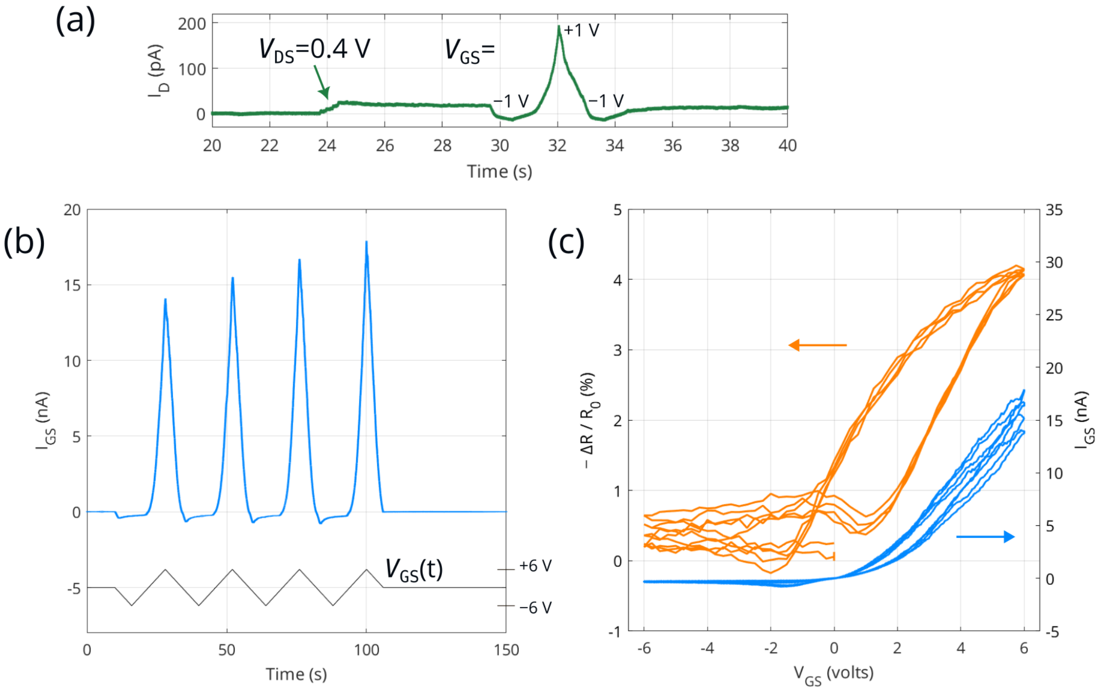

Figure 3.44: (a) Drain current $I_D$ versus time of a FET tested electrically before mounting it on the IRM/BALM microscope. Based on response to drain and gate shown, the $n$-type character of the $MoS_2$ FET is confirmed and operating as expected. However somewhere along the way channel was destroyed. (b) Gate leakage $I_{GS}$ measured during gate cycling from experiment in Figures 3.42 and 3.43. (c) Plotted as a function of $V_{GS}$ together with $-\Delta R/R_0$, illustrating the combining of XRM and electrical measurement.

semiconductor is accumulated or depleted.

The response versus $V_{GS}$ is ploted together with $-\Delta R/R_0$ in Figure 3.44(c). Although the ultimate goal would be to plot $I_D$ together with the reflectance change, this is at least a small milestone in that direction. It illustrates that powerful idea of combining electrical measurements with the IRM/BALM charge density imaging.

### 3.6.4 . Simulations of expected $\Delta R/R_0$ response in charging experiments

As mentioned before, Kravets et al. 2019 [170] measured $(n(\lambda), \kappa(\lambda))$ of CVD $MoS_2$ at different gate voltages. I digitized this data with WebPlot Digitizer [169] which allowed me to compute expected $\Delta R/R_0$ at various conditions such as for different $AlO_x$ thicknesses. Their data from the wavelength-by-wavelength fit is reproduced in Figure 3.45(a) for the gate voltages of 0 V, $+75$ V (accumulation) and $-100$ V (depletion). In the paper they also propose a disperion model consisting of five Lorentzians. By using these parameters provided in the paper and implementing a sum of Lorentzians I reproduced the expected (Kramers-Krönig consistent) $\tilde{n}(\lambda)$ in 3.45(b).

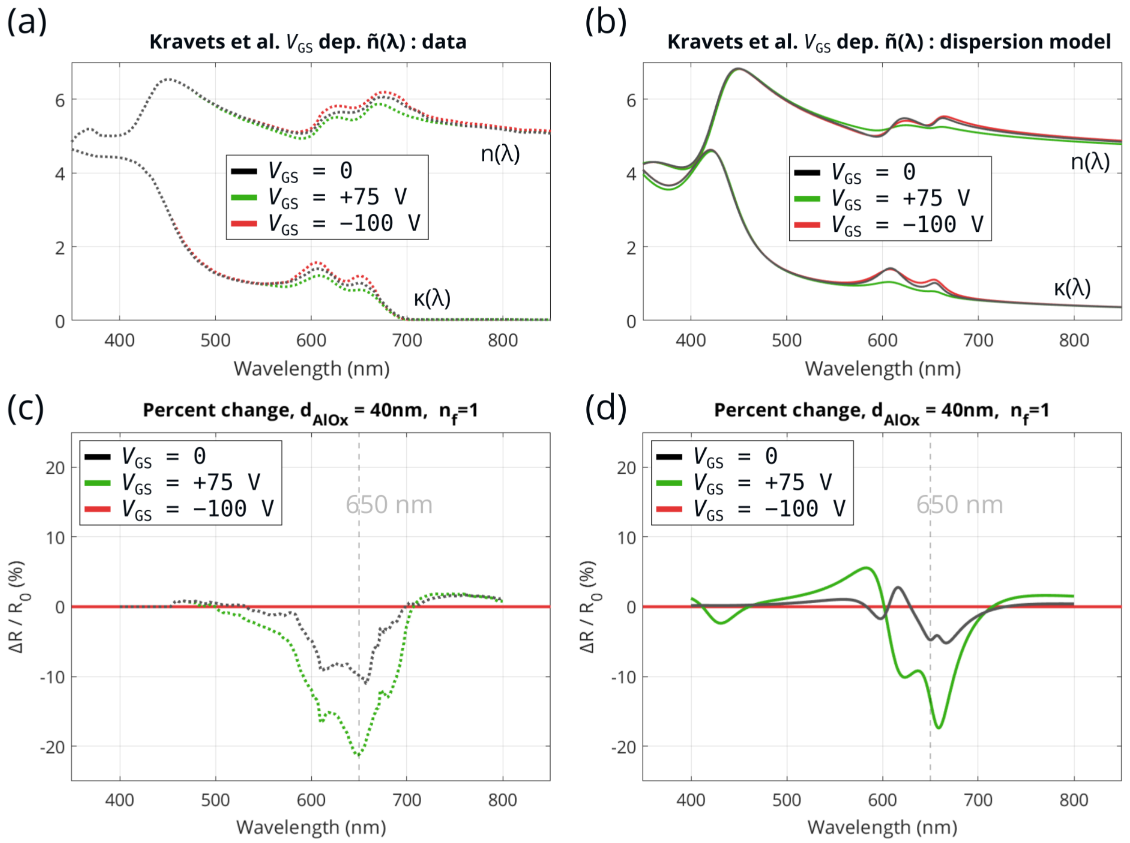

Figure 3.45: (a) Digitized data from Kravets et al. 2019 [170] from their wavelength-by-wavelength fit of ellipsometry data measuring $\tilde{n}(\lambda)$ of 2D $MoS_2$ as a function of gate voltage. (b) Dispersion model proposed by [170] for 2D $MoS_2$ gate-dependent $\tilde{n}(\lambda)$. (c) Simulations I performed for normal incidence BALM, using the Kravets $\tilde{n}(\lambda)$ data from (a) for the $MoS_2$ part of the stack, with 40 nm thick $AlO_x$, and the typical CrAu-GenMain parameters (see Table 2.6 for the Cr/Au 0.5/4.9 nm ARA. (d) Same as (c) but using Kravets disperion model.

Then, I recreated in code the entire optical stack consisting of the borosilicate coverslip, the Cr/Au ARA layer, the 40 nm $AlO_x$, the 2D $MoS_2$ (using the Kravets et al. values) and finally air at the final interface ($n_f = 1$). For the $MoS_2$ I computed the cases of both the wavelength-by-wavelength data and using the dispersion model. The respective results (normal incidence) are shown in Figure 3.45(c) and (d). I used the $V_{GS} = -100$ V as the reference $R(\tilde{n})$. In this particular case, the trend is such that accumulation results in a negative percent change at 650 nm. This is a good sign, because that is in fact what was observed experimentally as was covered in Figures 3.42 and 3.43.

Still, further work would need to be done to improve the simulations. The expected response should be computed across the range of angles of the NA$= 1.4$ objective, and also the 10 nm bandwidth should be taken into account. Also, it would be best to measure the gate-dependent $\tilde{n}(\lambda)$ of our home-grown $MoS_2$. It can be seen that the zero-volt case measured by Kravets et al. [170] differs to some extent from what was measured for our $MoS_2$ as shown earlier in Figures 2.27 and 2.28.

This concludes Chapter 3, in which IRM and BALM based eXcitonic reflection microscopy (XRM) results were presented, following the sections on background. Key take-aways and further perspectives are presented in the *Conclusions & perspectives* section.

# Conclusions & perspectives

Visibility and charge density imaging aspects for 2D $MoS_2$ (and other 2D materials) via IRM and BALM have been presented.

Many papers have been published in the last two decades on improving contrast and visibility of 2D materials. Yet, this area of research remains ripe, with various optical configurations that have either not been explored or where only the surface has been scratched. This rings true for IRM and BALM. This work thus represents an early "harvest" in that regard.

Looking back on Chapter 2, an optimal IRM condition for 2D $MoS_2$ was found that yielded $\approx$ 80% contrast for the monolayer, with the adlayers and other topography exhibiting strong visibility (Figure 2.34). In corresponding experimental and simulated contrast spectra, optical noise is considered as a possible actor (Figure 2.33). In air and water, IRM micrographs were found to yield strong visibility of topography (Figure 2.1). For 2D $MoS_2$ in air, taking into account the angular weight function of rays via simulation cemented the effect of angle as an important actor and improved the fit to experimental contrasts (Figure 2.37).

Independent of $MoS_2$, aspects of BALM were furthered in this work. For the first time, the optical properties of an experimental ARA layer were measured, and its effect on anti-reflection response was simulated and compared with literature values (Figure 2.49). A detailed investigation on the effect of illuminated aperture stop diameter (INA) was also simulated for the first time for BALM (Figure 2.51). Physical insights of BALM were also presented and simulated by considering independently the Drude and Lorentz contributions to the ARA dielectric function. Finally, an $AlO_x$ FP layer combined with the ARA layer was shown to be highly effective for red wavelengths where the anti-reflective properties of ARA alone are known to be ineffective (Figure 2.52).

Via BALM, 2D $MoS_2$ was imaged at multiple wavelengths on ARA layers in air and water (Figure 2.57) as well as on ARA+$AlO_x$ layers (Figure 2.58). In both cases the visibility and contrast were strong, with one particular condition (at 630 nm) yielding $\approx$ 79% contrast. Simulated contrasts of $MoS_2$ versus ARA (Figures 2.55 & 2.56) and versus ARA+$AlO_x$ (Figure 2.59) were presented and compared with data. The latter result predicts how certain FP layer thicknesses at certain INA could yield contrasts of hundreds of percent which could be useful in some contexts. It is important to recall however that ultra-high monolayer contrasts are not always required and depend on the aim. For example if mesoscopic adlayers are studied, visibility can be good even at moderate monolayer contrast, as was the case for a 450 nm image with $C_{\text{pc}} \approx -10\%$ (Figure 3.27). In that case those adlayers and other topographies did have high contrast even though the planar monolayer contrast itself was limited.

With regards to charge density imaging as covered in Chapter 3, the thesis work introduces the first time ever that optical microscopy is used for charge density imaging in the context of field-effect transistor devices of a 2D semiconductor. The work also introduced novel capacitor based experiments. The majority of the results were obtained in IRM mode using electrolyte liquid gating, and a submitted article is in review at the time of this writing [210]. The most striking capacitor based results are shown in Figures 3.17, 3.18, 3.22, which exhibited sub-second charging delays and local charge inhomogeneities at both inter- and intra-flake level. Results of ionic liquid gated Schottky barrier FET devices were presented first in Figures 3.31, where a charge density gradient from drain to source at both polarities was observed. For this device and especially the one detailed in Figures 3.32 & 3.33, the drain vs. gate competition over local charge in the channel was analyzed. Some of the $\Delta R/R_0$ data of both capacitor and FET systems were converted to charge density change $\Delta q$ via the $\alpha$ parameter in certain voltage ranges, per the model proposed by Hao Zhu et al. [246].

In BALM configuration, solid-state $MoS_2$ capacitor devices integrated in a BALM optical stacks consisting of 0.5/5 nm Cr/Au ARA layer for back-gate and ≈ 40 nm $AlO_x$ as dielectric were presented (Figures 3.39, 3.40, 3.41). The response yielded about $\pm 6\%$ change depending on the experiment, at typical operating voltages for that thickness of dielectric. Local charge variations could be analyzed to some degree. An FET configuration in a BALM optical stack was realized which at first was functioning (Figure 3.44(a)) but later broke down. Capacitive results of this device at 4 fps were presented (Figure 3.42) and plotted as a function of gate voltage. This indicated that local hysteresis mapping of charge could be observed at different regions of interest in the channel. Finally the leakage current and reflectance change were plotted in the same graph (Figure 3.44(c)), exemplifying the powerful idea of combining in the future BALM-based eXcitonic reflection microscopy (XRM) with electrical measurements.

In perspective, the visibility aspects provide various new avenues for studying 2D $MoS_2$ and other nanomaterials. IRM and BALM provide excellent vertical resolution thanks to interferences, and great lateral resolution because of the high NA by nature of oil immersion. The high NA means that angles play an important role, as was considered extensively in this work (Equation 2.3). Implementing a wheel of aperture stop diameters could be envisaged to further study the effects of INA, as well as some upgrades to the Köhler optics and an integrating sphere for the light source. In the future one could envisage other 2D material contrasts to be evaluated and simulated, which would have different optimal conditions for the BALM FP stack. Homo- and hetero-layers [259] would also be interesting, building on the results presented here (Figures 2.40 & 2.41). The IRM/BALM platform would also be ideal for studying effect of ambient or imposed environment like adsorbates or gaseous environments. Other examples would be tunable FP conditions [260], and Fourier imaging of BFP on the collection side [179].

In perspective, the new eXcitonic reflection microscopy (XRM) charge density imaging modalities via IRM and BALM open a door to many future opportunities. The greatest asset arguably is the sub-second throughput in widefield mode, which is able to capture charging dynamics over large areas of $\sim$ 10,000 $\mu m^2$, which could not have been measured by conventional techniques like KPFM. In the future though, it could be interesting to combine KPFM and XRM measurements in a complementary way for the same device. Ultra-fast ($\sim$ pico-second) reflectance spectroscopy configuration [261] could also be combined. This work focused mainly on 2D $MoS_2$, but other 2D TMD devices could also be tested, with the appropriate bandpass filter for differing exciton energies in for example $WS_2$ or $MoSe_2$, both of which have been shown to have modulation depths exceeding that of $MoS_2$ [144, 220]. For $MoS_2$, it was shown in this work that some wavelengths appear to be more sensitive to variations in charge (Figure 3.25) such as at 660 nm, which could be interesting to investigate further as well. For Schottky FET devices, it would be interesting to realize devices fabricated with source/drain contacts of different metals and compare the results with this work where Cr/Au was used. It can provide insights into the channel charge behavior for different Schottky barrier heights. For the solid-state BALM XRM mode, the goal would be to complete fabrication of fully functioning FETs so that both electrical and XRM measurements can be done in tandem. Furthermore, the FP layers of ARA and $AlO_x$ thicknesses could be simulated and realized experimentally, to find a resonance for maximum $\Delta R/R_0$ to $\Delta q$ charge sensitivity so that even smaller changes in drain and gate voltage could be detected.

Overall this thesis work has involved very novel configurations and imaging modes, both for visibility and charge imaging aspects. It also in various ways builds on prior studies and enters into a context of vibrant research activity in multiple fields including nanoscience, nanotechnology, optics, microscopy, image processing, devices, and more. It is the hope of the author that the work can be of value in future endeavors.

# Résumé étendu en Français

La recherche sur les nanomatériaux bidimensionnels (2D) est un domaine important et très dynamique, tant sur le plan fondamental que pour son fort potentiel applicatif. Dans cette catégorie de matériaux se trouvent notamment les monocouches de dichalcogénures de métaux de transition (TMD), un groupe de semi-conducteurs 2D comprenant par exemple $MoS_2$, $WS_2$, $SnS_2$, $MoSe_2$, $WSe_2$, $PtSe_2$ pour n'en nommer que quelques-uns.

De très nombreuses études ont été menées dans ce domaine depuis le milieu des années 2000, lorsqu'un TMD 2D a été isolé pour la première fois par exfoliation mécanique d'un cristal naturel massif [1]. Depuis lors, un large ensemble de propriétés et de prototypes de dispositifs basés sur ces matériaux ont été explorés.

De façon particulièrement remarquable, la forme 2D du cristal TMD possède des propriétés très différente de son homologue 3D, en raison du confinement dimensionnel imposé le long de l'axe orthogonal aux plans 2D. Ces nouvelles propriétés pourraient être exploitées dans certains cas pour améliorer l'état de l'art des technologies actuelles, notamment dans les secteurs de l'électronique [2, 3], de l'optique [4, 5, 6], de la photonique [4, 7, 8], de l'optoélectronique [9, 10] et de l'énergie [11, 12].

Lors de la réalisation de nouveaux dispositifs visant à exploiter leur potentiel, ces TMD 2D, subissent des étapes de procédés dont les conséquences sont tout aussi importantes que l'étape de synthèse du matériau elle-même. La fonctionnalisation chimique, les traitements thermiques, le dopage et les étapes de microfabrication en sont quelques exemples.

En outre, les TMD 2D sont rarement monocristallins. Les inhomogénéités et les défauts jouent ainsi un rôle déterminant dans les performances des dispositifs. Il est donc très important de réaliser des caractérisations spatialement résolues de différents types, notamment operando, c'est-à-dire sur des dispositifs en cours de fonctionnement. Parmi les différents outils de caractérisation, on trouve ceux basés sur les techniques de microscopie optique, qui jouent un rôle prépondérant dans l'essor du domaine.

De plus, divers dispositifs à base de TMD 2D reposent sur la modulation de la densité de charge dans ce semi-conducteur, et il est donc intéressant et important de mesurer localement les variations de charge pendant le fonctionnement de ces dispositifs. Il s'agit notamment de transistors à effet de champ (FET) pour l'électronique, de modulateurs pour la photonique ou d'électrodes redox pour l'électrochimie.

La microscopie de type IRM (interference reflection microscopy) et la microscopie de type BALM (backside absorbing layer microscopy) ont émergé comme des techniques puissantes pour étudier les matériaux 2D à la fois pour des analyses topographiques à fort contraste et pour des études in situ de différentes sortes [13]. Pourtant, leur utilisation reste largement inexploitée, en particulier pour les semi-conducteurs 2D et les dispositifs en 2D. Dans le cas des dispositifs, la très forte corrélation entre la charge et les propriétés optiques dans le cas spécifique des TMD 2D, ouvre une voie particulièrement originale pour l'imagerie operando de la densité de charge.

Dans ce contexte, l'objectif de cette thèse est de deux ordres : (1) contribuer aux développements des microscopies optiques IRM et BALM pour étudier la topographie du $MoS_2$ 2D en combinant expérience et simulations, et (2) introduire un nouveau mode d'imagerie de la densité de charge pour les condensateurs et les dispositifs FET à base de $MoS_2$ dans deux configurations distinctes, en utilisant une grille électrolytique ou une grille métallique transparente pour l'IRM et le BALM, respectivement.

L'IRM est une configuration de microscopie en réflexion qui satisfait à certains critères. Ceux-ci comprennent : l'utilisation d'un objectif inversé à immersion dans l'huile, d'une lamelle transparente comme substrat, d'un filtre optique pour augmenter la cohérence temporelle et, enfin, la présence d'interférences en couches minces dans l'échantillon lui-même ou dans l'espace entre l'échantillon et le substrat [101]. La modalité IRM a été introduite en 1964 par A. S. G. Curtis, qui a proposé le terme [102]. Il l'a utilisée pour étudier les mécanismes d'adhésion des cellules sur une lamelle couvre-objet en verre. Dans ce cas, les interférences ont lieu dans le mince espace d'air entre la lamelle de verre et la cellule, au lieu des interférences à l'intérieur de la cellule elle-même. Cela diffère du cas des matériaux 2D, où il n'y a pas de poche d'air et où les interférences se produisent donc dans le matériau 2D lui-même (et dans toutes les autres couches minces éventuellement présentes). Quelques études récentes montrent que la configuration IRM est utile pour étudier les matériaux 2D [82, 73].

En ce qui concerne le BALM, il s'agit essentiellement d'un microscope IRM, mais avec une couche supplémentaire, à la fois absorbante et antireflet (appelée couche ARA, anti-reflection absorbing layer) sur le substrat en verre. Cette couche ARA est constituée dans cette thèse d'un film d'or de 3 à 5 nm d'épaisseur et d'une sous-couche de Cr de moins d'1 nm pour assurer l'adhérence de l'or sur le verre. Cette couche ARA présente des interférences Fabry-Pérot (FP) favorables qui se manifestent par des propriétés antireflets et une sensibilité améliorée aux échantillons nanométriques pour certaines longueurs d'onde et certaines épaisseurs. En outre, la couche d'ARA étant conductrice, elle peut être utilisée comme électrode pour des expériences in situ nécessitant l'application d'une tension. La technique BALM a déjà été utilisé pour étudier des nanomatériaux avec un contraste élevé [88, 87, 184]. Les expériences in situ se sont principalement concentrées sur les études chimiques et électrochimiques. Aucun travail n'a été rapporté sur des transistors étudiés par cette voie.

L'objectif à immersion dans l'huile dans les configurations IRM et BALM a une ouverture numérique (NA) nominale très élevée. Dans la thèse, un objectif NA=1,4 a été utilisé. Comme pour la plupart des microscopes optiques, la configuration IRM dispose d'un diaphragme d'ouverture éclairé et d'un diaphragme de champ, dans le schéma d'éclairage connu sous le nom de Köhler. Cela signifie que le NA éclairé (INA) peut être modifié, ce qui permet d'obtenir une gamme d'angles d'incidence différente [67], comme indiqué dans le texte principal. Dans la thèse, le INA s'est révélé avoir une importance significative.

La modalité d'imagerie de la densité de charge est basée sur le fait que les propriétés optiques $\tilde{n}(\lambda) = n(\lambda) + i\kappa(\lambda)$ (ou $n$ est l'indice de réfraction et $\kappa$ le coefficient d'extinction) des TMD 2D sont couplées à la densité de charge aux énergie proches de celle des excitons. Dans la thèse, un filtre de 650 nm a été principalement utilisé dans les configurations IRM et BALM pour l'imagerie de la densité de charge. C'est-à-dire, à proximité de l'exciton dit "A" du $MoS_2$ 2D. En général, j'utiliserai le terme de "eXcitonic reflection microscopy" (XRM) pour désigner cette modalité en raison du rôle central que jouent les propriétés des excitons. D'importants travaux précédents sur ce sujet incluent Hao Zhu et al. 2019 [246] et d'autres, comme décrit en détail dans le texte principal. L'origine du changement des propriétés optiques en fonction de la charge est principalement liée à un transfert spectral des excitons neutres ($X^0$) vers des excitons chargés négativement ($X^-$), également connus sous le nom de trions, lorsque des charges sont accumulées dans le matériau [252]. Ce changement est dû à de multiples mécanismes physiques, notamment la diffusion, le blocage de Pauli, la modification de la largeur de la bande interdite et l'écrantage [26].

Au cours de cette thèse, du $MoS_2$ 2D a d'abord était synthétisé au laboratoire par CVD et caractérisé par différentes techniques. Ce travail est décrit au Chapitre 1. Ce matériau (et d'autres TMD) a ensuite été étudié par microscopie IRM et BALM, ce qui fait l'objet du Chapitre 2. Les mesures optiques de densité de charge dans des dispositifs à base de $MoS_2$ font l'objet du chapitre 3.

Pour résumer les principales conclusions et les principaux résultats du chapitre 2, une condition IRM optimale a été trouvée pour le $MoS_2$ 2D, qui a permis d'obtenir un contraste de $\approx 80$ % pour la monocouche, avec les couches supérieure (double-couches et fines multi-couches) et d'autres topographies présentant également une forte visibilité (figure 2.34). Dans les spectres de contraste expérimentaux et simulés correspondants, le bruit optique est considéré comme un acteur possible (figure 2.33). Dans l'air et dans l'eau, les micrographies IRM ont montré une forte visibilité de la topographie (figure 2.1). Pour le $MoS_2$ 2D dans l'air, la prise en compte de la fonction de poids angulaire des rayons par simulation a cimenté l'effet de l'angle en tant qu'acteur important et permet d'améliorer la correspondance entre contrastes simulés et contrastes expérimentaux (figure 2.37).

Indépendamment du $MoS_2$, certains aspects de la technique BALM ont été approfondis dans ce travail. Pour la première fois, les propriétés optiques d'une couche ARA expérimentale ont été mesurées, et leur effet sur les performances antireflet à différentes longueurs d'onde a été simulé et comparé aux valeurs de la littérature (figure 2.49). Une étude détaillée de l'effet du diamètre de l'ouverture éclairée (INA) a également été simulée pour la première fois pour la technique BALM (figure 2.51). Des principes physiques relatif à BALM ont également été présentés et simulés en considérant indépendamment les contributions de Drude et de Lorentz à la fonction diélectrique de la couche ARA. Enfin, une couche Fabry-Pérot d'alumine ($AlO_x$) combinée à la couche ARA s'est montrée extrêmement efficace pour les longueurs d'onde rouges pour lesquelles les propriétés antireflets de l'ARA seule sont inefficaces (figure 2.52). L'ajustement des épaisseurs de ces deux revêtements (ARA et diélectrique) permet ainsi le design de substrats adaptables à différentes expériences.

Via BALM, le $MoS_2$ 2D a été imagé à plusieurs longueurs d'onde sur des couches ARA dans l'air et l'eau (figure 2.57) ainsi que sur des couches d'ARA+$AlO_x$ (figure 2.58). Dans les deux cas, la visibilité et le contraste étaient forts, avec une condition particulière (à 630 nm) donnant $\approx$ 79% de contraste. Les contrastes simulés du $MoS_2$ par rapport à la couche ARA (figures 2.55 & 2.56) et par rapport à l'ensemble ARA+$AlO_x$ (figure 2.59) ont été présentés et comparés aux données. Ce dernier résultat prédit comment certaines épaisseurs de couches Fabry-Pérot à certains INA pourraient produire des contrastes de centaines de %, ce qui pourrait être utile dans certains contextes. Il est toutefois important de rappeler que des contrastes monocouches ultra-élevés ne sont pas toujours nécessaires et qu'ils dépendent de l'objectif visé. Par exemple, si des empilements mince mais multicouches sont étudiées, la visibilité peut être bonne même avec un contraste monocouche/substrat modéré (comme c'était le cas figure 3.27 à 450 nm). Dans ce cas, ces multicouches et d'autres topographies présentaient un contraste élevé, même si le contraste de la monocouche planaire était lui-même limité aux alentours de 10%.

En ce qui concerne l'imagerie de la densité de charge telle qu'elle est exposée au chapitre 3, le travail de thèse présente pour la première fois l'utilisation de la microscopie optique pour l'imagerie de la densité de charge dans le contexte des transistors à effet de champ. Le travail a également introduit de nouvelles expériences basées sur des condensateurs. La majorité des résultats ont été obtenus en mode IRM à l'aide d'une grille liquide électrolytique, et un article soumis est en cours de révision au moment de l'écriture [210]. Les résultats les plus intéressants obtenus avec des condensateurs sont présentés dans les figures 3.17, 3.18 et 3.22, qui montrent des délais de chargement inférieurs à la seconde et des irrégularités de charge locales au niveau inter- et intra-feuillets. Les résultats des dispositifs FET à barrière Schottky avec un liquide ionique comme électrolyte de grille sont présentés en premier dans (figures 3.31). Un gradient de densité de charge du drain à la source aux deux polarités a été observé. Pour ce dispositif, et en particulier pour celui présenté dans les figures 3.32 et 3.33, la compétition entre le drain et la grille pour le contrôle de la charge dans le canal a été analysée. Certaines des données de variation de réflectivité ($\Delta R/R_0$) issues des études des condensateurs et des transistors FET ont été converties en changement de densité de charge $\Delta q$ via le paramètre "alpha" ($\alpha$) dans certaines gammes de tension, selon le modèle proposé par Hao Zhu et al [246].

Dans la configuration BALM, des condensateurs à base de $MoS_2$ à l'état solide intégrés dans un empilement optique BALM constituée d'une couche Cr/Au ARA de 0,5/5 nm pour la grille arrière et de $\approx$ 40 nm d'$AlO_x$ comme diélectrique ont été présentés (figures 3.39, 3.40, 3.41). Le résultat est une variation de réflectivité en fonction de la polarisation d'environ $\pm 6\%$ en fonction de l'expérience, à des tensions de fonctionnement typiques pour cette épaisseur de diélectrique. Les variations locales de charge ont pu être analysées dans une certaine mesure. Une configuration FET dans un empilement optique BALM a été réalisée ; elle a d'abord fonctionné (figure 3.44(a)) mais s'est ensuite détériorée. Les résultats capacitifs de ce dispositif à 4 fps ont été présentés (figure 3.42) et tracés en fonction de la tension de grille. Ces résultats indiquent qu'une cartographie locale de l'hystérésis de la charge peut être observée dans différentes régions d'intérêt du canal. Enfin, le courant de fuite et le changement de réflectance ont été représentés dans le même graphique (figure 3.44(c)), illustrant l'idée intéressante de combiner à l'avenir la microscopie de réflexion eXcitonique (XRM) basée sur BALM avec des mesures électriques.

Globalement, ce travail de thèse a impliqué des configurations et des modes d'imagerie novateurs, à la fois pour les aspects de visibilité des matériaux 2D et d'imagerie de la densité de charge dans des dispositifs en fonctionnement. Il s'appuie, à divers degrés, sur des études précédentes et se situe dans un contexte d'activité de recherche dynamique à la jonctions de nombreux domaines, notamment les nanosciences, les nanotechnologies, l'optique, la microscopie, le traitement d'images, les dispositifs, etc. L'auteur espère que ce travail sera utile au domaine en élargissant notamment le potentiel de ces deux configurations d'observation des nanomatériaux que sont IRM et BALM.

# Bibliography

[1] K. S. Novoselov, D. Jiang, F. Schedin, T. J. Booth, V. V. Khotkevich, S. V. Morozov, and A. K. Geim. *Two-Dimensional Atomic Crystals*, *Proceedings of the National Academy of Sciences of the United States of America*, vol. 102, no. 30, pp. 10 451–10 453, 2005.

[2] G. Fiori, F. Bonaccorso, G. Iannaccone, T. Palacios, D. Neumaier, A. Seabaugh, S. K. Banerjee, and L. Colombo. *Electronics Based on Two-Dimensional Materials*, *Nature Nanotechnology*, vol. 9, no. 10, pp. 768–779, 2014.

[3] J.-y. Kim, X. Ju, K.-W. Ang, and D. Chi. *Van Der Waals Layer Transfer of 2D Materials for Monolithic 3D Electronic System Integration: Review and Outlook*, *ACS Nano*, vol. 17, no. 3, pp. 1831–1844, 2023.

[4] A. Singh, S. S. Jo, Y. Li, C. Wu, M. Li, and R. Jaramillo. *Refractive Uses of Layered and Two-Dimensional Materials for Integrated Photonics*, *ACS Photonics*, vol. 7, no. 12, pp. 3270–3285, 2020.

[5] P. Back, S. Zeytinoglu, A. Ijaz, M. Kroner, and A. Imamoğlu. *Realization of an Electrically Tunable Narrow-Bandwidth Atomically Thin Mirror Using Monolayer MoSe2*, *Physical Review Letters*, vol. 120, no. 3, p. 037401, 2018.

[6] J. van de Groep, J.-H. Song, U. Celano, Q. Li, P. G. Kik, and M. L. Brongersma. *Exciton Resonance Tuning of an Atomically Thin Lens*, *Nature Photonics*, vol. 14, no. 7, pp. 426–430, 2020.

[7] T. Vincent, J. Liang, S. Singh, E. G. Castanon, X. Zhang, A. McCreary, D. Jariwala, O. Kazakova, and Z. Y. Al Balushi. *Opportunities in Electrically Tunable 2D Materials beyond Graphene: Recent Progress and Future Outlook*, *Applied Physics Reviews*, vol. 8, no. 4, p. 041320, 2021.

[8] X. Gan, D. Englund, D. Van Thourhout, and J. Zhao. *2D Materials-Enabled Optical Modulators: From Visible to Terahertz Spectral Range*, *Applied Physics Reviews*, vol. 9, no. 2, p. 021302, 2022.

[9] S. Hwangbo, L. Hu, A. T. Hoang, J. Y. Choi, and J.-H. Ahn. *Wafer-Scale Monolithic Integration of Full-Colour Micro-LED Display Using MoS2 Transistor*, *Nature Nanotechnology*, 2022.

[10] J. Ahn, P. J. Jeon, S. R. A. Raza, A. Pezeshki, S.-W. Min, D. K. Hwang, and S. Im. *Transition Metal Dichalcogenide Heterojunction PN Diode toward Ultimate Photovoltaic Benefits*, *2D Materials*, vol. 3, no. 4, p. 045011, 2016.

[11] L. Dong, S. Guo, Y. Wang, Q. Zhang, L. Gu, C. Pan, and J. Zhang. *Activating MoS2 Basal Planes for Hydrogen Evolution through Direct CVD Morphology Control*, *Journal of Materials Chemistry A*, vol. 7, no. 48, pp. 27 603–27 611, 2019.

[12] D. Voiry, M. Salehi, R. Silva, T. Fujita, M. Chen, T. Asefa, V. B. Shenoy, G. Eda, and M. Chhowalla. *Conducting MoS2 Nanosheets as Catalysts for Hydrogen Evolution Reaction*, *Nano Letters*, vol. 13, no. 12, pp. 6222–6227, 2013.

[13] K. Jaouen. *Backside absorbing layer microscopy: a new tool for the investigation of 2D materials*, Ph.D. dissertation, Université Paris-Saclay, 2020.

[14] K. S. Novoselov, A. K. Geim, S. V. Morozov, D. Jiang, Y. Zhang, S. V. Dubonos, I. V. Grigorieva, and A. A. Firsov. *Electric Field Effect in Atomically Thin Carbon Films*, *Science*, vol. 306, no. 5696, pp. 666–669, 2004.

[15] B. Radisavljevic, A. Radenovic, J. Brivio, V. Giacometti, and A. Kis. *Single-Layer MoS2 Transistors*, *Nature Nanotechnology*, vol. 6, no. 3, pp. 147–150, 2011.

[16] K. F. Mak, C. Lee, J. Hone, J. Shan, and T. F. Heinz. *Atomically Thin MoS2: A New Direct-Gap Semiconductor*, *Physical Review Letters*, vol. 105, no. 13, p. 136805, 2010.

[17] R. Beal and H. P. Hughes. *Kramers–Krönig Analysis of the Reflectivity Spectra of 2H-MoS2, 2H-MoSe2 and 2H-MoTe2*, *Journal of Physics C: Solid State Physics*, vol. 12, no. 5, p. 11, 1979.

[18] P.-C. Shen, C. Su, Y. Lin, A.-S. Chou, C.-C. Cheng, J.-H. Park, M.-H. Chiu, A.-Y. Lu, H.-L. Tang, M. M. Tavakoli, G. Pitner, X. Ji, Z. Cai, N. Mao, J. Wang, V. Tung, J. Li, J. Bokor, A. Zettl, C.-I. Wu, T. Palacios, L.-J. Li, and J. Kong. *Ultralow Contact Resistance between Semimetal and Monolayer Semiconductors*, *Nature*, vol. 593, no. 7858, pp. 211–217, 2021.

[19] V. L. Nguyen, M. Seol, J. Kwon, E.-K. Lee, W.-J. Jang, H. W. Kim, C. Liang, J. H. Kang, J. Park, M. S. Yoo, and H.-J. Shin. *Wafer-Scale Integration of Transition Metal Dichalcogenide Field-Effect Transistors Using Adhesion Lithography*, *Nature Electronics*, vol. 6, no. 2, pp. 146–153, 2022.

[20] M.-L. Tsai, S.-H. Su, J.-K. Chang, D.-S. Tsai, C.-H. Chen, C.-I. Wu, L.-J. Li, L.-J. Chen, and J.-H. He. *Monolayer MoS2 Heterojunction Solar Cells*, *ACS Nano*, vol. 8, no. 8, pp. 8317–8322, 2014.

[21] H. Chang, M. N. Yogeesh, R. Ghosh, A. Rai, A. Sanne, S. Yang, N. Lu, S. K. Banerjee, and D. Akinwande. *Large-Area Monolayer MoS2 for Flexible Low-Power RF Nanoelectronics in the GHz Regime*, *Advanced Materials*, vol. 28, no. 9, pp. 1818–1823, 2016.

[22] R. Cheng, S. Jiang, Y. Chen, Y. Liu, N. Weiss, H.-C. Cheng, H. Wu, Y. Huang, and X. Duan. *Few-Layer Molybdenum Disulfide Transistors and Circuits for High-Speed Flexible Electronics*, *Nature Communications*, vol. 5, p. 5143, 2014.

[23] H. Casademont. *2D semiconductors for flexible electronics: assessment of the potential of MoS2 monolayers as channel material*, Ph.D. dissertation, 2016.

[24] I. Datta, S. H. Chae, G. R. Bhatt, M. A. Tadayon, B. Li, Y. Yu, C. Park, J. Park, L. Cao, D. N. Basov, J. Hone, and M. Lipson. *Low-Loss Composite Photonic Platform Based on 2D Semiconductor Monolayers*, *Nature Photonics*, vol. 14, no. 4, pp. 256–262, 2020.

[25] J. B. Khurgin, V. J. Sorger, and R. Amin. *Charge and Field Driven Integrated Optical Modulators: Comparative Analysis: Opinion*, *Optical Materials Express*, vol. 12, no. 5, p. 1784, 2022.

[26] M. Li, C. U. Hail, S. Biswas, and H. A. Atwater. *Excitonic Beam Steering in an Active van Der Waals Metasurface*, *Nano Letters*, vol. 23, no. 7, pp. 2771–2777, 2023.

[27] A. Mahmoudi, M. Bouaziz, A. Chiout, G. Di Berardino, N. Ullberg, G. Kremer, P. Dudin, J. Avila, M. Silly, V. Derycke, D. Romanin, M. Pala, I. C. Gerber, J. Chaste, F. Oehler, and A. Ouerghi. *Electronic Properties of Rhombohedrally Stacked Bilayer WSe2 Obtained by Chemical Vapor Deposition*, *Physical Review B*, vol. 108, no. 4, p. 045417, 2023.

[28] A. Guinier (Chairman), G. B. Bokij, K. Boll-Dornberger, J. M. Cowley, S. Ďurovič, H. Jagodzinski, P. Krishna, P. M. De Wolff, B. B. Zvyagin, D. E. Cox, P. Goodman, Th. Hahn, K. Kuchitsu, and S. C. Abrahams. *Nomenclature of Polytype Structures. Report of the International Union of Crystallography Ad Hoc Committee on the Nomenclature of Disordered, Modulated and Polytype Structures*, *Acta Crystallographica Section A Foundations of Crystallography*, vol. 40, no. 4, pp. 399–404, 1984.

[29] I. Song, C. Park, and H. C. Choi. *Synthesis and Properties of Molybdenum Disulphide: From Bulk to Atomic Layers*, *RSC Advances*, vol. 5, no. 10, pp. 7495–7514, 2015.

[30] J. Yan, J. Xia, X. Wang, L. Liu, J.-L. Kuo, B. K. Tay, S. Chen, W. Zhou, Z. Liu, and Z. X. Shen. *Stacking-Dependent Interlayer Coupling in Trilayer MoS2 with Broken Inversion Symmetry*, *Nano Letters*, vol. 15, no. 12, pp. 8155–8161, 2015.

[31] W. Zhao, J. Pan, Y. Fang, X. Che, D. Wang, K. Bu, and F. Huang. *Metastable MoS2: Crystal Structure, Electronic Band Structure, Synthetic Approach and Intriguing Physical Properties*, *Chemistry – A European Journal*, vol. 24, no. 60, pp. 15 942–15 954, 2018.

[32] Y. Yu, G.-H. Nam, Q. He, X.-J. Wu, K. Zhang, Z. Yang, J. Chen, Q. Ma, M. Zhao, Z. Liu, F.-R. Ran, X. Wang, H. Li, X. Huang, B. Li, Q. Xiong, Q. Zhang, Z. Liu, L. Gu, Y. Du, W. Huang, and H. Zhang. *High Phase-Purity 1T'-MoS2- and 1T'-MoSe2-Layered Crystals*, *Nature Chemistry*, vol. 10, no. 6, pp. 638–643, 2018.

[33] S. Manzeli, D. Ovchinnikov, D. Pasquier, O. V. Yazyev, and A. Kis. *2D Transition Metal Dichalcogenides*, *Nature Reviews Materials*, vol. 2, no. 8, p. 17033, 2017.

[34] W. Choi, N. Choudhary, G. H. Han, J. Park, D. Akinwande, and Y. H. Lee. *Recent Development of Two-Dimensional Transition Metal Dichalcogenides and Their Applications*, *Materials Today*, vol. 20, no. 3, pp. 116–130, 2017.

[35] P. Miró, M. Audiffred, and T. Heine. *An Atlas of Two-Dimensional Materials*, *Chem. Soc. Rev.*, vol. 43, no. 18, pp. 6537–6554, 2014.

[36] Q. H. Wang, K. Kalantar-Zadeh, A. Kis, J. N. Coleman, and M. S. Strano. *Electronics and Optoelectronics of Two-Dimensional Transition Metal Dichalcogenides*, *Nature Nanotechnology*, vol. 7, no. 11, pp. 699–712, 2012.

[37] Y. Li, A. Chernikov, X. Zhang, A. Rigosi, H. M. Hill, A. M. van der Zande, D. A. Chenet, E.-M. Shih, J. Hone, and T. F. Heinz. *Measurement of the Optical Dielectric Function of Monolayer Transition-Metal Dichalcogenides: MoS2, MoSe2, WS2, and WSe2*, *Physical Review B*, vol. 90, no. 20, p. 205422, 2014.

[38] A. Chernikov, T. C. Berkelbach, H. M. Hill, A. Rigosi, Y. Li, O. B. Aslan, D. R. Reichman, M. S. Hybertsen, and T. F. Heinz. *Exciton Binding Energy and Nonhydrogenic Rydberg Series in Monolayer WS2*, *Physical Review Letters*, vol. 113, no. 7, p. 076802, 2014.

[39] M. Ye, D. Winslow, D. Zhang, R. Pandey, and Y. Yap. *Recent Advancement on the Optical Properties of Two-Dimensional Molybdenum Disulfide (MoS2) Thin Films*, *Photonics*, vol. 2, pp. 288–307, 2015.

[40] A. M. van der Zande, P. Y. Huang, D. A. Chenet, T. C. Berkelbach, Y. You, G.-H. Lee, T. F. Heinz, D. R. Reichman, D. A. Muller, and J. C. Hone. *Grains and Grain Boundaries in Highly Crystalline Monolayer Molybdenum Disulphide*, *Nature Materials*, vol. 12, no. 6, pp. 554–561, 2013.

[41] S. Najmaei, Z. Liu, W. Zhou, X. Zou, G. Shi, S. Lei, B. I. Yakobson, J.-C. Idrobo, P. M. Ajayan, and J. Lou. *Vapour Phase Growth and Grain Boundary Structure of Molybdenum Disulphide Atomic Layers*, *Nature Materials*, vol. 12, no. 8, pp. 754–759, 2013.

[42] Y. Liu, R. Ghosh, D. Wu, A. Ismach, R. Ruoff, and K. Lai. *Mesoscale Imperfections in MoS2 Atomic Layers Grown by a Vapor Transport Technique*, *Nano Letters*, vol. 14, no. 8, pp. 4682–4686, 2014.

[43] O. Henrotte, T. Bottein, H. Casademont, K. Jaouen, T. Bourgeteau, S. Campidelli, V. Derycke, B. Jousselme, and R. Cornut. *Electronic Transport of MoS2 Monolayered Flakes Investigated by Scanning Electrochemical Microscopy*, *ChemPhysChem*, vol. 18, no. 19, pp. 2777–2781, 2017.

[44] H.-Y. Du, Y.-F. Huang, D. Wong, M.-F. Tseng, Y.-H. Lee, C.-H. Wang, C.-L. Lin, G. Hoffmann, K.-H. Chen, and L.-C. Chen. *Nanoscale Redox Mapping at the MoS2-Liquid Interface*, *Nature Communications*, vol. 12, no. 1, p. 1321, 2021.

[45] T. F. Jaramillo, K. P. Jørgensen, J. Bonde, J. H. Nielsen, S. Horch, and I. Chorkendorff. *Identification of Active Edge Sites for Electrochemical H2 Evolution from MoS2 Nanocatalysts*, *Science*, vol. 317, no. 5834, pp. 100–102, 2007.

[46] N. Salazar, S. Rangarajan, J. Rodríguez-Fernández, M. Mavrikakis, and J. V. Lauritsen. *Site-Dependent Reactivity of MoS2 Nanoparticles in Hydrodesulfurization of Thiophene*, *Nature Communications*, vol. 11, no. 1, p. 4369, 2020.

[47] K. Hayashi, M. Kataoka, H. Jippo, J. Yamaguchi, M. Ohfuchi, and S. Sato. *Highly Sensitive NO2 Detection by TVS-Grown Multilayer MoS2 Films*, *ACS Omega*, vol. 7, no. 2, pp. 1851–1860, 2022.

[48] S. Kim, H. Park, S. Choo, S. Baek, Y. Kwon, N. Liu, J. Y. Yang, C.-W. Yang, G. Yoo, and S. Kim. *Active-Matrix Monolithic Gas Sensor Array Based on MoS2 Thin-Film Transistors*, *Communications Materials*, vol. 1, no. 1, p. 86, 2020.

[49] P. Yasaei, B. Kumar, R. Hantehzadeh, M. Kayyalha, A. Baskin, N. Repnin, C. Wang, R. F. Klie, Y. P. Chen, P. Král, and A. Salehi-Khojin. *Chemical Sensing with Switchable Transport Channels in Graphene Grain Boundaries*, *Nature Communications*, vol. 5, p. 4911, 2014.

[50] F. Veliev, A. Cresti, D. Kalita, A. Bourrier, T. Belloir, A. Briançon-Marjollet, M. Albrieux, S. Roche, V. Bouchiat, and C. Delacour. *Sensing Ion Channel in Neuron Networks with Graphene Field Effect Transistors*, *2D Materials*, vol. 5, no. 4, p. 045020, 2018.

[51] A. Salehi-Khojin, D. Estrada, K. Y. Lin, M.-H. Bae, F. Xiong, E. Pop, and R. I. Masel. *Polycrystalline Graphene Ribbons as Chemiresistors*, *Advanced Materials*, vol. 24, pp. 53–57, 2012.

[52] L. Liu, K. Ye, C. Lin, Z. Jia, T. Xue, A. Nie, Y. Cheng, J. Xiang, C. Mu, B. Wang, F. Wen, K. Zhai, Z. Zhao, Y. Gong, Z. Liu, and Y. Tian. *Grain-Boundary-Rich Polycrystalline Monolayer WS2 Film for Attomolar-Level Hg2+ Sensors*, *Nature Communications*, vol. 12, no. 1, p. 3870, 2021.

[53] M. Magnozzi, T. Pflug, M. Ferrera, S. Pace, L. Ramó, M. Olbrich, P. Canepa, H. Ağircan, A. Horn, S. Forti, O. Cavalleri, C. Coletti, F. Bisio, and M. Canepa. *Local Optical Properties in CVD-Grown Monolayer WS2 Flakes*, *The Journal of Physical Chemistry C*, vol. 125, no. 29, pp. 16 059–16 065, 2021.

[54] H. Xin, J. Zhang, C. Yang, and Y. Chen. *Direct Detection of Inhomogeneity in CVD-Grown 2D TMD Materials via K-Means Clustering Raman Analysis*, *Nanomaterials*, vol. 12, no. 3, p. 414, 2022.

[55] A. Senkić, J. Bajo, A. Supina, B. Radatović, and N. Vujičić. *Effects of CVD Growth Parameters on Global and Local Optical Properties of MoS2 Monolayers*, *Materials Chemistry and Physics*, vol. 296, p. 127185, 2023.

[56] X. Wang, K. Tantiwanichapan, J. W. Christopher, R. Paiella, and A. K. Swan. *Uniaxial Strain Redistribution in Corrugated Graphene: Clamping, Sliding, Friction, and 2D Band Splitting*, *Nano Letters*, vol. 15, no. 9, pp. 5969–5975, 2015.

[57] X. Wang, J. W. Christopher, and A. K. Swan. *2D Raman Band Splitting in Graphene: Charge Screening and Lifting of the K-Point Kohn Anomaly*, *Scientific Reports*, vol. 7, p. 13539, 2017.

[58] J. W. Christopher, B. B. Goldberg, and A. K. Swan. *Long Tailed Trions in Monolayer MoS2: Temperature Dependent Asymmetry and Resulting Red-Shift of Trion Photoluminescence Spectra*, *Scientific Reports*, vol. 7, p. 14062, 2017.

[59] Z. Chen, N. Ullberg, M. Vutukuru, D. Barton, and A. K. Swan. *Ultra-Low Doping and Local Charge Variation in Graphene Measured by Raman: Experiment and Simulation*, *arXiv*, 2020.

[60] M. Vutukuru, H. Ardekani, Z. Chen, R. L. Wilmington, K. Gundogdu, and A. K. Swan. *Enhanced Dielectric Screening and Photoluminescence from Nanopillar-Strained MoS2 Nanosheets: Implications for Strain Funneling in Optoelectronic Applications*, *ACS Applied Nano Materials*, vol. 4, no. 8, pp. 8101–8107, 2021.

[61] I. S. Kim, V. K. Sangwan, D. Jariwala, J. D. Wood, S. Park, K.-S. Chen, F. Shi, F. Ruiz-Zepeda, A. Ponce, M. Jose-Yacaman, V. P. Dravid, T. J. Marks, M. C. Hersam, and L. J. Lauhon. *Influence of Stoichiometry on the Optical and Electrical Properties of Chemical Vapor Deposition Derived MoS2*, *ACS Nano*, vol. 8, no. 10, pp. 10 551–10 558, 2014.

[62] X. Zhang, Q. Liao, S. Liu, Z. Kang, Z. Zhang, J. Du, F. Li, S. Zhang, J. Xiao, B. Liu, Y. Ou, X. Liu, L. Gu, and Y. Zhang. *Poly(4-Styrenesulfonate)-Induced Sulfur Vacancy Self-Healing Strategy for Monolayer MoS2 Homojunction Photodiode*, *Nature Communications*, vol. 8, no. 1, p. 15881, 2017.

[63] P. Vancsó, G. Z. Magda, J. Pető, J.-Y. Noh, Y.-S. Kim, C. Hwang, L. P. Biró, and L. Tapasztó. *The Intrinsic Defect Structure of Exfoliated MoS2 Single Layers Revealed by Scanning Tunneling Microscopy*, *Scientific Reports*, vol. 6, no. 1, p. 29726, 2016.

[64] L. Zhu, J. Tang, B. Li, T. Hou, Y. Zhu, J. Zhou, Z. Wang, X. Zhu, Z. Yao, X. Cui, K. Watanabe, T. Taniguchi, Y. Li, Z. V. Han, W. Zhou, Y. Huang, Z. Liu, J. C. Hone, and Y. Hao. *Artificial Neuron Networks Enabled Identification and Characterizations of 2D Materials and van Der Waals Heterostructures*, *ACS Nano*, vol. 16, no. 2, pp. 2721–2729, 2022.

[65] S. Y. Lee, U. J. Kim, J. Chung, H. Nam, H. Y. Jeong, G. H. Han, H. Kim, H. M. Oh, H. Lee, H. Kim, Y.-G. Roh, J. Kim, S. W. Hwang, Y. Park, and Y. H. Lee. *Large Work Function Modulation of Monolayer MoS2 by Ambient Gases*, *ACS Nano*, vol. 10, no. 6, pp. 6100–6107, 2016.

[66] A. Kozbial, X. Gong, H. Liu, and L. Li. *Understanding the Intrinsic Water Wettability of Molybdenum Disulfide (MoS2)*, *Langmuir*, vol. 31, no. 30, pp. 8429–8435, 2015.

[67] J. M. Katzen, M. Velický, Y. Huang, S. Drakeley, W. Hendren, R. M. Bowman, Q. Cai, Y. Chen, L. H. Li, and F. Huang. *Rigorous and Accurate Contrast Spectroscopy for Ultimate Thickness Determination of Micrometer-Sized Graphene on Gold and Molecular Sensing*, *ACS Applied Materials & Interfaces*, vol. 10, no. 26, pp. 22 520–22 528, 2018.

[68] J.-H. Ahn, W. M. Parkin, C. H. Naylor, A. T. C. Johnson, and M. Drndić. *Ambient Effects on Electrical Characteristics of CVD-Grown Monolayer MoS2 Field-Effect Transistors*, *Scientific Reports*, vol. 7, no. 1, p. 4075, 2017.

[69] P. Klement, C. Steinke, S. Chatterjee, T. O. Wehling, and M. Eickhoff. *Effects of the Fermi Level Energy on the Adsorption of O2 to Monolayer MoS2*, *2D Materials*, vol. 5, no. 4, p. 045025, 2018.

[70] P. Gallagher, Y. Li, K. Watanabe, T. Taniguchi, T. F. Heinz, and D. Goldhaber-Gordon. *Optical Imaging and Spectroscopic Characterization of Self-Assembled Environmental Adsorbates on Graphene*, *Nano Letters*, vol. 18, no. 4, pp. 2603–2608, 2018.

[71] C. R. Zhu, G. Wang, B. L. Liu, X. Marie, X. F. Qiao, X. Zhang, X. X. Wu, H. Fan, P. H. Tan, T. Amand, and B. Urbaszek. *Strain Tuning of Optical Emission Energy and Polarization in Monolayer and Bilayer MoS2*, *Physical Review B*, vol. 88, no. 12, p. 121301, 2013.

[72] P. E. Gaskell, H. S. Skulason, C. Rodenchuk, and T. Szkopek. *Counting Graphene Layers on Glass via Optical Reflection Microscopy*, *Applied Physics Letters*, vol. 94, no. 14, p. 143101, 2009.

[73] W. Li, S. Moon, M. Wojcik, and K. Xu. *Direct Optical Visualization of Graphene and Its Nanoscale Defects on Transparent Substrates*, *Nano Letters*, vol. 16, no. 8, pp. 5027–5031, 2016.

[74] P. Blake, E. W. Hill, A. H. Castro Neto, K. S. Novoselov, D. Jiang, R. Yang, T. J. Booth, and A. K. Geim. *Making Graphene Visible*, *Applied Physics Letters*, vol. 91, no. 6, p. 063124, 2007.

[75] V. Panchal, Y. Yang, G. Cheng, J. Hu, M. Kruskopf, C.-I. Liu, A. F. Rigosi, C. Melios, A. R. Hight Walker, D. B. Newell, O. Kazakova, and R. E. Elmquist. *Confocal Laser Scanning Microscopy for Rapid Optical Characterization of Graphene*, *Communications Physics*, vol. 1, p. 83, 2018.

[76] P. Romagnoli, H. G. Rosa, D. Lopez-Cortes, E. A. T. Souza, J. C. Viana-Gomes, W. Margulis, and C. J. S. de Matos. *Making Graphene Visible on Transparent Dielectric Substrates: Brewster Angle Imaging*, *2D Materials*, vol. 2, no. 3, p. 035017, 2015.

[77] T. Potočnik, O. Burton, M. Reutzel, D. Schmitt, J. P. Bange, S. Mathias, F. R. Geisenhof, R. T. Weitz, L. Xin, H. J. Joyce, S. Hofmann, and J. A. Alexander-Webber. *Fast Twist Angle Mapping of Bilayer Graphene Using Spectroscopic Ellipsometric Contrast Microscopy*, *Nano Letters*, vol. 23, no. 12, pp. 5506–5513, 2023.

[78] H.-L. Kim and F. Wang. *Reflective Phase-Contrast for High-Contrast Imaging of van Der Waals Heterostructure*, *Nano Letters*, vol. 23, no. 7, pp. 2898–2904, 2023.

[79] P. Braeuninger-Weimer, S. Funke, R. Wang, P. Thiesen, D. Tasche, W. Viöl, and S. Hofmann. *Fast, Noncontact, Wafer-Scale, Atomic Layer Resolved Imaging of Two-Dimensional Materials by Ellipsometric Contrast Micrography*, *ACS Nano*, vol. 12, no. 8, pp. 8555–8563, 2018.

[80] D. Ausserré and M.-P. Valignat. *Surface Enhanced Ellipsometric Contrast (SEEC) Basic Theory and $\lambda/4$ Multilayered Solutions*, *Optics Express*, vol. 15, no. 13, p. 8329, 2007.

[81] J.-L. Buraud, O. Noël, and D. Ausserré. *From Permeation to Pore Nucleation in Smectic Stacks*, *Langmuir*, vol. 29, no. 28, pp. 8944–8949, 2013.

[82] D. M. Goggin, H. Zhang, E. M. Miller, and J. R. Samaniuk. *Interference Provides Clarity: Direct Observation of 2D Materials at Fluid–Fluid Interfaces*, *ACS Nano*, vol. 14, no. 1, pp. 777–790, 2020.

[83] M. Wojcik, Y. Li, W. Li, and K. Xu. *Spatially Resolvedin Situ Reaction Dynamics of Graphene via Optical Microscopy*, *Journal of the American Chemical Society*, vol. 139, no. 16, pp. 5836–5841, 2017.

[84] W. Li, M. Wojcik, and K. Xu. *Optical Microscopy Unveils Rapid, Reversible Electrochemical Oxidation and Reduction of Graphene*, *Nano Letters*, vol. 19, no. 2, pp. 983–989, 2019.

[85] D. M. Goggin and J. R. Samaniuk. *2D Colloids: Size- and Shape-Controlled 2D Materials at Fluid–Fluid Interfaces*, *Langmuir*, vol. 37, no. 48, pp. 14 157–14 166, 2021.

[86] D. M. Goggin, R. Bei, R. Anderson, D. A. Gómez-Gualdrón, and J. R. Samaniuk. *Stacking of Monolayer Graphene Particles at a Water–Vapor Interface*, *The Journal of Physical Chemistry C*, vol. 125, no. 14, pp. 7880–7888, 2021.

[87] S. Campidelli, R. A. Khachfe, K. Jaouen, J. Monteiller, C. Amra, M. Zerrad, R. Cornut, V. Derycke, and D. Ausserré. *Backside Absorbing Layer Microscopy: Watching Graphene Chemistry*, *Science Advances*, vol. 3, no. 5, p. e1601724, 2017.

[88] D. Ausserré, A. R. Khachfe, L. Roussille, G. Brotons, L. Vonna, F. Lemarchand, M. Zerrad, and C. Amra. *Anti-Reflecting Absorbing Layers for Electrochemical and Biophotonic Applications*, *Journal of Nanomedicine & Nanotechnology*, vol. 5, no. 4, 2014.

[89] S. Wang, X. Shan, U. Patel, X. Huang, J. Lu, J. Li, and N. Tao. *Label-Free Imaging, Detection, and Mass Measurement of Single Viruses by Surface Plasmon Resonance*, *Proceedings of the National Academy of Sciences*, vol. 107, no. 37, pp. 16 028–16 032, 2010.

[90] E. Hecht. *Optics, 4th ed.*, 2001.

[91] M. A. Van Dijk, A. L. Tchebotareva, M. Orrit, M. Lippitz, S. Berciaud, D. Lasne, L. Cognet, and B. Lounis. *Absorption and Scattering Microscopy of Single Metal Nanoparticles*, *Physical Chemistry Chemical Physics*, vol. 8, no. 30, p. 3486, 2006.

[92] D. Cole, G. Young, A. Weigel, A. Sebesta, and P. Kukura. *Label-Free Single-Molecule Imaging with Numerical-Aperture-Shaped Interferometric Scattering Microscopy*, *ACS Photonics*, vol. 4, no. 2, pp. 211–216, 2017.

[93] O. Avci, N. Ünlü, A. Özkumur, and M. Ünlü. *Interferometric Reflectance Imaging Sensor (IRIS)—A Platform Technology for Multiplexed Diagnostics and Digital Detection*, *Sensors*, vol. 15, no. 7, pp. 17 649–17 665, 2015.

[94] R. W. Taylor and V. Sandoghdar. *Interferometric Scattering Microscopy: Seeing Single Nanoparticles and Molecules via Rayleigh Scattering*, *Nano Letters*, vol. 19, no. 8, pp. 4827–4835, 2019.

[95] E. Ozkumur, J. W. Needham, D. A. Bergstein, R. Gonzalez, M. Cabodi, J. M. Gershoni, B. B. Goldberg, and M. S. Ünlü. *Label-Free and Dynamic Detection of Biomolecular Interactions for High-Throughput Microarray Applications*, *Proceedings of the National Academy of Sciences of the United States of America*, vol. 105, no. 23, pp. 7988–7992, 2008.

[96] O. Avci, R. Adato, A. Y. Ozkumur, and M. S. Ünlü. *Physical Modeling of Interference Enhanced Imaging and Characterization of Single Nanoparticles*, *Optics Express*, vol. 24, no. 6, p. 6094, 2016.

[97] C. Yurdakul, O. Avci, A. Matlock, A. J. Devaux, M. V. Quintero, E. Ozbay, R. A. Davey, J. H. Connor, W. C. Karl, L. Tian, and M. S. Ünlü. *High-Throughput, High-Resolution Interferometric Light Microscopy of Biological Nanoparticles*, *ACS Nano*, vol. 14, no. 2, pp. 2002–2013, 2020.

[98] R. Attota, P. P. Kavuri, H. Kang, R. Kasica, and L. Chen. *Nanoparticle Size Determination Using Optical Microscopes*, *Applied Physics Letters*, vol. 105, no. 16, p. 163105, 2014.

[99] H. Kang, R. Attota, V. Tondare, A. E. Vladár, and P. Kavuri. *A Method to Determine the Number of Nanoparticles in a Cluster Using Conventional Optical Microscopes*, *Applied Physics Letters*, vol. 107, no. 10, p. 103106, 2015.

[100] R. K. Attota and H. Kang. *Parameter Optimization for Through-Focus Scanning Optical Microscopy*, *Optics Express*, vol. 24, no. 13, p. 14915, 2016.

[101] A. Abdelrahman, A.-S. Smith, and K. Sengupta. *Observing Membrane and Cell Adhesion via Reflection Interference Contrast Microscopy*, 2023.

[102] A. S. G. Curtis. *The Mechanism of Adhesion of Cells to Glass: A Study by Interference Reflection Microscopy*, *Journal of Cell Biology*, vol. 20, no. 2, pp. 199–215, 1964.

[103] J. S. Ploem. *Reflection-contrast Microscopy as a Tool for Investigation of the Attachment of Living Cells to a Glass Surface*, in *Mononuclear Phagocytes: In Immunity, Infection, and Pathology*, R. v. Furth, Ed., 1975, pp. 405–421.

[104] C. S. Izzard and L. R. Lochner. *Cell-to-Substrate Contacts in Living Fibroblasts: An Interference Reflection Study with an Evaluation of the Technique*, *Journal of Cell Science*, vol. 21, no. 1, p. 32, 1976.

[105] D. Gingell and I. Todd. *Interference Reflection Microscopy. A Quantitative Theory for Image Interpretation and Its Application to Cell-Substratum Separation Measurement*, *Biophysical Journal*, vol. 26, no. 3, pp. 507–526, 1979.

[106] K. Beck and J. Bereiter-Hahn. *Evaluation of Reflection Interference Contrast Microscope Images of Living Cells*, *Microscopica Acta*, vol. 84, no. 2, pp. 153–178, 1981.

[107] H. Verschueren. *IRM in Cell Biology: Methodology and Applications*, *Journal of Cell Science*, vol. 75, no. 1, p. 24, 1985.

[108] J. S. Ploem and F. A. Prins. *Reflection-Contrast Microscopy – Review*, *infocus Magazine*, no. 47, pp. 38–56, 2017.

[109] K. Klein, C. E. Rommel, V. C. Hirschfeld-Warneken, and J. P. Spatz. *Cell Membrane Topology Analysis by RICM Enables Marker-Free Adhesion Strength Quantification*, *Biointerphases*, vol. 8, no. 1, p. 28, 2013.

[110] L. Limozin and K. Sengupta. *Quantitative RICM in Soft Matter and Cell Adhesion*, *ChemPhysChem*, vol. 10, no. 16, pp. 2752–2768, 2009.

[111] O. Theodoly, Z.-H. Huang, and M.-P. Valignat. *New Modeling of Reflection Interference Contrast Microscopy Including Polarization and Numerical Aperture Effects: Application to Nanometric Distance Measurements and Object Profile Reconstruction*, *Langmuir*, vol. 26, no. 3, pp. 1940–1948, 2010.

[112] C. Hammond. *Symmetrical Ray Diagrams of the Optical Pathways in Light Microscopes*, *Microscopy and Analysis*, vol. 20, no. 5, pp. 5–8, 2006.

[113] A. Köhler. *Ein neues Beleuchtungsverfahren für mikrophotographische Zwecke*, *Zeitschrift für wissenschaftliche Mikroskopie und für Mikroskopische Technik*, vol. 10, no. 4, pp. 433–440, 1893.

[114] J. Madrid-Wolff and M. Forero-Shelton. *4f Koehler Transmitted Illumination Condenser for Teaching and Low-Cost Microscopic Imaging*, *The Biophysicist*, vol. 1, no. 2, p. 10, 2020.

[115] E. Agocs and R. K. Attota. *Enhancing Optical Microscopy Illumination to Enable Quantitative Imaging*, *Scientific Reports*, vol. 8, no. 1, p. 4782, 2018.

[116] M. Mahamdeh, S. Simmert, A. Luchniak, E. Schäffer, and J. Howard. *Label-Free High-Speed Wide-Field Imaging of Single Microtubules Using Interference Reflection Microscopy*, *Journal of Microscopy*, vol. 272, no. 1, pp. 60–66, 2018.

[117] C. Yurdakul and M. S. Ünlü. *Computational Nanosensing from Defocus in Single Particle Interferometric Reflectance Microscopy*, *Optics Letters*, vol. 45, no. 23, p. 6546, 2020.

[118] https://www.prizmatix.com/optogenetics/liquid_light_guide.htm.

[119] https://www.excelitas.com/file-download/download/public/73356?filename=x-cite_120pc_q_user_manual.pdf.

[120] E. A. Patterson and M. P. Whelan. *Optical Signatures of Small Nanoparticles in a Conventional Microscope*, *Small*, vol. 4, no. 10, pp. 1703–1706, 2008.

[121] R. Attota, R. M. Silver, and J. Potzick. *Optical Illumination and Critical Dimension Analysis using the Through-Focus Focus Metric Method*, in *Novel Optical Systems Design and Optimization IX*, vol. 6289. SPIE, 2006, pp. 232–241.

[122] O. Avci, M. I. Campana, C. Yurdakul, and M. Selim Ünlü. *Pupil Function Engineering for Enhanced Nanoparticle Visibility in Wide-Field Interferometric Microscopy*, *Optica*, vol. 4, no. 2, p. 247, 2017.

[123] S. Berciaud, L. Cognet, P. Tamarat, and B. Lounis. *Observation of Intrinsic Size Effects in the Optical Response of Individual Gold Nanoparticles*, *Nano Letters*, vol. 5, no. 3, pp. 515–518, 2005.

[124] J.-F. Lemineur, P. Ciocci, J.-M. Noël, H. Ge, C. Combellas, and F. Kanoufi. *Imaging and Quantifying the Formation of Single Nanobubbles at Single Platinum Nanoparticles during the Hydrogen Evolution Reaction*, *ACS Nano*, vol. 15, no. 2, pp. 2643–2653, 2021.

[125] G. Brooker. *Modern Classical Optics*. Oxford University Press, 2003.

[126] C. Maurer, A. Jesacher, S. Bernet, and M. Ritsch-Marte. *What Spatial Light Modulators Can Do for Optical Microscopy*, *Laser & Photonics Reviews*, vol. 5, no. 1, pp. 81–101, 2011.

[127] C. J. Sheppard. *Introduction to optical microscopy: fundamental concepts and developments in modern microscopy*, 2017.

[128] C. J. R. Sheppard. *Resolution and Super-Resolution*, *Microscopy Research and Technique*, vol. 80, no. 6, pp. 590–598, 2017.

[129] F. Huang. *Optical Contrast of Atomically Thin Films*, *The Journal of Physical Chemistry C*, vol. 123, no. 12, pp. 7440–7446, 2019.

[130] https://www.telescope-optics.net/eye_intensity_response.htm.

[131] G. E. Donnelly, M. Velický, W. R. Hendren, R. M. Bowman, and F. Huang. *Achieving Extremely High Optical Contrast of Atomically-Thin MoS2*, *Nanotechnology*, vol. 31, no. 14, p. 145706, 2020.

[132] M. Velický, W. R. Hendren, G. E. Donnelly, J. M. Katzen, R. M. Bowman, and F. Huang. *Optimising the Visibility of Graphene and Graphene Oxide on Gold with Multilayer Heterostructures*, *Nanotechnology*, vol. 29, no. 27, p. 275205, 2018.

[133] E. Peli. *Contrast in Complex Images*, *Journal of the Optical Society of America A*, vol. 7, no. 10, pp. 2032–2040, 1990.

[134] A. D. Hwang and E. Peli. *New Contrast Metric for Realistic Display Performance Measure*, *SID Symposium Digest of Technical Papers*, vol. 47, no. 1, pp. 982–985, 2016.

[135] L. Miquilini, N. A. Walker, E. A. Odigie, D. L. Guimarães, R. C. Salomão, E. M. C. B. Lacerda, M. I. T. Cortes, L. C. De Lima Silveira, M. E. C. Fitzgerald, D. F. Ventura, and G. S. Souza. *Influence of Spatial and Chromatic Noise on Luminance Discrimination*, *Scientific Reports*, vol. 7, no. 1, p. 16944, 2017.

[136] M. Hunter, B. Godde, and B. Olk. *Effects of Absolute Luminance and Luminance Contrast on Visual Discrimination in Low Mesopic Environments*, *Attention, Perception, & Psychophysics*, vol. 79, no. 1, pp. 243–252, 2017.

[137] M. Fox. *Optical Properties of Solids, 2nd ed.* Oxford University Press, 2010.

[138] H. Fujiwara. *Spectroscopic Ellipsometry: Principles and Applications*. John Wiley & Sons, 2007.

[139] O. Stenzel. *The Physics of Thin Film Optical Spectra, 2nd ed.* Springer, 2016.

[140] S. J. Orfanidis. *Electromagnetic Waves and Antennas*, 2016.

[141] A. Pekker, F. Borondics, K. Kamarás, A. G. Rinzler, and D. B. Tanner. *Calculation of Optical Constants from Carbon Nanotube Transmission Spectra*, *physica status solidi (b)*, vol. 243, no. 13, pp. 3485–3488, 2006.

[142] V. Lucarini, J. J. Saarinen, K.-E. Peiponen, and E. M. Vartiainen. *Kramers–Kronig Relations in Optical Materials Research*. Springer, 2005.

[143] H. R. Philipp and E. A. Taft. *Optical Constants of Germanium in the Region 1 to 10 eV*, *Physical Review*, vol. 113, no. 4, pp. 1002–1005, 1959.

[144] Y. Yu, Y. Yu, L. Huang, H. Peng, L. Xiong, and L. Cao. *Giant Gating Tunability of Optical Refractive Index in Transition Metal Dichalcogenide Monolayers*, *Nano Letters*, vol. 17, no. 6, pp. 3613–3618, 2017.

[145] J. S. C. Prentice. *Coherent, Partially Coherent and Incoherent Light Absorption in Thin-Film Multilayer Structures*, *Journal of Physics D: Applied Physics*, vol. 33, no. 24, pp. 3139–3145, 2000.

[146] C. C. Katsidis and D. I. Siapkas. *General Transfer-Matrix Method for Optical Multilayer Systems with Coherent, Partially Coherent, and Incoherent Interference*, *Applied Optics*, vol. 41, no. 19, p. 3978, 2002.

[147] E. Centurioni. *Generalized Matrix Method for Calculation of Internal Light Energy Flux in Mixed Coherent and Incoherent Multilayers*, *Applied Optics*, vol. 44, no. 35, p. 7532, 2005.

[148] M. C. Troparevsky, A. S. Sabau, A. R. Lupini, and Z. Zhang. *Transfer-Matrix Formalism for the Calculation of Optical Response in Multilayer Systems: From Coherent to Incoherent Interference*, *Optics Express*, vol. 18, no. 24, p. 24715, 2010.

[149] R. Santbergen, A. H. Smets, and M. Zeman. *Optical Model for Multilayer Structures with Coherent, Partly Coherent and Incoherent Layers*, *Optics Express*, vol. 21, no. S2, p. A262, 2013.

[150] M.-J. Dejardin, A. Hemmerle, A. Sadoun, Y. Hamon, P.-H. Puech, K. Sengupta, and L. Limozin. *Lamellipod Reconstruction by Three-Dimensional Reflection Interference Contrast Nanoscopy (3D-RICN)*, *Nano Letters*, vol. 18, no. 10, pp. 6544–6550, 2018.

[151] R. C. Rumpf. *EMPossible: Lecture – Transfer Matrices*, 2020.

[152] P. Yeh. *Optical Waves in Layered Media*. John Wiley & Sons, 1988.

[153] S. J. Byrnes. *Multilayer Optical Calculations*, *arXiv*, no. 1603.02720, 2020.

[154] C. Casiraghi, A. Hartschuh, E. Lidorikis, H. Qian, H. Harutyunyan, T. Gokus, K. S. Novoselov, and A. C. Ferrari. *Rayleigh Imaging of Graphene and Graphene Layers*, *Nano Letters*, vol. 7, no. 9, pp. 2711–2717, 2007.

[155] I. Jung, M. Pelton, R. Piner, D. A. Dikin, S. Stankovich, S. Watcharotone, M. Hausner, and R. S. Ruoff. *Simple Approach for High-Contrast Optical Imaging and Characterization of Graphene-Based Sheets*, *Nano Letters*, vol. 7, no. 12, pp. 3569–3575, 2007.

[156] L. Gao, W. Ren, F. Li, and H.-M. Cheng. *Total Color Difference for Rapid and Accurate Identification of Graphene*, *ACS Nano*, vol. 2, no. 8, pp. 1625–1633, 2008.

[157] M. Bruna and S. Borini. *Assessment of Graphene Quality by Quantitative Optical Contrast Analysis*, *Journal of Physics D: Applied Physics*, vol. 42, no. 17, p. 175307, 2009.

[158] R. V. Gorbachev, I. Riaz, R. R. Nair, R. Jalil, L. Britnell, B. D. Belle, E. W. Hill, K. S. Novoselov, K. Watanabe, T. Taniguchi, A. K. Geim, and P. Blake. *Hunting for Monolayer Boron Nitride: Optical and Raman Signatures*, *Small*, vol. 7, no. 4, pp. 465–468, 2011.

[159] I. Jung, J.-S. Rhyee, J. Y. Son, R. S. Ruoff, and K.-Y. Rhee. *Colors of Graphene and Graphene-Oxide Multilayers on Various Substrates*, *Nanotechnology*, vol. 23, no. 2, p. 025708, 2012.

[160] D. Bing, Y. Wang, J. Bai, R. Du, G. Wu, and L. Liu. *Optical Contrast for Identifying the Thickness of Two-Dimensional Materials*, *Optics Communications*, vol. 406, pp. 128–138, 2018.

[161] T. S. Menon, S. Mishra, V. C. Antony, K. Dixit, S. Kakkar, T. Ahmed, S. Islam, A. Jayaraman, K. Hsieh, P. Karnatak, and A. Ghosh. *Optimising Graphene Visibility in van Der Waals Heterostructures*, *Nanotechnology*, vol. 30, no. 39, p. 395704, 2019.

[162] N. Saigal, A. Mukherjee, V. Sugunakar, and S. Ghosh. *Angle of incidence averaging in reflectance measurements with optical microscopes for studying layered two-dimensional materials*, *Review of Scientific Instruments*, vol. 85, no. 7, p. 073105, 2014.

[163] Y. Hattori, H. Takahashi, N. Ikematsu, and M. Kitamura. *Chain-Length Dependence of Optical Properties for an Alkanethiol Monolayer on an Ultrathin Gold Film Revealed via Reflected Light Microscopy*, *The Journal of Physical Chemistry C*, vol. 125, no. 27, pp. 14 991–14 999, 2021.

[164] Y. Hattori, T. Taniguchi, K. Watanabe, and M. Kitamura. *Visualization of a Hexagonal Boron Nitride Monolayer on an Ultra-Thin Gold Film via Reflected Light Microscopy*, *Nanotechnology*, vol. 33, no. 6, p. 065702, 2021.

[165] Y. Hattori and M. Kitamura. *Reflected Light Microscopy of a Gold Oxide Layer Formed on a Au Film by Ultraviolet/Ozone Treatment*, *Thin Solid Films*, vol. 764, p. 139631, 2023.

[166] Y. Hattori, T. Taniguchi, K. Watanabe, and M. Kitamura. *Identification of the Monolayer Thickness Difference in a Mechanically Exfoliated Thick Flake of Hexagonal Boron Nitride and Graphite for van Der Waals Heterostructures*, *Nanotechnology*, vol. 34, no. 29, p. 295701, 2023.

[167] G. Hu, G. P. Pandey, Q. Liu, R. S. Anaredy, C. Ma, M. Liu, J. Li, S. K. Shaw, and J. Wu. *Self-Organization of Ions at the Interface between Graphene and Ionic Liquid DEME-TFSI*, *ACS Applied Materials & Interfaces*, vol. 9, no. 40, pp. 35 437–35 443, 2017.

[168] M. N. Polyanskiy. *Refractive index database*.

[169] A. Rohatgi. *Webplotdigitizer: Version 4.2*, 2020.

[170] V. G. Kravets, F. Wu, G. H. Auton, T. Yu, S. Imaizumi, and A. N. Grigorenko. *Measurements of electrically tunable refractive index of MoS2 monolayer and its usage in optical modulators*, *npj 2D Materials and Applications*, vol. 3, no. 36, 2019.

[171] H. Zhang, Y. Ma, Y. Wan, X. Rong, Z. Xie, W. Wang, and L. Dai. *Measuring the Refractive Index of Highly Crystalline Monolayer MoS2 with High Confidence*, *Scientific Reports*, vol. 5, no. 1, p. 8440, 2015.

[172] A. Castellanos-Gomez, N. Agraït, and G. Rubio-Bollinger. *Optical Identification of Atomically Thin Dichalcogenide Crystals*, *Applied Physics Letters*, vol. 96, no. 21, p. 213116, 2010.

[173] Y. Li and T. F. Heinz. *Two-Dimensional Models for the Optical Response of Thin Films*, *2D Materials*, vol. 5, no. 2, p. 025021, 2018.

[174] Y. V. Morozov and M. Kuno. *Optical Constants and Dynamic Conductivities of Single Layer MoS2, MoSe2, and WSe2*, *Applied Physics Letters*, vol. 107, no. 8, p. 083103, 2015.

[175] B. Majérus, L. Henrard, and P. Kockaert. *Optical Modeling of Single and Multilayer Two-Dimensional Materials and Heterostructures*, *Physical Review B*, vol. 107, no. 4, p. 045429, 2023.

[176] Z. Xu, D. Ferraro, A. Zaltron, N. Galvanetto, A. Martucci, L. Sun, P. Yang, Y. Zhang, Y. Wang, Z. Liu, J. D. Elliott, M. Marsili, L. Dell'Anna, P. Umari, and M. Merano. *Optical Detection of the Susceptibility Tensor in Two-Dimensional Crystals*, *Communications Physics*, vol. 4, no. 1, p. 215, 2021.

[177] G. A. Ermolaev, D. V. Grudinin, Y. V. Stebunov, K. V. Voronin, V. G. Kravets, J. Duan, A. B. Mazitov, G. I. Tselikov, A. Bylinkin, D. I. Yakubovsky, S. M. Novikov, D. G. Baranov, A. Y. Nikitin, I. A. Kruglov, T. Shegai, P. Alonso-González, A. N. Grigorenko, A. V. Arsenin, K. S. Novoselov, and V. S. Volkov. *Giant Optical Anisotropy in Transition Metal Dichalcogenides for Next-Generation Photonics*, *Nature Communications*, vol. 12, no. 1, p. 854, 2021.

[178] B. Munkhbat, P. Wróbel, T. J. Antosiewicz, and T. O. Shegai. *Optical Constants of Several Multilayer Transition Metal Dichalcogenides Measured by Spectroscopic Ellipsometry in the 300–1700 Nm Range: High Index, Anisotropy, and Hyperbolicity*, *ACS Photonics*, vol. 9, no. 7, pp. 2398–2407, 2022.

[179] A. Canales, O. Kotov, and T. O. Shegai. *Perfect Absorption and Strong Coupling in Supported MoS2 Multilayers*, *ACS Nano*, vol. 17, no. 4, pp. 3401–3411, 2023.

[180] E. Peci, M. Magnozzi, L. Ramó, M. Ferrera, D. Convertino, S. Pace, G. Orlandini, A. Sharma, I. Milekhin, G. Salvan, C. Coletti, D. R. T. Zahn, F. Bisio, and M. Canepa. *Dielectric Function of 2D Tungsten Disulfide in Homo- and Heterobilayer Stacking*, *Advanced Materials Interfaces*, vol. 10, no. 3, p. 2201586, 2022.

[181] I. Paradisanos, S. Shree, A. George, N. Leisgang, C. Robert, K. Watanabe, T. Taniguchi, R. J. Warburton, A. Turchanin, X. Marie, I. C. Gerber, and B. Urbaszek. *Controlling Interlayer Excitons in MoS2 Layers Grown by Chemical Vapor Deposition*, *Nature Communications*, vol. 11, no. 1, p. 2391, 2020.

[182] V. Nguyen, W. Li, J. Ager, K. Xu, and H. Taylor. *Optical Reflectance Imaging Reveals Interlayer Coupling in Mechanically Stacked MoS2 and WS2 Bilayers*, *Optics Express*, vol. 31, no. 2, p. 3291, 2023.

[183] K. M. McCreary, M. Phillips, H.-J. Chuang, D. Wickramaratne, M. Rosenberger, C. S. Hellberg, and B. T. Jonker. *Stacking-Dependent Optical Properties in Bilayer WSe2*, *Nanoscale*, vol. 14, pp. 147–156, 2022.

[184] K. Jaouen, R. Cornut, D. Ausserré, S. Campidelli, and V. Derycke. *Ideal Optical Contrast for 2D Material Observation Using Bi-Layer Antireflection Absorbing Substrates*, *Nanoscale*, vol. 11, no. 13, pp. 6129–6135, 2019.

[185] J.-F. Lemineur, J.-M. Noël, D. Ausserré, C. Combellas, and F. Kanoufi. *Combining Electrodeposition and Optical Microscopy for Probing Size-Dependent Single-Nanoparticle Electrochemistry*, *Angewandte Chemie International Edition*, vol. 57, no. 37, pp. 11 998–12 002, 2018.

[186] J.-F. Lemineur, J.-M. Noël, A. Courty, D. Ausserré, C. Combellas, and F. Kanoufi. *In Situ Optical Monitoring of the Electrochemical Conversion of Dielectric Nanoparticles: From Multistep Charge Injection to Nanoparticle Motion*, *Journal of the American Chemical Society*, vol. 142, no. 17, pp. 7937–7946, 2020.

[187] R. A. Khachfe and D. Ausserre. *Backside Absorbing Layer Microscopy: A Universal Relationship between Physical Thickness and Reflectivity*, *Optics Express*, vol. 28, no. 4, p. 4836, 2020.

[188] J. Bompard, O. Maniti, R. A. Khachfe, D. Ausserrée, and A. Girard-Egrot. *BALM: Watching the Formation of Tethered Bilayer Lipid Membranes with Submicron Lateral Resolution*, *Langmuir*, vol. 37, no. 31, pp. 9457–9471, 2021.

[189] D. Ausserré, R. Abou Khachfe, T. Taniguchi, K. Watanabe, and F. Vialla. *Backside Absorbing Layer Microscopy: Monolayer Counting in 2D Crystal Flakes*, *physica status solidi (b)*, p. 2300068, 2023.

[190] M. Watanabe and K. Kajikawa. *An Optical Fiber Biosensor Based on Anomalous Reflection of Gold*, *Sensors and Actuators B: Chemical*, vol. 89, no. 1-2, pp. 126–130, 2003.

[191] S. Watanabe, K. Usui, K.-y. Tomizaki, K. Kajikawa, and H. Mihara. *Anomalous Reflection of Gold Applicable for a Practical Protein-Detecting Chip Platform*, *Molecular BioSystems*, vol. 1, pp. 363–365, 2005.

[192] A. Syahir, K.-y. Tomizaki, K. Kajikawa, and H. Mihara. *Poly(Amidoamine)-Dendrimer-Modified Gold Surfaces for Anomalous Reflection of Gold To Detect Biomolecular Interactions*, *Langmuir*, vol. 25, no. 6, pp. 3667–3674, 2009.

[193] S.-y. Fukuba, R. Naraoka, K. Tsuboi, and K. Kajikawa. *A New Imaging Method for Gold-Surface Adsorbates Based on Anomalous Reflection*, *Optics Communications*, vol. 282, no. 16, pp. 3386–3391, 2009.

[194] A. Syahir, H. Mihara, and K. Kajikawa. *A New Optical Label-Free Biosensing Platform Based on a Metal–Insulator–Metal Structure*, *Langmuir*, vol. 26, no. 8, pp. 6053–6057, 2010.

[195] M. A. Kats, R. Blanchard, P. Genevet, and F. Capasso. *Nanometre Optical Coatings Based on Strong Interference Effects in Highly Absorbing Media*, *Nature Materials*, vol. 12, no. 1, pp. 20–24, 2013.

[196] S. Huang, J. Chen, T. Zhang, X. Dai, X. Wang, J. Zhou, W. Kong, Q. Liu, J. Qu, and Y. Shao. *Recent Advances in Surface Plasmon Resonance Microscopy*, *Chemosensors*, vol. 10, no. 12, p. 509, 2022.

[197] H. Nguyen, J. Park, S. Kang, and M. Kim. *Surface Plasmon Resonance: A Versatile Technique for Biosensor Applications*, *Sensors*, vol. 15, no. 5, pp. 10 481–10 510, 2015.

[198] Y. Tang, X. Zeng, and J. Liang. *Surface Plasmon Resonance: An Introduction to a Surface Spectroscopy Technique*, *Journal of Chemical Education*, vol. 87, no. 7, pp. 742–746, 2010.

[199] X. Zhou, Y. Yang, S. Wang, and X. Liu. *Surface Plasmon Resonance Microscopy: From Single-Molecule Sensing to Single-Cell Imaging*, *Angewandte Chemie International Edition*, vol. 59, no. 5, pp. 1776–1785, 2020.

[200] B. Huang, F. Yu, and R. N. Zare. *Surface Plasmon Resonance Imaging Using a High Numerical Aperture Microscope Objective*, *Analytical Chemistry*, vol. 79, no. 7, pp. 2979–2983, 2007.

[201] A. W. Peterson, M. Halter, A. Tona, and A. L. Plant. *High Resolution Surface Plasmon Resonance Imaging for Single Cells*, *BMC Cell Biology*, vol. 15, no. 1, p. 35, 2014.

[202] https://www.horiba.com/int/scientific/technologies/surface-plasmon-resonance-imaging/instrument-presentation.

[203] K. M. McPeak, S. V. Jayanti, S. J. P. Kress, S. Meyer, S. Iotti, A. Rossinelli, and D. J. Norris. *Plasmonic Films Can Easily Be Better: Rules and Recipes*, *ACS Photonics*, vol. 2, no. 3, pp. 326–333, 2015.

[204] L. Gao, F. Lemarchand, and M. Lequime. *Comparison of Different Dispersion Models for Single Layer Optical Thin Film Index Determination*, *Thin Solid Films*, vol. 520, no. 1, pp. 501–509, 2011.

[205] A. D. Rakić, A. B. Djurišić, J. M. Elazar, and M. L. Majewski. *Optical Properties of Metallic Films for Vertical-Cavity Optoelectronic Devices*, *Applied Optics*, vol. 37, no. 22, p. 5271, 1998.

[206] B. Ung and Y. Sheng. *Interference of Surface Waves in a Metallic Nanoslit*, *Optics Express*, vol. 15, no. 3, p. 1182, 2007.

[207] https://www.jawoollam.com.

[208] R. Boidin, T. Halenkovič, V. Nazabal, L. Beneš, and P. Němec. *Pulsed Laser Deposited Alumina Thin Films*, *Ceramics International*, vol. 42, pp. 1177–1182, 2016.

[209] R. Galceran, E. Gaufres, A. Loiseau, M. Piquemal-Banci, F. Godel, A. Vecchiola, O. Bezencenet, M.-B. Martin, B. Servet, F. Petroff, B. Dlubak, and P. Seneor. *Stabilizing Ultra-Thin Black Phosphorus with In-Situ-Grown 1 Nm-Al2O3 Barrier*, *Applied Physics Letters*, vol. 111, no. 24, p. 243101, 2017.

[210] N. Ullberg, A. Filoramo, S. Campidelli, and V. Derycke. *In Operando Study of Charge Modulation in MoS2 Transistors by Excitonic Reflection Microscopy*, *ACS Nano*, vol. XX, no. XX, pp. XXXX–XXXX, 2024.

[211] C. F. Klingshirn. *Semiconductor Optics, 4th ed.* Springer, 2012.

[212] N. Ma and D. Jena. *Carrier Statistics and Quantum Capacitance Effects on Mobility Extraction in Two-Dimensional Crystal Semiconductor Field-Effect Transistors*, *2D Materials*, vol. 2, no. 1, p. 015003, 2015.

[213] Y.-J. Yu, Y. Zhao, S. Ryu, L. E. Brus, K. S. Kim, and P. Kim. *Tuning the Graphene Work Function by Electric Field Effect*, *Nano Letters*, vol. 9, no. 10, pp. 3430–3434, 2009.

[214] M. S. Fuhrer and J. Hone. *Measurement of Mobility in Dual-Gated MoS2 Transistors*, *Nature Nanotechnology*, vol. 8, no. 3, pp. 146–147, 2013.

[215] B. Radisavljevic and A. Kis. *Reply to 'Measurement of Mobility in Dual-Gated MoS2 Transistors'*, *Nature Nanotechnology*, vol. 8, no. 3, pp. 147–148, 2013.

[216] A. Kis. *How We Made the 2D Transistor*, *Nature Electronics*, vol. 4, no. 11, pp. 853–853, 2021.

[217] D. S. Schulman, A. J. Arnold, and S. Das. *Contact Engineering for 2D Materials and Devices*, *Chemical Society Reviews*, vol. 47, no. 9, pp. 3037–3058, 2018.

[218] C. Kim, I. Moon, D. Lee, M. S. Choi, F. Ahmed, S. Nam, Y. Cho, H.-J. Shin, S. Park, and W. J. Yoo. *Fermi Level Pinning at Electrical Metal Contacts of Monolayer Molybdenum Dichalcogenides*, *ACS Nano*, vol. 11, no. 2, pp. 1588–1596, 2017.

[219] Y. Liu, J. Guo, E. Zhu, L. Liao, S.-J. Lee, M. Ding, I. Shakir, V. Gambin, Y. Huang, and X. Duan. *Approaching the Schottky–Mott Limit in van Der Waals Metal–Semiconductor Junctions*, *Nature*, vol. 557, no. 7707, pp. 696–700, 2018.

[220] M. Li, S. Biswas, C. U. Hail, and H. A. Atwater. *Refractive Index Modulation in Monolayer Molybdenum Diselenide*, *Nano Letters*, vol. 21, no. 18, pp. 7602–7608, 2021.

[221] C. Hu. *Modern semiconductor devices for integrated circuits*. Prentice Hall, 2010.

[222] K. Smaali, D. Guérin, V. Passi, L. Ordronneau, A. Carella, T. Mélin, E. Dubois, D. Vuillaume, J. Simonato, and S. Lenfant. *Physical Study by Surface Characterizations of Sarin Sensor on the Basis of Chemically Functionalized Silicon Nanoribbon Field Effect Transistor*, *The Journal of Physical Chemistry C*, vol. 120, no. 20, pp. 11 180–11 191, 2016.

[223] https://www.nanoworld.com/blog/kpfm-surface-photovoltage-measurement-and-numerical-simulation.

[224] L.-E. Cheran, S. Johnstone, S. Sadeghi, and M. Thompson. *Work-Function Measurement by High-Resolution Scanning Kelvin Nanoprobe*, *Measurement Science and Technology*, vol. 18, no. 3, pp. 567–578, 2007.

[225] M. Precner, T. Polaković, D. J. Trainer, A. V. Putilov, C. Di Giorgio, I. Cone, X. X. Xi, M. Iavarone, and G. Karapetrov. *Metastable Defects in Monolayer and Few-Layer Films of MoS2*, in *Proceedings of the International Workshop on Advanced Materials (IWAM-2017)*, vol. 2005. Berhampur, Odisha, India: AIP, 2018, p. 020004.

[226] K. M. Burson, W. G. Cullen, S. Adam, C. R. Dean, K. Watanabe, T. Taniguchi, P. Kim, and M. S. Fuhrer. *Direct Imaging of Charged Impurity Density in Common Graphene Substrates*, *Nano Letters*, vol. 13, no. 8, pp. 3576–3580, 2013.

[227] A. Senkić, A. Supina, M. Akturk, C. Gadermaier, M. Maiuri, G. Cerullo, and N. Vujičić. *Microscopic Investigation of Intrinsic Defects in CVD Grown MoS2 Monolayers*, *Nanotechnology*, vol. 34, no. 47, p. 475705, 2023.

[228] A. Arrighi, N. Ullberg, V. Derycke, and B. Grévin. *A Simple KPFM-Based Approach for Electrostatic-Free Topographic Measurements: The Case of MoS2 on SiO2*, *Nanotechnology*, vol. 34, no. 21, p. 215705, 2023.

[229] Y. Li, C.-Y. Xu, B.-Y. Zhang, and L. Zhen. *Work Function Modulation of Bilayer MoS2 Nanoflake by Backgate Electric Field Effect*, *Applied Physics Letters*, vol. 103, no. 3, p. 033122, 2013.

[230] R. Dagan, Y. Vaknin, A. Henning, J. Y. Shang, L. J. Lauhon, and Y. Rosenwaks. *Two-Dimensional Charge Carrier Distribution in MoS2 Monolayer and Multilayers*, *Applied Physics Letters*, vol. 114, no. 10, p. 101602, 2019.

[231] Y. Vaknin, R. Dagan, and Y. Rosenwaks. *Schottky Barrier Height and Image Force Lowering in Monolayer MoS2 Field Effect Transistors*, *Nanomaterials*, vol. 10, no. 12, p. 2346, 2020.

[232] A. Matković, A. Petritz, G. Schider, M. Krammer, M. Kratzer, E. Karner-Petritz, A. Fian, H. Gold, M. Gärtner, A. Terfort, C. Teichert, E. Zojer, K. Zojer, and B. Stadlober. *Interfacial Band Engineering of MoS2/Gold Interfaces Using Pyrimidine-Containing Self-Assembled Monolayers: Toward Contact-Resistance-Free Bottom-Contacts*, *Advanced Electronic Materials*, vol. 6, no. 5, p. 2000110, 2020.

[233] Y. Vaknin, R. Dagan, and Y. Rosenwaks. *Pinch-Off Formation in Monolayer and Multilayers MoS2 Field-Effect Transistors*, *Nanomaterials*, vol. 9, no. 6, p. 882, 2019.

[234] R. Dagan, Y. Vaknin, D. Weisman, I. Amit, and Y. Rosenwaks. *Accurate Method To Determine the Mobility of Transition-Metal Dichalcogenides with Incomplete Gate Screening*, *ACS Applied Materials & Interfaces*, vol. 11, no. 47, pp. 44 406–44 412, 2019.

[235] R. Dagan, Y. Vaknin, and Y. Rosenwaks. *Gap State Distribution and Fermi Level Pinning in Monolayer to Multilayer MoS2 Field Effect Transistors*, *Nanoscale*, vol. 12, no. 16, pp. 8883–8889, 2020.

[236] M. A. Aslam, T. H. Tran, A. Supina, O. Siri, V. Meunier, K. Watanabe, T. Taniguchi, M. Kralj, C. Teichert, E. Sheremet, R. D. Rodriguez, and A. Matković. *Single-Crystalline Nanoribbon Network Field Effect Transistors from Arbitrary Two-Dimensional Materials*, *npj 2D Materials and Applications*, vol. 6, no. 1, p. 76, 2022.

[237] S. G. Noyce, J. L. Doherty, S. Zauscher, and A. D. Franklin. *Understanding and Mapping Sensitivity in MoS2 Field-Effect-Transistor-Based Sensors*, *ACS Nano*, vol. 14, no. 9, pp. 11 637–11 647, 2020.

[238] F. Giannazzo, M. Bosi, F. Fabbri, E. Schilirò, G. Greco, and F. Roccaforte. *Direct Probing of Grain Boundary Resistance in Chemical Vapor Deposition-Grown Monolayer MoS2 by Conductive Atomic Force Microscopy*, *physica status solidi – Rapid Research Letters*, vol. 14, no. 2, p. 1900393, 2020.

[239] D. Wu, X. Li, L. Luan, X. Wu, W. Li, M. N. Yogeesh, R. Ghosh, Z. Chu, D. Akinwande, Q. Niu, and K. Lai. *Uncovering Edge States and Electrical Inhomogeneity in MoS2 Field-Effect Transistors*, *Proceedings of the National Academy of Sciences of the United States of America*, vol. 113, no. 31, pp. 8583–8588, 2016.

[240] Z. Chu, L. Zheng, and K. Lai. *Microwave Microscopy and Its Applications*, *Annual Review of Materials Research*, vol. 50, pp. 105–130, 2020.

[241] Y. Liu, C. Tan, H. Chou, A. Nayak, D. Wu, R. Ghosh, H.-Y. Chang, Y. Hao, X. Wang, J.-S. Kim, R. Piner, R. S. Ruoff, D. Akinwande, and K. Lai. *Thermal Oxidation of WSe2 Nanosheets Adhered on SiO2/Si Substrates*, *Nano Letters*, vol. 15, no. 8, pp. 4979–4984, 2015.

[242] D. Wu, W. Li, A. Rai, X. Wu, H. C. P. Movva, M. N. Yogeesh, Z. Chu, S. K. Banerjee, D. Akinwande, and K. Lai. *Visualization of Local Conductance in MoS2 / WSe2 Heterostructure Transistors*, *Nano Letters*, vol. 19, no. 3, pp. 1976–1981, 2019.

[243] M. H. Alam, Z. Xu, S. Chowdhury, Z. Jiang, D. Taneja, S. K. Banerjee, K. Lai, M. H. Braga, and D. Akinwande. *Lithium-ion electrolytic substrates for sub-1v high-performance transition metal dichalcogenide transistors and amplifiers*, *Nature Communications*, vol. 11, no. 1, p. 3203, 2020.

[244] M. Matsunaga, A. Higuchi, G. He, T. Yamada, P. Krüger, Y. Ochiai, Y. Gong, R. Vajtai, P. M. Ajayan, J. P. Bird, and N. Aoki. *Nanoscale-Barrier Formation Induced by Low-Dose Electron-Beam Exposure in Ultrathin MoS2 Transistors*, *ACS Nano*, vol. 10, no. 10, pp. 9730–9737, 2016.

[245] S. Tezuka, T. Seki, T. Ohnishi, H. Noguchi, M. Tanaka, M. Okochi, and Y. Hayamizu. *In Situ Bioimaging of Lactobacillus by Photoluminescence of MoS2*, *2D Materials*, vol. 7, no. 2, p. 024002, 2020.

[246] H. Zhu, F. Zhang, H. Wang, Z. Lu, H.-Y. Chen, J. Li, and N. Tao. *Optical imaging of charges with atomically thin molybdenum disulfide*, *ACS Nano*, vol. 13, no. 2, pp. 2298–2306, 2019.

[247] G. Scuri, Y. Zhou, A. A. High, D. S. Wild, C. Shu, K. De Greve, L. A. Jauregui, T. Taniguchi, K. Watanabe, P. Kim, M. D. Lukin, and H. Park. *Large Excitonic Reflectivity of Monolayer MoSe2 Encapsulated in Hexagonal Boron Nitride*, *Physical Review Letters*, vol. 120, no. 3, p. 037402, 2018.

[248] D. Vella, M. B. Barbosa, P. E. Trevisanutto, I. Verzhbitskiy, J. Y. Zhou, K. Watanabe, T. Taniguchi, K. Kajikawa, and G. Eda. *In-Plane Field-Driven Excitonic Electro-Optic Modulation in Monolayer Semiconductor*, *Advanced Optical Materials*, vol. 10, no. 4, p. 2102132, 2021.

[249] H. Zhu, Z. Chen, Y. Chen, and J. Zhu. *Affinities and Kinetics Detection of Protein–Small Molecule Interactions with a Monolayer MoS2-Based Optical Imaging Platform*, *Small*, vol. 18, no. 29, p. 2202622, 2022.

[250] X. Zhao, X.-L. Zhou, S.-Y. Yang, Y. Min, J.-J. Chen, and X.-W. Liu. *Plasmonic Imaging of the Layer-Dependent Electrocatalytic Activity of Two-Dimensional Catalysts*, *Nature Communications*, vol. 13, p. 7869, 2022.

[251] D. Vella, D. Ovchinnikov, N. Martino, V. Vega-Mayoral, D. Dumcenco, Y.-C. Kung, M.-R. Antognazza, A. Kis, G. Lanzani, D. Mihailovic, and C. Gadermaier. *Unconventional Electroabsorption in Monolayer MoS2*, *2D Materials*, vol. 4, no. 2, p. 021005, 2017.

[252] K. F. Mak, K. He, C. Lee, G. H. Lee, J. Hone, T. F. Heinz, and J. Shan. *Tightly bound trions in monolayer MoS2*, *Nature Materials*, vol. 12, no. 3, pp. 207–211, 2013.

[253] B. Mukherjee, F. Tseng, D. Gunlycke, K. K. Amara, G. Eda, and E. Simsek. *Complex electrical permittivity of the monolayer molybdenum disulfide (MoS2) in near UV and visible*, *Optical Materials Express*, vol. 5, no. 2, pp. 447–455, 2015.

[254] M. Khademi and D. P. J. Barz. *Structure of the Electrical Double Layer Revisited: Electrode Capacitance in Aqueous Solutions*, *Langmuir*, vol. 36, no. 16, pp. 4250–4260, 2020.

[255] Y. Zhao, M. Tripathi, K. Čerņevičs, A. Avsar, H. G. Ji, J. F. Gonzalez Marin, C.-Y. Cheon, Z. Wang, O. V. Yazyev, and A. Kis. *Electrical Spectroscopy of Defect States and Their Hybridization in Monolayer MoS2*, *Nature Communications*, vol. 14, p. 44, 2023.

[256] P. V. Kolesnichenko, Q. Zhang, T. Yun, C. Zheng, M. S. Fuhrer, and J. A. Davis. *Disentangling the Effects of Doping, Strain and Disorder in Monolayer WS2 by Optical Spectroscopy*, *2D Materials*, vol. 7, no. 2, p. 025008, 2020.

[257] M. M. Perera, M.-W. Lin, H.-J. Chuang, B. P. Chamlagain, C. Wang, X. Tan, M. M.-C. Cheng, D. Tománek, and Z. Zhou. *Improved Carrier Mobility in Few-Layer MoS2 Field-Effect Transistors with Ionic-Liquid Gating*, *ACS Nano*, vol. 7, no. 5, pp. 4449–4458, 2013.

[258] N. Peimyoo, T. Deilmann, F. Withers, J. Escolar, D. Nutting, T. Taniguchi, K. Watanabe, A. Taghizadeh, M. F. Craciun, K. S. Thygesen, and S. Russo. *Electrical Tuning of Optically Active Interlayer Excitons in Bilayer MoS2*, *Nature Nanotechnology*, vol. 16, no. 8, pp. 888–893, 2021.

[259] A. F. Rigosi, H. M. Hill, Y. Li, A. Chernikov, and T. F. Heinz. *Probing Interlayer Interactions in Transition Metal Dichalcogenide Heterostructures by Optical Spectroscopy: MoS2/WS2 and MoSe2/WSe2*, *Nano Letters*, vol. 15, no. 8, pp. 5033–5038, 2015.

[260] J. Wenus, R. Parashkov, S. Ceccarelli, A. Brehier, J.-S. Lauret, M. S. Skolnick, E. Deleporte, and D. G. Lidzey. *Hybrid Organic-Inorganic Exciton-Polaritons in a Strongly Coupled Microcavity*, *Physical Review B*, vol. 74, no. 23, p. 235212, 2006.

[261] K. Chen, A. Roy, A. Rai, H. C. P. Movva, X. Meng, F. He, S. K. Banerjee, and Y. Wang. *Accelerated Carrier Recombination by Grain Boundary/Edge Defects in MBE Grown Transition Metal Dichalcogenides*, *APL Materials*, vol. 6, no. 5, p. 056103, 2018.